

**IMPACT BEHAVIOUR OF ALKALI-ACTIVATED SLAG CONCRETE  
UNDER AMBIENT AND ELEVATED TEMPERATURE CONDITIONS**

**Ahmed Esmat Soltan Abubakr**

A Thesis  
In the Department  
of  
Building, Civil and Environmental Engineering

Presented in Partial Fulfillment of the Requirements  
For the Degree of  
Doctor of Philosophy (Civil Engineering) at  
Concordia University  
Montreal, Quebec, Canada

April 2021

© Ahmed Esmat Soltan Abubakr, 2021

**CONCORDIA UNIVERSITY**  
**school of graduate studies**

This is to certify that the thesis prepared

By: Ahmed Esmat Soltan Abubakr

Entitled: Impact Behaviour of Alkali-Activated Slag Concrete Under Ambient  
and Elevated Temperature Conditions

and submitted in partial fulfillment of the requirements for the degree of

**DOCTOR OF PHILOSOPHY (Civil Engineering)**

Complies with the regulations of the University and meets the accepted standards with respect to originality and quality.

Signed by the final examining committee:

_____	Chair
Dr. Roch Glitho	
_____	External Examiner
Dr. Khandaker Hossain	
_____	External to Program
Dr. Mehdi Hojjati	
_____	Examiner
Dr. Michelle Nokken	
_____	Examiner
Dr. Mohamed Ouf	
_____	Thesis Supervisor
Dr. Ahmed Soliman	

Approved by \_\_\_\_\_  
Graduate Program Director

April 19<sup>th</sup> 2021 \_\_\_\_\_  
Dean of Gina Cody School of Engineering &  
Computer Science

## **ABSTRACT**

### **Impact Behaviour of Alkali-Activated Slag Concrete Under Ambient and Elevated Temperature Conditions**

**Ahmed Esmat Soltan Abubakr, Ph.D.**

**Concordia university, 2021**

In military applications, concrete structures are intended to withstand impact loads induced by missiles and bombs. Under such attacks, elevated temperatures induced by fire are expected to increase the concrete damage. Several research studies have explored cement-based concrete performance under such loading conditions. However, limited studies in the literature investigated alkali-activated concrete behaviour under impact loads and elevated temperatures. Therefore, this dissertation aims to cover this knowledge gap regarding alkali-activated slag (AAS) impact behaviour.

A comprehensive experimental program was conducted to investigate the effects of activator nature on mechanical and impact performance of the developed AAS binding system at ambient and elevated temperatures. The results represented a benchmark for the following phase focusing on AAS concrete mixtures properties and degradation. Finally, the study assessed the potential enhancement in the static and dynamic performance by applying different strategies (i.e. rubber and fibre incorporations).

Generally, AAS exhibited better static and dynamic performance after exposure to elevated temperatures than ordinary Portland cement (OPC) systems. Alkali activator properties significantly affected AAS impact performance. Moreover, the difference in hydration products nature between AAS and OPC systems had a dominating effect. Improvement of impact

performance due to rubber addition was limited to ambient temperature and up to 200°C. At higher temperatures, the melting and decomposition of rubber eliminated the desired improvement. Fibre-reinforced alkali-activated slag concrete exhibited significantly higher mechanical properties and impact energy absorption capacity at ambient temperature. However, at elevated temperatures, the improvement was mainly controlled by the fibre stability at various temperature levels. Hence, the dissertation provides a fundamental understanding and first-time data on AAS impact behaviour at various exposure conditions, emphasizing different mixture ingredients' roles.

## CO-AUTHORSHIP STATEMENT

This thesis has been prepared in accordance with the regulation of the Faculty of Graduate Studies at Concordia University. Substantial parts of this thesis were either published in or submitted for publication to peer-reviewed technical journals and an international conference. All experimental work, data analysis, modeling process and writing of initial versions of all publications listed below were carried out by the candidate himself. The contribution of his research advisor and any other co-author, if applicable, consisted of either providing advice, and/or helping in the development of the final versions of publications:

1. “Effect of Activator Nature on The Impact Behavior of Alkali- Activated Slag Mortar”, A.E. Abubakr, A.M. Soliman, S.H. Diab. *Construction and Building Material Journal*, 257 (2020), Article 119531.
2. “Residual Impact Resistance of Alkali Activated Slag Systems After Elevated Temperature Exposure” Submitted to *Cement and Concrete Composites Journal*. manuscript number: CCC-D-20-01664
3. “Impact Behaviours of Alkali-Activated Slag Concrete after Exposure to Elevated Temperatures” Submitted to *Construction and Building Material Journal*, manuscript number: CONBULDMAT-D-21-00995
4. “The Impact Behaviour of Rubberized Alkali-Activated Concrete at Ambient and Elevated Temperatures” Submitted to *Construction and Building Material Journal*, manuscript number: CONBULDMAT-D-21-01792.
5. “Impact Behaviour of Steel Fibre-Reinforced Alkali-Activated Slag Concrete Exposed to Elevated Temperatures” Submitted to *Cement and Concrete Composites Journal*. manuscript number: CCC-D-21-00456
6. “Effects of Activator Properties on Impact Behavior of Alkali Activated Slag Mortar” CSCE Annual Conference, Laval (Greater Montreal). June 12-15, 2019.

7. “Review of Mechanical Properties and Durability of Alkali Activated Systems” CSCE Annual Conference, Laval (Greater Montreal). June 12-15, 2019.
8. “Impact Behavior of Alkali Activated Slag Concrete at Ambient and Elevated Temperatures” CSCE Annual Conference, May 24 and 25th, 2021.
9. “Effects of Fiber Type on The Performance of Fiber-Reinforced Alkali Activated Slag Concrete” Submitted to CSCE 2021 international conference” CSCE Annual Conference, May 24 and 25th, 2021.

## **ACKNOWLEDGMENTS**

I would like to acknowledge everyone who played a role in my academic achievements. Deep thanks to my supervisor, Dr. Ahmed Soliman, for his continuous support during my research period. I would like to thank my committee members for their fruitful academic guiding through my PhD. Moreover, I sincerely appreciate the Concordia staff and technicians for their cooperation.

Furthermore, I am so grateful to all the companies that supported my research through material donations: Lafarge Canada and Sika Canada.

## DEDICATION

TO MY LOVELY PARENTS, WHO WERE ALWAYS SUPPORTING ME WITH LOVE

AND UNDERSTANDING

“Esmat Soltan & Salwa Abdallah”

WITHOUT YOU, I COULD NEVER HAVE REACHED THIS LEVEL OF SUCCESS.

TO MY SISTER AND BROTHER

“NERMEEN & MOHAMED”

TO THE BEST IN MY LIFE

MY WIFE AND KIDS

“MARWA AHMED”

“FARES & SIRENE”

TO MY TEACHERS

AND

FRIENDS

## TABLE OF CONTENTS

<b>List of Figures .....</b>	<b>xv</b>
<b>List of Tables.....</b>	<b>xxiii</b>
<b>Nomenclature.....</b>	<b>xxiv</b>
<b>Chapter 1 Introduction.....</b>	<b>1</b>
1.1 Background and problem definition .....	1
1.2 Scope of work .....	4
1.3 Dissertation organization .....	5
<b>Chapter 2 Literature review .....</b>	<b>7</b>
2.1 Historical background.....	8
2.2 Types of precursors, activators and reaction models .....	9
2.2.1 Alumino-silicate precursors .....	9
2.2.2 Alkaline activator solutions .....	11
2.2.3 Reaction models and mechanisms .....	13
2.2.4 Hydration products.....	16
2.3 Durability of alkali-activated systems .....	16
2.3.1 Acid attack .....	16
2.3.2 Sulfate attack.....	17
2.3.3 Alkali silica reaction .....	18
2.3.4 Carbonation and permeability.....	19

2.4	Behaviour under impact loads .....	20
2.5	Behaviour of cementitious material under exposure to elevated temperature .....	24
<b>Chapter 3</b>	<b>Methodology &amp; Experimental work.....</b>	<b>26</b>
3.1	Introduction.....	26
3.2	Experimental work phases .....	26
3.2.1	Phase I.....	26
3.2.2	Phase II.....	28
3.2.3	Phase III .....	30
3.3	Material.....	33
3.3.1	Slag .....	33
3.3.2	Cement .....	33
3.3.3	Fine aggregate.....	34
3.3.4	Coarse aggregate.....	35
3.3.5	Chemical material.....	35
3.3.6	Crumb rubber .....	35
3.3.7	Fibre .....	37
3.3.8	Water.....	37
3.3.9	Admixtures.....	38
3.4	Testing procedures .....	38
3.4.1	Heat of hydration .....	38
3.4.2	X-Ray diffraction (XRD).....	38
3.4.3	Thermogravimetric analysis (TGA).....	39

3.4.4	Viscosity test.....	39
3.4.5	Workability .....	40
3.4.6	Compressive and tensile strength tests .....	40
3.4.7	Modulus of elasticity test.....	42
3.4.8	Shrinkage micro-strain test .....	43
3.4.9	Water absorption test .....	44
3.4.10	Ultra-sonic pulse velocity test (USPV).....	45
3.4.11	Drop weight impact test.....	46
3.5	Curing regime elevated temperatures exposure routine.....	48
 <b>Chapter 4 Effect of Activator Nature on the Impact Behaviour of Alkali-Activated Slag Mortar.....</b>		<b>50</b>
4.1	Introduction.....	50
4.2	Results and discussion .....	51
4.2.1	Flowability .....	51
4.2.2	Hydration products.....	53
4.2.2.1	Heat of hydration.....	55
4.2.2.2	X-Ray diffraction.....	57
4.2.2.3	Thermogravimetric analysis .....	59
4.2.3	Compressive strength.....	62
4.2.4	Tensile strength.....	69
4.2.5	Impact absorption.....	74
4.2.6	Ball Penetration.....	79

4.3	Conclusions.....	93
<b>Chapter 5 Impact Behaviours of Alkali-Activated Slag Concrete after Exposure to Elevated Temperatures .....</b>		<b>95</b>
5.1	Introduction.....	95
5.2	Results and discussion .....	96
5.2.1	Slump test .....	96
5.2.2	Under ambient conditions .....	97
5.2.2.1	Compressive strength .....	97
5.2.2.2	Tensile strength .....	99
5.2.2.3	Water absorption .....	102
5.2.2.4	Impact energy absorption capacity and penetration resistance .....	103
5.2.3	After exposure to elevated temperatures.....	105
5.2.3.1	Compressive strength .....	108
5.2.3.2	Tensile strength .....	109
5.2.3.3	Impact energy absorption capacity.....	112
5.3	Conclusions.....	115
<b>Chapter 6 Impact Behavior of Rubberized AAS Concrete at Ambient and Elevated Temperatures.....</b>		<b>117</b>
6.1	Introduction.....	117
6.2	Results and discussion .....	118
6.2.1	Degradation mechanism.....	118
6.2.2	Concrete compressive strength .....	120

6.2.3	Concrete tensile strength.....	123
6.2.4	Concrete static modulus of elasticity .....	126
6.2.5	Impact energy absorption.....	127
6.3	Conclusions.....	134
<b>Chapter 7 Impact Behaviour of Fibre Reinforced Alkali-Activated Slag Concrete</b>		
<b>Exposed to Elevated Temperatures..... 135</b>		
7.1	Polypropylene fibre.....	137
7.1.1	Compressive strength.....	139
7.1.2	Tensile strength.....	142
7.1.3	Modulus of elasticity.....	144
7.1.4	Impact energy absorption.....	146
7.2	Basalt fibre .....	153
7.2.1	Compressive strength.....	153
7.2.2	Tensile strength.....	155
7.2.3	Modulus of elasticity.....	158
7.2.4	Impact energy absorption.....	160
7.3	Steel fibre .....	167
7.3.1	Compressive strength.....	167
7.3.2	Tensile strength.....	170
7.3.3	Modulus of elasticity and modulus of resilience .....	173
7.3.4	Impact energy absorption.....	176
7.4	Conclusions.....	186

<b>Chapter 8</b>	<b>Summary, Conclusions and Recommendations</b> .....	<b>189</b>
<b>References</b>	.....	<b>193</b>

## List of Figures

Fig. 2.1 Example of different threateners against concrete structures.....	20
Fig. 2.2 Concrete damaging model proposed by. ....	21
Fig. 2.3 Failure modes of unconfined concrete vs confined concrete (Pham, Chen et al. 2018). 22	
Fig. 2.4 Failure modes of steel fibre reinforced concrete vs plain concrete .....	24
Fig. 2.5 Concrete deterioration mechanisms due to internal stresses during exposure to elevated temperatures (Fu and Li 2011).....	25
Fig. 3.1 Experimental work program phases. ....	26
Fig. 3.2 Phase I description and testing chart .....	27
Fig. 3.3 Phase II description and testing chart.....	29
Fig. 3.4 Phase III description and testing chart.....	31
Fig. 3.5 Detaled experimental work plan.....	32
Fig. 3.6 Sieve analysis of fine aggregate. ....	34
Fig. 3.7 Sieve analysis of coarse aggregate. ....	35
Fig. 3.8 Fine crumb rubber .....	36
Fig. 3.9 Sieve analysis of crumb rubber. ....	36
Fig. 3.10 Different types of fibre. ....	37
Fig. 3.11 Sample preparation for XRD test and TGA test.....	39
Fig. 3.12 Viscosity test setup for (MCR 502) rheometer. ....	40
Fig. 3.13 Compressive and tensile strength test setup for mortar and concrete specimens.....	42
Fig. 3.14 Modulus of elasticity test setup. ....	43
Fig. 3.15 Shrinkage micro-strain test setup. ....	44
Fig. 3.16 Water absorption test method.....	45

Fig. 3.17 Ultra-sonic pulse velocity (USPV) test. ....	45
Fig. 3.18 Schematic drawing for the drop weight impact test machine.....	46
Fig. 3.19 Drop weight impact test machine. ....	47
Fig. 3.20 Exposure to various elevated temperatures routine.....	48
Fig. 3.21 Specimen core temperature monitoring during exposure to elevated temperatures.....	49
Fig. 4.1 Different specimens of mixture (M 1-8) after demolding. ....	50
Fig. 4.2 Viscosity vs flowability for mixtures of $M_s=1$ . ....	53
Fig. 4.3 Reaction mechanism model for (Si+Ca) precursor activated with MOH .....	54
Fig. 4.4 Reaction mechanism model for (Si+Ca) precursor activated with M OH + water glass	55
Fig. 4.5 Heat of hydration for different silica modulus values at the same $Na_2O$ % dosage.....	56
Fig. 4.6 The heat of hydration evolution at different $Na_2O$ % dosages. ....	57
Fig. 4.7 X-ray diffraction patterns of AAS activated at different levels of Modulus ( $M_s$ ).....	58
Fig. 4.8 X-ray diffraction patterns of AAS activated at different levels of dosage ( $Na_2O\%$ ). ....	59
Fig. 4.9 Thermographic analysis (TGA) of hardened OPC vs. AAS with different levels of modulus ( $M_s$ ). ....	60
Fig. 4.10 Thermogravimetric analysis for binder before and after exposure to various elevated temperatures.....	62
Fig. 4.11 Compressive strength for various mixtures. ....	63
Fig. 4.12 TGA and TDG curves for mixtures of $M_s=1$ .....	64
Fig. 4.13 Early age compressive strength (3 days) at constant $Na_2O\%$ .....	65
Fig. 4.14 Compressive strength vs. Modulus at ages (3, 7 and 28) days.....	66
Fig. 4.15 Mortar residual compressive strength (%) after elevated temperature exposure. ....	67

Fig. 4.16 Thermographic analysis of AAS mixture M 1.5-8 after exposure to different levels of temperatures.....	68
Fig. 4.17 Mortar residual compressive strength at $M_s=1$ .....	69
Fig. 4.18 AAS mortar tensile strength.....	70
Fig. 4.19 Change in tensile strength with respect to compressive strength at (28 days).....	71
Fig. 4.20 Tensile strength development with age (7 to 28 days).....	72
Fig. 4.21 Tensile strength for various mixtures with 8% $Na_2O$ dosage.....	73
Fig. 4.22 Mortar residual tensile strength (%) after elevated temperature exposure.....	74
Fig. 4.23 Impact energy absorbed for various mixtures.....	75
Fig. 4.24 Impact energy absorbed at $Na_2O\%=4$ .....	76
Fig. 4.25 Impact energy absorbed at $Na_2O\%=8$ .....	76
Fig. 4.26 Drying shrinkage strain at $Na_2O\%=8$ .....	77
Fig. 4.27 Absorbed impact energy vs. compressive strength at different dosages.....	79
Fig. 4.28 Impact energy absorbed at $M_s=1.25$ .....	79
Fig. 4.29 Formation of hydrostatic core and large strain zone in a brittle material.....	80
Fig. 4.30 Formed large strain zone observed after sample failure.....	81
Fig. 4.31 Steel ball penetration level ( $L_p$ ) at $M_s=1$ .....	82
Fig. 4.32 Samples of $M_s=1$ at Steel ball penetration level of ( $L_p = -1.25$ mm).....	83
Fig. 4.33 Penetration resistance of mixtures with ( $M_s=1$ ) simulated by spring constant.....	85
Fig. 4.34 Thermographic analysis of OPC after exposure to different levels of temperatures.....	86
Fig. 4.35 Mortar residual impact absorption energy after elevated temperature exposure.....	87
Fig. 4.36 Mortar impact samples of $M_s=1$ after exposure to 600 °C at failure.....	87
Fig. 4.37 Thermographic analysis of AAS with different levels of dosage at the same $M_s=1.5$ .....	88

Fig. 4.38 X-ray diffraction patterns of AAS at different levels of exposure to elevated temperatures (200, 400, and 600 °C) .....	89
Fig. 4.39 Residual impact absorption capacity vs. residual weight after exposure to different levels of temperatures for M 1.5-8.....	90
Fig. 4.40 Thermographic analysis of AAS activated by NaOH ( $M_s=0$ ) after exposure to different levels of temperatures. ....	92
Fig. 5.1 Cont'd AAS and OPC prepared concrete specimens. ....	96
Fig. 5.2 Concrete compressive strength at 28 days.....	97
Fig. 5.3 Compressive strength Vs binder weight loss.....	98
Fig. 5.4 Ultrasonic pulse velocity results for AAS concrete mixtures.....	99
Fig. 5.5 Concrete tensile strength at 28 days. ....	100
Fig. 5.6 Concrete impact energy absorption capacity at ambient temperature.....	101
Fig. 5.7 Concrete drying shrinkage micro-strain. ....	102
Fig. 5.8 AAS concrete water absorption capacity.....	103
Fig. 5.9 Concrete impact force vs penetration model. ....	104
Fig. 5.10 Concrete impact force vs penetration. ....	105
Fig. 5.11 Cont'd SEM of mixture 1.25-6 after exposure to various elevated temperatures. ....	107
Fig. 5.12 Residual compressive strength percentage after exposure to elevated temperatures. .	109
Fig. 5.13 Concrete residual tensile strength (%) after elevated temperature exposure.....	110
Fig. 5.14 Cont'd Concrete specimens exposed to various elevated temperatures after tensile strength test. ....	112
Fig. 5.15 Residual impact energy absorption capacity after exposure to temperatures.....	113
Fig. 5.16 Failure modes of impact test specimens exposed to 400 °C.....	115

Fig. 6.1 Effect of various elevated temperatures on rubber particles. ....	118
Fig. 6.2 Thermogravimetric analysis (TGA) of rubber.....	119
Fig. 6.3 Compressive strength for all mixtures at ambient temperature. ....	121
Fig. 6.4 Ultrasonic pulse velocity results for various tested concrete mixtures. ....	122
Fig. 6.5 Concrete residual compressive strength (%) after elevated temperature exposure. ....	123
Fig. 6.6 Tensile strength for all mixtures at ambient temperature. ....	124
Fig. 6.7 Drying shrinkage micro-strain for all mixtures at ambient temperature. ....	125
Fig. 6.8 Concrete residual tensile strength (%) after elevated temperature exposure.....	126
Fig. 6.9 Concrete modulus of elasticity before and after exposure to elevated temperature.....	127
Fig. 6.10 Concrete impact absorption for plain and rubber AAS concrete.....	128
Fig. 6.11 Concrete dynamic increase factor (DIF) at different levels of rubber incorporation. .	129
Fig. 6.12 Steel ball penetration level vs applied impact force. ....	130
Fig. 6.13 The effect of various elevated temperatures on impact test samples. ....	131
Fig. 6.14 Concrete residual impact energy absorption after exposure to various elevated temperatures levels.....	132
Fig. 6.15 Concrete modulus of resilience Vs modulus of elasticity at ambient and various elevated temperatures. ....	133
Fig. 7.1 Cylinder fibre reinforced AAS concrete specimens before and after exposure to elevated temperatures.....	135
Fig. 7.2 AAS plain and polypropylene fibre concrete water absorption. ....	138
Fig. 7.3 Polypropylene fibre mechanism during exposure to elevated temperatures. ....	139
Fig. 7.4 Compressive strength of plain and polypropylene fibre concrete at 7 and 28 days. ....	140
Fig. 7.5 Residual compressive strength after exposure to elevated temperatures. ....	141

Fig. 7.6 Tensile strength of plain and fibre reinforced concrete at 7 and 28 days.....	142
Fig. 7.7 Residual splitting tensile strength after exposure to elevated temperatures.....	143
Fig. 7.8 AAS polypropylene fibre of content 1% at failure before and after exposure to elevated temperatures.....	144
Fig. 7.9 stress zoning due to polypropylene fiber clumping at high contents. ....	145
Fig. 7.10 Modulus of elasticity of polypropylene fibre concrete before and after exposure to elevated temperatures.....	146
Fig. 7.11 Impact energy absorption of plain and fibre AAS at ambient temperature.....	147
Fig. 7.12 Drying shrinkage micro-strain of AAS concrete with different contents of fibre.....	148
Fig. 7.13 Impact ductility index of AAS with different fibre content. ....	149
Fig. 7.14 Residual impact absorption capacity of PFC after exposure to various elevated temperatures.....	151
Fig. 7.15 Number of successive blows after the first visual crack for PFC.....	152
Fig. 7.16 Concrete compressive strength at ambient temperature.....	153
Fig. 7.17 Effect of fiber density on the crack limiting ability.....	154
Fig. 7.18 Residual compressive strength of AAS plain and basalt fibrous concrete after exposure to various elevated temperatures.....	155
Fig. 7.19 Concrete tensile strength at ambient temperature.....	156
Fig. 7.20 Main and secondary developed cracks during splitting tensile test.....	157
Fig. 7.21 AAS plain and basalt fiber concrete drying shrinkage micro-strain. ....	158
Fig. 7.22 Residual tensile strength of AAS plain and basalt fibrous concrete after exposure to various elevated temperatures.....	158

Fig. 7.23 Modulus of elasticity of AAS plain and basalt fiber concrete before and after exposure to various elevated temperatures.....	160
Fig. 7.24 Impact energy absorption of plain and fibrous concrete at ambient temperature. ....	160
Fig. 7.25 Different crack propagation behavior according to the load strain rate. ....	161
Fig. 7.26 Fiber crack bridging after development of the 1st crack. ....	162
Fig. 7.27 Penetration level achieved by the steel ball below the concrete specimen surface. ....	163
Fig. 7.28 Failure of AAS basalt fiber concrete with different fiber contents. ....	164
Fig. 7.29 Residual impact absorption capacity of BFC after exposure to various elevated temperatures.....	165
Fig. 7.30 Number of successive blows after the first visual crack for BFC. ....	166
Fig. 7.31 Compressive strength of plain and steel fibre concrete at ambient temperature. ....	168
Fig. 7.32 Ultra-sonic pulse velocity of all concrete mixtures. ....	169
Fig. 7.33 Residual compressive strength of all concrete mixtures after exposure to different levels of elevated temperatures. ....	170
Fig. 7.34 Tensile strength of plain and steel fibre concrete at ambient temperature. ....	171
Fig. 7.35 Specimen's failure after tensile strength test at ambient temperature.....	171
Fig. 7.36 Concrete drying shrinkage micro-strain. ....	172
Fig. 7.37 Concrete residual tensile strength after exposure to different levels of elevated temperatures.....	173
Fig. 7.38 Concrete modulus of elasticity at ambient temperature and after exposure to various elevated temperatures.....	174
Fig. 7.39 Concrete modulus of resilience at ambient temperature and after exposure to various elevated temperatures.....	176

Fig. 7.40 Concrete Impact energy absorption capacity at ambient temperature.....	177
Fig. 7.41 Steel fibre concrete dynamic increase factor (DIF).....	178
Fig. 7.42 Steel fibre mechanism to limit the initiated crack propagation. ....	179
Fig. 7.43 Cont'd First crack and secondary developed cracks at the failure of AAS concrete. .	180
Fig. 7.44 Penetration level by steel ball below AAS fibrous and the plain concrete surface. ....	181
Fig. 7.45 Relative residual impact absorption capacity vs the binder relative weight loss during exposure to elevated temperatures. ....	182
Fig. 7.46 Number of successive blows after the first visual crack for SFC.....	184
Fig. 7.47 Residual impact absorption capacity of SFC after exposure to various elevated temperatures.....	185

## **List of Tables**

Table 3.1 Chemical and physical properties of slag .....	33
Table 3.2 Chemical and physical properties of cement and slag.....	34
Table 3.3 Specifications of different fibre.....	37
Table 4.1 Mixture proportions.....	51
Table 4.2 Flowability measurements.....	52
Table 5.1 Selected concrete mixture proportions.....	96
Table 5.2 Slump measures of fresh concrete .....	97
Table 6.1 Concrete mixture proportions.....	117
Table 7.1 plain concrete and Fibre reinforced Concrete mixing proportions.....	136
Table 7.2 Number of successive blows at 1 <sup>st</sup> crack and failure of PFC.....	149
Table 7.3 Number of successive blows at 1 <sup>st</sup> crack and failure of BFC.....	166
Table 7.4 Number of successive blows at 1 <sup>st</sup> crack and failure of SFC.....	183

## Nomenclature

<i>AAM</i>	<i>Alkali Activated Material</i>
<i>AAS</i>	<i>Alkali Activated Slag</i>
<i>AASHTO</i>	<i>American Association of State Highway and Transportation Officials</i>
<i>ACI</i>	<i>American Concrete Institute</i>
<i>AF<sub>m</sub></i>	<i>Aluminate-Ferrite-Mono Sulfate</i>
<i>Al</i>	<i>Alumina</i>
<i>ASTM</i>	<i>American Society for Testing and Materials</i>
<i>BFC</i>	<i>Basalt Fiber Concrete</i>
<i>Ca</i>	<i>Calcium</i>
<i>CR</i>	<i>Rubberized Concrete</i>
<i>D</i>	<i>Diameter</i>
<i>DIF</i>	<i>Dynamic Increase Factor</i>
<i>D<sub>P</sub></i>	<i>Penetration Depth</i>
<i>ε</i>	<i>Strain</i>
<i>E<sub>d</sub></i>	<i>Dynamic Modulus Of Elasticity</i>
<i>EDX</i>	<i>Energy Dispersive X-Ray</i>
<i>E<sub>s</sub></i>	<i>Static Modulus Of Elasticity</i>
<i>F</i>	<i>Force</i>
<i>FA</i>	<i>Fly Ash</i>
<i>F<sub>p</sub></i>	<i>Penetration Force</i>
<i>g</i>	<i>Gravity Acceleration</i>
<i>GU</i>	<i>General Use</i>
<i>H</i>	<i>Height</i>
<i>H<sub>t</sub></i>	<i>Hydrotalcite</i>
<i>K</i>	<i>Spring Constant</i>

<b><i>K<sub>b</sub></i></b>	<b><i>Basicity Coefficient</i></b>
<b><i>ke</i></b>	<b><i>Kinetic Energy</i></b>
<b><i>L<sub>P</sub></i></b>	<b><i>Penetration Level</i></b>
<b><i>M<sub>s</sub></i></b>	<b><i>Silica Modulus</i></b>
<b><i>Na</i></b>	<b><i>Sodium</i></b>
<b><i>N<sub>c</sub></i></b>	<b><i>Number of Blows At First Crack</i></b>
<b><i>N<sub>f</sub></i></b>	<b><i>Number of Blows At Failure</i></b>
<b><i>°C</i></b>	<b><i>Celsius Degree</i></b>
<b><i>OH</i></b>	<b><i>Hydroxide</i></b>
<b><i>OPC</i></b>	<b><i>Ordinary Portland Cement</i></b>
<b><i>P</i></b>	<b><i>Penetration</i></b>
<b><i>PC</i></b>	<b><i>Plain Concrete</i></b>
<b><i>P<sub>f</sub></i></b>	<b><i>Penetration at Failure</i></b>
<b><i>PFC</i></b>	<b><i>Polypropylene Fiber Reinforced Concrete</i></b>
<b><i>pH</i></b>	<b><i>Potential of Hydrogen</i></b>
<b><i>s</i></b>	<b><i>Second</i></b>
<b><i>S</i></b>	<b><i>Slope</i></b>
<b><i>SEM</i></b>	<b><i>Scanning Electron Microscopy</i></b>
<b><i>SFC</i></b>	<b><i>Steel Fiber Reinforced Concrete</i></b>
<b><i>Si</i></b>	<b><i>Silica</i></b>
<b><i>TGA</i></b>	<b><i>Thermogravimetric Analysis</i></b>
<b><i>USPV</i></b>	<b><i>Ultra-Sonic Pulse Velocity</i></b>
<b><i>V</i></b>	<b><i>Velocity</i></b>
<b><i>w/b</i></b>	<b><i>Water to Binder Ratio</i></b>
<b><i>X</i></b>	<b><i>Displacement</i></b>
<b><i>XRD</i></b>	<b><i>X-Ray Diffraction</i></b>
<b><i>ρ</i></b>	<b><i>Density</i></b>

**Chapter 1 Introduction**

**1.1 Background and problem definition**

Throughout human history, nations' civilizations were always recognized through their construction. Egyptian, Roman, and Incan are examples of inspiring civilizations who left us a hefty fortune proving their ample knowledge, especially in the construction and building sector. Their buildings were even considered miracles during this period. Natural rocks were mostly used in building, such as in Giza pyramids. Other buildings, such as temples, were involved by binder materials to shape their great art in architectural masterpieces. Hence, construction material development and enhancement became a primary target to meet the construction sector's needs with time.

Binder materials were always a matter of study as they are an essential element for any construction process. For the last decades, ordinary Portland cement (OPC) has been the main binder material, and the demand for OPC has been continuously increasing as infrastructure activities grow worldwide. Approximately 15 billion tons of concrete are produced annually by the concrete industry, consuming about 2 billion tons of OPC (Malhotra and Mehta 2002). However, for many concerns, developing a new binder material became a must.

Environmentally, carbon dioxide (CO<sub>2</sub>) emission to the atmosphere is the main concern reaching uncontrollable levels (Costello, Abbas et al. 2009). Cement manufacture contributes about 5~7% of the globe CO<sub>2</sub> emission (Huntzinger and Eatmon 2009, Meyer 2009, Turner and Collins 2013). Moreover, as recorded by the International Energy Authority, the cement industry

is responsible for consuming about 5% of the worldwide industrial energy (Hendriks, Worrell et al. 1998). Besides, cement production consumes considerable amounts of virgin materials and natural resources. For all these reasons, the scientific community focused on finding a new technique to develop a modern binder material with a lower environmental impact.

While many green labelling programs were established, some industrial sectors were suffering from massive amounts of waste material with different natures. Many byproducts, which have high silica and alumina content, did attract the scientific community interest to be used in construction materials, such as fly ash, silica fume, and slag. Recycling these byproducts through a new production phase will reduce the industrial negative environmental impact, save disposing of cost, and convert it to a valuable product. All that together paved the way for this aluminosilicates rich material to be a good alternative binder to OPC.

This new binding system is known as alkali-activated materials (AAM). The term (alkali-activated) came through the aluminosilicate precursor activation using an alkaline solution. Under highly alkaline conditions, reactive aluminosilicates are rapidly dissolved, and free  $[\text{SiO}_4]^-$  and  $[\text{AlO}_4]^-$  tetrahedral units are released in the solution. By sharing oxygen atoms, these tetrahedral units are alternatively linked to the polymeric precursor to form Si–O–Al–O bonds (Malhotra and Mehta 2002). Many alkaline solutions such as sodium hydroxide (NaOH), potassium hydroxide (KOH), sodium silicate ( $\text{Na}_2\text{SiO}_3$ ), and potassium silicate ( $\text{K}_2\text{SiO}_3$ ) were used as an activator, whose chemical composition was found to have different effects on the final products. These binders (i.e. AAM) are characterized by low  $\text{CO}_2$  emission (Davidovits 1993, Turner and Collins 2013). They were reported to have superior properties, including high chemical resistance (Singh, Ishwarya et al. 2015), outstanding mechanical properties (Gruskovnjak, Lothenbach et al. 2006, Neupane, Chalmers et al. 2018), and durability performance compared to that of the OPC systems

## *Chapter 1*

(Cheema, Lloyd et al. 2009, Singh, Ishwarya et al. 2015, Neupane, Chalmers et al. 2018). Then, as a good candidate for the green concrete technology.

On the other side, durability was always an important target to achieve to flatten the maintenance curve with time. For such reason, other types of concrete, including high and ultra-high-performance concrete, were developed having better mechanical properties and higher resistance to degradation agents such as acid attack and sulphate attack, carbonation and permeability. As a result, the changeable concrete behaviour with its different types was always a matter of study to standardize required properties for structural design purposes. Moreover, the response to different types of loads was identified as dependent on the concrete type or grade since concrete as a brittle material is sensitive to strain rates. For instance, the conventional static loading properties cannot be used to predict the behaviour under high strain rate loading, such as impact loads.

Under impact loads, a large amount of energy is transferred to the concrete over a very short period. Many techniques were developed to assess concrete's energy absorption capacity to identify its resistance to such load. A great job was also done to develop new methodologies to enhance the concrete performance under impact loads and to implement the output results and the variation in the concrete modified properties into the structural design codes used around the world.

A wide sector of field applications has a critical need to use concrete with high resistance to impact loads such as military applications. In military attacks, concrete structure threatens are mainly missiles or projectiles, which will produce a single point impact load or a blasting wave (distributed impact), and in most cases, it is accompanied by elevated temperatures induced by fire. For such an application, OPC systems would not be the best choice due to their un-pretentious

resistance to elevated temperatures due to the nature of the formed hydration products. Conversely, AAM was found to have high chemical and physical stability during exposure to elevated temperatures (Rashad, Sadek et al. 2016). However, the hydration products nature is mainly dependent on the synthesizing process of these binders. Many studies were done to understand the behaviour of AAM towards impact loads. However, limited studies investigated the effect of the synthesizing process on the behaviour. While the impact behaviour after exposure to elevated temperatures is not understood yet, a good understanding of the synthesizing process should be provided to evaluate properties and how elevated temperature exposure will affect behaviour. The maximum benefit of the synthesizing process to achieve adequate impact resistance after elevated temperature exposure can be achieved. Moreover, it's essential to assess how successful are the possible techniques to enhance this behaviour. This would help to provide the design manual's developers with the different measures needed to articulate the effect of various conditions such as elevated temperatures on the static and dynamic mechanical properties of alkali-activated material.

## **1.2 Scope of work**

To address the aforementioned research needs, the fundamental theme of this research is improving the current level of knowledge on the impact behaviour of AAS under ambient and elevated temperature conditions. The specific objectives of the research are multi-fold:

- 1- Investigate the effect of using different activator properties in sodium oxide dosage ( $\text{Na}_2\text{O}\%$ ) and silica modulus ( $M_s$ ) in synthesizing alkali-activated slag mortar. The first step is to understand the activator nature's effect on alkali-activated binder behaviour exposed to both static and impact loading. Also, the behaviour of the AAS mortar after exposure to elevated temperature conditions will be studied.

## *Chapter 1*

- 2- For the concrete level, mixtures will be investigated to optimize a balanced performance through studying the behaviour based on different criteria's such as mechanical properties (static), impact resistance and behaviour after elevated temperature exposure.
- 3- Investigating the achieved enhancement in impact behaviour of AAM through rubber incorporation as a passive agent to dissipate the absorbed impact energy, and how stable is this technique during exposure to various elevated temperatures, and what is the optimum incorporation level regarding the effect of each temperature level.
- 4- Investigate the ability of different fibre types with different contents to boost the impact energy absorption capacity of AAM concrete after exposure to different elevated temperatures levels.

### **1.3 Dissertation organization**

The targeted goals are to optimize a synthesizing process of AAM, then to control the required criteria serving the main purpose of the developed concrete, and finally, to achieve possible benefits of the proposed enhancement techniques. This dissertation covers all the mentioned tasks through seven chapters.

**Chapter 1** states the recent advances and the problem background, and the main research objectives. **Chapter 2** provides a review about the alkali-activated material commence, the reaction models, the hydration products, and the different consequent properties. **Chapter 3** details the conducted experimental work program, the material properties and specifications, and the performed tests to achieve the research goals. **Chapter 4** focuses on the synthesizing and activation process of alkali-activated slag (AAS) mortar to understand the activator nature's effect on the activator dosage and the silica modulus the impact behaviour at ambient temperature and after exposure to various elevated temperatures. **Chapter 5** discusses AAS concrete's behaviour

## *Chapter 1*

regarding three main criteria; the static mechanical properties, the impact behaviour, and the deterioration level after exposure to elevated temperatures. **Chapter 6** represents the positive and the opposing sides of using crumb rubber as a sand replacement regarding the impact behaviour at ambient temperature and after exposure to elevated temperatures. **Chapter 7** evaluates the capability of different fibre types to enhance AAS concrete's performance towards impact loads after exposure to various elevated temperatures and the limitations for each type regarding the exposure temperature level. **Chapter 8** briefs the general research conclusions, the research contribution significance, and the recommended future work.

**Chapter 2 Literature review**

During the last few decades, the scientific community sought an alternative to the ordinary Portland cement (OPC) systems to overcome environmental and durability problems. Cement industry as one of the most important industrial sectors is responsible for a major portion of the worldwide industrial energy consumption as reported by the International Energy Authority (Hendriks, Worrell et al. 1998). Also, carbon dioxide (CO<sub>2</sub>) emissions is reaching unacceptable levels which have a severe effect on the climate changes (Keller, Feng et al. 2014). Moreover, OPC concrete structures recently showed a low potential having different durability problems due to deterioration, which consequently raise the cost demand for repair. Many cases for deteriorated structures were mentioned by researchers. For example, around 250,000 bridges out of 600,000 bridges existed in the United States were classified to require major repair as a result of corrosion deterioration. The estimated cost for the required repair hit the amount of 50 billion dollars (Pacheco-Torgal, Castro-Gomes et al. 2008). Other deteriorating symptoms such as carbonation, acid attack, sulphate attack, alkali silica reactions were reported by the construction material community (Gruber, Ramlochan et al. 2001, Beddoe and Dorner 2005, Chang and Chen 2006, Rozière, Loukili et al. 2009). Therefore, the demand for alternative binder system is turning a necessity. Alkali-activated material (AAM) as a promising candidate for the binding systems acquired the scientific community attraction. While, this new binders systems are still in its development early stages, the research work carried out so far showed superior performance comparing to that of OPC (Bakharev, Sanjayan et al. 2003, Olivia and Nikraz 2012, Kupwade-Patil and Allouche 2013).

## **2.1 Historical background**

In the early forties of the last century, Victor Glukhovsky, as one of the godfathers for AAM science, had investigated the ancient Egyptians' structures. He believed that the used binders were composed of alumino-silicate calcium hydrates (Glukhovsky 1959). Also, he had the first assumption that the formation of sedimentary rocks in their zeolite form takes place through a geological process, in which, under certain temperature and pressure conditions, the volcanic rocks turn to the form of zeolite. Then, he assumed that this process might be used as a cementitious system model. He also believed that controlling such a phase composition of alumino-silicate minerals can lead to highly durable artificial zeolite-like material. This proposed cementitious system was firstly named "soil silicates" (Glukhovsky 1959, Glukhovsky 1965). On this basis, he investigated the possible ways to develop alkali-activated binders using ground alumino-silicates and rich alkalis industrial wastes. Later in 1972, Davidovits presented the expression "tri dimensional alumino-silicates" to describe the naturally formed zeolite-like materials. Then, to provide a chemical description of the formed phases, he proposed a formula shaping the poly (sialate) types as chains accommodating Si and Al species by sharing oxygen in coordination depending on the degree of polycondensation (Davidovits 1988). In 1978, Davidovits represented the first clear methodology to produce alkali-activated metakaolin (Davidovits and Cordi 1979). However, he highlighted a difference between the geopolymerization process, which involves leaching, diffusion and condensation, and the zeolite formation in which there are nucleation and crystal growth. Also, he stated that the temperature needed for each process is different (Davidovits 1991). During and After this period, many researchers studied the development of alumino-silicate binders based on that model (Davidovits 1984, Davidovits 1994). A few years later, other researchers implemented chemical thermodynamic analysis to understand the formation of the

geopolymer binder as a commonly used expression. They assumed that the binder phase formation occurs through the agglomeration of zeolite nano-crystallites bonded by a gel described as an alumino-silicate gel (Provis, Lukey et al. 2005, Provis 2006). Recently, abundant names and descriptions were committed to the alkali-activated systems. Alkali bounded ceramics and alkali-activated cement are examples of the used terms to describe this novel binder's system. However, the common essential factor in all cases is the alkali activation. Alumino-silicate precursors such as slag, fly ash, and silica fume attracted the researcher's attention to be used as binders through an activation process. All these precursors are considered as by-product waste. Hence, implementing them into the construction material sector will lead to both economic and environmental benefits. A crucial investigation was made at the beginning to figure out the adequate activators and the nature of the reaction products for each class of activator (Glukhovskiy, Rostovskaja et al. 1980, Glukhovskiy 1981). Since that time, studies in this area have been increasing exponentially. Moreover, alkali-activated systems were implemented in many applications. However, the wide spreading of this generation of binders is still limited and restricted by a good understanding of the chemical composition and the mechanical and thermal behaviour. Rather than that, AAM must overcome the conservative industrial community's barrier to accept the implementation of such new technology since it has many advantages compared to the ordinary Portland cement.

## **2.2 Types of precursors, activators and reaction models**

### **2.2.1 Alumino-silicate precursors**

The nature of each type of precursors has a great effect on the final product's properties and behaviour. Firstly, the precursor effect on the reaction mechanism will consequently affect the nature and the chemical composition of the binder phase at its final profile. A variety of alumino-

## *Chapter 2*

silicate materials such as kaolinite, mine tailing and industrial by-products such as fly ash and slag have been used as solid raw materials in the alkali-activated systems. The reactivity of these alumino-silicate sources depends on their chemical make-up and composition. Generally, while the chemical profile of some materials that are used as precursors such as metakaolinite (a product of heating the mineral kaolin up to 600 °C to 800 °C) depends mainly on the chemical weathering of these formed minerals, the chemical composition of precursors in case of industrial waste by-product materials depends on the chemical make-up of the original manufacture process. Moreover, treatment processes, such as calcination, were also an influential factor that enhances early strength. Those that were not calcination processed exhibited their higher strength at later ages (Barbosa, MacKenzie et al. 2000, Van Jaarsveld, Lukey et al. 2000, Xu and Van Deventer 2000, Xu, Van Deventer et al. 2001). Besides, at some cases, alkali-activated systems that are synthesized using multiple alumino-silicates source might be beneficial by exploiting their chemical composition and physical properties. However, the associated reaction mechanism needs to be optimized by developing the proper activation conditions in terms of activator type, activator properties and activator pH. On another scale, the hydraulic activity of the alumino-silicate precursor represented in its chemical composition is important to understand the alkali activation process needs. Various ways can be used to calculate the hydraulic activity of the alumino-silicate precursors. One of them is to calculate the basicity coefficient ( $K_b$ ). The basicity of precursor material is the ratio of basic constituents' total content to acidic constituents' total content. Then, the basicity coefficient ( $K_b$ ) can be used as a partial determinant for the activator properties (Chang 2003). knowing this coefficient helps choose the most suitable activator properties. Secondly, From the reaction mechanism perspective, depending on the precursor chemical composition, there are two models of alkali activation processes. The first case is when the precursor primarily

contains Silicates and Calcium, such as slag. In this case, activation takes place by low to mild alkaline solution. The product will be (C-S-H) gel-like OPC hydration products but with a lower Ca/Si ratio. The second mechanism involves activating a material containing primarily silicates and aluminates like fly ash using a highly alkaline solution. This reaction will form an inorganic binder through the polymerization process, and the term geopolymer is used to characterize this type of reaction. The geopolymer reaction differentiates geopolymers from other types of AAM (such as alkali-activated slag) since the product is geopolymer rather than C-S-H gel. It is reported that the hydration products of metakaolin or fly ash (FA) activation are zeolite type which is sodium alumino-silicate hydrate gels with different Si/Al ratio. In contrast, the major phase produced in case of slag activation is calcium silicate hydrate with a low Ca/Si ratio.

### **2.2.2 Alkaline activator solutions**

Different types of alkaline activators were used with alkali-activated systems such as sodium hydroxide, potassium hydroxide, sodium silicate, sodium carbonates (Palomo, Grutzeck et al. 1999, Hardjito, Wallah et al. 2004, Fernández-Jiménez and Palomo 2005). Many researches stated that the activated material characteristics are dominated by the selection of the alkaline activator properties. Among all these types, sodium hydroxide mixed with sodium silicates was the most efficient alkaline activator solution. Moreover, the type of used precursor is also a determinant for the activator properties selection. For precursors whose main constituents are (Si+Al) such as fly ash, the activation reaction of internal Si and Al components is initiated by the breakage of the glassy chain of fly ash, which is provoked by the high alkalinity of the solution. Nevertheless, in (Ca+Si) precursors such as slag, by using alkaline activator solution which does not contain silicates such as sodium hydroxide, the product is a semi-crystalline long linear chain of calcium silicate hydrate (C-S-H) with a C/S ratio of (0.8 – 1.0). However, by incorporating silicate species

## Chapter 2

in the alkaline solution, the silicate ions dissolved from precursor and supplied by the activator during the reaction provide the system with the necessary species to promote reactions  $\text{Ca}^{2+}$  ions released from the alumino-silicate source. As the reaction progresses further, the activator's silicate ions become depleted, but precursor dissolution continues. Condensation and accommodating these species through cross-linking leads to gelation forming C-S-H with a low to moderate Ca/Si ratio of (0.6 – 0.8) (Wang and Scrivener 1995, Fernández-Jiménez, Puertas et al. 2003, Wang and Scrivener 2003). To control the activation reaction, alkali activating solutions were found to have two predominant properties. These two characteristics were proposed to describe the chemical composition of the activator as well as its amount. The dosage of an activator accompanied by the modulus can describe this activator's ability to dissolve the alumino-silicate source and the ability to supply the system by Si species. Dosage of activator ( $\text{Na}_2\text{O}\%$ ) is the amount of sodium oxide  $\text{Na}_2\text{O}$  as a ratio of the binder weight, which is a function of the bulk concentration of hydroxide ions. This determinant is responsible for controlling the surface concentration of hydroxide ions, which directly affects the precursor particles' dissolution rate. It improves the dissolution rate of Si and Si–Al phases, leading to high Si and Al contents in the aqueous phase of alkali-activated systems. This will later help form the hydration product depending on each alumino-silicate's chemical composition; there is a threshold for  $\text{Na}_2\text{O}\%$  dosage, after which no further significant benefit is achieved. Moreover, detrimental properties such as brittleness may increase at higher  $\text{Na}_2\text{O}\%$  dosage due to more free alkalis in the product (Metso and Kajaus 1983, Parameswaran 1986, Wang, Scrivener et al. 1994). The other main property of an alkaline activator is the activator modulus ( $M_s$ ). Activator modulus is the ratio of  $\text{SiO}_2$  to  $\text{Na}_2\text{O}$  in the activator. Soluble silicates incorporation enriches the aqueous phase with silica species, accommodated by the Al-O-Al structure to enhance it. In systems whose precursor is (Al+Si) source such as fly ash, soluble

silicate species are necessary to initiate oligomers formation, favouring polycondensation of geopolymeric products with good mechanical properties. The relative concentration of silicate anions is presented as a function of the weight ratio of  $\text{SiO}_2$  to  $\text{Na}_2\text{O}$  in the aqueous solution. This gradually shifts the chemical system to species with larger rings and complex three-dimensional polymeric structures providing good mechanical properties (Falcone 1982). Although higher silicates modulus has a positive effect on the mechanical properties of the geopolymeric materials, the viscosity of the geopolymeric pastes should be taken into consideration. The viscosity of the aqueous phase was found to increase substantially at high  $\text{SiO}_2$  to  $\text{Na}_2\text{O}$  ratios. This would result in low workability affecting the hardened mechanical properties (Panias, Giannopoulou et al. 2007). While in systems with precursor with (Ca+Si) as main constituents such as slag, as the formation of silica gel makes a significant contribution to strength, there is an obvious interaction between activator modulus ( $\text{SiO}_2/\text{Na}_2\text{O}$ ) and  $\text{Na}_2\text{O}$  content. These competing effects result in a variable optimum modulus, depending on the precursor fineness and curing condition. Darko et al. investigated the heat of hydration of alkali-activated slag with different  $\text{Na}_2\text{O}\%$  dosages and different modulus values. They reported that higher values of both dosage and modulus were associated with higher reaction products development level observed through three heat flow peaks during the early age reaction (Krizan and Zivanovic 2002).

### **2.2.3 Reaction models and mechanisms**

AAM and OPC have a common zone of the alkaline aqueous phase. However, in the OPC reaction mechanism, the liquid used (i.e., water) initiates the reaction with neutral pH, while in alkali-activated systems, the alkaline solution is the initiation agent for the reaction. This can be explained by the reaction mechanism of the alumino-silicate sources when they are used in a blend with OPC. For example, once slag is mixed with water, it develops its hydraulic reaction, and it

starts to dissolve. However, a protective film is quickly formed on the grain's surface, inhibiting further reaction (Taylor 1997). However, in blending with cement, a three stages reaction took place, starting with cement hydration followed by slag hydraulic reaction and finally slag pozzolanic reaction (Mehta 1989). Once a blend of cement and slag mixed with water, slag particles are immediately coated by an alumino-silicate hydrates layer impermeable to water. As cement hydration progress, alkali calcium hydroxides  $\text{Ca(OH)}_2$  and sulphates are available. These hydroxide ions ( $-\text{OH}$ ) break down the coating and activate the hydration of glasses present in slag. Finally, the pozzolanic reaction occurs in which calcium hydroxide is consumed to form a secondary C-S-H gel resulting in a dense concrete microstructure and discontinuous pore structure. It is also clear that the late strength gaining is due to the pozzolanic reaction of slag, which depends on cement hydration progress. The role of alkali hydroxides was found twofold to provide ( $-\text{OH}$ ) ions in the system at the initial stage, then become part of the reaction at a later stage. Like  $\text{Ca(OH)}_2$  from OPC hydration in blended (slag – OPC), the function of the alkaline activator is to maintain the supply of ( $-\text{OH}$ ) ions in the system that is needed to break down the formed coating allowing further reaction. Glukhovsky gave the first proposal to describe the reaction mechanism of alkali-activated binders. Regardless of the precursor material and the alkaline solution as the predominant ingredients controlling the reaction dynamics, he described the reaction from a wide scope as destruction then condensation in a conjoined mechanism. According to this proposal, the alkaline activator is responsible for destroying the precursor represented in alumina and silicates bonds with oxygen into smaller species of low stability. Then, through this colloid phase, these destroyed structures accumulate to create a condensed structure (Glukhovsky, Rostovskaja et al. 1980). Fly ash, slag and metakaolin are examples of the known alumino-silicate materials. All these precursors can be altogether considered to be under the same umbrella of the alkali-activated

material. However, the reaction mechanism is not the same for all of them. Precursors of a high content (Al+Si), such as fly ash, react through breakage, polycondensation through geopolymerization reaction. This is similar to zeolite formation, in which the inorganic polymeric system is formed by the oriented species resulted from the dissolution of the precursor material by hydroxide ions (Van Jaarsveld, Van Deventer et al. 2002). Reaction products were reported to include tetrahedral silica and alumina coordinated in polymeric chains by replacing the Si with Al ions and a metal cation to compensate for the negative charge (Criado, Palomo et al. 2005). The term geopolymers apply only in this case. Davidovits also described Geopolymerization as an exothermic reaction in which aluminosilicate oxides and alkali polysilicates yielding Si-O-Al bonds in a polymeric form (Davidovits 1988). Many researches explained the geopolymerization steps, which involve the dissolution of the aluminosilicate source in an alkaline solution. Then, diffusion of the dissolved Si and Al species followed by gel formation and condensation. However, other researchers reported that these changes are hard to be analyzed into transportation and polycondensation separately as the two actions take place simultaneously (Davidovits 1988, Van Jaarsveld, Van Deventer et al. 1998, Palomo, Grutzeck et al. 1999). Other researchers reported water percentage has a great role in the polycondensation mechanism since the alkali metal cations are ordering water molecules through a nucleation mechanism. They believed that higher water percentage results in a highly condensed structure (van Jaarsveld and Van Deventer 1999). Also, it was reported that after a critical size is reached by these nucleation sites they start to turn into crystalline form considering the long time that would be taken for this process to be complete (Criado, Palomo et al. 2005). In another attempt to propose a model for the geopolymerization reaction, J. L. Provis et. al suggested that gelation and crystallization are the two scenarios for the

zeolite phase formation in the geopolymerization due to alumino-silicate oligomerization after dissolution by the alkaline.

#### **2.2.4 Hydration products**

As mentioned earlier, for (Ca+Si) precursors, the main hydration products of AAM are known to be calcium silicate hydrates like OPC but with different Ca/Si ratio. (Fernandez-Jimenez, Puertas et al. 2002, Puertas, Palacios et al. 2011, Myers, Bernal et al. 2013). However, other hydration products form as a reaction development due to the continuous dissolution of the precursor particles and the available species supplied by the activator. Which highlight the activator role in controlling the nature of the formed hydration products. For example, Al species would participate in hydrotalcite ( $H_t$ ) formation or be accommodated in the formed C-S-H through the free bridges to upgrade the C-S-H phase to the C-A-S-H phase. These phases have a vital role in profiling the final product mechanical and thermal properties. Unlike the OPC systems, portlandite does not show up as a formed hydration product. This also would affect the volume stability of the binder at elevated temperatures.

### **2.3 Durability of alkali-activated systems**

Besides the environmental concerns, durability problems were considered as a major motive to look for an alternative binding system rather than OPC binders. Over the past 50 years, researchers investigated and assessed alkali-activated systems to understand their behaviour towards deteriorating agents.

#### **2.3.1 Acid attack**

During an acid attack on concrete, the extent of degradation depends on the acid solution's concentration and the exposure period's length (Singh, Ishwarya et al. 2015). The resistance is

measured in terms of weight loss, reduction in compressive strength, and microstructure changes (depolymerization of the alumino-silicate network). Around 33% reduction in strength of slag based concrete compared to 47% in OPC concrete when exposed to an acetic acid solution of (pH =4) for 12 months was reported (Bakharev, Sanjayan et al. 2003). The slag particles and low calcium C-S-H, with an average, Ca/Si ratio of 1, were more stable in the acid solution than the OPC pastes. During immersion in 2% sulfuric acid ( $H_2SO_4$ ) solution, for 40 MPa slag-based concrete, the strength loss was about 11% compared to 36.2% for OPC concrete. For metakaolin based geopolymer, tested pastes by Davidovits et al. (Davidovits 1991) exhibited only 7% mass loss when immersed in 5%  $H_2SO_4$  for 30 days. Also, it was reported that fly ash-based geopolymer pastes retained a dense microstructure after 3 months of exposure to nitric acid ( $HNO_3$ ).

### 2.3.2 Sulfate attack

The sulfate attack mechanism on OPC concrete usually involves tricalcium aluminate ( $C_3A$ ) and portlandite in the cement matrix and sulfate ions (Rozière, Loukili et al. 2009). Sulfate ions react with portlandite to form gypsum, which then reacts with the hydration products of  $C_3A$  to form ettringite. This final product was reported to cause expansion, leading to a concrete failure (Cohen 1983, Mehta 1983, Odler and Gasser 1988).

In AAM, sulfate attack is mainly destroying the alumino-silicate skeleton. Several attempts (Hardjito, Wallah et al. 2004, Rajamane, Nataraja et al. 2012) have been made to study sulfate resistance of AAM. The deterioration in concrete was evaluated in terms of visual appearance, weight loss and residual compressive strength. Thokchom et al. (Thokchom, Ghosh et al. 2010) tested geopolymer mortar specimens manufactured by activating low calcium fly ash with a mixture of (NaOH) and ( $Na_2SiO_3$ ) solution. He reported that specimens' surfaces received white

deposits (flaky and elongated white deposits) throughout exposure. These deposits were more obvious as the  $\text{Na}_2\text{O}$  content increased. He also reported a variation in pH value of the sulfate solution. The increase in pH may be attributed to the migration of alkalis from the specimen into the solution, as reported by Bakharev (Bakharev 2005). After 24 weeks of exposure to 10% magnesium sulfate solution, the residual compressive strength was varying with the  $\text{Na}_2\text{O}$  content. The more the  $\text{Na}_2\text{O}$  content, the less the compressive strength loss. Scanning electron microscopy (SEM) and EDX tests showed that according to traces of constituent elements at some spots, gypsum and ettringite formation was possible. Localized cracks were noticed which could be attributed to the formation of ettringite.

### **2.3.3 Alkali silica reaction**

Severe deterioration of hardened Portland cement concrete is gradually caused by Alkali-silica reaction in terms of strength loss, cracking and volume expansion. It takes place through reactions between the hydroxyl ions in the pore solution within the concrete matrix and reactive silica of the used aggregate. These reactions are generally occurring in stages. In the first stage, the hydrolysis of reactive silica react with hydroxyl ions to form alkali-silica gel, then absorption of water by the gel will result in a volume increase (Hester, McNally et al. 2005). In geopolymer concrete, the unutilized alkali after geopolymerization of alumino-silicates is expected to react with the silica of the aggregates causing disruption to bridging process. Geopolymers with aggregates of different reactivity were reported to achieve less expansion relative to OPC mixtures (Kupwade-Patil and Allouche 2013). Fly ash based geopolymers generally exhibited no significant expansion. This was attributed to the formation of crystalline zeolites, at a very slow rate. Moreover, minerals are usually found in the gaps of the matrix, hence, stress that might generate cracking is unlikely (García-Lodeiro, Palomo et al. 2007). For slag-based mortars, an expansion

less than 0.05 % was reported which is lower than that of the OPC. This might be attributed to the presence of portlandite in OPC which favors ASR as it provides  $\text{Ca}^{2+}$  ions in solution. Conversely, in AAS, alkalis are parts in different reaction products such as C-S-H formed with low Na and Al content. Therefore, a competition between the slag and ASR is established. This factor, together with the absence of free  $\text{Ca}^{2+}$  ions, justifies the low expansion of the AAS mortars stored in water compared to that of the OPC mortars.

#### **2.3.4 Carbonation and permeability**

Carbon dioxide is always around and capable of penetrating into concrete and dissolve in pore water forming carbonic acid. The carbonic acid that forms in the concrete's pores reacts with portlandite (CH) and produces calcium carbonate.

This process replaces the relatively large CH molecules with relatively small calcium carbonate molecules. This replacement increases concrete's porosity and decreases its pH. Although the concrete absolute volume may remain the same, the increase in porosity reduces this desirable product's relative volume and decreases its strength.

The most significant effect of carbonation on concrete is reducing its durability by reducing its pH. The highly alkaline concrete environment, which usually has a pH above 12, creates a protective, passivating oxide layer around steel, protecting the reinforcement from corrosion. Carbonation can reduce a concrete pH to a value less than 9, which significantly weakens or even eliminate, the steel's protective layer (Leelalerkiet, Kyung et al. 2004). This reduction in pH can be explained as follows: calcium hydroxide contains two hydrogen ions while calcium carbonate contains zero hydrogen ions. After some of the calcium hydroxides is consumed during the carbonation process and partially replaced by calcium carbonate, hydrogen ions still exist in the

matrix but at a lower concentration. The weaker hydrogen ion concentration reduces concrete pH leading to steel corrosion. As a result of cracks or excessive porosity, highly permeable concrete has an increased likelihood for carbonation.

Olivia et al. (Olivia and Nikraz 2012) reported low water permeability of fly ash-based geopolymer concrete cured at 60 °C for 24 h compared to that of the OPC concrete due to its denser paste and smaller pore interconnectivity. Bernal et al. (Bernal, de Gutiérrez et al. 2012) studied slag/metakaolin-based concretes (water to binder ratio (w/b)= 0.47) under an accelerated carbonation test. They reported that the compressive strength decreased as the carbonation proceeds. It is important to notice that the relationship between the pore volume and extent of carbonation was much more similar with samples with different percentages of metakaolin contrary to the slag-based samples. This can be attributed to calcium carbonate formation in both types of concrete proving that porosity is not the only factor causing strength loss.

#### 2.4 Behaviour under impact loads

Military structures should always be better protected than civilian ones against threats. These threats are usually missiles or projectiles (**Fig. 2.1**).



**Fig. 2.1** Example of different threats against concrete structures.

These kinds of threats mainly result in impact loads (high loading rate). Concrete materials, in general, are counted as sensitive material to stress and strain rate (Banthia, Mindess et al. 1989, Malvar and Ross 1998, Cusatis 2011). Many studies were investigating the behaviour of OPC concrete under impact loads and the induced damages due to projectiles impact (**Fig. 2.2**), and how to improve its impact absorption capacity (Vossoughi, Ostertag et al. 2007).

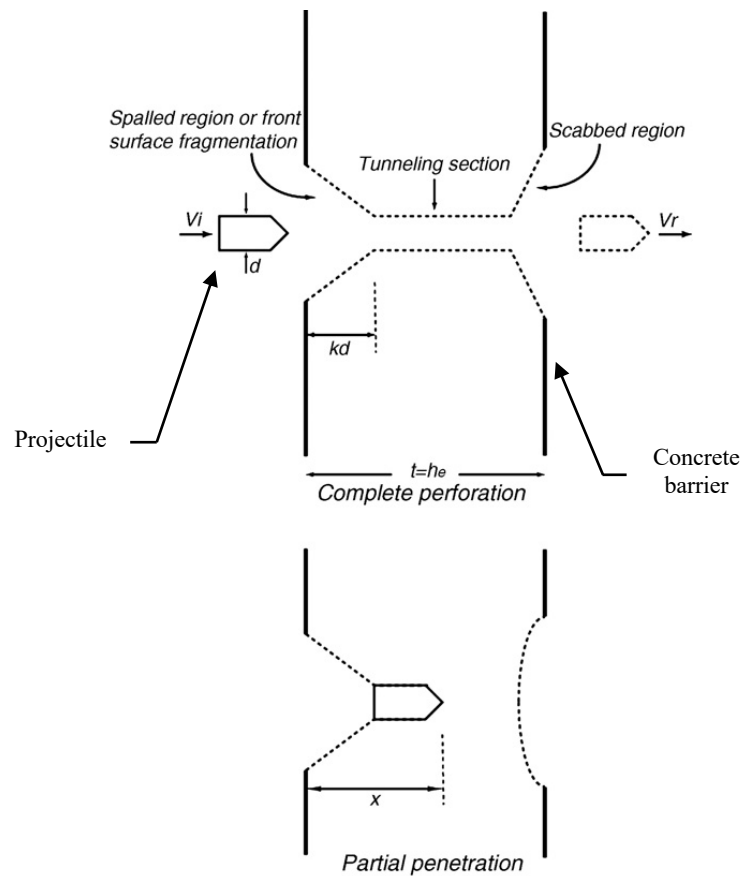


**Fig. 2.2 Concrete damaging model proposed by (Vossoughi, Ostertag et al. 2007).**

Researchers suggested some techniques to enhance concrete behaviour under impact loads. One approach was confining concrete with FRP (**Fig. 2.3**). This technique enhances the impact absorption capacity by about 500% comparing to plain concrete (Pham, Chen et al. 2018).

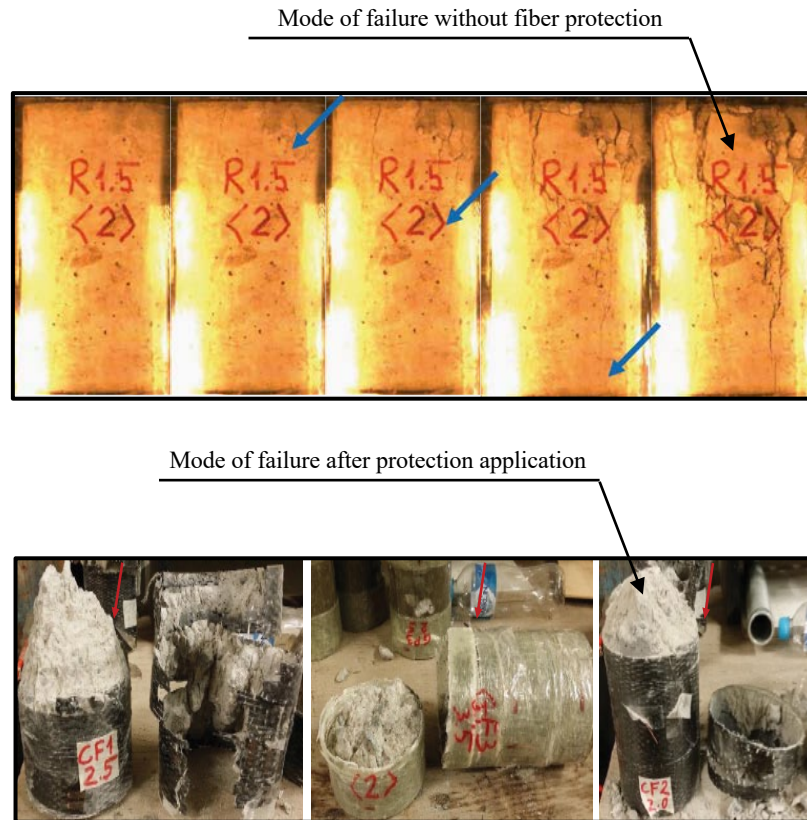


**Fig. 2.3 Failure modes of unconfined concrete vs confined concrete (Pham, Chen et al. 2018).**

However, this approach is still hard to be implemented for all element's categories. Another approach was to incorporate fibres to enhance the performance of concrete subjected to dynamic loading. Incorporating steel fibres with different volume fractions and shapes on concrete structures' behaviour under dynamic loads was reviewed. It was reported that using steel fibres in concrete added many advantages, which will lead to better performance under impact loads. Generally, the impact resistance was enhanced by increasing the fibre volume fraction, and the shape was found to be very useful since it can achieve better bonding with the concrete mix (Soufeiani, Raman et al. 2016). It was stated that the enhancement of impact resistance came

through improving the cracking behaviour achieving a ductile failure and increasing the ability of concrete to dissipate a higher amount of energy (Bindiganavile, Banthia et al. 2002, Maalej, Quek et al. 2005, Zhang, Maalej et al. 2007). Also, increased DIF (dynamic increase factor) of the concrete through fibres resulted in better behaviour in scabbing, spalling, and fragmentation (Maalej, Quek et al. 2005). Waste rubber fibre was also proposed to be used in concrete to provide better impact resistance. Trilok Gupta et al. investigated the impact resistance of concrete containing waste rubber as a replacement of fine aggregates; they reported that rubber existence improved the impact resistance (Gupta, Sharma et al. 2015).

For AAM, similar approaches were applied and examined to investigate the impact of energy absorption capacity and adequate ways to enhance this capacity. MY Yardimci et al. studied the performance of AAM under static and dynamic loads. They reported that activator nature has a significant effect on the mechanical behaviour of AAM in both static and dynamic loading cases. Also, DIF was affected by the mixture design (Yardimci, Aydin et al. 2017). As an approach to enhance the impact energy absorption of AAM, Y Zhang et al. studied the effect of incorporating PVA fibres to fly ash geopolymer on the impact behaviour. They reported that adding a high fraction of short fibres could enhance the impact energy absorption, and it was also effective in changing the failure pattern from brittle to ductile (Yunsheng, Wei et al. 2006). Weimin Li et al. studied the influence of using basalt fibre on the impact behaviour of geopolymer concrete. Basalt fibre was reported to improve deformation behaviour and geopolymer concrete's energy absorption (Li and Xu 2009). Azizul et al. reported that using steel fibre with lightweight geopolymer concrete has a positive effect on the mechanical properties in terms of strength and modulus of elasticity. Also, it improved the concrete failure mode (**Fig. 2.4**).

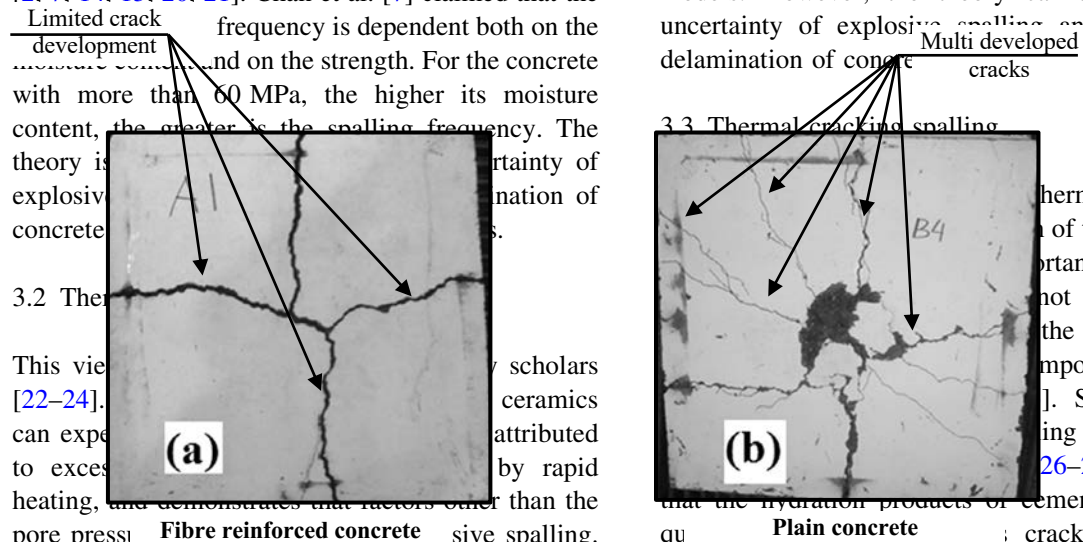


**Fig. 2.4 Failure modes of steel fibre reinforced concrete vs plain concrete (Islam et al. 2017)**

## **2.5 Behaviour of cementitious material under exposure to elevated temperature**

During exposure to elevated temperatures, OPC binders suffer considerable degradation due to different hydration products decomposition at different temperatures levels. Moreover, portlandite decomposition is a two-way reaction. During the rehydration, during cooling down, its volume increases by about 9%, inducing internal stresses that contribute to increasing the severity of the damage (Alarcon-Ruiz, Platret et al. 2005). Rather than that, high-temperature gradient, hotter external exposed layers tend to separate and spall from the cooler interior (Hertz 2003). Yufang Fu. et al. studied the different concrete spalling mechanisms induced by exposure to elevated temperatures. Pore pressure spalling, Thermal cracking spalling, and thermal stress spalling can be considered the three leading causes of concrete spalling due to exposure to elevated temperatures (Fig. 2.5) (Fu and Li 2011).

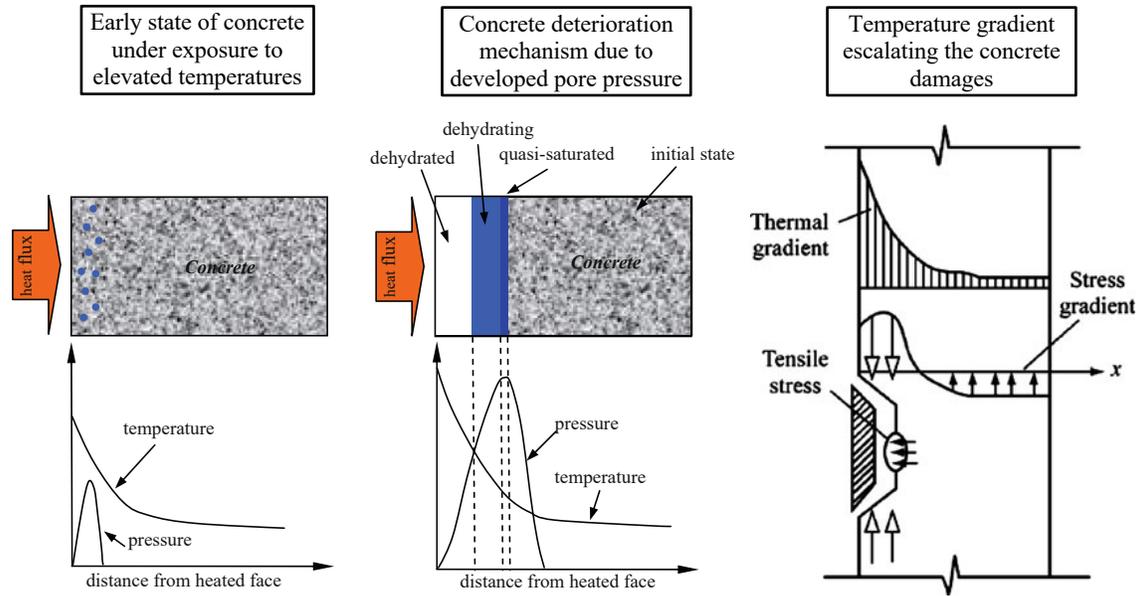


**Fig. 2.5 Concrete deterioration mechanisms due to internal stresses during exposure to elevated temperatures (Fu and Li 2011).**

For AAM, the different nature of the formed hydration products compared to OPC binders resulted in higher stability during exposure to elevated temperatures (Park, Jang et al. 2016, Rashad, Sadek et al. 2016, Yang, Wu et al. 2017). Moreover, AAM was reported to have highly distributed nanopores allowing physically and chemically bonded water to evaporate without damaging the alumino-silicate network (Duxson, Fernández-Jiménez et al. 2007). It was even reported that residual strength after exposure to elevated temperatures might be higher than the original strength. This increase might be attributed to unreacted precursor particles' sintering action leading to the recrystallization in a denser phase (Kong and Sanjayan 2008, Reddy, Tulyaganov et al. 2013), and it possesses higher spalling resistance under fire than the OPC concrete. However, all these privileges should be firstly controlled through a proper synthesizing process targeting these criteria.

---

## Chapter 3 Methodology & Experimental work

### 3.1 Introduction

This chapter includes the considered methodology to achieve the targeted goals of the research. The experimental work was divided into three phases. The description of each phase and the done experimental tests will be discussed representing the experimental work structure to achieve each phase's aim. Moreover, the used materials and their specification will be detailed.

### 3.2 Experimental work phases

The experimental plan serving the main objectives of the research are represented in **Fig. 3.1**.

3.1.

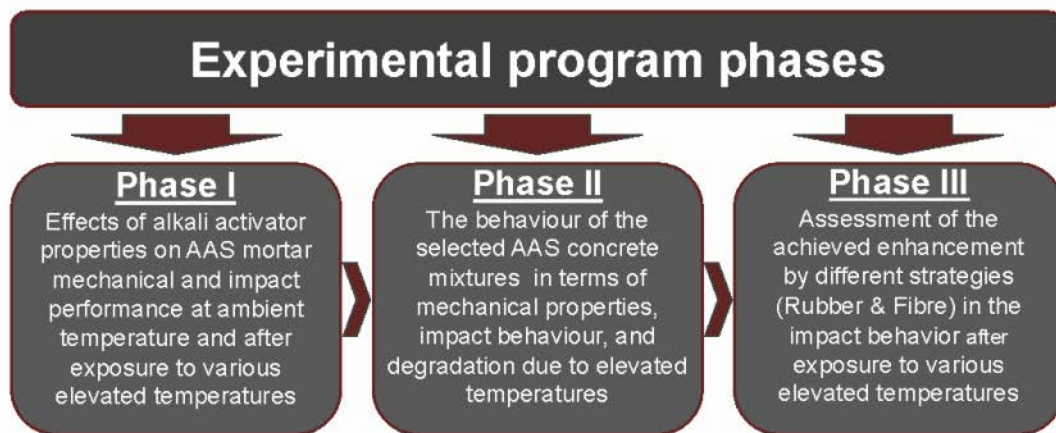


**Fig. 3.1 Experimental work program phases.**

#### 3.2.1 Phase I

Phase one's target was to quantify the effect of the alkaline activator nature in terms of dosage ( $\text{Na}_2\text{O} \%$ ) and silica modulus ( $M_s$ ) on the fresh and hardened properties of AAS mortar. Sodium

hydroxide and sodium silicates were used to achieve each mixture's targeted activator properties. The water in the sodium silicate was subtracted from the mixing water to calculate the added water for each mixture. Eleven AAS mixtures were investigated in this phase. Three levels of silica modulus (1, 1.25, and 1.5) were tested with three dosage values (4%, 6%, and 8%) at each level of silica modulus. Also, a different mixture for  $M_s=1.25$  at a higher dosage (10%) was included to understand the effect of excessive dosages on the final product properties. One mixture was mixed with sodium hydroxide individually as an activating agent of relatively high dosage to secure high dissolution rate conditions to quantify the silica incorporation function. Beside the AAS mixtures, an OPC mixture was prepared at the same binder content and water to binder (w/b) for comparison purposes. The mixing proportions of all prepared mixtures were detailed in **chapter 4**. Two mixtures sets were prepared to be tested. The first set was tested at ambient temperature at ages 3,7 and 28 days. The second was tested 28 days after exposure to three assigned elevated temperatures levels (200 °C, 400 °C, 600 °C). **Fig. 3.2** summarises the performed tests and the number of prepared specimens in the first experimental phase.

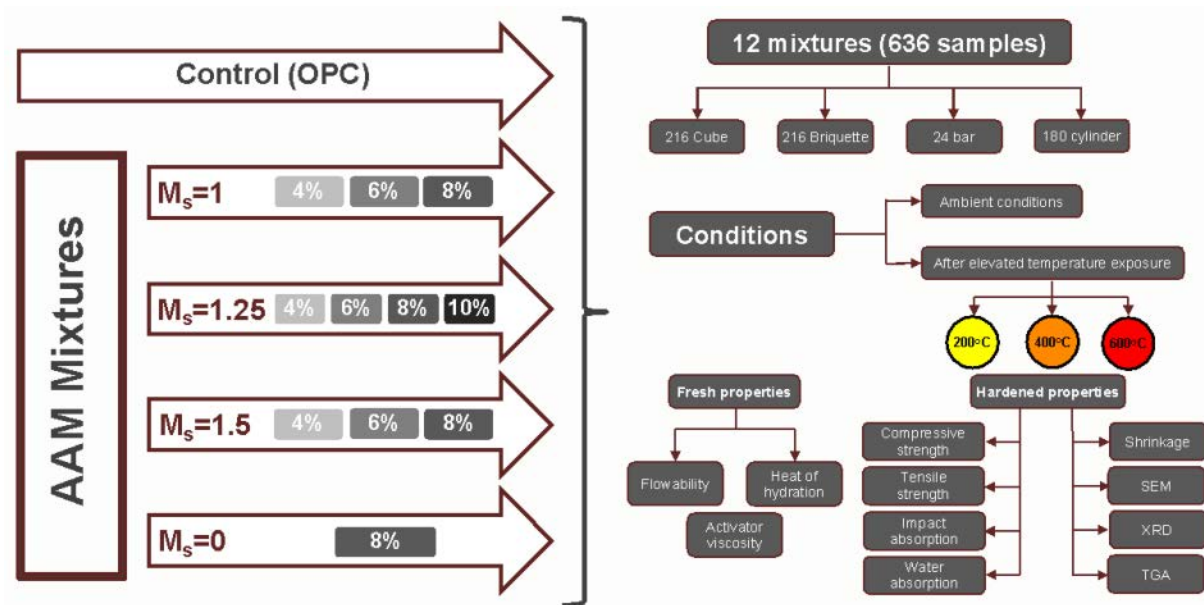


**Fig. 3.2** Phase I description and testing chart

Mortar samples were prepared using a binder/fine aggregate ratio of 1: 2.75 by weight for both OPC and AAS mixtures. Binder and sand were dry mixed for 1 minute, then water or alkaline activator solution was added and mixed for an extra three minutes. Then, samples were cast in molds in two layers and compacted using a tamping rod. For the activator solution viscosity, liquid solutions of different activator properties were prepared and tested at 23 °C, at variable shear rates rheometer. Flowability for all mortar mixtures was measured using a flow table method, according to ASTM C230 (ASTM 2021). 50 mm x 50 mm x 50 mm cubes were prepared for compressive strength testing according to ASTM C109/109M standards (ASTM 2020). Dog-bone shaped briquette of size 75 mm length, 25 mm thickness, and 625 mm<sup>2</sup> cross-section area at the mid-length and enlarged ends to allow a passive gripping of the specimens were prepared and tested for tensile strength according to AASHTO T132 (AASHTO 2009). For drying shrinkage, prismatic specimens 25 × 25 × 285 mm for each mixture were made according to ASTM C 157 (ASTM 2019). For mortar impact energy absorption, cylinders of diameter 100 mm and height 50 mm were prepared for the drop weight impact test according to ACI committee 544.

### 3.2.2 Phase II

In Phase two, three mixtures were chosen depending on phase one's acquired results regarding three desirable criteria: Static mechanical properties, Impact absorption capacity, and the performance after exposure to various elevated temporaries. **Fig. 3.3** summarize the achieved criteria by each chosen mixture. For low activation level (i.e., Ms=1 & dosage=4%), the static mechanical properties and the impact absorption capacity at ambient temperature were relatively low compared to other mixtures of higher activation level. However, after exposure to elevated temperatures, this mixture exhibited the lowest degradation level. For the high activation level (i.e., Ms=1.5 & dosage=8%), the mechanical properties and the impact absorption capacity were

superior among other mixtures. However, after exposure to elevated temperatures, this mixture showed the worst performance. Mixture of medium activation (i.e.,  $M_s=1.25$  & dosage=6%) represents the moderate performance regarding the three assigned criteria. Rather than AAS concrete, an OPC concrete mixture was prepared at the same coarse to fine aggregate ratio, binder content, and (w/b) ratio for comparison. The concrete mixing proportions are mentioned in Chapter 5.

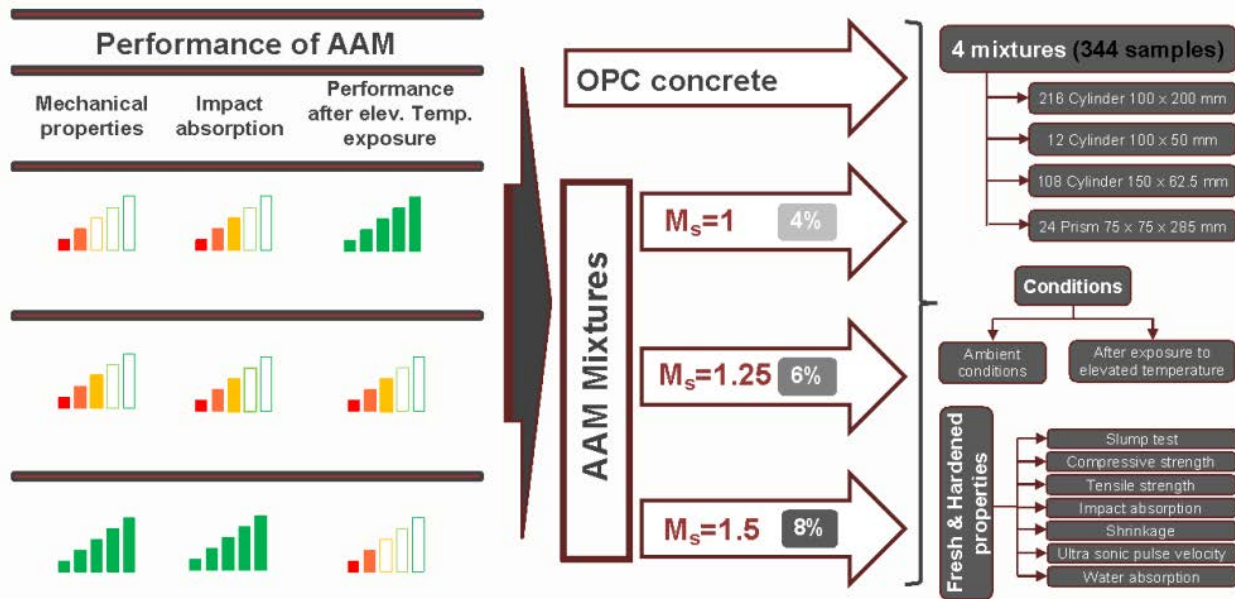


Fig. 3.3 Phase II description and testing chart.

Concrete mixtures were prepared and cast following ASTM C192 "Standard Practice for Making and Curing Concrete Test Specimens in the Laboratory." (ASTM 2019). Initially, dry sand, crushed stone, slag were mixed for 1 minute. The water and alkaline activator solution were then added gradually to the dry mixture and mixed for three minutes until achieving homogenous mixtures. Various specimens were cast for each test on three layers and compacted over a vibrating table. For compressive strength, indirect splitting tensile strength, and modulus of elasticity tests, cylindrical specimens of a diameter 100 mm and 200 mm length were prepared and tested

according to ASTM C39 "Standard Test Method for Compressive Strength of Cylindrical Concrete Specimens"(ASTM 2020), ASTM C496 "Standard Test Method for Splitting Tensile Strength of Cylindrical Concrete Specimens", and ASTM C469 "Standard Test Method for Static Modulus of Elasticity and Poisson's Ratio of Concrete in Compression" (ASTM 2014) at ages 7 and 28 days, respectively. Shrinkage ultra-sonic pulse velocity tests were performed on prismatic specimens  $75 \times 75 \times 285$  for each mixture according to ASTM C 157 "Standard Test Method for Length Change of Hardened Hydraulic-Cement Mortar and Concrete" (ASTM 2017) and ASTM C597 "Standard Test Method for Pulse Velocity through Concrete" (ASTM 2016), respectively. Water Absorption (i.e., sorptivity) testing of concrete was performed according to ASTM C 1585 "Standard Test Method for Measurement of Rate of Absorption of Water by Hydraulic-Cement Concretes" (ASTM 2020). Pre-dried cylinder disk specimens with a diameter of 100 mm and height of 50 mm. For the impact test, 150 mm diameter cylindrical specimens with 63 mm height were cast and tested according to ACI Committee 544 (drop weight test).

### 3.2.3 Phase III

For Phase three, one AAS concrete mixture was selected based on the most desirable criteria at ambient temperature to assess the enhancement techniques capability of mitigating the performance degradation after exposure to elevated temperatures. The used enhancement strategies in this phase, along with the performed tests, are summarized in (**Fig. 3.4**)

Rubber incorporation as a replacement of fine aggregate was used to add a passive agent dissipating the impact energy delivered to concrete. Three contents (5%, 10%, and 15%) were used to understand this technique's limitations in terms of rubber content regarding exposure to elevated temperatures. According to the previous research, crumb rubber was pretreated by mixing with the sodium hydroxide solution to achieve good rubber particle's roughness (Youssf, Mills et al. 2016,

Li, Zhang et al. 2019). The rubber was firstly stirred with the solution to confirm uniform surface treatment, then soaked for 40 minutes. Afterword, rubber was rinsed with distilled water and left to dry for 24 hours at 60 °C. Three more subphases were concerned with the fibre incorporation in the selected AAS concrete mixture to evaluate different fibre's ability to enhance the AAS concrete performance after elevated temperatures exposure. Steel fibre, basalt fibre, and polypropylene fibre were used in three contents per each type (0.125%, 0.5%, and 1%) by volume of concrete. According to ASTM standards, concrete mixing and specimen's preparation and testing were performed as mentioned earlier in section 3.2.2.

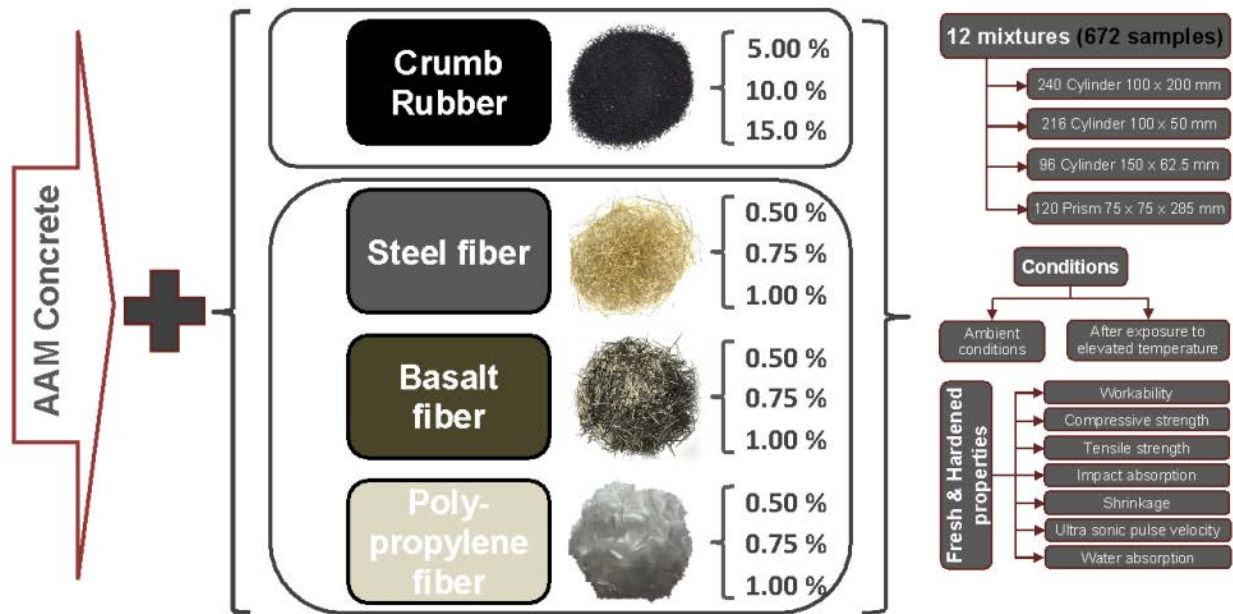


**Fig. 3.4 Phase III description and testing chart.**

A full detailed description of the experimental program, with the numbers of prepared specimens per each phase, is illustrated in (Fig. 3.5).

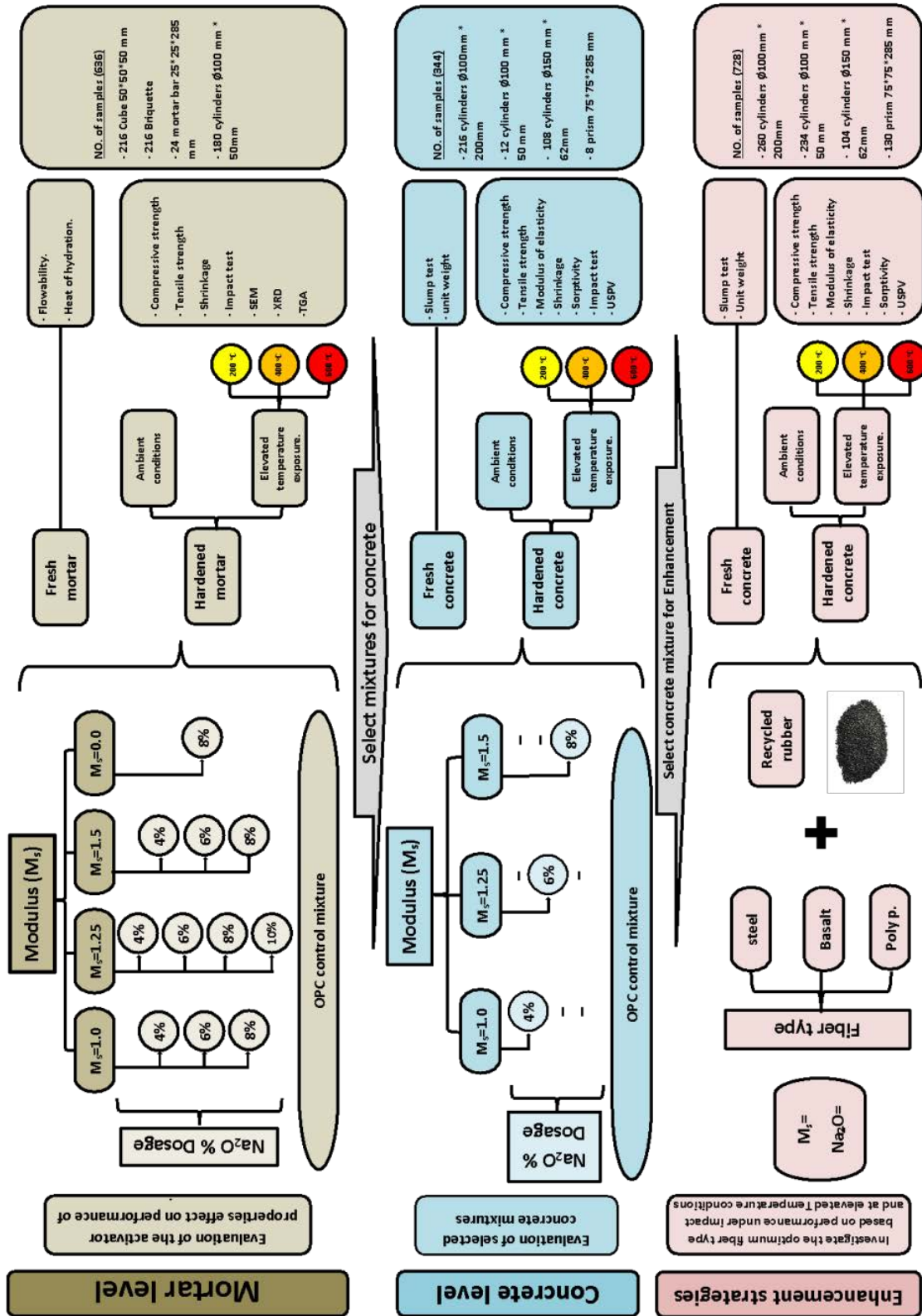


Fig. 3.5 Detailed experimental work plan.

### 3.3 Material

The specifications of all used material are listed in this section according to the datasheet provided by each material's supplier.

#### 3.3.1 Slag

As a precursor for all alkali-activated mortar and concrete mixtures, granulated blast furnace slag (i.e., will be called "slag" later) of specific gravity and surface area of 2.92 and 515 m<sup>2</sup>/kg was used as a precursor, respectively. The chemical compositions of slag are listed in **Table 3.1**.

**Table 3.1 Chemical and physical properties of slag.**

Constituent/property (%)	Slag
SiO <sub>2</sub>	36.1
Al <sub>2</sub> O <sub>3</sub>	10.1
CaO	37
MgO	12
K <sub>2</sub> O	0.5
Na <sub>2</sub> O	0.4
Fe <sub>2</sub> O <sub>3</sub>	0.7
SO <sub>3</sub>	3
Other minor elements	0.2

#### 3.3.2 Cement

For control cement-based mixtures, general use (GU) hydraulic cement with specific gravity and surface area of 3.15 and 371 m<sup>2</sup>/kg according to the CSA-3001-03 was used, respectively. The chemical compositions of cement are listed in **Table 3.2**.

**Table 3.2 Chemical and physical properties of cement and slag.**

Constituent/property (%)	OPC
SiO <sub>2</sub>	19.4
Al <sub>2</sub> O <sub>3</sub>	4.6
CaO	61.1
MgO	3.3
K <sub>2</sub> O	0.7
Na <sub>2</sub> O	2
Fe <sub>2</sub> O <sub>3</sub>	2
SO <sub>3</sub>	2.3
Other minor elements	4.6

**3.3.3 Fine aggregate**

Riverside sand, with a fineness modulus and specific gravity of 2.70, 2.67 determined according to ASTM C136 (2014), ASTM C 128 (2015), was used as fine aggregate, respectively.

The sieve analysis of the used sand is represented in **Fig. 3.6**.

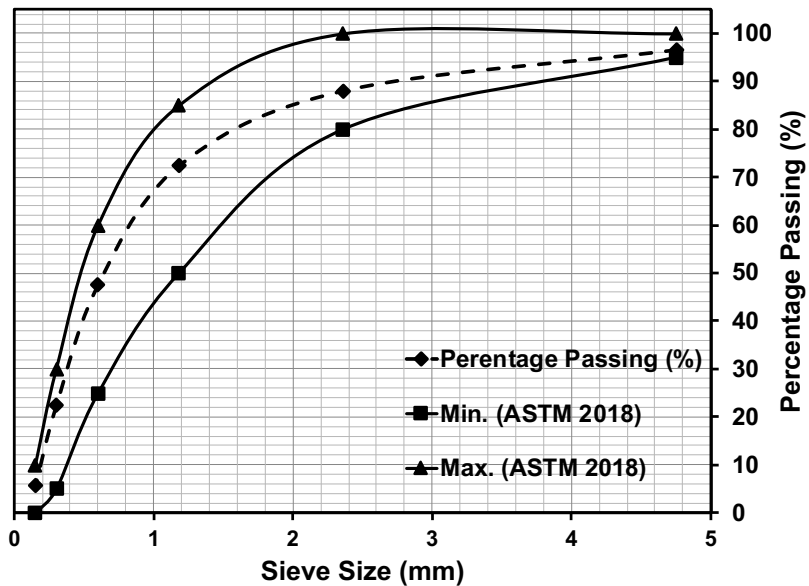


**Fig. 3.6 Sieve analysis of fine aggregate.**

### 3.3.4 Coarse aggregate

Crushed stone with specific gravity, water absorption, and maximum nominal size of 2.70, 1.3%, and 19 mm was used as the coarse aggregate for concrete mixtures, respectively. The sieve analysis of the used aggregate is represented in **Fig. 3.7**.

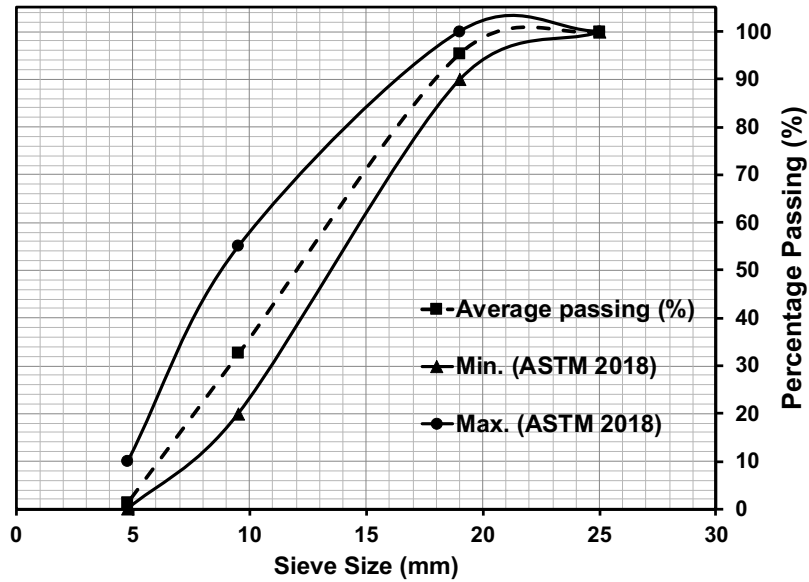


**Fig. 3.7 Sieve analysis of coarse aggregate.**

### 3.3.5 Chemical material

For the activating solutions, Sodium hydroxide flakes with >99% purity and sodium silicate were used to achieve the targeted dosage and silica modulus of each mixture. The used sodium silicate consisted of 28.78% SiO<sub>2</sub>, 9.01% Na<sub>2</sub>O, and 62.2% H<sub>2</sub>O content by mass and had a density of 1410 kg/m<sup>3</sup> and pH of 12.7, according to the manufacturer datasheet.

### 3.3.6 Crumb rubber

Fine crumb waste rubber (**Fig. 3.8**) with a maximum grain size of 2.5 mm was used to replace sand. The sieve analysis of the rubber is illustrated in **Fig. 3.9**. According to the previous research,

crumb rubber was pretreated by mixing with the sodium hydroxide solution to achieve good rubber particle's roughness (Youssf, Mills et al. 2016, Li, Zhang et al. 2019). The rubber was firstly stirred with the solution to confirm uniform surface treatment, then soaked for 40 minutes. Afterword, rubber was rinsed with distilled water and left to dry for 24 hours at 60 °C.



Fig. 3.8 Fine crumb rubber

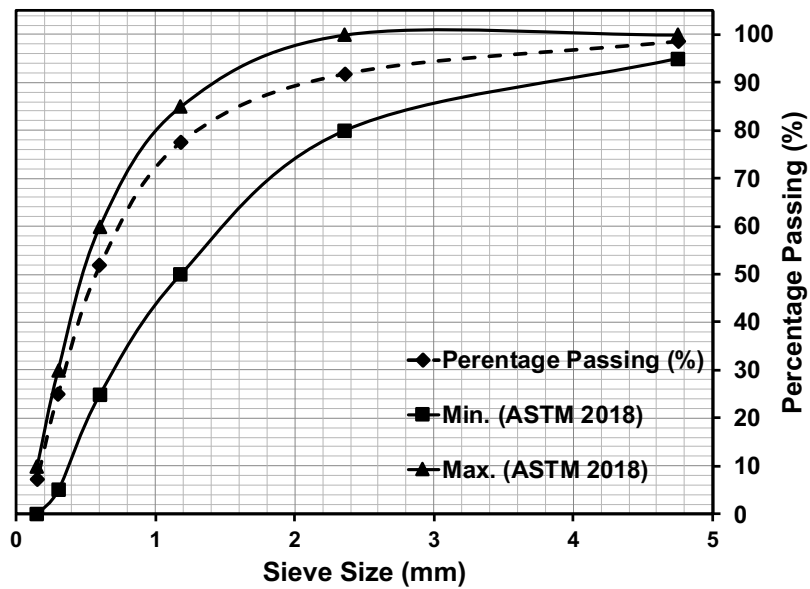
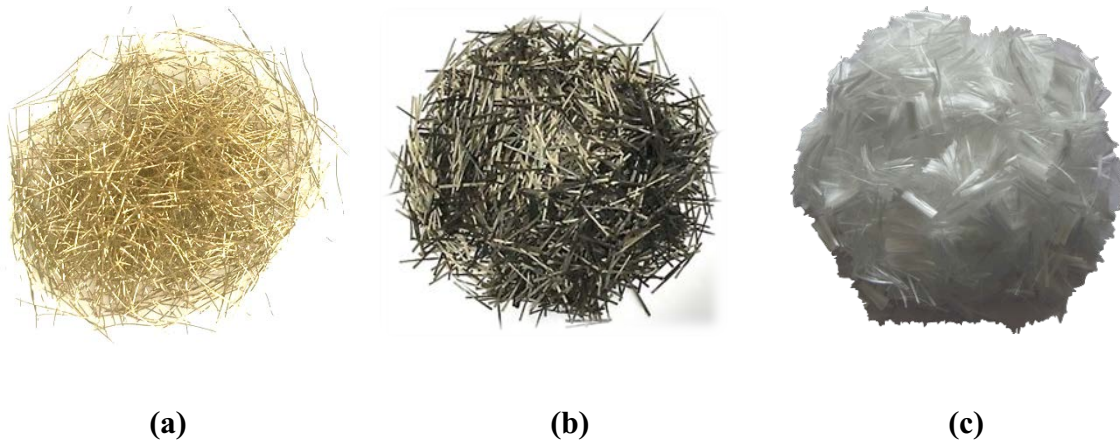


Fig. 3.9 Sieve analysis of crumb rubber.

### 3.3.7 Fibre

Three different fibre types (Steel fibre, Basalt fibre, and polypropylene fibre) were implemented in the enhancement techniques experimental phase (**Fig. 3.10 a, b, and c**). The specifications of each type of these fibres are indicated in **Table 3.3**.



**Fig. 3.10** Different types of fibre.

**Table 3.3** Specifications of different fibre.

Fibre type	Shape	Length (mm)	Diameter (mm)	Tensile strength (MPa)	Modulus of elasticity (GPa)	Specific gravity
Steel fibre	Straight	14 ± 1	0.2±0.02	2600 ~ 3400	> 200	7.85
Basalt fibre	Helix	20	0.72	> 900	44	2.1
Polypropylene fibre	Straight	12	0.019	570	3.6	0.91

### 3.3.8 Water

All mixtures were prepared using potable water of temperature 23 °C at mixing.

### 3.3.9 Admixtures

High range water reducer Sika Viscocrete 2100 was used for concrete mixtures to achieve adequate workability for fibre incorporated mixtures according to ASTM C494 (2017) and AASHTO M-194 Type A and F (2006).

## 3.4 Testing procedures

In this section, a full description of the performed tests and the tests procedures according to standards, will be described in detail.

### 3.4.1 Heat of hydration

I-CAL 2000 HPC Calmetrix was used to quantify the hydration heat evolution of all mixtures. Pastes containing 50 g of the precursor with different activation levels were prepared and mixed for 30 seconds in a plastic container according to EN 196-11. Then, containers were placed in the device environmental chamber to observe the heat evolution for 72 hours.

### 3.4.2 X-Ray diffraction (XRD)

For hydration product characterizations, small chunks of hardened paste samples (**Fig. 3.11**) were immersed in acetone solvent for two days to release any existing water, then dry heated in a vacuum oven for another two days to stop the reaction process. The chunks were ground and sieved using No. 200 sieve to obtain a convenient grain size for XRD sampling. The test was operated in a 2 theta range of (10°-60°). The step size was set up at 0.02°, counting 2 seconds per step.

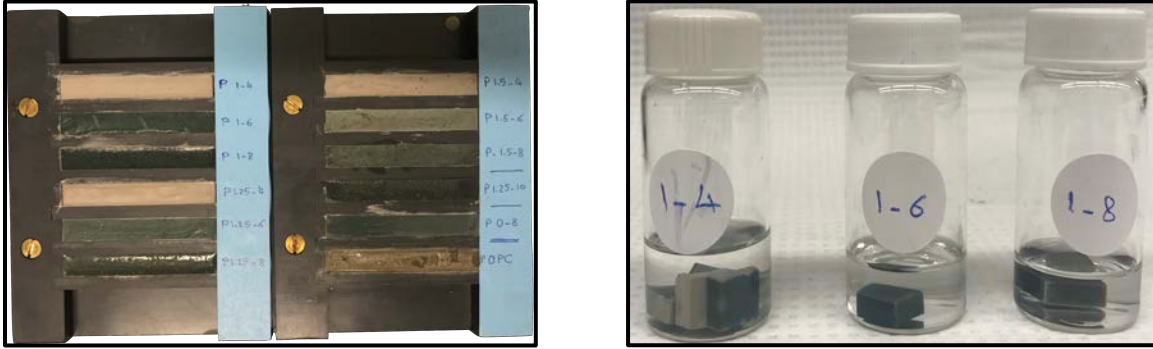


**Fig. 3.11** Sample preparation for XRD test and TGA test.

### 3.4.3 Thermogravimetric analysis (TGA)

Thermogravimetric analyses were conducted on powder samples heated up to 650 °C with a heating rate of 5°C per minute, using Discovery 5500, with weighing precision of 0.01% . For samples representing the exposed mixtures to various elevated temperatures, the powder sample was taken from a ground chunk extracted from specimens that were already exposed to these temperatures.

### 3.4.4 Viscosity test

A 50 gm sample was tested for the activator solutions using MCR 502 Rheometer using minimum and maximum angular velocity of  $10^{-9}$  and 314 %/Sec, speeding in a log. scale acceleration (**Fig. 3.12**).

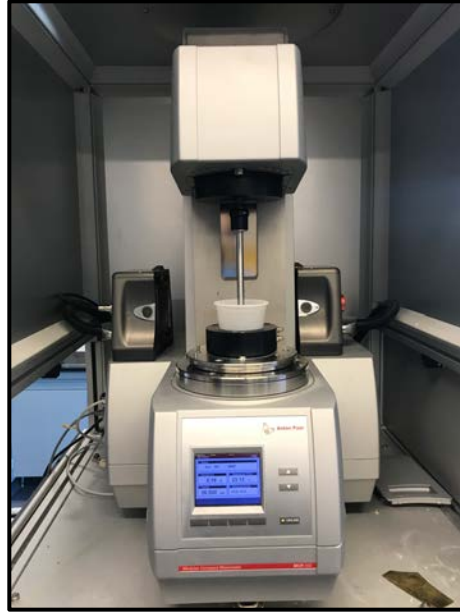


**Fig. 3.12** Viscosity test setup for (MCR 502) rheometer.

#### **3.4.5 Workability**

Mortar flowability test was performed according to ASTM C1437 "Standard Test Method for Flow of Hydraulic Cement Mortar" (ASTM 2020). For concrete mixtures, slump test was performed following ASTM C143 "Standard Test Method for Slump of Hydraulic-Cement Concrete." (ASTM 2020).

#### **3.4.6 Compressive and tensile strength tests**

Forney compression machine was used for the compressive strength measurement of mortar and concrete specimens. For mortar specimens, compression load was applied at a loading rate of 0.9 to 1.8 kN/s as per test standard (ASTM C109/109M) on 50 mm x 50 mm x 50 mm cube (**Fig. 3.13 a**). For Dog-bone shaped mortar briquettes, specimens are placed on the machine grabbing roller to insure passive gripping and failure due to pure tensile load at the mid-span cross-section

(Fig. 3.13 b). Then, the tensile load is applied at a loading rate of 2.7 kN/min as recommended by AASHTO T132.

For the Concrete compressive strength test, specimens are placed between two rubber cups (Fig. 3.13 c). Then, a uniaxial load is applied at a rate of 0.15-0.35 MPa/s according to ASTM C39. For splitting the tensile strength test, specimens are placed horizontally between two wooden strips (top and bottom). Then, the compression load is applied at a loading rate of 1.15 MPa/min. (Fig. 3.13 d) according to ASTM C496 2017.



(a)



(b)



(c)

(d)

**Fig. 3.13 Compressive and tensile strength test setup for mortar and concrete specimens.**

### 3.4.7 Modulus of elasticity test

Concrete modulus of elasticity evaluation was performed according to ASTM C496 for specimens before and after exposure to different elevated temperatures. All specimens were tested at 23 °C. Prior to the test, the compressive strength of tested specimens was evaluated according to ASTM C39. The specimen is placed in the strain measurement equipment (**Fig. 3.14**). The specimen should be comfortably seated before rings tightening. One loading cycle is performed up to 40% of the ultimate load without taking the strain readings to ensure gauges well seating. For the next cycle, the strain at 40% loading of the specimen capacity is measured. The modulus of elasticity (E) is calculated as follow:

$$E = (S_2 - S_1) / (\epsilon_2 - 0.000050) \quad (\text{Eq. 3.1})$$

Where:

E= Modulus of elasticity (psi)

S<sub>2</sub>= stress corresponding to 40% of the ultimate load

S<sub>1</sub>= stress corresponds to 0.000050 longitudinal strain

ε<sub>2</sub> = longitudinal strain achieved at 40% of the ultimate load



**Fig. 3.14 Modulus of elasticity test setup.**

#### **3.4.8 Shrinkage micro-strain test**

A shrinkage test was performed on prismatic specimens  $75 \times 75 \times 285$  for each mixture according to ASTM C 157. The unrestrained one-dimensional deformations were measured using a dial gauge with an accuracy of 0.01 mm/m in the room temperature (23 °C), and relative humidity of 45%. Shrinkage bars were measured daily for the first week after casting. Then the measurements were performed weekly for up to 56 days (**Fig. 3.15**).



**Fig. 3.15 Shrinkage micro-strain test setup.**

### **3.4.9 Water absorption test**

Water Absorption (i.e., sorptivity) testing of concrete was performed according to ASTM C 1585 "Standard Test Method for Measurement of Rate of Absorption of Water by Hydraulic-Cement Concretes". Pre-dried cylinder disk specimens, with a diameter of 100 mm and height of 50 mm, were placed on a plastic mesh to have the bottom face submerged 2 mm below water level. Other exposed faces were sealed to ensure one-dimensional absorption (**Fig. 3.16**). The absorbed water was then measured frequently as a function of the specimen weight. The absorption rate represented the relationship between the cumulative absorbed water and the elapsed time square root.



**Fig. 3.16 Water absorption test method.**

### 3.4.10 Ultra-sonic pulse velocity test (USPV)

Ultra-sonic pulse velocity test was performed according to ASTM C597 on prismatic specimens using directly arrayed two longitudinal transducers (**Fig. 3.17**). The average of the pulse velocity at three fixed points at each specimen side was repeatedly measured to identify specimens' quality in terms of micro-cracking development. The pulse wave velocity depends on the crossed media homogeneity and density, which make pulse passing through concrete with a high void or crack content take a long time as it will turn around the different media with lower density (i.e., voids or cracks).



**Fig. 3.17 Ultra-sonic pulse velocity (USPV) test.**

### 3.4.11 Drop weight impact test

Impact test was performed following ACI Committee 544 drop weight impact test. In this test, a hammer of mass ( $m$ ) is being repeatedly dropped freely with gravity acceleration ( $g$ ) from a height ( $h$ ) of 457 mm on a 63.5 mm diameter steel ball centred on the top surface of the specimen (**Fig. 3.18**). Just before striking the steel ball, the velocity ( $v$ ) of the hammer can be calculated by (**Eq. 3.2**).

$$v = (2gh)^{1/2} \quad \text{(Eq. 3.2)}$$

At this velocity, the hammer has kinetic energy ( $ke$ ) given by (**Eq. 3.3 and 3.4**)

$$ke = \frac{1}{2} m v^2 \quad \text{(Eq. 3.3)}$$

$$ke = mgh \quad \text{(Eq. 3.4)}$$

The failure strength was defined as the number of successive blows to spread the cracks sufficiently (number of blows to failure) so that the pieces of specimen touched three of the steel lugs. The specimen's absorbed energy can be then calculated by multiplying the number of blows by the amount of energy transferred per blow.

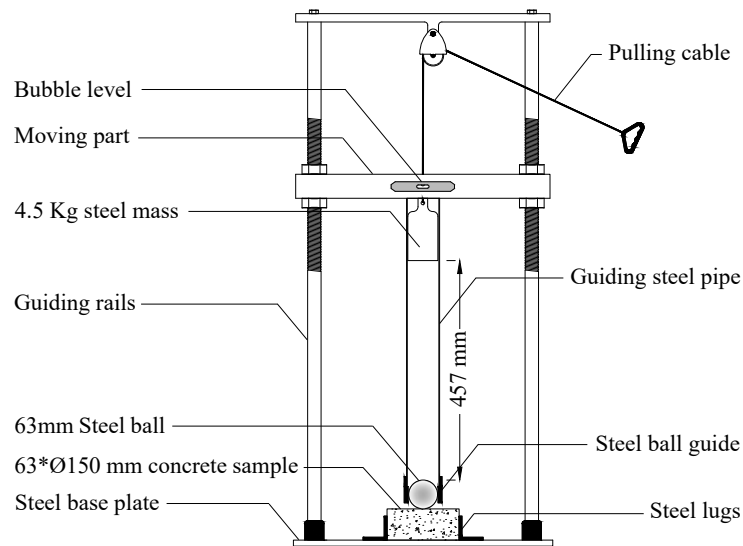


**Fig. 3.18 Schematic drawing for the drop weight impact test machine.**

Chapter 3

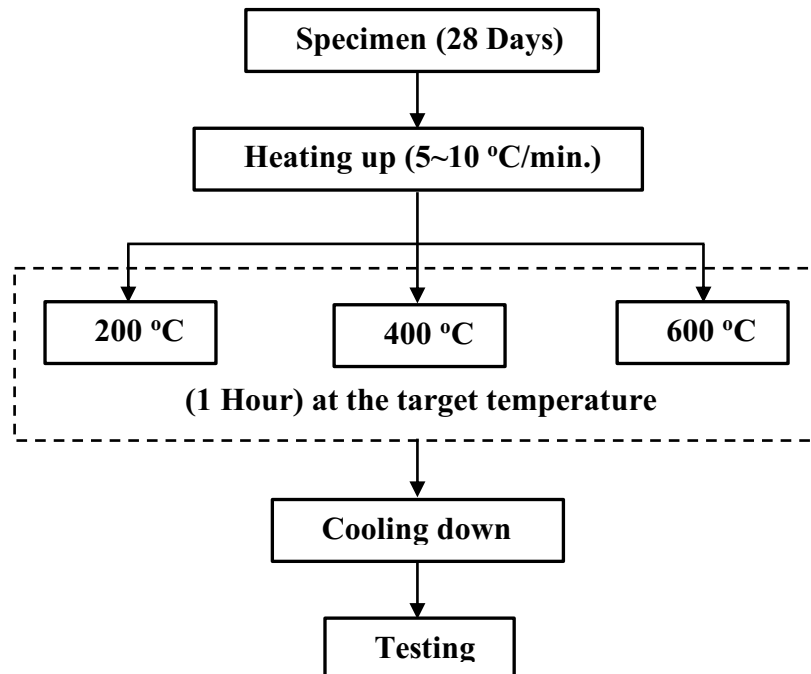
The used drop weight impact test machine for this research was designed and built up in Concordia labs (Fig. 3.19).



Fig. 3.19 Drop weight impact test machine.

### 3.5 Curing regime elevated temperatures exposure routine

All specimens were demolded after 24 hours. OPC specimens were continuously cured in a lime water tank at temperature  $23 \pm 1^\circ\text{C}$  until testing ages. AAS samples were stored in sealed bags after demolding at the laboratory ambient condition (Temperature =  $23 \pm 1^\circ\text{C}$  and  $45 \pm 3\%$  relative humidity). For elevated temperature exposure, as most of the hydration products are expected to decompose at temperature levels up to  $600^\circ\text{C}$ , three levels of elevated temperatures ( $200^\circ\text{C}$ ,  $400^\circ\text{C}$ , and  $600^\circ\text{C}$ ) were used to obtain determinant results that can show a contrast at each level. Agreeing with previous studies (Yang, Lin et al. 2009, Kong and Sanjayan 2010, Siddique and Kaur 2012), Samples were heated for one hour, starting after the assigned temperature level is reached by the oven. Then, they were left to cool down in the oven before testing (Fig. 3.20).



**Fig. 3.20 Exposure to various elevated temperatures routine.**

### Chapter 3

Moreover, to ensure that the specimen core reached the exposure temperature, a thermocouple type K was attached to a trial specimen core, and the temperature reading was simultaneously observed along with the oven temperature (Fig. 3.21 a, b, and c).

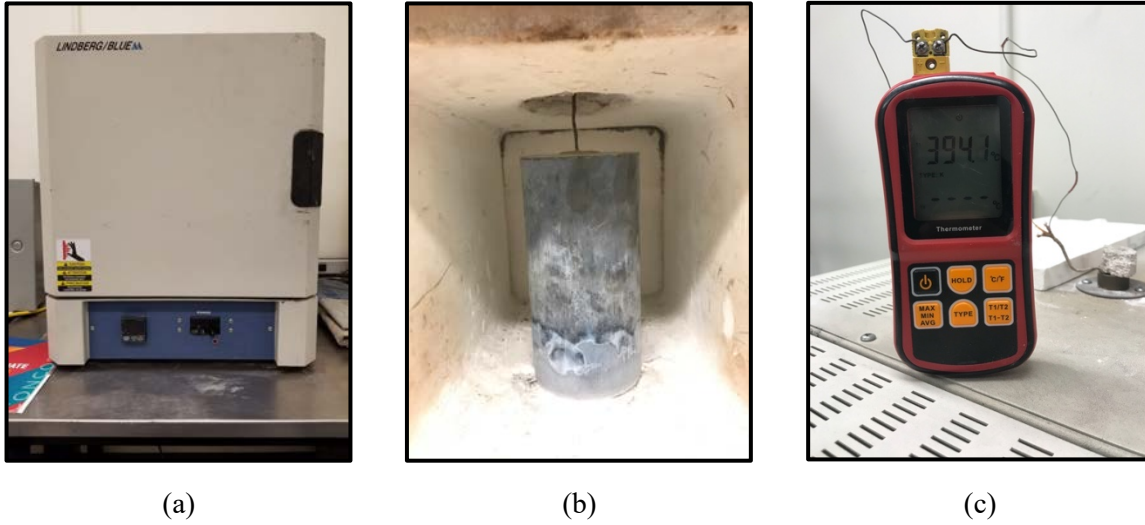


**Fig. 3.21 Specimen core temperature monitoring during exposure to elevated temperatures.**

---

## Chapter 4 Effect of Activator Nature on the Impact Behaviour of Alkali-Activated Slag Mortar

### 4.1 Introduction

Twelve mortar mixtures were prepared in this phase (**Fig. 4.1**), as mentioned earlier in **Section 3.2.1**. For each AAS mixtures, the name for the mixture has a letter, and two numbers, the letter (M) refers to mortar, and the first number refers to the silica modulus ( $M_s$ ), and the second refers to  $\text{Na}_2\text{O}\%$  dosage. The mixing proportions for all mixtures are listed in **Table 4.1** Mixture proportions..

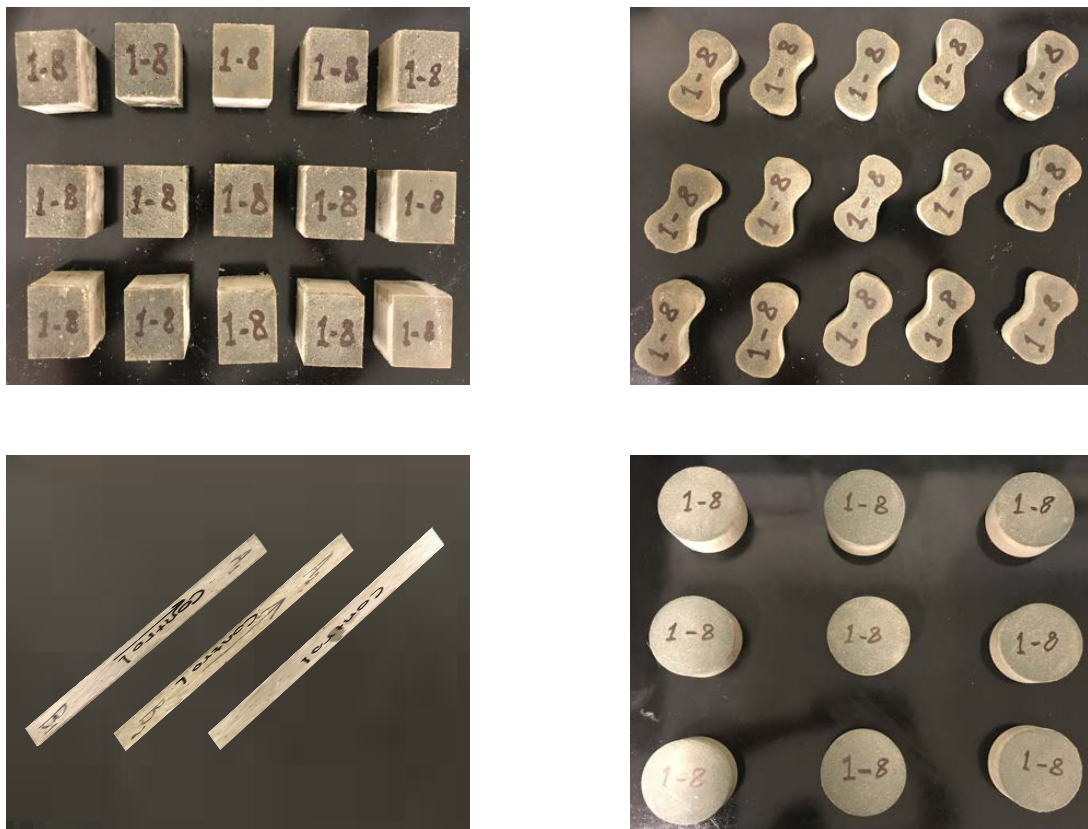


**Fig. 4.1** Different specimens of mixture (M 1-8) after demolding.

**Table 4.1 Mixture proportions.**

Mixture	Modulus (SiO <sub>2</sub> /Na <sub>2</sub> O)	Dosage (Na <sub>2</sub> O %)	Binder (kg/m <sup>3</sup> )	Sand (kg/m <sup>3</sup> )	NaOH (kg/m <sup>3</sup> )	Na <sub>2</sub> SiO <sub>3</sub> (kg/m <sup>3</sup> )	Water (L/m <sup>3</sup> )
OPC	NA	NA	549	1509	0	0	241
M 1-4	1	4 %	540	1485	19	75	191
M 1-6	1	6 %	536	1474	28	112	166
M 1-8	1	8 %	532	1462	38	148	142
M 1.25-4	1.25	4 %	540	1484	17	94	179
M 1.25-6	1.25	6 %	535	1472	25	140	149
M 1.25-8	1.25	8 %	531	1461	33	185	119
M 1.25-10	1.25	10 %	527	1449	41	229	89
M 1.5-4	1.5	4 %	539	1483	15	112	167
M 1.5-6	1.5	6 %	535	1471	22	167	131
M 1.5-8	1.5	8 %	531	1459	29	221	96
M 0-8	0	8 %	534	1469	55	0	235

## 4.2 Results and discussion

### 4.2.1 Flowability

**Table 4.2** shows flowability measurements for OPC and AAS mixtures. Results indicated that for all AAS mixtures, flowability was higher than that of the OPC mixture. This agreed with previous research stating that alkali-activated slag mortar has better flowability than OPC, while it has a shorter setting time (Yang, Song et al. 2008).

Generally, the changes in AAS mortar flowability was insignificant regardless of the activator Ms and Na<sub>2</sub>O%, which agrees with previous findings (Yang, Song et al. 2008, Jang, Lee

et al. 2014, Puertas, Varga et al. 2014). For instance, at  $M_s = 1$ , an 8%  $\text{Na}_2\text{O}$  mixture exhibited about 4% lower flowability than the 4%  $\text{Na}_2\text{O}$  mixture. This slight decrease can be attributed to the increase in the activator's alkalinity, which in turn increases the dissolution rate of the slag particles. This high dissolution rate favoured the faster formation of gel reaction products, consequently reducing the flowability (Fernández-Jiménez and Puertas 2003, Hajimohammadi, Provis et al. 2010). On the other hand, increasing the  $M_s$  value was reported to increase the mortar flowability regardless of  $\text{Na}_2\text{O}\%$ . For instance, at  $\text{Na}_2\text{O}$  dosage of 8%, increasing the  $M_s$  value up to 1.5 resulted in only 3% increase in flowability. This can be attributed to the increased surface tension of the activator liquid, which hinders the slag particles dissolution and consequently retarding the formation of the reaction products (Puertas, Varga et al. 2014).

**Table 4.2 Flowability measurements.**

Mix.	M-OPC	M1-4	M1-6	M1-8	M1.25-4	M1.25-6	M1.25-8	M1.25-10	M1.5-4	M1.5-6	M1.5-8
Flowability (mm)	134	165	160	158	172	168	162	160	175	170	163

In addition to the effect of the activator properties on the rate of reaction and, consequently, the flowability, the activator liquid's viscosity might also affect the flowability of fresh AAS mortar. Viscosity test results showed that the activator liquid viscosity increases by increasing the dosage ( $\text{Na}_2\text{O}\%$ ) regardless of the modulus. For instance, at  $M_s = 1$ , increasing the activator dosage from 4% to 8% resulted in increasing the viscosity at all shear rates during the test. This might be a contributing agent in decreasing the mortar flowability at higher dosages (**Fig. 4.2**).

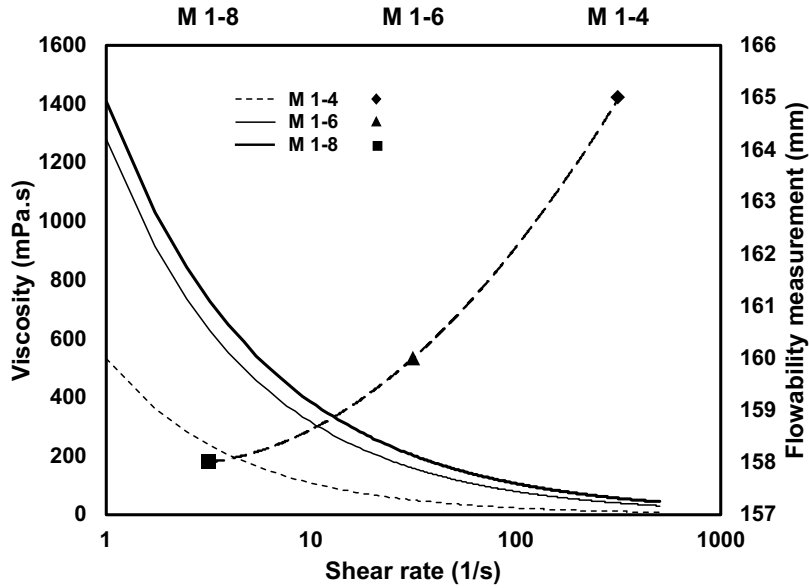
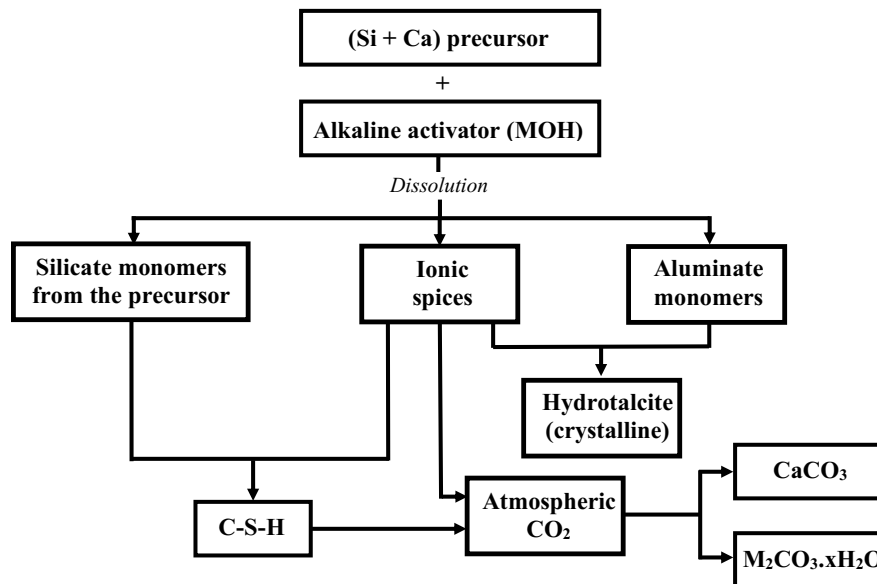


Fig. 4.2 Viscosity vs flowability for mixtures of  $M_s=1$ .

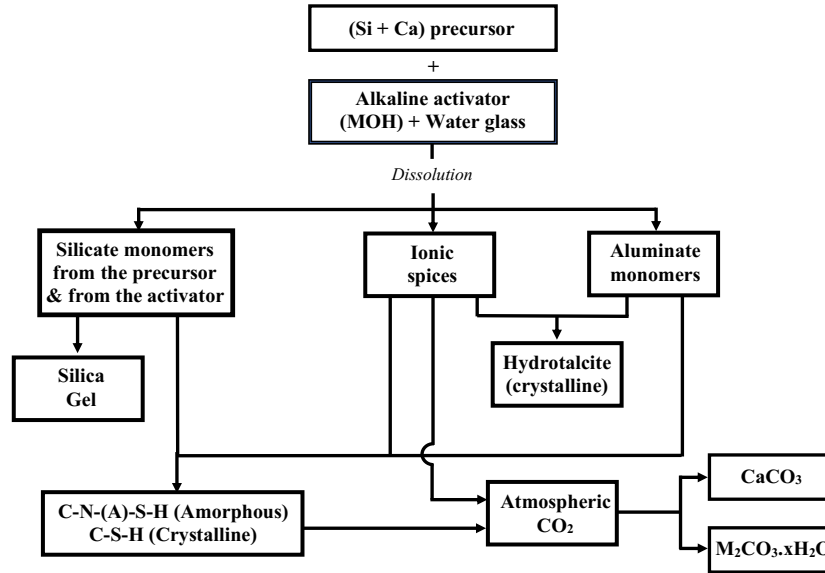
#### 4.2.2 Hydration products

Fig. 4.3 and Fig. 4.4 represent the proposed reaction mechanism for alkali-activated slag. According to the most commonly proposed reaction mechanisms, the activator agent chemical composition is highly affects the reaction kinetics (Haha, Le Saout et al. 2011). In the slag case as a (Si+Ca) precursor, the reaction can be considered through four stages. Regardless of the activator nature in terms of including water glass or not, the first stage would be described as a dissolution phase. In this phase, the alkaline activator attacks the precursor particles destroying the chemical bonds such as Al-O-Al, Si-O-Si, and Ca-O (Glukhovsky, Rostovskaja et al. 1980). In this while, the aqueous phase is being enriched with  $Ca^{+2}$  and  $Mg^{+2}$  from the precursor reducing the media pH gradually (Zhang, Zhao et al. 2008, White, Provis et al. 2011). The second stage is the formation of different species. The mainly formed species are believed to be  $Si(OH)_4$  and  $Al(OH)_4$ , and while the reaction is in progress, more  $(OH)^-$  ions are being involved with the species producing more complex formations (Provis, Duxson et al. 2005). Afterwards, the activator type

defines the nature of the further formed hydration products. In the case of an activator without water glass, the precursor is the dominant agent of Si releasing and  $\text{Si(OH)}^{-4}$  species formation. In this case,  $\text{Ca}^{+2}$  and  $\text{Si(OH)}^{-4}$  group up together, forming C-S-H. However, and especially at high dosages of  $\text{Na}_2\text{O}$ , the high pH may affect the Ca reactivity and direct it to react with  $\text{CO}_2$  from the atmosphere along with the unreacted Na from the activator to form calcium and sodium carbonates and no silica gel is supposed to condensate within the structure (Fernandez-Jimenez, Puertas et al. 2002, Puertas, Palacios et al. 2011, Myers, Bernal et al. 2013). In a parallel mechanism, Al and Mg group up together, forming the hydrotalcite phase (Wang and Scrivener 1995). For activators with water glass, similar products are expected to form. However, Al and Na species would be accommodated in the structure of C-S-H, favoring the formation of amorphous products such as C-A-S-H (Richardson, Brough et al. 1994). Another portion of cross-linked silica gel may condense within the reaction products microstructure. The last reaction stage occurs in a solid-state process forming more highly intermixed hydration products (Wang and Scrivener 1995, Fernández-Jiménez and Puertas 1997).



**Fig. 4.3 Reaction mechanism model for (Si+Ca) precursor activated with MOH**



**Fig. 4.4 Reaction mechanism model for (Si+Ca) precursor activated with M OH + water glass**

#### 4.2.2.1 Heat of hydration

**Fig. 4.5** shows the heat of hydration for samples at the same  $\text{Na}_2\text{O}$  dosage of 8% with three silica modulus values (1, 1.25, and 1.5). The first peak represents the dissolution of the slag particles. The rate of dissolution can be assigned to the dosage, as explained previously. As shown in the figure, the three different activator silica modulus peaks vary in a very narrow range. This is attributed to the similarity in the dissolution rates achieved by the same  $\text{Na}_2\text{O}$  % dosage for the three mixtures. However, the second peak, which is assigned to the formation of different species, was markedly different for each mixture. For lower silica modulus, the peak tends to take place earlier and more intense. That can be explained by the higher rate of precipitation of the hydration products on the slag grains surfaces, accommodating less Si species in less dense microstructure (Haha, Le Saout et al. 2011). As a side effect, this might hinder further reaction of the unreacted inner core. Moreover, for the delayed second peak that corresponds to high silica modulus, the

high availability of silicates results in delayed dissolute aluminate, and consequently, delay the formation of hydration products accommodating Al (Puertas, Varga et al. 2014).

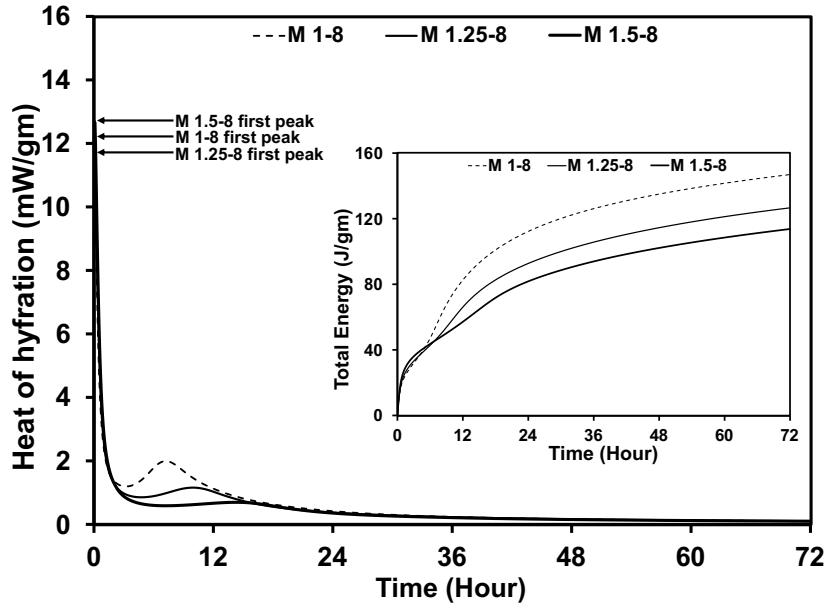


**Fig. 4.5 Heat of hydration for different silica modulus values at the same Na<sub>2</sub>O % dosage.**

On the other hand, **Fig. 4.6** shows the heat of hydration rates for three different Na<sub>2</sub>O % dosage mixtures at the same silica modulus. The first peak for each mixture indicates the activator's ability to achieve a higher dissolution rate. Consequently, the second peak becomes significantly earlier due to the earlier formation of the hydration products. For low Na<sub>2</sub>O % dosage (i.e., 4%), the second peak was found to take place through a more extended period. This happens due to the smooth, gradual concentration shifting between the slag grain and the surrounding hydration products, favouring a kind of reaction reinitiating through a diffusion mechanism (Fernández-Jiménez and Puertas 1997).

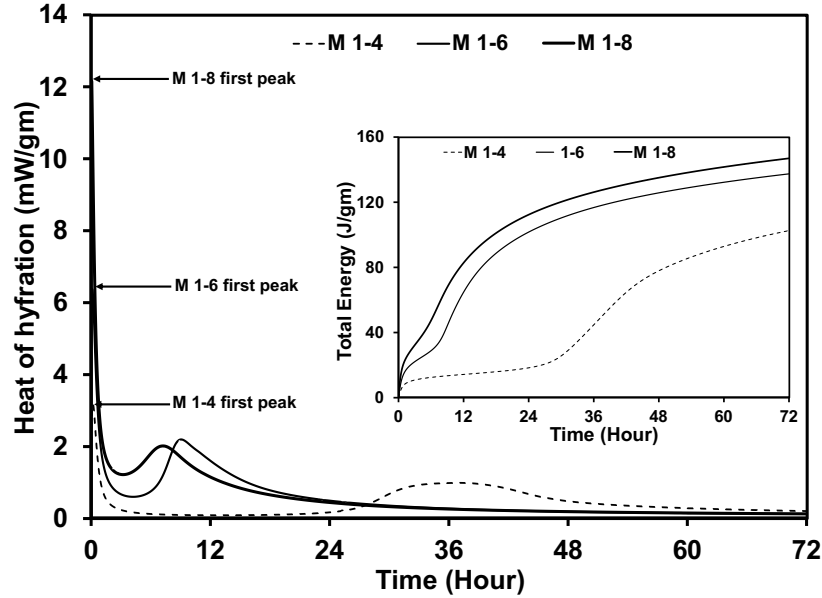
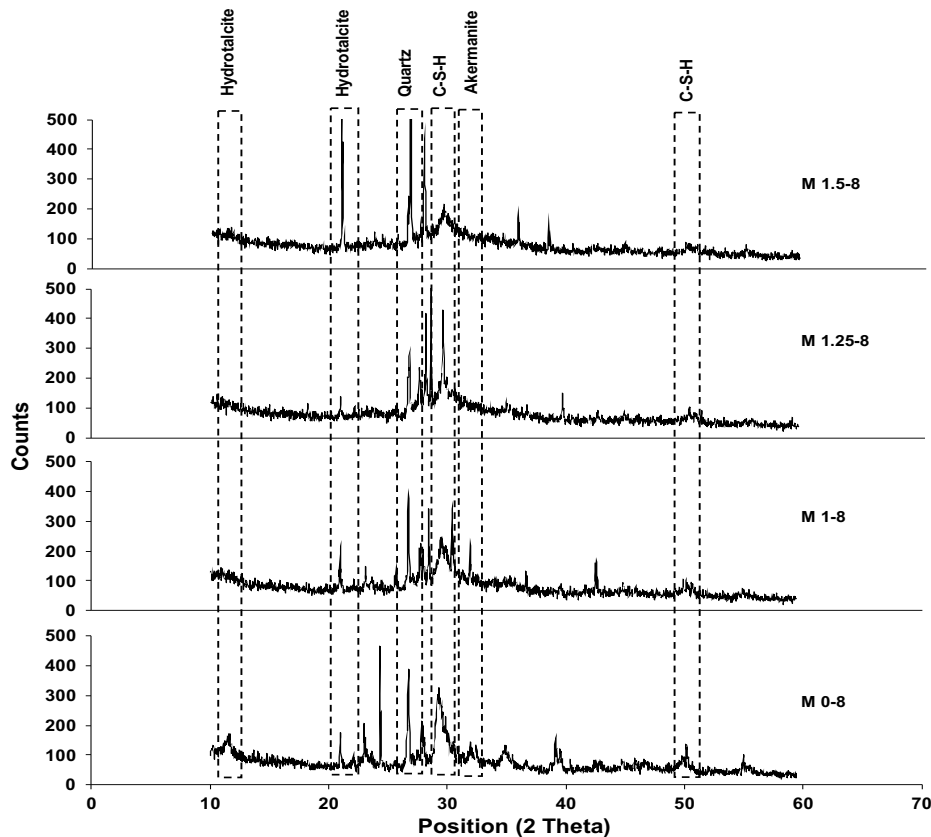


Fig. 4.6 The heat of hydration evolution at different  $\text{Na}_2\text{O}$  % dosages.

#### 4.2.2.2 X-Ray diffraction

Previous studies had compared the formed hydration products in both OPC and AAS systems. In OPC systems, C-S-H and  $\text{AF}_m$  are the main hydration products formed along with ettringite and CH (Lothenbach and Winnefeld 2006). In AAS, the proposed reaction models suggested that different C-S-H phases with low Ca/Si ratio, hydrotalcite, and  $\text{AF}_m$  are the main formed hydration products (Wang and Scrivener 1995, Jiang, Silsbee et al. 1997). The nature of these hydration products is directly associated with the chemical characteristics for the used precursor and activator (Caijun and Yinyu 1989, Wang, Scrivener et al. 1994, Pal, Mukherjee et al. 2003, Shi, Roy et al. 2003). Different phases of C-S-H were identified for mixtures activated by both NaOH and water glass according to the XRD results (Fig. 4.7). The availability of Si species in the pore solution results in longer Si-O-Si chains. As a result, more bridging sites are ready for substituting Si by Al, forming C-S-H with higher Al content (Taylor 1986, Nonat 2004, Myers, Bernal et al. 2013). However, the composed C-S-H has an amorphous fraction associated

with incorporating Na species from the activator and Al provided by the precursor dissolution process (C-N-(A)-S-H). The XRD cannot detect this amorphous fraction. This can explain the reduction in C-S-H peaks as silica modulus increased for the same Na<sub>2</sub>O% dosage. Conversely, crystalline C-S-H peaks were clear for the mixture activated by only NaOH (without water glass) since the C-S-H formed was highly crystalline (Burciaga-Díaz and Escalante-García 2013). The formed hydrotalcite phase (highly crystalline) showed more observed peaks in the absence of water glass (i.e., M 0-8). This may be attributed to the complete tendency of the dissolute Al and Mg species to form hydrotalcite instead of sharing some Si species to form the amorphous C-N-(A)-S-H phase (Wang and Scrivener 1995, Shi, Roy et al. 2003).



**Fig. 4.7 X-ray diffraction patterns of AAS activated at different levels of Modulus (M<sub>s</sub>).**

On the other hand, at a fixed modulus value, increasing the  $\text{Na}_2\text{O}\%$  dosage increased dissolve Al and Mg from the precursor and Ca and Si species. This favored C-S-H and (C-N-(A)-S-H) formation in a synergetic way (Burciaga-Díaz and Escalante-García 2013). Moreover, the hydrotalcite phase precipitation increased by increasing the  $\text{Na}_2\text{O}\%$  dosage (Fig. 4.8). This can be ascribed to the higher availability of Al achieved at higher dissolution rates.

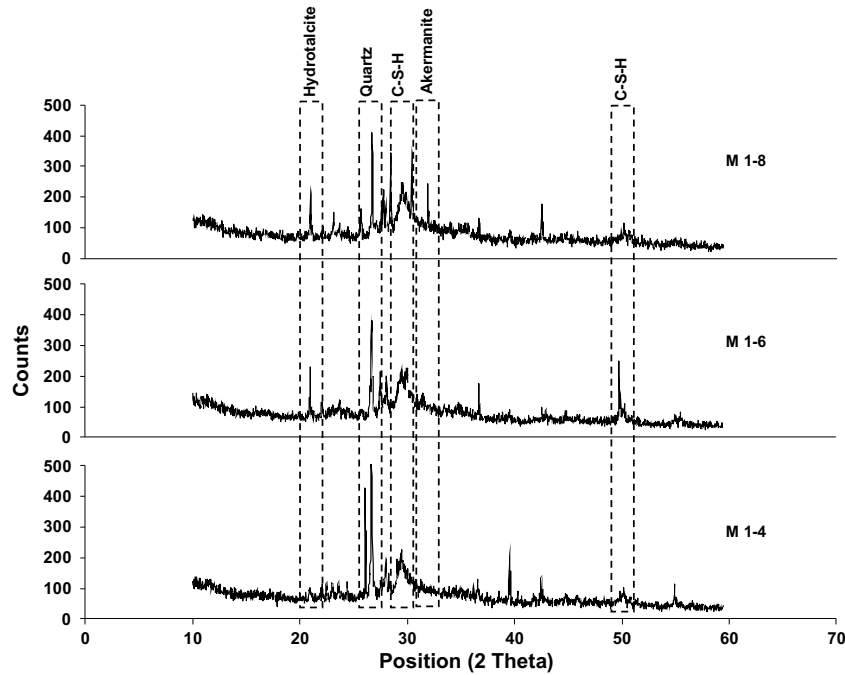


Fig. 4.8 X-ray diffraction patterns of AAS activated at different levels of dosage ( $\text{Na}_2\text{O}\%$ ).

#### 4.2.2.3 Thermogravimetric analysis

Fig. 4.9 represents the thermogravimetric test results obtained for OPC mixture and AAS mixtures with different silica modulus levels. All curves are representing tested samples before exposure to elevated temperatures. It was clear that typical peaks represent common hydration products between OPC and AAS, such as different phases of C-S-H, which show heat flow peaks within the temperature range of (100-200 °C). However, the OPC sample showed an individual peak between (450-500 °C), which corresponds to the portlandite. For AAS mixtures, results

confirm the variations in the formed hydrations products regarding the amount which resulted from changing activator nature. Both dosage and silica modulus were found to affect the formation of hydration products. The high alkalinity achieved by higher dosages resulted in a higher dissolution of the precursor favouring the release of more species to the aqueous phase such as Mg and Al.

Consequently, more hydration products were formed, such as hydrotalcite. Moreover, increasing the silica modulus increased the Si species accommodated at the C-S-H, providing more links to accommodate Al species. For instance, the heat flow behaviour reflected in the derivative weight losses at the C-S-H peak was doubled by increasing the modulus from 0 to 1.5.

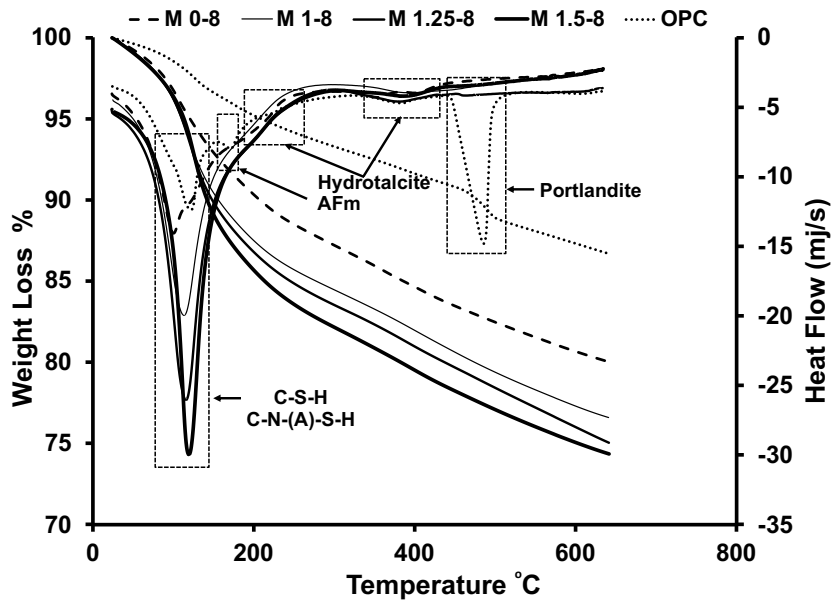


**Fig. 4.9 Thermogravimetric analysis (TGA) of hardened OPC vs. AAS with different levels of modulus ( $M_s$ ).**

On the other hand, the binder deterioration was assessed in terms of weight loss during the thermogravimetric analysis. A portion of the formed hydration products decomposed according to each hydration product type and stability at elevated temperatures at each temperature levels. **Fig. 4.10** Represents the decomposed and retained percentages of AAS binder after exposure to the three assigned elevated temperatures compared to the percentages decomposed for the binder without pre-exposure. It can be observed that the tested binder sample without exposure to elevated temperature showed higher total weight loss during the test compared to samples exposed to different elevated temperatures before testing. After exposure to 200 °C and 400 °C, samples showed 18% and 14% total weight loss compared to 25% for the tested sample without exposure to elevated temperatures. However, the sample which pre-exposed to 600 °C showed only 5% weight loss, which indicates the severity of hydration products decomposition at this relatively high temperature, while after exposure to lower levels of elevated temperatures (i.e. 200 °C and 400 °C), the binder hydration products could show convenient stability. Moreover, by comparing the decomposed and the retained hydration products percentage at each temperature level to the total decomposed portion without exposure at the same temperature during the test, it was found that at 200 °C, 400 °C, and 600 °C, the retained percentages were 60%, 50%, and 20%. This confirms the high stability of the formed hydration products as at least 50% of it can withstand exposure to 400 °C.

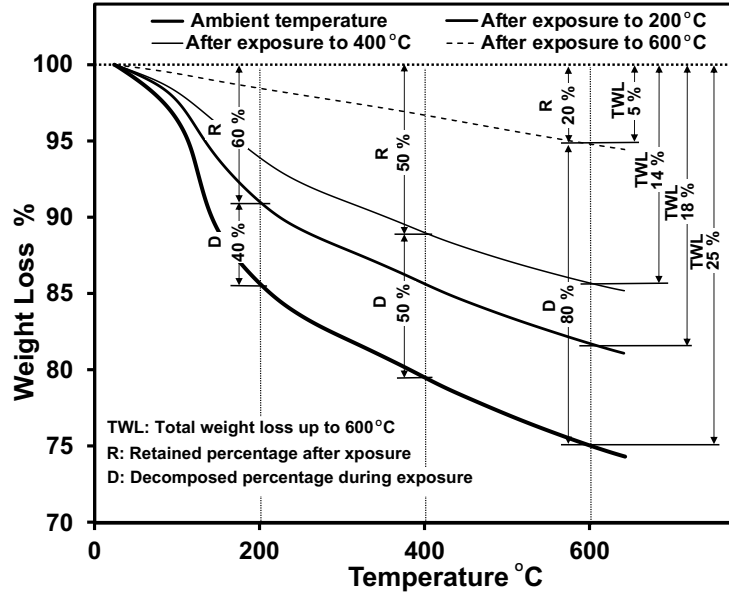


**Fig. 4.10 Thermogravimetric analysis for binder before and after exposure to various elevated temperatures.**

### 4.2.3 Compressive strength

**Fig. 4.11** summarizes the compressive strength for all tested samples without exposure to elevated temperatures. All AAS specimens exhibited better 28 days compressive strength than that of the cement-based mixtures, in agreement with previous findings (Bilim, Karahan et al. 2013). Regardless of the  $M_s$  value, increasing  $Na_2O\%$  resulted in a considerable increment in early age compressive strength (i.e., up to 7 days). For instance, at  $M_s=1.25$ , the mixture with 8%  $Na_2O$  exhibited 3 days compressive strength about double that of the 4%  $Na_2O$  mixture. This might be attributed to the early high rate of dissolution achieved by increasing  $Na_2O\%$ ; consequently, the early formation of gel products that favour early strength gaining. However, at later ages (i.e., 28 days), increasing  $Na_2O\%$  up to 6% resulted in a significant increase in compressive strength (about 25%). At  $Na_2O\%$  above 6%, the corresponding increase in compressive strength seemed to be

insignificant. For example, increasing  $\text{Na}_2\text{O}\%$  from 6% to 8% resulted in only a 5% increase in compressive strength regardless of the  $M_s$  value.

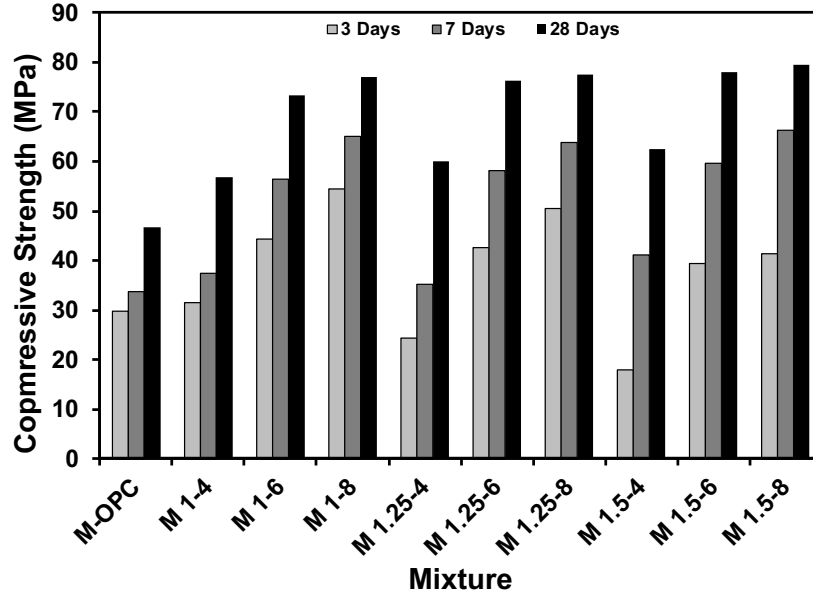
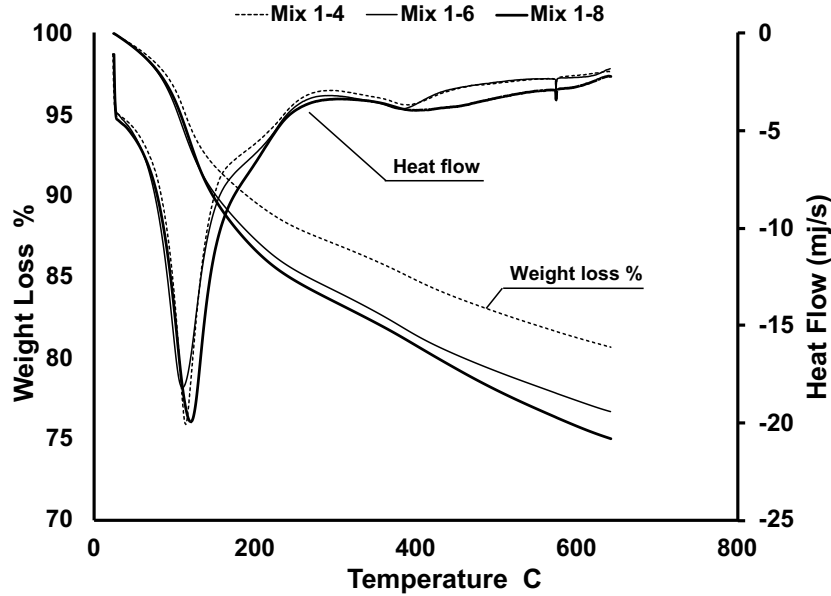


Fig. 4.11 Compressive strength for various mixtures.

Thermogravimetric and derivative Thermogravimetric analysis (TGA & DTG) came to confirm the strength results for alkali-activated slag mixtures. Results showed that increasing the  $\text{Na}_2\text{O}\%$  dosage was related to weight loss %. This could be explained by the amount of C-S-H gel as it is being burnt. For instance, at  $M_s=1$ , increasing the dosage from 4 to 6% resulted in 4% increase in weight loss. However, increasing the dosage from 6 to 8% was recorded to increase the weight losses by only 1.5 % (Fig. 4.12). The reported weight losses are related to the increased formed C-S-H gel amount at higher dosages. These results agreed with the compressive strength results as the compressive strength was significantly increasing by increasing the  $\text{Na}_2\text{O}\%$  dosage up to 6 %, which is directly related to the amount of formed C-S-H gel in the binder.



**Fig. 4.12** TGA and TDG curves for mixtures of  $M_s=1$ .

This indicates that a 6% dosage seems to be a threshold value for  $\text{Na}_2\text{O}\%$  that provides enough dissolution rate to achieve adequate strength. Increasing  $\text{Na}_2\text{O}\%$  supplies more network breaking cations that control the formation of Al-O-Al framework. This eventually would accommodate the Si species. Hence, the formed reaction products at this level of alkalinity will be enough to surround the slag particles preventing further reaction (Fernández-Jiménez, Palomo et al. 2005).

On the other hand,  $M_s$  showed a significant effect on the early age compressive strength. **Fig. 4.13** indicated that increasing the  $M_s$  value had led to a significant decrease at the early age compressive strength regardless of the  $\text{Na}_2\text{O}\%$  dosage. For instance, at 4%  $\text{Na}_2\text{O}$  dosage, increasing  $M_s$  up to 1.5 resulted in about 50% reduction in the 3 days strength compared to that of mixtures with  $M_s=1$  at the same age. Increasing the  $M_s$  value resulted in higher surface tension of the activator (Puertas, Varga et al. 2014). Therefore, this reduction in early strength can be attributed to the limitation of particle dissolution resulting from the activator's high surface tension.

This, in turn, will limit the availability of formed alumina rich gel framework needed to accommodate the silicates species through Si-O-Al bonds (Fernández-Jiménez, Palomo et al. 2006, Puertas, Varga et al. 2014).

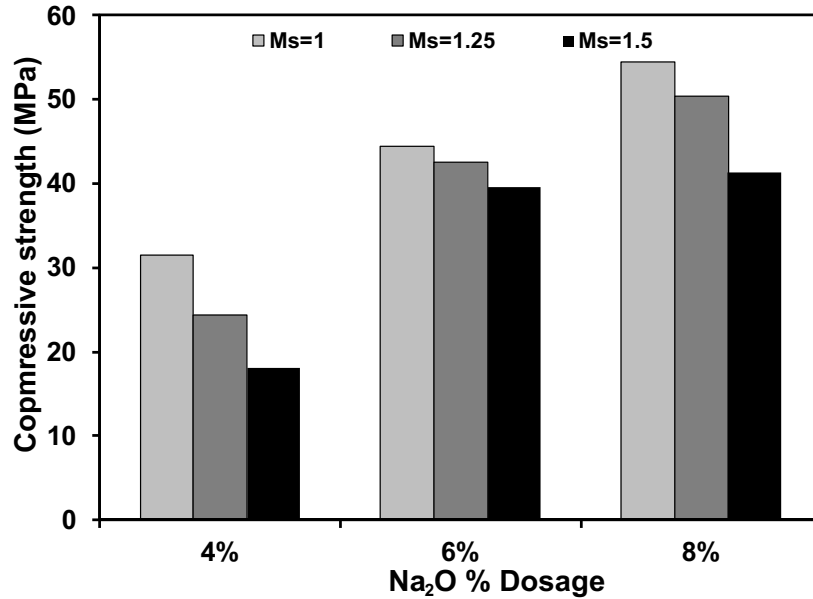


**Fig. 4.13** Early age compressive strength (3 days) at constant Na<sub>2</sub>O%.

**Fig. 4.14** confirms the vital role of silicate species provided by sodium silicate in the activation process and strength development for AAS. Compressive strength dramatically decreased in the absence of the sodium silicate (i.e., mixtures activated by sodium hydroxide only). For instance, at Na<sub>2</sub>O = 8%, mixtures activated by sodium hydroxide only achieved about 65 % lower 28 days compressive strength than that of the mixtures with sodium silicates and sodium hydroxide. This agrees with other researches indicating that incorporating silicates in the activator significantly affects the mechanical properties. This highlights the soluble silicate species' role as it gradually shifts the system to species with larger chemical rings structure leading to good mechanical properties (Davidovits 2008). Also, in the absence of silicates, the reaction products formed around the slag particles were reported to be less porous, limiting the diffusion of the newly

formed gel to fill the spaces between the particles (Haha, Le Saout et al. 2011). This is anticipated to affect strength development significantly.

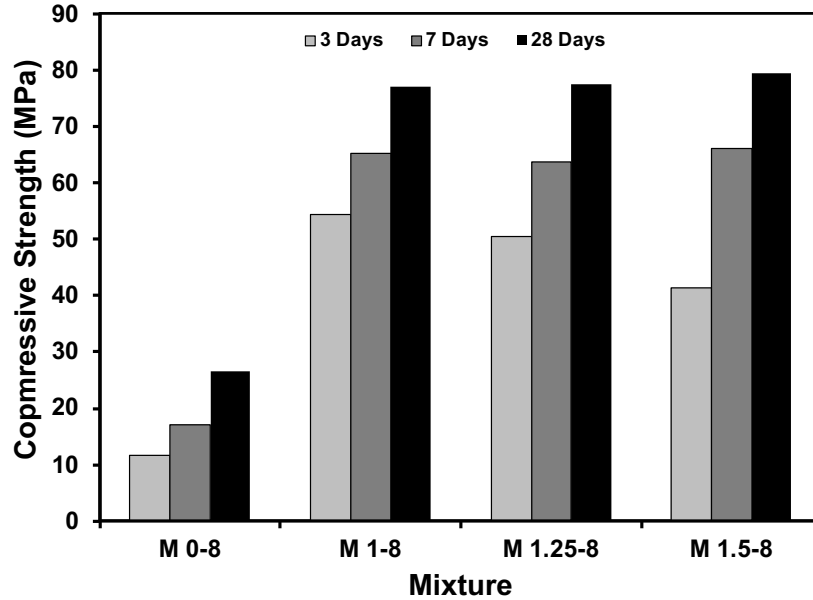


**Fig. 4.14 Compressive strength vs. Modulus at ages (3, 7 and 28) days.**

**Fig. 4.15** summarizes the residual compressive strength for all mortar mixtures after exposure to different levels of elevated temperature. The reduction in OPC mixture compressive strength increased as exposure temperature increased. For instance, OPC specimens exposed to elevated temperatures up to 200 °C and 600 °C exhibited 24% and 61% losses of their original 28 days strength, respectively. This reduction can be ascribed to the losses of calcium silicate hydrated (C-S-H) gel at the range of 200 °C, the main hydration product responsible for the strength development in the OPC system (Richardson 2000, Peng and Huang 2008). Moreover, during cooling down after exposure to 400 °C or higher, the decomposed hydration products, specially portlandite, started a rehydration process accompanied by an increased volume, inducing internal stresses. These internal stresses consequently resulted in internal micro-cracks that negatively affected the strength (Petzold and Röhrs 1970, Bažant, Kaplan et al. 1996, Georgali and Tsakiridis

2005). For AAS mixtures, the nature of alkaline activator properties (i.e., silica modulus and dosage) were found to have substantial effects on both original strength and the residual strength after exposure to elevated temperatures.

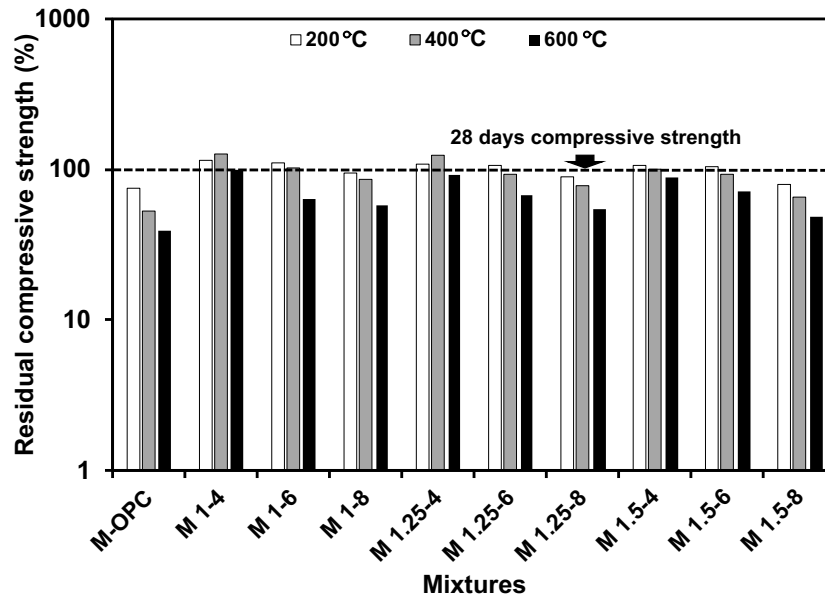


**Fig. 4.15 Mortar residual compressive strength (%) after elevated temperature exposure.**

After exposure to elevated temperatures, by observing AAS mixtures individually, it was found that the residual strength was affected by the decomposed hydration products amount. In other words, each hydration product starts to decompose at a specific temperature. Consequently, it is expected that the degradation grades will vary at each level of elevated temperatures. For example, mixture M 1.5-8 showed different residual compressive strength levels after exposure to different levels of temperatures, as illustrated in **Fig. 4.15**. This is correlated to the weight loss at each level of temperature due to the hydration products decomposition. For example, C-S-H, which represents the main hydration product in AAS systems, as explained previously, starts to decompose at a temperature range of (120-200 °C). It was evident through the heat flow peaks for tested samples after heating up to 200 °C or more as they showed lower peaks at this range of

temperature comparing to that tested without temperature exposure (Fig. 4.16). This is ascribed to the CSH decomposition, leading to strength degradation after exposure to elevated temperatures at each level.

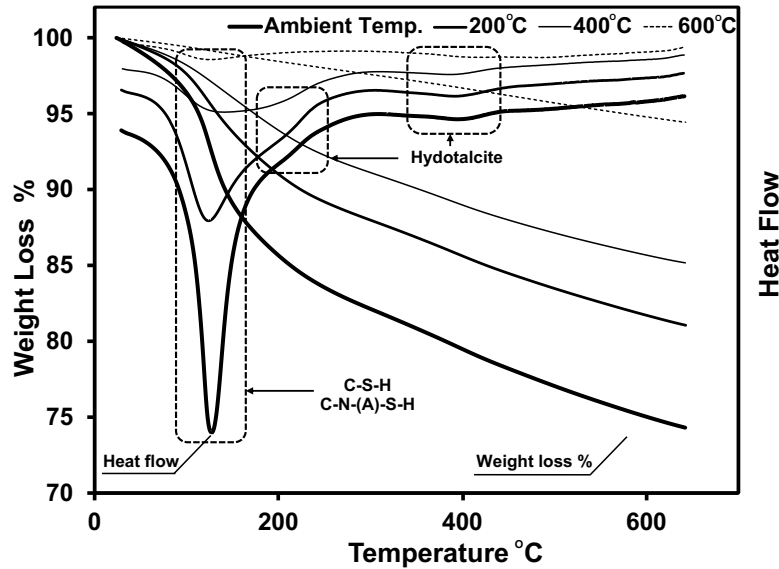


**Fig. 4.16 Thermogravimetric analysis of AAS mixture M 1.5-8 after exposure to different levels of temperatures.**

Another critical parameter affecting the residual strength is the amount of unreacted particles that may shift at elevated temperatures to other phases. The akermanite corresponding to the unreacted slag is believed to get a more densified structure at high temperatures. This might be favourable for the residual strength under quasi-static loading (Kong and Sanjayan 2008, Reddy, Tulyaganov et al. 2013). For instance, mixture M 1-4, which is assigned to the lowest level of activation in terms of  $\text{Na}_2\text{O}$  % dosage and silica modulus, had shown the best performance after exposure to three levels of elevated temperatures. At the highest level of exposure (i.e., 600 °C), mixture M 1-4 exhibited the same compressive strength as the original before elevated temperature exposure. Conversely, due to the high amount of decomposed hydration products within the

structure at a high level of alkaline activation, the degradation in compressive strength was significant at all levels of elevated temperature exposure (**Fig. 4.17**).

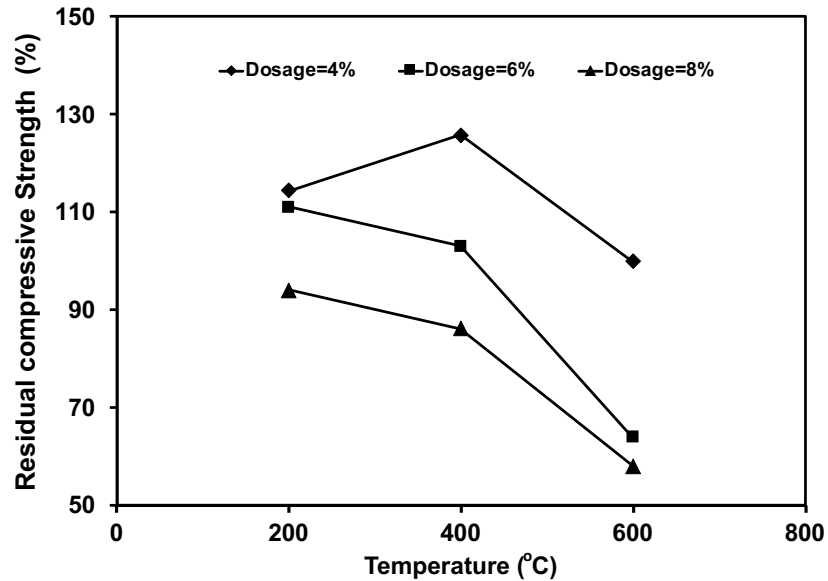


**Fig. 4.17** Mortar residual compressive strength at  $M_s=1$ .

#### 4.2.4 Tensile strength

It was found that the behaviour of the tested specimens is not matching that of the compressive strength. As shown in **Fig. 4.18**, increasing  $\text{Na}_2\text{O}\%$  from 4% to 6% resulted in a better tensile strength regardless of the  $M_s$  value. However, the achieved tensile strength for mixtures with  $\text{Na}_2\text{O}\%$  above 6% had decreased.

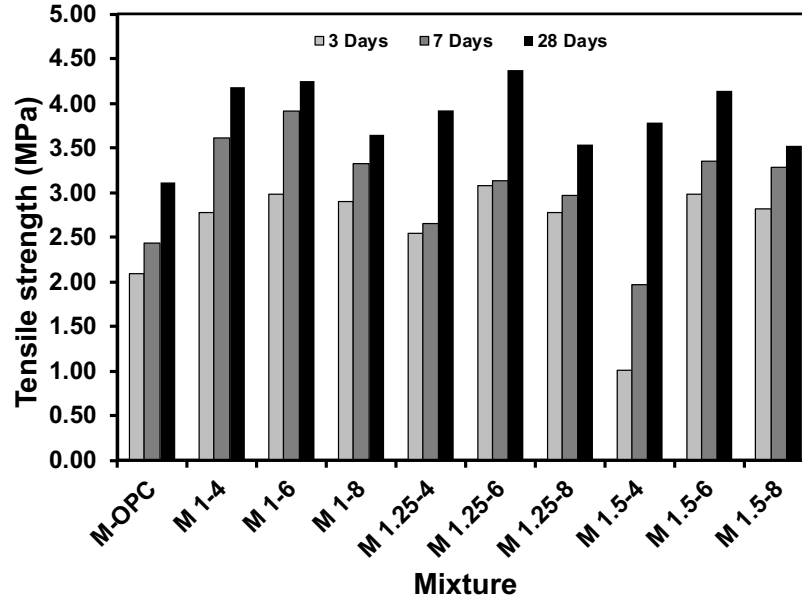


**Fig. 4.18 AAS mortar tensile strength.**

This indicated that the tensile strength's optimum dosage might be different from that of the compressive strength (i.e., 8%). For instance, at the age of 28 days, all samples with  $\text{Na}_2\text{O} = 6\%$  achieved its highest tensile strength, while the compressive strength was still increasing by increasing  $\text{Na}_2\text{O}\%$  above 6% (**Fig. 4.19**). This is in agreement with the previous research, which stated that for AAS, the tensile strength has different behaviour compared to that of the compressive strength with respect to activator concentration changes (Atiş, Bilim et al. 2009). Increasing the compressive strength was accompanied by a higher brittleness of the binder material. Consequently, the tensile strength decreased (Callister and Rethwisch 2007). Successive

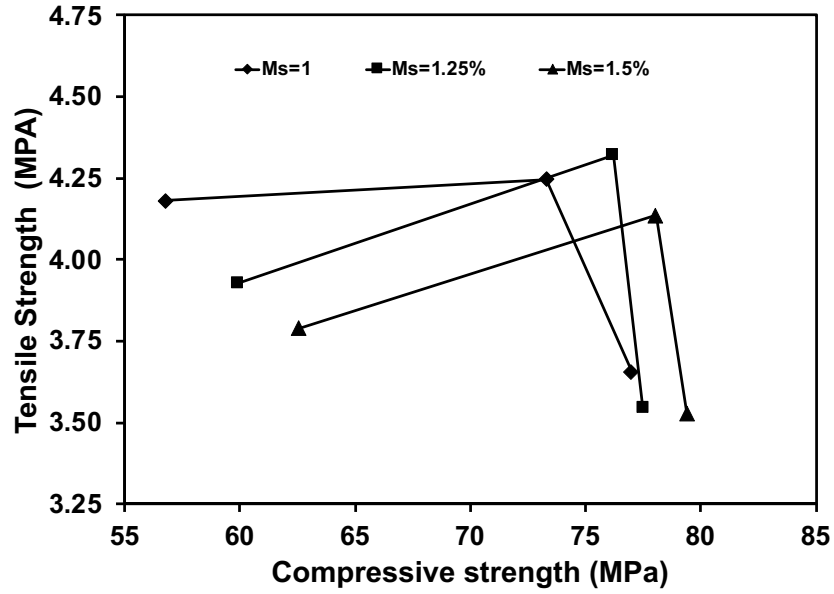


**Fig. 4.19** Change in tensile strength with respect to compressive strength at (28 days).

Also, it was observed that the tensile strength development with age is decreasing with increasing  $\text{Na}_2\text{O}\%$  regardless of silica modulus. For example, at  $M_s = 1.5$ , mixtures with the highest  $\text{Na}_2\text{O}\%$  exhibited the lowest tensile strength development between 7 and 28 days (**Fig. 4.20**). High  $\text{Na}_2\text{O}\%$  accelerate the dissolution rate of the slag particles and the start-up of strength gaining, which promotes the reaction product formation and strength development at early ages.

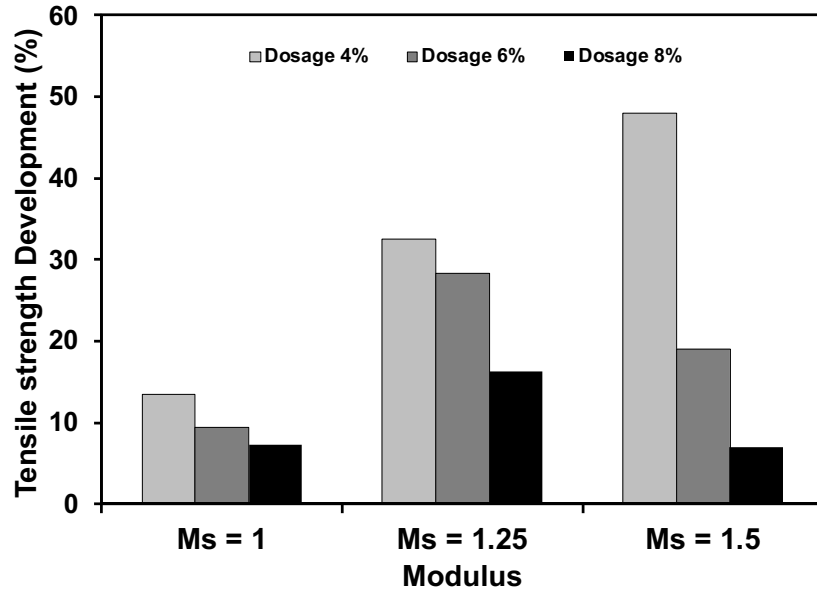


**Fig. 4.20** Tensile strength development with age (7 to 28 days).

Activating with sodium hydroxide alone did not significantly affect tensile strength. Samples activated by sodium hydroxide only exhibited a comparable tensile strength to those activated by sodium silicate and sodium hydroxide, as shown in **Fig. 4.21**. This may be attributed to the lower drying shrinkage and associated micro-cracking for mixtures activated by sodium hydroxide only. This can be ascribed to the fewer brittle phases formed inside these mixtures during the reaction, and consequently, relatively good tensile strength (Atiş, Bilim et al. 2009). Also, it was evident that for mixtures containing sodium silicate, changing  $M_s$  value had an insignificant effect on the achieved tensile strength, which confirms that sodium silicate had a minor effect on tensile strength.

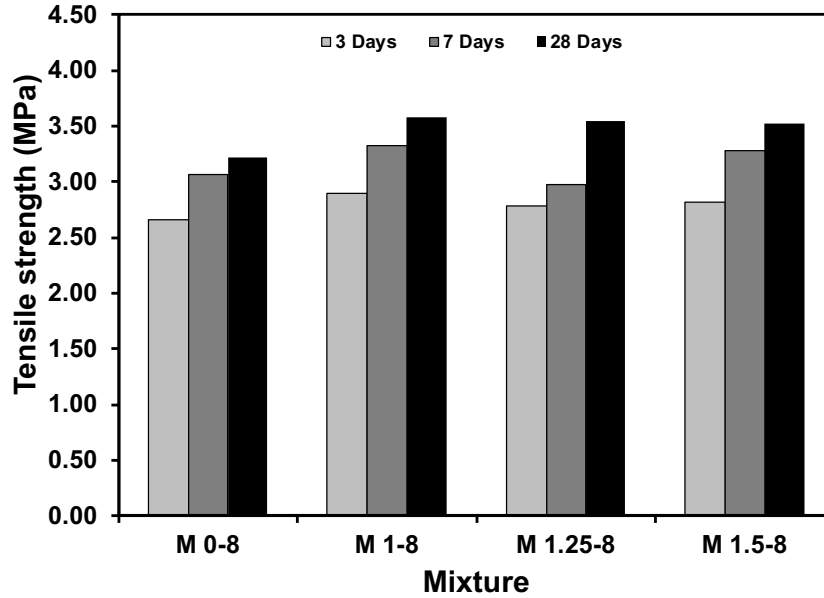


**Fig. 4.21 Tensile strength for various mixtures with 8% Na<sub>2</sub>O dosage.**

After exposure to elevated temperature, the residual tensile strength was dominantly affected by the amount and the nature of the formed hydration products at each activation level. For instance, the mixture assigned to  $M_s=1.5$ , Na<sub>2</sub>O% dosage of 8% had shown the lowest residual tensile strength at 600 °C comparing to other mixtures prepared at the same silica modulus. This confirms that the higher amount of decomposed hydration products achieved at the high level of activation (i.e., 8% dosage) was the main reason behind tensile strength degradation after exposure to elevated temperatures (**Fig. 4.22**).

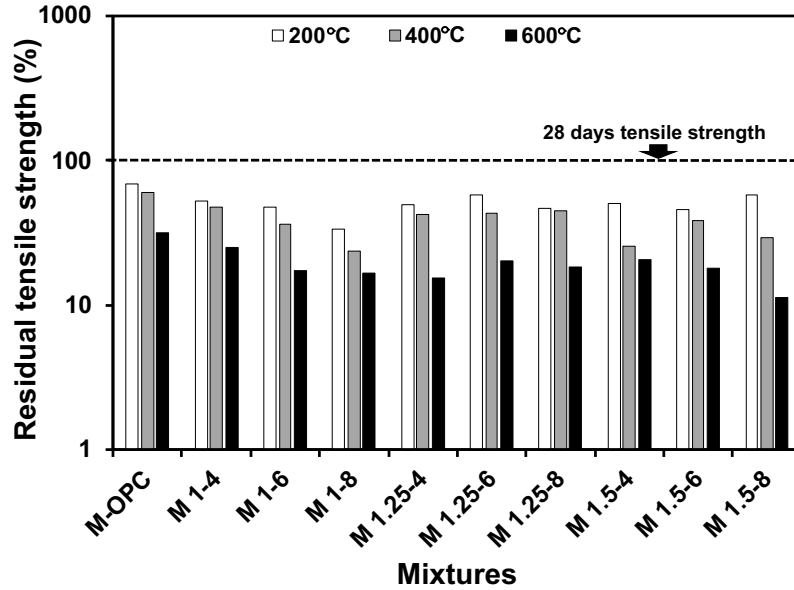


Fig. 4.22 Mortar residual tensile strength (%) after elevated temperature exposure.

#### 4.2.5 Impact absorption

Impact energy absorbed by each sample was represented by the number of successive blows up to failure. Each blow gives an amount of energy equivalent to the kinetic energy transferred from the drop weight to the sample. Compared to cement-based specimens, AAS showed relatively better behaviour in terms of impact energy absorption (Fig. 4.23). Under impact loadings, once the load strikes the sample, a contact force between the hammer and the sample is developed. However, this contact force is not the actual fracturing force as it is balanced with the inertia force during impact. This means that fracture energy is greatly affected by sample shape and size. Also, the hammer velocity at the impact event has a significant effect on fracture energy. The fracture energy absorbed usually increases with higher impact velocity. At constant impact velocity and sample size, which is the case in this study, the fracture energy will mainly be affected by mixture properties. Generally, AAS mixtures exhibited higher impact energy absorption capacity compared to OPC mixture. For AAS, mixtures with high  $\text{Na}_2\text{O}\%$  exhibited significantly better

impact absorption at 28 days regardless of silica modulus. This may be attributed to the denser microstructure with well packed formed gel due to a higher amount of dissolution slag particles at such high higher  $\text{Na}_2\text{O}\%$  (Komnitsas and Zaharaki 2007). Cracking and failure mode was not significantly different for all mixtures since no fibre was added to the mixtures. However, the ball penetration level was significantly affected by the activator properties.

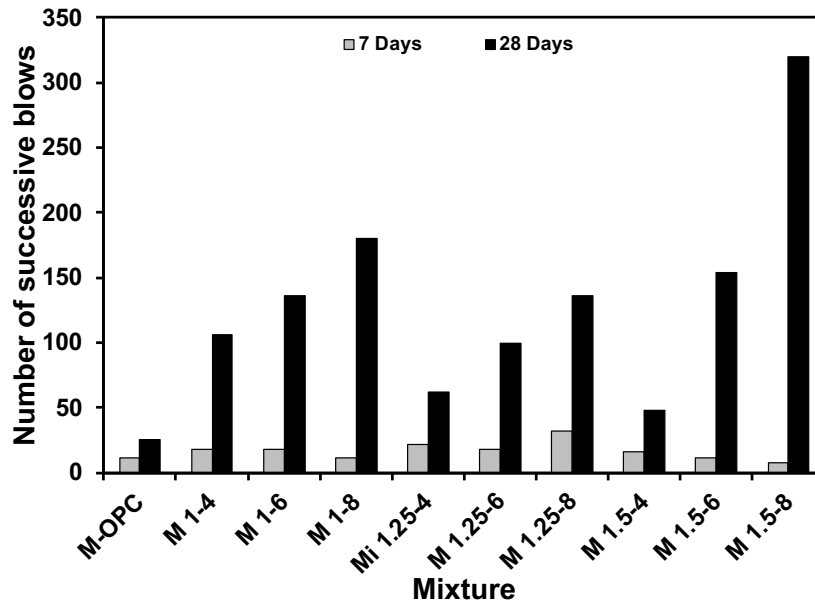


Fig. 4.23 Impact energy absorbed for various mixtures.

Moreover, varying the  $M_s$  value exhibited different behaviours depending on the  $\text{Na}_2\text{O}\%$  dosage. For low dosage (i.e., 4%), increasing the  $M_s$  value was found to reduce the impact energy absorption (Fig. 4.24). On the other hand, at high dosage (i.e., 8%), increasing the  $M_s$  value up to 1.25 resulted in a decrease in the impact energy absorption (Fig. 4.25). Conversely, mixtures with high  $M_s$  values (i.e.,  $\geq 1.5$ ) exhibited relatively a very high impact energy absorption. These results showed that there is a different optimum  $M_s$  value for each value of  $\text{Na}_2\text{O}\%$ . This can be explained by the different effects of each activator variable and its power to affect the formed microstructure behaviour. For example, at low  $\text{Na}_2\text{O}\%$  dosages, while the alumina dissolution rate from the

precursor is low, the effect of high availability of silicates on delaying the alumina dissolution will be magnified (Puertas, Varga et al. 2014).

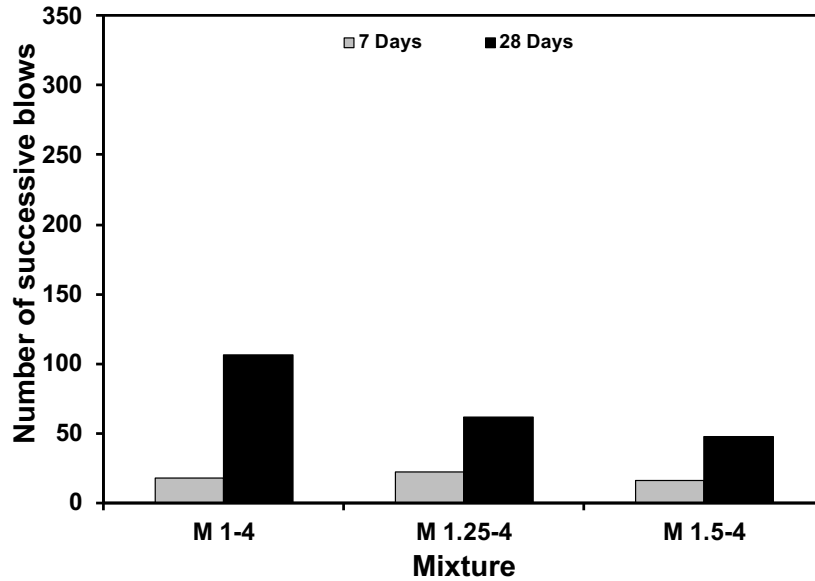


Fig. 4.24 Impact energy absorbed at  $\text{Na}_2\text{O}\%=4$ .

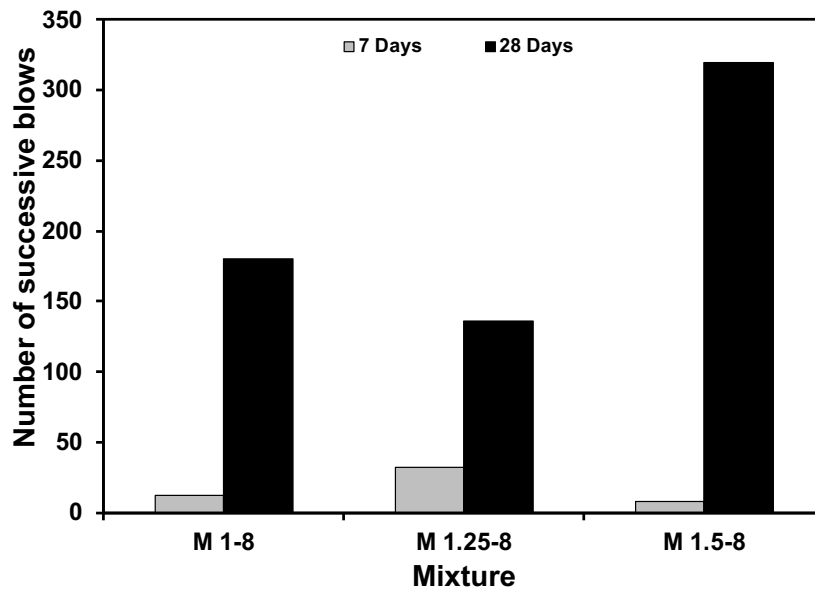


Fig. 4.25 Impact energy absorbed at  $\text{Na}_2\text{O}\%=8$ .

At a high  $\text{Na}_2\text{O}\%$  (i.e., 8%), other factors also affect the impact behaviour significantly, such as drying shrinkage. At  $\text{Na}_2\text{O}\% = 8$ , increasing  $M_s$  up to 1.25 resulted in higher drying shrinkage and, consequently, more micro cracks development (Eguchi and Teranishi 2005). However, at  $M_s=1.5$ , the observed drying shrinkage strain was significantly low (Fig. 4.26). Hence, there is always a need to balance the silicate species available in the polycondensation phase and the sodium and aluminium species existing to control the geopolymerization process itself (Hajimohammadi and van Deventer 2017).

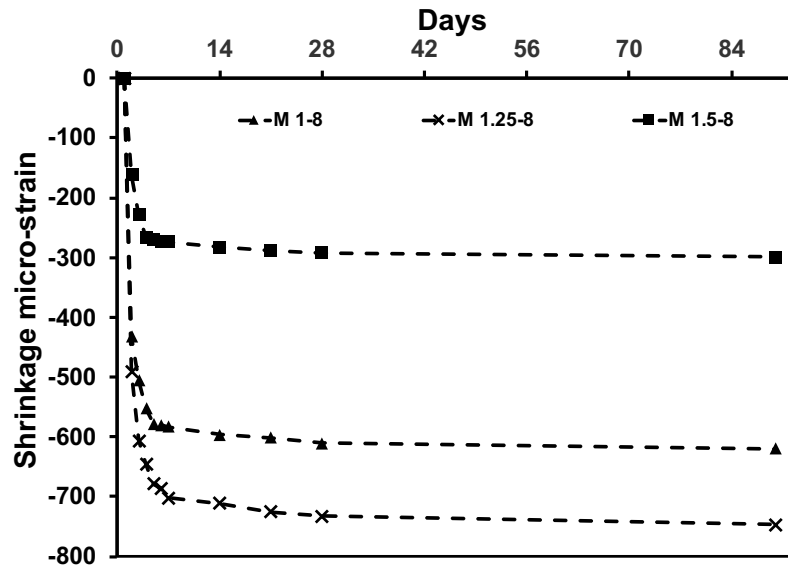


Fig. 4.26 Drying shrinkage strain at  $\text{Na}_2\text{O}\%=8$ .

Fig. 4.27 shows that increasing  $\text{Na}_2\text{O}\%$  increased the compressive strength and the impact energy absorption, regardless of the  $M_s$  value. However, the increase in compressive strength and the impact energy absorption did not follow the same rate. For instance, at  $M_s=1.25$ , increasing  $\text{Na}_2\text{O}\%$  up to 6% resulted in about 28% and 61% increase in the compressive strength and the impact energy absorption, respectively. Simultaneously, increasing  $\text{Na}_2\text{O}\%$  above 6% resulted in a marginal increase in compressive strength, while the impact energy absorption increased

significantly. Moreover, it seems that the increasing trend of the impact energy absorption continues even up to a very high dosage (i.e., 10%) as shown in **(Fig. 4.28)**. Moving laterally in the  $M_s$  values, it was found that the rate of change of the absorbed impact energy with the increase in the compressive strength (in terms of the slope) is not the same for all  $M_s$  values, especially at higher dosages (i.e., > 6%). For example, at  $M_s=1$ , increasing  $\text{Na}_2\text{O}\%$  from 6% to 8% resulted in around 5% and 32% increase in compressive strength and impact energy absorption, respectively. However, at high values of  $M_s$  (i.e., 1.5), the increase in compressive strength and impact energy absorption was around 2% and 107% at the same change in  $\text{Na}_2\text{O}\%$ , respectively.

In the event of transferring a sudden amount of energy to the material, energy is dissipated, and strength significantly increases differently depending on the material nature (Sierakowski and Chaturvedi 1997). For cementitious material, the strength and the modulus of elasticity are generally increased as the loading rate increased (Fu, Erki et al. 1991, Sierakowski and Chaturvedi 1997). This rational increasing is expressed as a Dynamic Increase Factor (DIF), which is defined as the ratio between the dynamic and quasi-static value. Consequently, under compression impact loads, the cementitious material's stress-strain behaviour will depend on the loading rate (Ross 1996). However, the loading rate for the drop weight test is almost constant. Hence, the effects of  $M_s$  and  $\text{Na}_2\text{O}\%$  on the compressive strength and DIF are expected to be different. This explained the variations in the ratio of increase between the compressive strength and impact energy absorption.

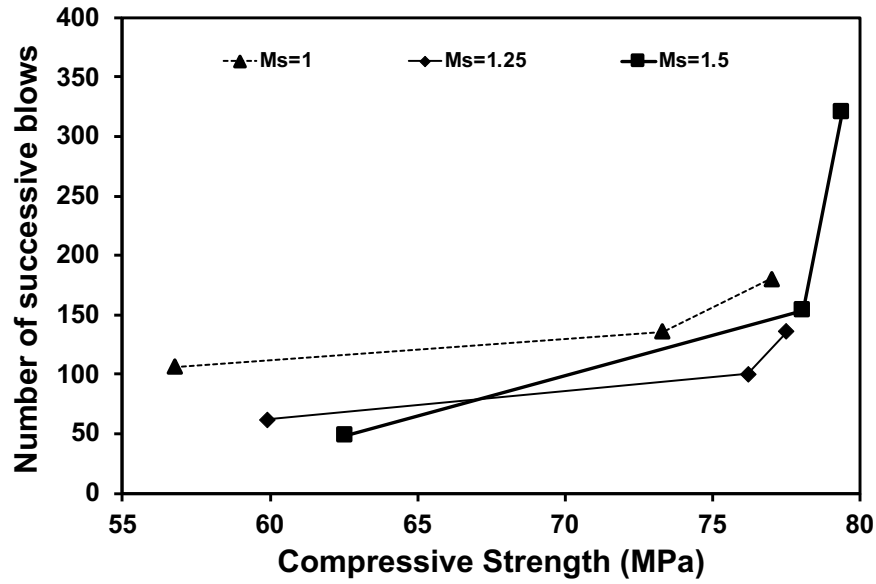


Fig. 4.27 Absorbed impact energy vs. compressive strength at different dosages.

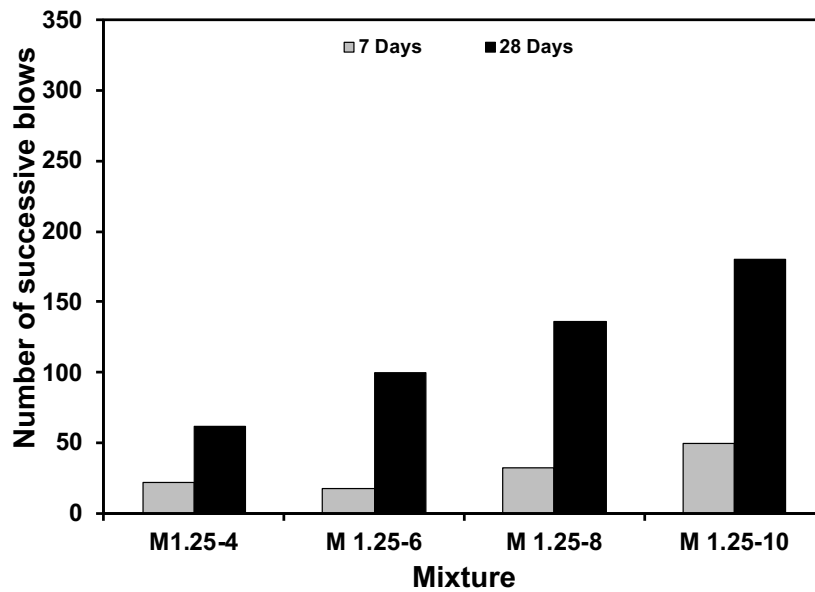
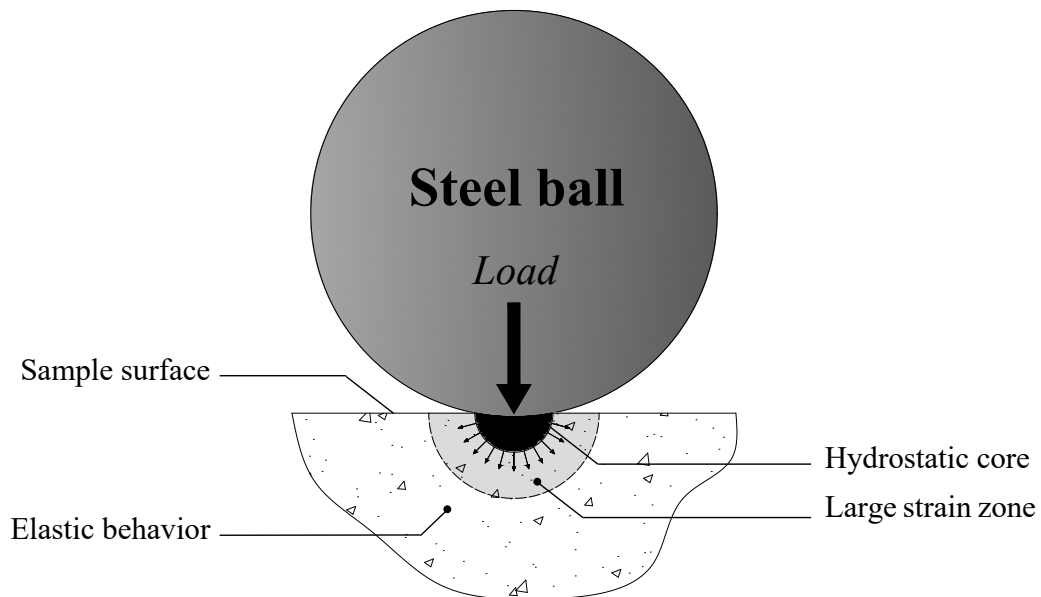


Fig. 4.28 Impact energy absorbed at  $M_s=1.25$ .

#### 4.2.6 Ball Penetration.

Under impact load, alkali-activated slag, as a brittle material, is supposed to have a damage mechanism immediately below the indenter (i.e., the steel ball) depending on its shape. Just below

the contact point or surface between the steel ball and the mortar sample, three zones can be distinguished below the sample surface (**Fig. 4.29**). The first zone is the hydrostatic core, which forms as a result of the compression below the contact surface. This zone usually collapses in a crushing mechanism. Surrounding this core, a high strain zone due to the core pressure is then developed. In this zone, radial cracks might be initiated and developed, starting from any pre-existed flaws in the mortar and depending on the brittleness. These cracks are usually observed as ring cracks on the surface around the contact area. Out of the high strain zone, the mortar is supposed to perform in an elastic behaviour (Dragon and Mroz 1979, Chiaia 2001). After failure, the high strain zone (cracking zone) was clear to observe, as shown in **Fig. 4.30**.



**Fig. 4.29 Formation of hydrostatic core and large strain zone in a brittle material.**

During the impact test, the penetration diameter ( $D_p$  cm) by steel ball of diameter ( $d_b$  cm) was monitored to understand the brittleness behaviour during impact loading. Penetration level

( $L_p$ ) was calculated according to  $L_p \text{ (mm)} = -10 * [(d_b/2) - ((d_b^2 - D_p^2)/4)^{1/2}]$

(Eq. 4.1).

$$L_p \text{ (mm)} = -10 * [(d_b/2) - ((d_b^2 - D_p^2)/4)^{1/2}] \quad \text{(Eq. 4.1)}$$

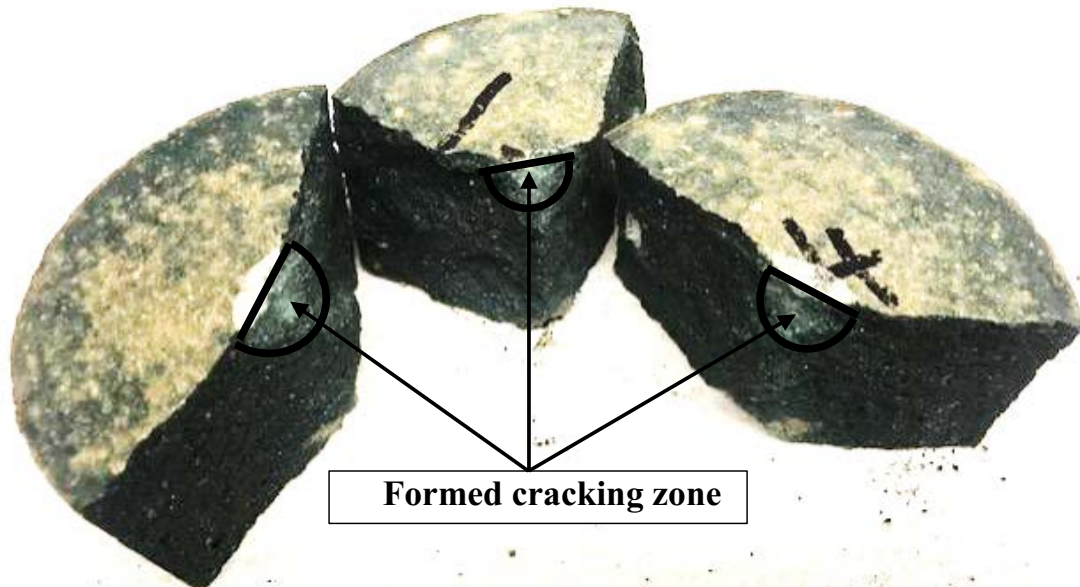


**Fig. 4.30 Formed large strain zone observed after sample failure.**

The steel ball penetration level was relatively very high for all specimens that exhibited low impact energy absorption. For instance, at  $M_s=1$ , increasing  $\text{Na}_2\text{O}\%$  resulted in high fracture energy and a less penetrated level by the steel ball (**Fig. 4.31**). This means that the higher the achieved fracture energy, the more the brittleness of AAS. This observed high brittleness of samples at high dosages indicates the low ductility index.

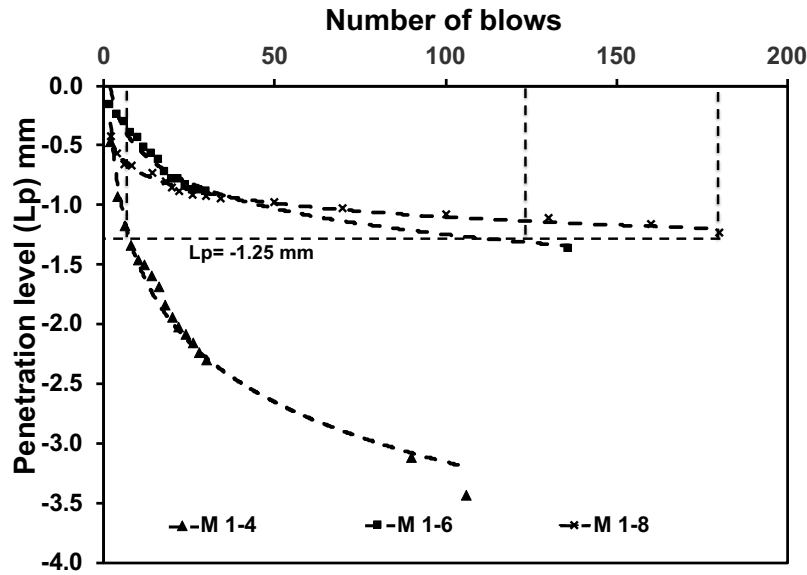


**Fig. 4.31** Steel ball penetration level ( $L_p$ ) at  $M_s=1$ .

**Fig. 4.32** shows tested samples at  $M_s=1$  and three different  $\text{Na}_2\text{O}\%$  dosage values. The level of penetration of (-1.25 mm) was observed for  $\text{Na}_2\text{O}\% = 8\%$ , which failed after 180 blows. The same penetration level was observed for  $\text{Na}_2\text{O}\% = 6\%$  just before failure at 128 blows, while the sample with  $\text{Na}_2\text{O}\% = 4\%$  achieved this level of penetration after only 14 blows before failing at 100 blows. This indicates that samples with high  $\text{Na}_2\text{O}\%$  exhibited higher energy of fracture along with lower ball penetration levels.

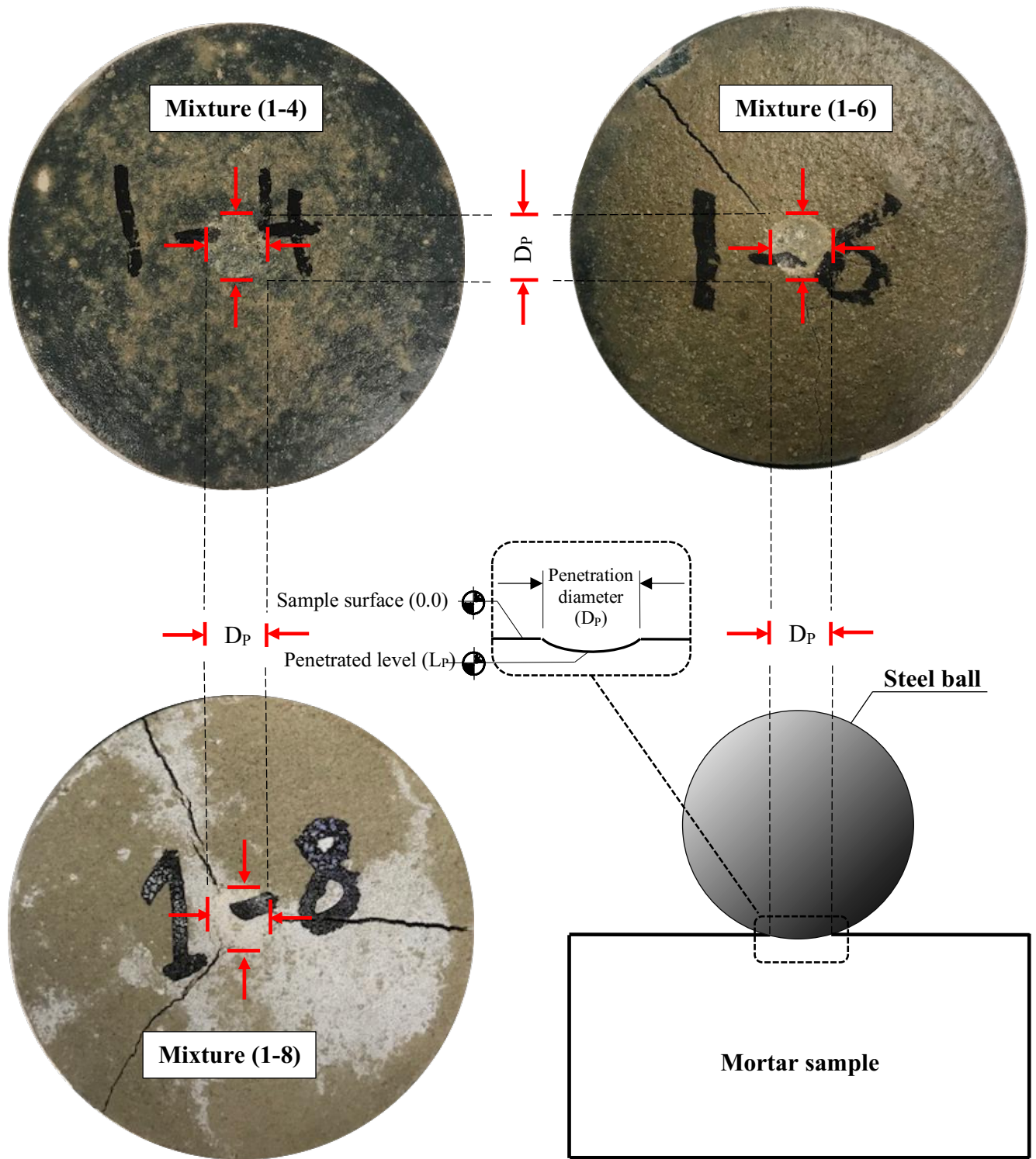
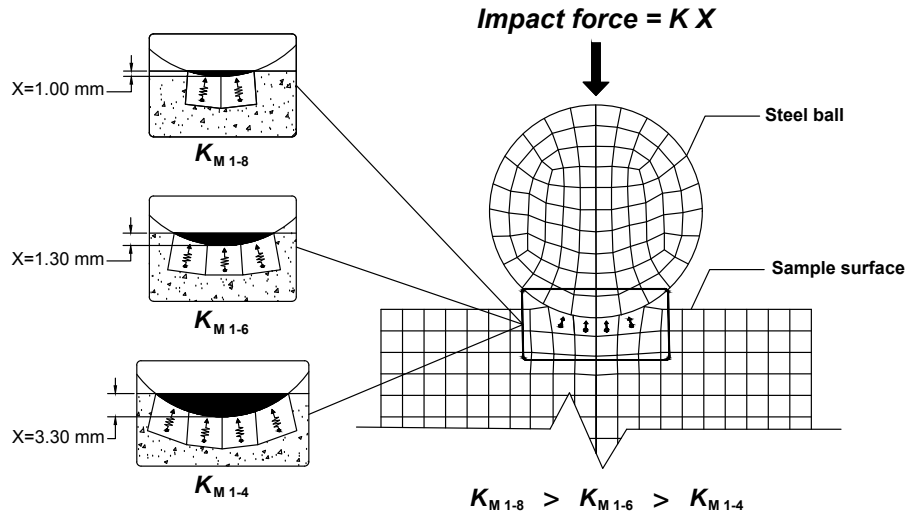


Fig. 4.32 Samples of  $M_s=1$  at Steel ball penetration level of ( $L_p = -1.25$  mm).

Regarding the work done by the specimen to resist the penetration, during the impact event, the ball's absorbed energy can be equated to the potential energy of the drop weight, which is turned by dropping into kinetic energy. The impact force applied to the steel ball can be expressed by the absorbed energy and the displacement represented by the sample surface's penetration. This penetration level is a function of the sample stiffness (Callister Jr and Rethwisch 2020). Understanding the contact interface between the steel ball and the sample surface was more intuitive to rescale the impact event contact surface into simpler elements. Many approaches to simulate this interface would provide a good understanding of different parameters that may affect this event (Heinstein, Mello et al. 2000, Mohammadi, Forouzan-Sephehr et al. 2002). In this approach, the sample surface resistance to penetration at the contact area was simulated as node springs per area element to understand the effect of varying the activator properties on the surface penetration resistance. The spring constant (K) can be representative of the penetration resistance. Hence, the total penetration resistance at any penetration level can be described by the energy absorbed and the penetration level (**Fig. 4.33**). By examining the penetration levels by the steel ball in the surface of each mixture sample, it was found that the penetration profile was highly affected by the level of activation in terms of activator  $M_s$  and  $Na_2O$  % dosage. Increasing  $M_s$  value was found to increase the resistance to penetration, especially at high dosages. Also, increasing the dosage was found to be significantly affecting the penetration resistance. For instance, increasing the dosage to up to 8% at  $M_s=1$ , triplicated the penetration resistance represented in the spring constant at the same energy absorption level.



**Fig. 4.33 Penetration resistance of mixtures with ( $M_s=1$ ) simulated by spring constant.**

After exposure to elevated temperatures, the OPC mixture lost more than 90% at 600 °C, of its original capacity to absorb impact energy. This can be ascribed to the aggressive losses in the main hydration product (i.e., C-S-H) at high temperatures and internal micro-cracks development during cooling down. **Fig. 4.34** shows the thermogravimetric analysis of OPC samples at ambient temperature and after exposure to different levels of elevated temperatures. Results indicate that for the sample tested without exposure to elevated temperature, around 14% weight loss was exhibited by heating up to 650 °C. For samples tested after exposure to elevated temperatures, the heat flow peaks showed a significant reduction reflecting the decomposed amount of hydration products. For instance, at 400 °C the peak representing C-S-H decomposition was almost flattened due to semi-full decomposition of C-S-H via a one-way reaction. However, the peak representing the portlandite didn't show significant change even for the highest level of temperature exposure (i.e., 600 °C), at which relative reduction was expected to be observed in this peak considering the heat exposure before the test. This might be attributed to the reversible reaction of portlandite dihydroxylation and the amorphous part recrystallization during the cooling down (Morsy, Galal et al. 1998).

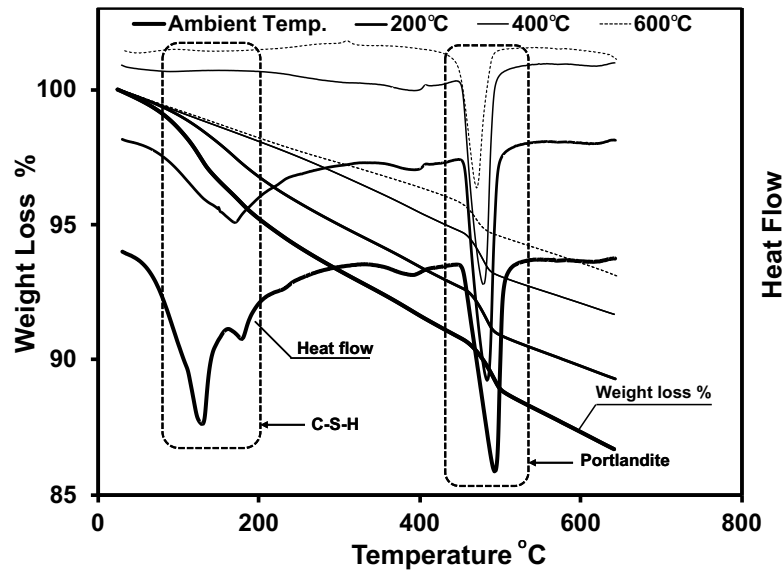


**Fig. 4.34 Thermographic analysis of OPC after exposure to different levels of temperatures.**

On the other side, AAS mixtures Showed a relatively similar reduction in the impact energy absorption capacity by increasing the exposure temperature (**Fig. 4.35**). Moreover, significant deterioration was obvious on impact test samples before testing, especially samples assigned to high activation levels. **Fig. 4.36 a, b, and c** are showing impact samples of  $M_s=1$  after exposure to 600 °C. Obviously, samples surface that lower activated samples were reserving some integrity and lower surface cracking after exposure to such high temperature.

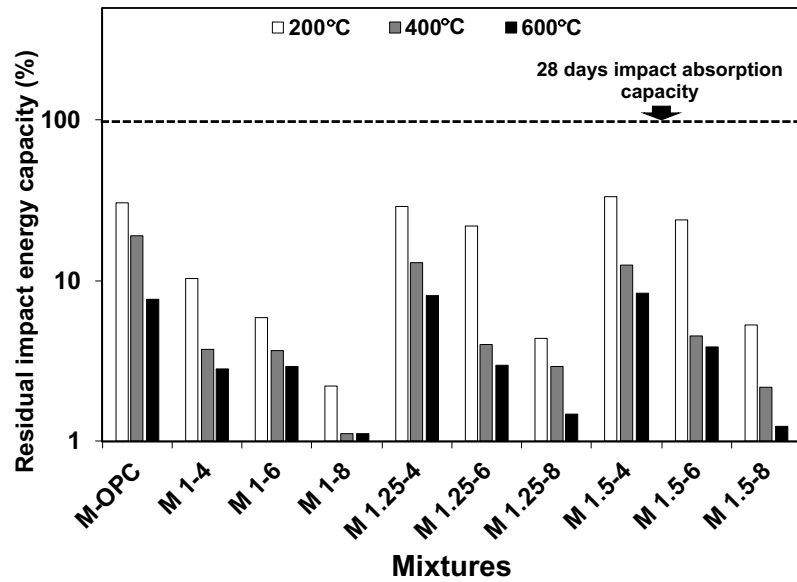


Fig. 4.35 Mortar residual impact absorption energy after elevated temperature exposure.

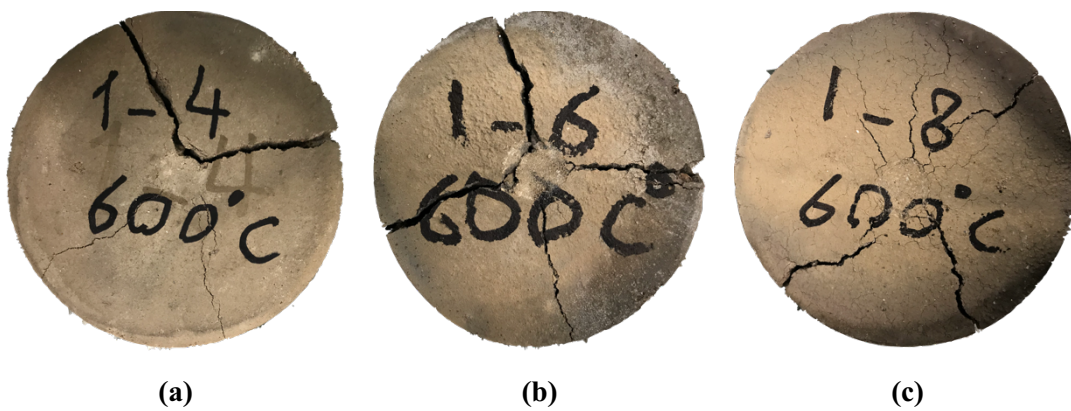
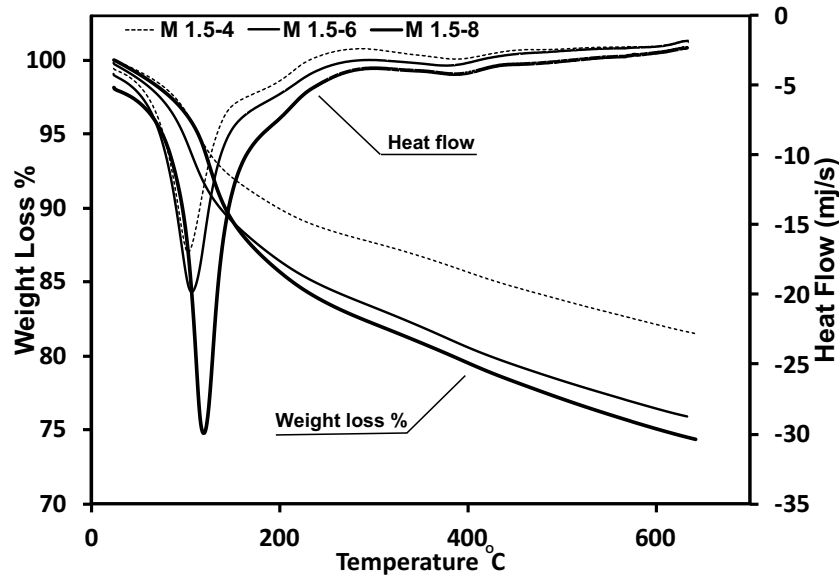


Fig. 4.36 Mortar impact samples of  $M_s=1$  after exposure to 600 °C at failure.

During exposure to elevated temperature, two different mechanisms are taking place. Firstly, decomposition of the main hydration products such as C-S-H,  $AF_m$ , and hydrotalcite ( $H_t$ ) at different temperatures (Wang and Scrivener 1995, Gruskovnjak, Lothenbach et al. 2006). This will weaken the microstructure and, accordingly, the capacity to absorb impact energy. Thermogravimetric analysis and XRD for AAS samples confirmed that the activator properties control both the nature and the amount of hydration products. Consequently, the weakening

mechanism during the decomposition of these products exposed to elevated temperature will also be controlled by activator properties. As explained before, activator  $\text{Na}_2\text{O}$  % dosage is believed to define the amount of dissolute precursor favouring the formation of a higher amount of hydration products. For instance, at  $M_s$  of 1.5, a mixture of dosage 8% showed relatively higher peaks reflecting a higher amount of hydration products (**Fig. 4.37**).



**Fig. 4.37** Thermogravimetric analysis of AAS with different levels of dosage at the same  $M_s=1.5$ .

The XRD results also indicated that the crystalline hydration products' level decreased as exposure temperature increased (**Fig. 4.38**). For instance, after exposing mixture C 1.5-8 to 200°C, 400°C, and 600 °C, the detected retained crystalline hydration products such as C-S-H was 19.8%, 6.7%, and 0%, respectively. In contrast, crystalline akermanite percentage had increased to 25%, 25.2%, and 31.8% of the detected crystalline phases for 200°C, 400°C, and 600 °C, respectively. The crystallinity of akermanite, representing the unreacted slag particles transformed phase, was found to increase by increasing the exposure temperature as it starts to recrystallize at elevated

temperatures (Kong and Sanjayan 2008, Reddy, Tulyaganov et al. 2013). This confirms the effect of increasing temperature level on the microstructure in different phases.

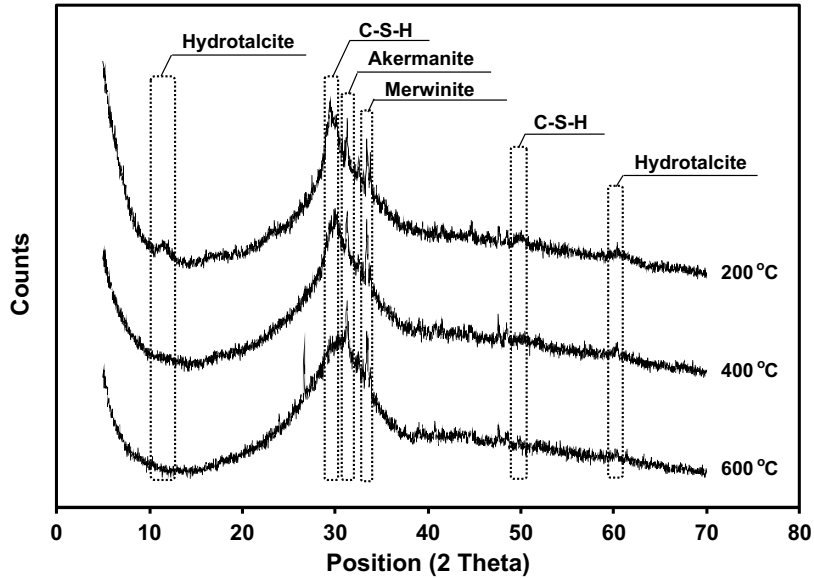


**Fig. 4.38 X-ray diffraction patterns of AAS at different levels of exposure to elevated temperatures (200, 400, and 600 °C)**

In a closer focus on the impact behaviour after temperature exposure, it was clear that the capacity to absorb impact energy is highly related to the amount of decomposed hydration products. For instance, at  $M_s=1.5$ , the residual weights recorded at the thermogravimetric analysis test after exposure to different levels of elevated temperatures were decreasing by increasing the dosage. Similarly, the impact energy absorption behaviour was negatively affected by residual absorption capacity by increasing the dosage. This can be explained by the higher amount of decomposed hydration products at different levels of exposures (**Fig. 4.39**).

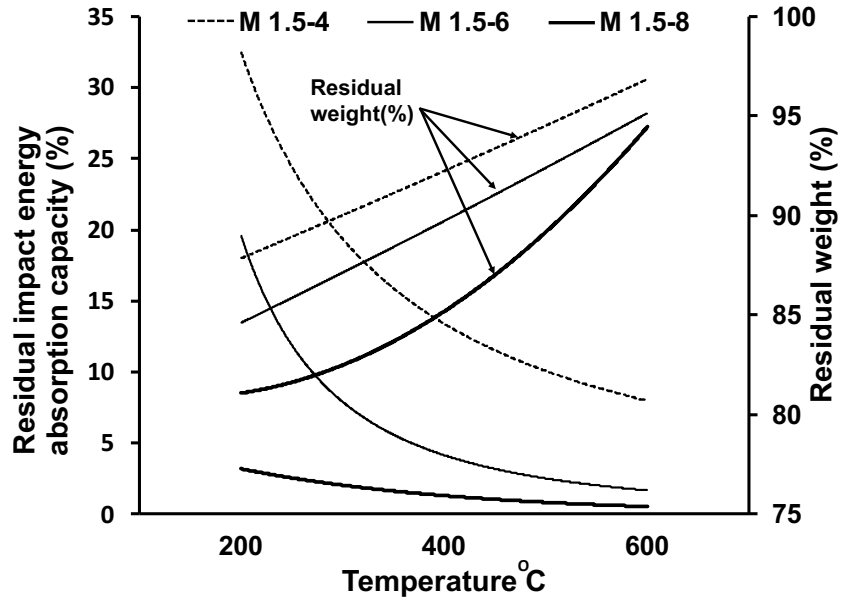


**Fig. 4.39 Residual impact absorption capacity vs. residual weight after exposure to different levels of temperatures for M 1.5-8.**

Also, silica modulus is the main factor that controls the supply of silica through the activating agent and consequently controls the nature of the formed hydration products. Hence,  $M_s$  was found to significantly affect the impact of behaviour after exposure to elevated temperature. The ratio between Si /Al in the formed products was the main determinant of these products' type. Poly-sialate (-Si-O-Al-O), poly-sialate-siloxo (-Si-O-Al-O-Si-O), and poly-sialate-disiloxo (-Si-O-Al-O-Si-O-Si-O) are examples of the formed products depending on the ratio Si/Al (Davidovits 2005).

**Fig. 4.35** shows that as  $M_s$  increased, the impact absorption capacity after elevated temperatures exposure was enhanced at the temperature range of (200-400 °C). This is the range at which the activator nature effect can be dominating. At higher temperatures, a significant portion of the hydration products will decompose, and the behaviour will be mainly dependent on the amount of the hydration products, but not their nature. For example, at a 4% dosage, samples impact absorption behaviour had shown enhancement as the modulus increased up to 1.5 at all exposure

temperatures. However, at a dosage of 8%, all samples exhibited an accepted capacity to absorb impact energy at 200 °C, especially at high silica modulus. However, at higher temperatures, relatively high degradation took place in all mixtures of this dosage due to the decomposition of higher amounts of hydration products achieved by increasing the Na<sub>2</sub>O% dosage. Moreover, for mixture M 0-8, which represents the activation without water glass achieving the minimum Si supply (only by the precursor), the impact behaviour after exposure to elevated temperatures represented a weak structure of the formed hydration products. This mixture's capacity to absorb impact energy recorded aggressive degradation, starting at the lowest temperature exposure level. Also, the thermogravimetric analysis for this sample at ambient temperature and after exposure to elevated temperatures shows that the C-S-H peak was vanishing at 400 °C (**Fig. 4.40**), relatively close to OPC records, considering the difference in type and nature of other hydration products that resulted in different behaviour. That can be attributed to the low Si level in this mixture and, consequently, C-S-H formation with a high Ca/Si ratio close to OPC. This confirms that the more supplied silica beside the cations such as Na, which controls the degree of polymerization, favour the formation of more rigid and more stable products at high temperatures.

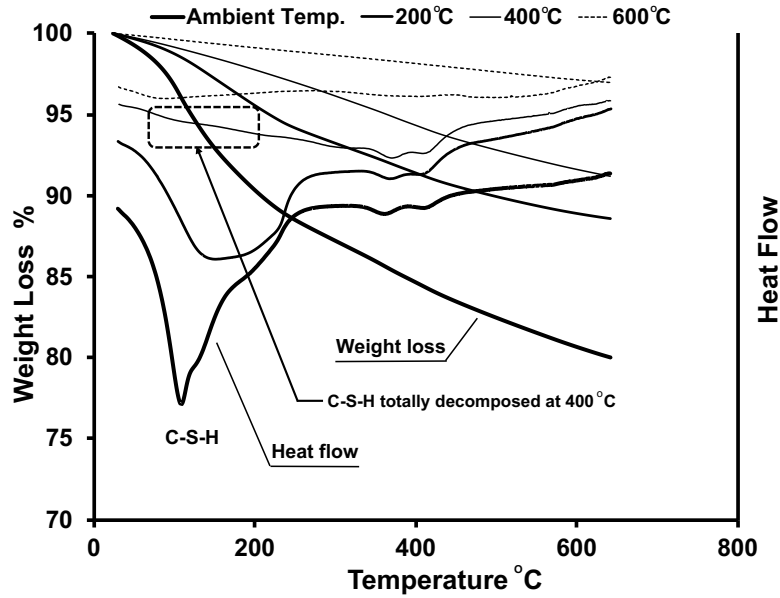


**Fig. 4.40 Thermogravimetric analysis of AAS activated by NaOH ( $M_s=0$ ) after exposure to different levels of temperatures.**

Another mechanism is the sintering action for the unreacted slag particles to turn it into a less harmful phase (Kong and Sanjayan 2008). However, at higher temperature levels (i.e., more than 400 °C), this phase's ceramic-like nature might help increase the brittleness of AAS. This will result in an aggressive degradation in the impact absorption capacity due to the synergetic effect of the high decomposition level and the higher brittleness achieved by such a high-temperature level.

### 4.3 Conclusions

- 1- AAS mixtures showed better mechanical properties compared to cement-based mixtures in terms of compressive, tensile, and impact absorption.
- 2- Activator nature has a significant effect on the developed AAS systems. Generally, increasing the  $M_s$  and  $Na_2O\%$  improve compressive strength and impact energy absorption.
- 3- The optimum values for  $M_s$  and  $Na_2O\%$  vary based on the desired property.
- 4- Many factors are affecting the behaviour of alkali-activated slag in terms of impact energy absorption. Consequently, there might be different criteria to find the optimum value for the sodium oxide dosage ( $Na_2O\%$ ) that act the end will achieve the best performance for each silica modulus value ( $M_s$ ).
- 5- The rate of change of the impact energy absorption capacity with respect to the change of the achieved compressive strength when using different activator chemical compositions is different according to the DIF exhibited.
- 6- Compared to the OPC mixture, all alkali-activated slag mixtures had shown better behaviour in terms of mechanical properties and performance under impact loads at ambient temperatures.
- 7- According to the proposed models of reaction, the type and nature of alkali activator were found to be significantly influential on the nature of formed reaction products. Also, that might influence other phenomena such as drying shrinkage, which would be a reason for pre-existed micro-cracks in the hardened state.
- 8- After exposure to elevated temperatures, alkali-activated slag mixtures exhibited higher residual compressive strength up to different temperature levels depending on the activator properties in terms of activator  $Na_2O\%$  dosage and modulus.

#### *Chapter 4*

- 9- Both dosage and modulus were found very effective on the impact behaviour of alkali-activated slag at both ambient and elevated temperatures. However, what may be a benefit at ambient temperature would be the same reason for degradation at exposure to elevated temperatures.
- 10- At elevated temperature levels up to 200 °C, the dominant factor affecting the AAS mixtures behaviour is the nature of formed hydration products and their stability. However, above this level, the dominant factor is the amount of formed hydration products and the degradation following their decomposition.

---

## Chapter 5 Impact Behaviours of Alkali-Activated Slag Concrete after Exposure to Elevated Temperatures

### 5.1 Introduction

After investigating the AAS mortar different behaviours through the previous chapter (i.e., **Chapter 4**), Based on results, three combinations of  $\text{Na}_2\text{O}$  % and  $M_s$  were selected to reflect three consecutive activation levels according to the mentioned criteria in **section 3.2.2** to be studied at the concrete level. In addition, an OPC concrete mixture was included for comparison purposes. A total of 344 concrete specimens were cast for this phase (i.e., Phase II) as shown in **Fig. 5.1**. Mixing proportions for the selected concrete mixtures are shown in **Table 5.1**. All concrete mixtures were mixed at a coarse to fine aggregate ratio of 1:1.75. w/b was fixed at 0.44 as for mortar mixtures. The first litter of each mixture's name (C) refers to concrete, followed by the silica modulus value and the dosage.



**Fig. 5.1** AAS and OPC prepared concrete specimens.



Fig. 5.1 Cont'd AAS and OPC prepared concrete specimens.

Table 5.1 Selected concrete mixture proportions.

Mixture	$M_s$ ( $\text{SiO}_2/\text{Na}_2\text{O}$ )	Dosage ( $\text{Na}_2\text{O}$ %)	Binder ( $\text{kg}/\text{m}^3$ )	Fine Agg. ( $\text{kg}/\text{m}^3$ )	Coarse agg. ( $\text{kg}/\text{m}^3$ )	NaOH ( $\text{kg}/\text{m}^3$ )	$\text{Na}_2\text{SiO}_3$ ( $\text{kg}/\text{m}^3$ )	Water ( $\text{L}/\text{m}^3$ )
Control C-OPC	-	-	400	674	1179	-	-	176
Low C 1-4	1	4	400	662	1159	14	56	141
Medium C 1.25-6	1.25	6	400	656	1148	19	104	111
High C 1.5-8	1.5	8	400	649	1136	22	167	72

\*The first number of each mixture's names refers to the silica modulus ( $M_s$ ), and the second refers to  $\text{Na}_2\text{O}$ %.

## 5.2 Results and discussion

### 5.2.1 Slump test

Table 5.2 represent the slump values of OPC and AAS concrete. Generally, all concrete mixtures exhibited acceptable slump measures. However, in a closer focus, AAS of high activation level (i.e. C 1.5-8), exhibited the lowest slump value among the AAS mixtures. This would be attributed to the high rate of dissolution, and consequently, faster consumption of the solution by

the slag particles along with the higher viscosity of the activator solution, as mentioned in **section 4.2.1.**

**Table 5.2 Slump measures of fresh concrete**

Mix.	C-OPC	C 1-4	M 1.25-6	M 1.5-8
Slump (mm)	70	85	88	78

**5.2.2 Under ambient conditions**

**5.2.2.1 Compressive strength**

**Fig. 5.2** summarizes the compressive strength results for all tested mixtures. Generally, AAS concrete specimens exhibited a better 28 days compressive strength than OPC, except for mixture C 1-4. For instance, mixture C 1.5-8 exhibited 67.8 MPa compressive strength at 28 days. This was almost 170% of the compressive strength achieved by C 1-4 (i.e., 40.55 MPa) at the same age.

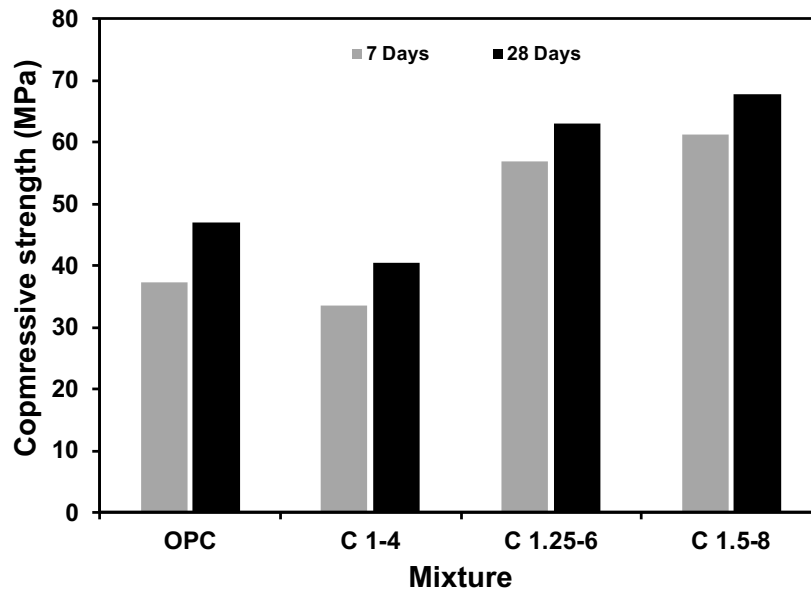


**Fig. 5.2 Concrete compressive strength at 28 days.**

The low strength for mixture C 1-4 can be ascribed to its low activation level, and consequently, a relatively low amount of formed hydration products, as explained earlier. Conversely, at higher activation levels, AAS mixtures exhibited relatively higher compressive strengths due to increased amounts of formed hydration products, favouring a denser well-packed structure. This can also be observed by comparing the compressive strength achieved by each mixture and the weight loss during the TGA test (**Fig. 5.3**). These weight loss percentages represent the decomposable hydration products during the test. Higher percentages mean more hydration products were decomposed during the test.

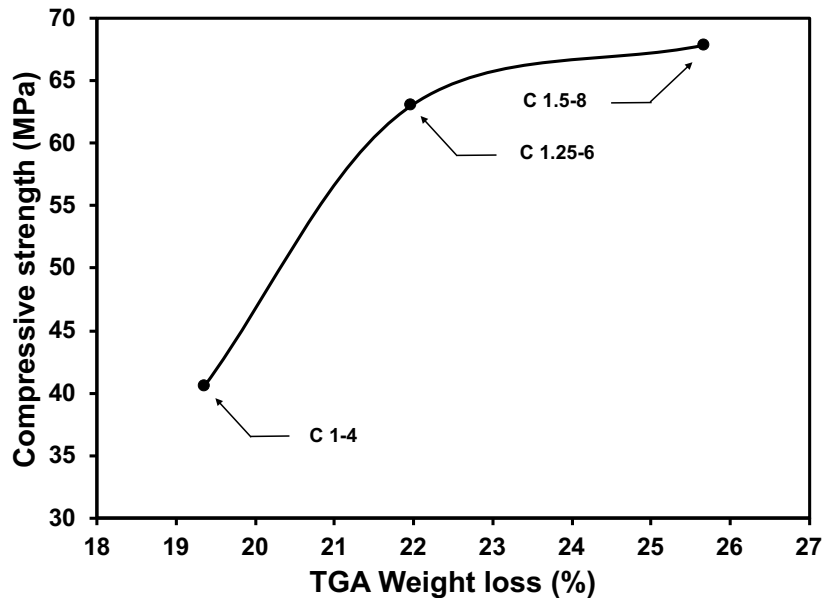


**Fig. 5.3 Compressive strength Vs binder weight loss.**

Moreover, ultrasonic pulse velocity test results (**Fig. 5.4**) confirmed denser and homogeneous microstructures for high activation level mixtures compared to lower activated mixtures. For instance, mixture C 1.5-8 recorded around 5 km/s pulse velocity at 28 days, while mixture C 1-4 recorded 4.4 km/s. This can be attributed to the higher dissolution rate and high

availability of silica species at the high activation level, which boosts the formation of hydration products, favouring a better microstructure.

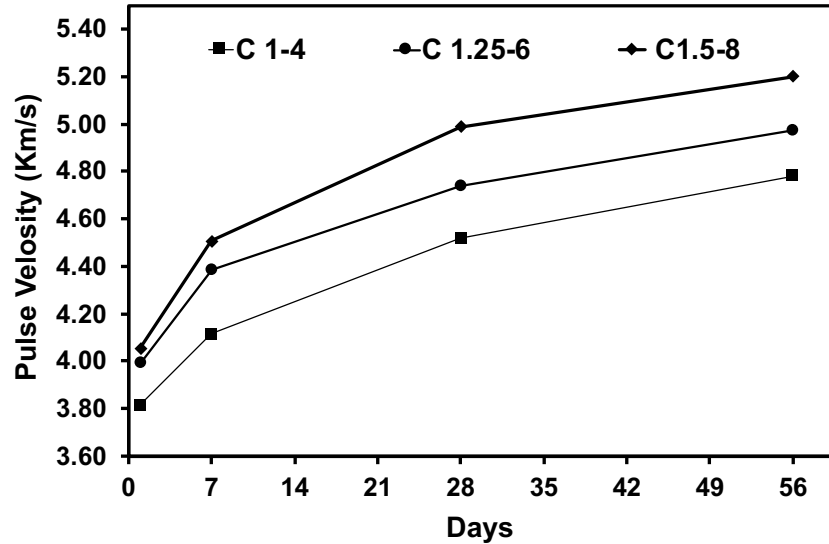
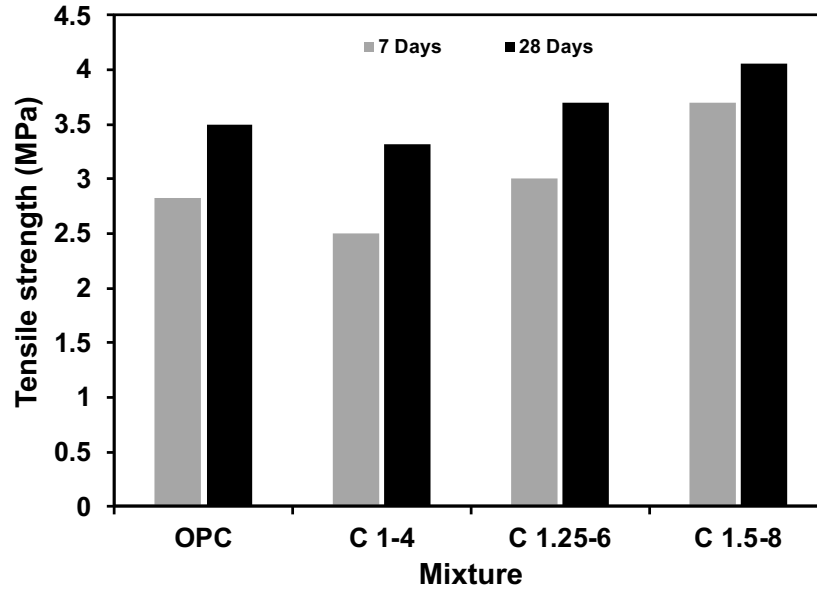


Fig. 5.4 Ultrasonic pulse velocity results for AAS concrete mixtures.

### 5.2.2.2 Tensile strength

Tensile strength results agreed with the compressive strength results (Fig. 5.5). Increasing the activation level, in terms of modulus and dosage, resulting in higher tensile strength. That might also be correlated to the drying shrinkage micro-strain, which usually results in pre-existing micro-cracks, and consequently, negatively affect the resistance of concrete to tensile loading. This would also be ascribed to the high bond between the binder and the aggregate surface at the interfacial transition zone (ITZ) (Singh, Rahman et al. 2016, Zhang, Ji et al. 2020). More C-S-H and C-A-(N)-S-H are formed at high activation levels, resulting in a strong and denser ITZ, which in turns enhance tensile strength.



**Fig. 5.5 Concrete tensile strength at 28 days.**

**Fig. 5.6** illustrates the impact of energy absorption in terms of the number of successive blows recorded for different specimens. AAS concrete specimens exhibited significantly higher impact energy absorption capacity than that of the OPC concrete. As mentioned earlier, this can be assigned to the difference in hydration products' nature between OPC and AAS systems. Besides the high Ca/Si ratio C-S-H, the formed amount of portlandite in the OPC system and its distribution through the binder microstructure may develop internal micro-cracking paths due to nonuniform resistance to stresses which resulted from the mechanical properties heterogeneity through the microstructure (Hajilar and Shafei 2016). On the other hand, the AAS hydration products were more consistent and well-packed depending on the activation degree. This would help to maintain a strong structure with minimal crack development during impact loadings. For instance, mixture C 1-4, which represents the weakest AAS concrete in terms of impact energy absorption, exhibited almost double the impact energy absorption capacity achieved by the OPC concrete specimen at age 28 days.

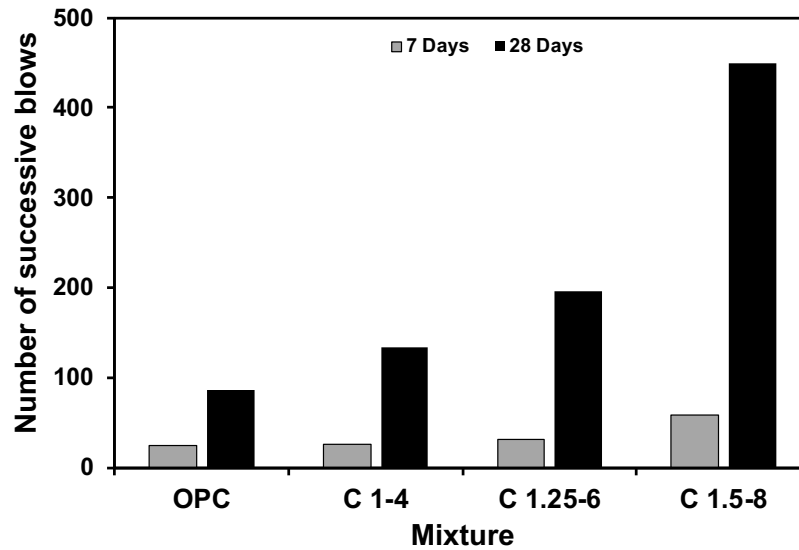


**Fig. 5.6 Concrete impact energy absorption capacity at ambient temperature.**

It is logically expected that pre-existing micro-cracks will significantly affect concrete behaviour as a brittle material towards impact loads. A dominant reason for these existing micro-cracks is the partially restrained drying shrinkage. Coarse aggregate (i.e., rigid ingredient) restrain the volumetric changes due to drying shrinkage leading to internal tensile stresses (Bisschop and Van Mier 2002, Grassl, Wong et al. 2010, Idiart, Bisschop et al. 2012). These internal stresses will result in microcracks formation once the low tensile strength of the binder is exceeded. Surface micro-cracks might also be involved in differential drying between the specimen's surface and core (de Sa, Benboudjema et al. 2008). These micro-cracks might be partially mitigated through the continuous hydration products formation, which is originally dependent on the activation level. **Fig. 5.7** represents the drying shrinkage micro-strain measured up to 56 days. The higher the activation level, the lower the drying shrinkage, and consequently, the lower development of micro-cracks. The micro-strain for the AAS concrete specimens can partially explain the varied

AAS concrete capacity measurements regarding the activation level beside nature and the amount of formed hydration products.

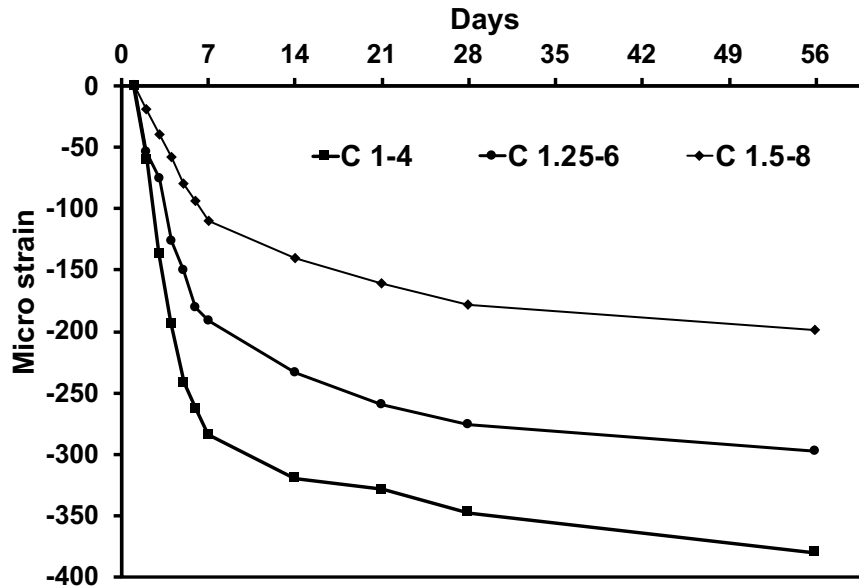


Fig. 5.7 Concrete drying shrinkage micro-strain.

### 5.2.2.3 Water absorption

The water absorption capacities for various mixtures were evaluated to confirm the activation level's effect on the developed micro-cracks. During the initial stage of the water absorption test, the accessible micro-cracks tend to accommodate a certain amount of water, depending on their widths and densities (i.e., the total length of existing cracks per unit area) (Wu, Wong et al. 2015). The rate of absorption will be high and dependable on the existing amount of drying shrinkage micro-cracks. The rate of water absorption during this stage is represented as the slope ( $S_1$ ). After micro-cracks saturation, water is being absorbed through capillary pores, either from the water exposed surface or from the saturated micro-cracks at a relatively slower rate ( $S_2$ ) (Wu, Wong et al. 2019). The transition point between the two absorption mechanisms (i.e., the change in slope from  $S_1$  to  $S_2$ ) for mixtures with high activation levels occurred relatively earlier

than those mixtures with lower activation levels and at a lower amount of absorbed water. This means that the amount of water absorbed to fill the existing micro-cracks in mixtures with high activation levels was lower than those with lower activation levels, indicating the lower micro-cracking development (Fig. 5.8). Results agreed with the drying shrinkage results confirming that a high activation level favoured lower shrinkage and fewer micro-cracks.

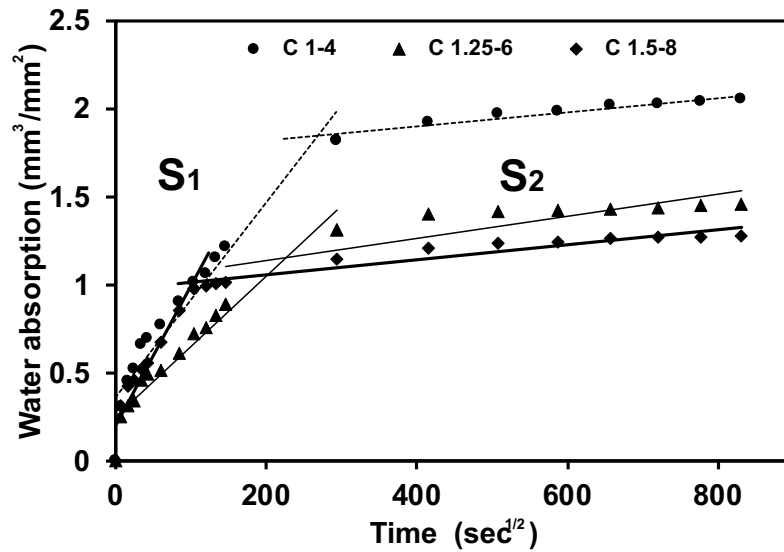


Fig. 5.8 AAS concrete water absorption capacity.

#### 5.2.2.4 Impact energy absorption capacity and penetration resistance

During the impact test, the indenter's penetration levels (i.e., the steel ball) were reported at sequent numbers of successive blows. Before experience any penetration, the specimen behaved elastically until it reached the threshold level of transferred impact force ( $F_P$ ), then the steel ball starts to penetrate the specimen. This threshold force needed to overcome the elastic behaviour is very small for concrete as a brittle material (i.e., can be neglected) (Mainstone 1975, Hughes 1984). According to the penetration theory, the penetration ( $P$ ) starts and increases by increasing the accumulated applied force ( $F$ ) (Hughes 1984). Simultaneously, the specimen resisting force starts

to decrease to equalate the accumulated applied impact force, while the penetration increases in a parabolic behaviour until the failure at penetration level ( $P_f$ ). **Fig. 5.9** represents the resistance to impact force behaviour with penetration. The linear part of this curve can be neglected since the penetration starts at a relatively early applied impact force, as mentioned earlier. After that, the resisting force ( $F$ ) by the specimen can be expressed following the force penetration function:

$$F = F_p [1 - (P / P_f)]^2 \quad (\text{Eq. 5.1})$$

The work done by the falling load and that resisted by the specimen can be represented as a function of the impact force and the penetration achieved as the area under the force-penetration curve. This amount of work can also be expressed as the energy transferred by a falling load to the specimen. Hence, the absorbed impact energy can be expressed as a function of the penetration as follow:

$$\text{Absorbed Impact energy} = \int_0^{P_f} \mathbf{d}(P) \quad (\text{area under the curve}) \quad (\text{Eq. 5.2})$$

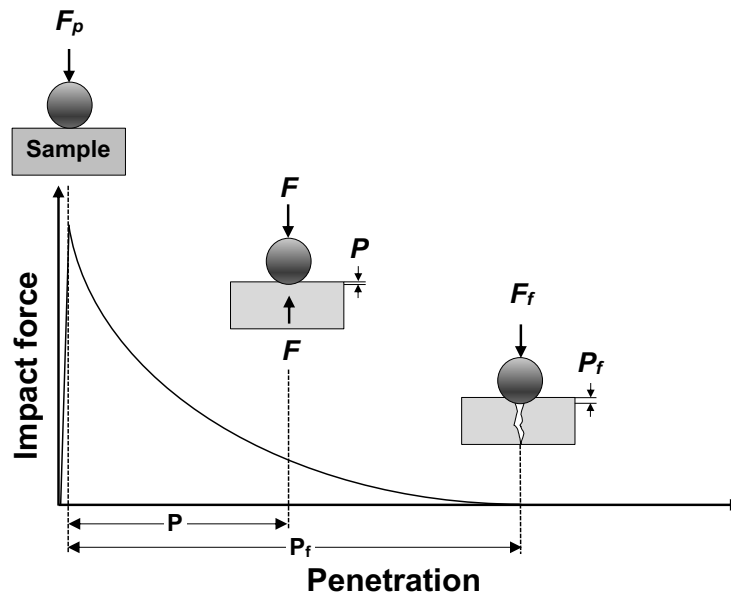


**Fig. 5.9 Concrete impact force vs penetration model.**

Recorded penetration levels at different impact force measures for all tested mixtures are represented in **Fig. 5.10**. The specimens' resistance to penetration agrees with its absorbed impact energy at failure. By observing the force-penetration results, it can be concluded that all AAS specimens exhibited better penetration performance in terms of the absorbed impact energy for achieved penetration compared to OPC. Moreover, it was clear that increasing the mixture activation level had significantly enhanced the specimen energy absorption. Consequently, the needed impact force before achieving a certain penetration level increased. For instance, the impact forces needed to make the steel ball penetrates 1 mm in specimens for C 1.5-8, C 1.25-6, and C 1-4 mixtures were 3.45, 1.65, and 0.95 kN, respectively.

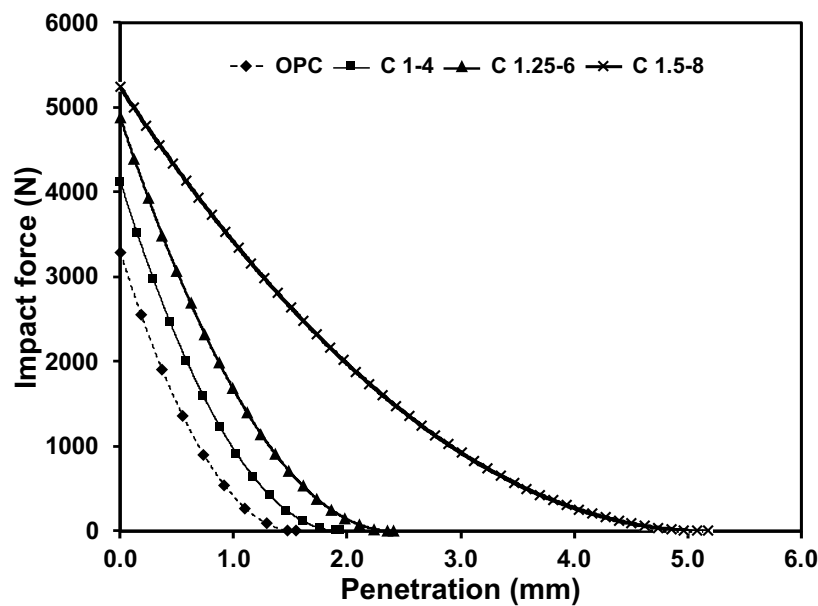
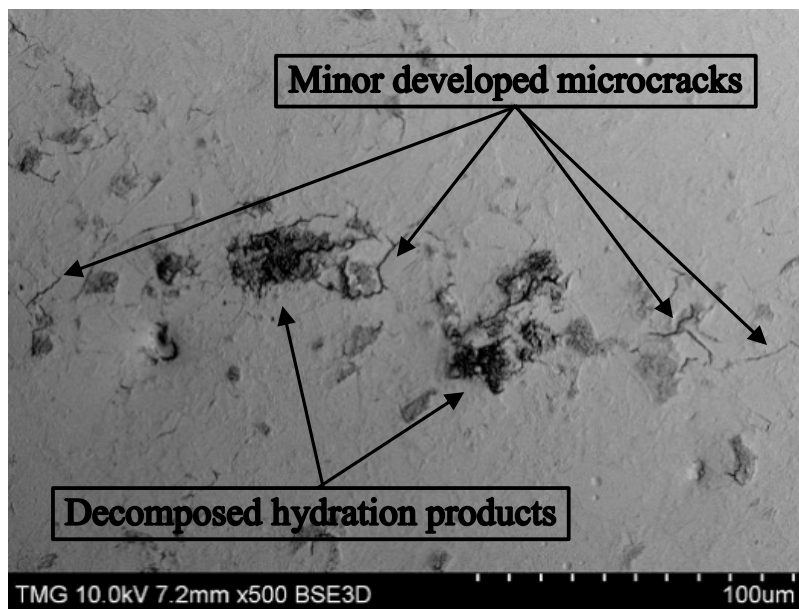


**Fig. 5.10 Concrete impact force vs penetration.**

### 5.2.3 After exposure to elevated temperatures

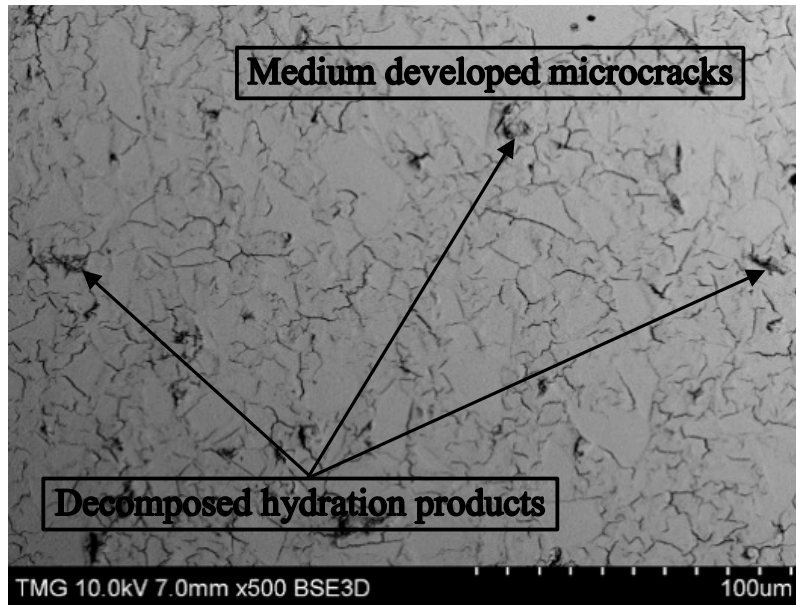
After exposure to different elevated temperatures, static mechanical properties and impact energy absorption capacity for all mixtures had changed significantly. For OPC concrete mixture, the main reason for degradation after exposure to elevated temperature is the decomposition of the

formed hydration products such as C-S-H with a high Ca/Si ratio (Khoury 1992, Alarcon-Ruiz, Platret et al. 2005). For AAS concrete mixtures, the activation level significantly affected the microstructure deterioration. Along with the TGA analysis mentioned earlier in **section 4.2.3**, scanning electron microscopy (SEM) images showed clear evidence for the microstructure degradation level at each exposure temperature (**Fig. 5.11 a, b and c**). Increasing the exposure temperature increased the amount of decomposed hydration products and the developed microcracks, which was intensified at high AAS activation levels. At high temperatures (especially 400 and 600 °C), the main dominant factor affecting the microstructure degradation is the amount of decomposed hydration products, leaving a weak structure. SEM images show the microstructure of mixture C 1.25-6 after exposure to different temperature levels. Images prove the adverse effects of elevated temperatures on the binder microstructure.

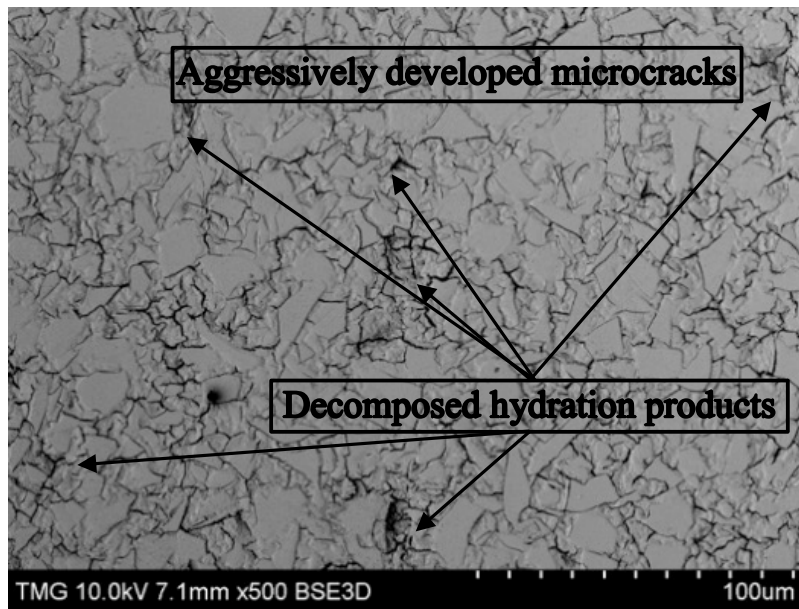


(a)

**Fig. 5.11 SEM of mixture 1.25-6 after exposure to various elevated temperatures.**



(b)



(c)

Fig. 5.11 Cont'd SEM of mixture 1.25-6 after exposure to various elevated temperatures.

### 5.2.3.1 Compressive strength

**Fig. 5.12** shows residual compressive strength for tested mixtures after exposure to elevated temperatures (i.e., 200 °C, 400 °C, and 600 °C). As expected, the OPC concrete mixture residual compressive strength decreased as the exposure temperature increased. For instance, the strength decreased by about 35% at 200 °C, while the reduction was 50% at 400 °C. Hence, the rate of strength reduction was more significant at the first 200 °C. This is attributed to the decomposition of hydration products committed to this range of exposure (i.e., up to 200 °C). Conversely, AAS mixtures did not suffer the same degradation at 200 °C. This is ascribed to the low Ca/Si ratio in the formed C-S-H due to the high availability of silica species supplied by the activator. Such a low Ca/Si ratio C-S-H favoured higher stability at elevated temperatures (Rashad, Sadek et al. 2016). Moreover, the involved Al and Na species in the C-S-H forming C-A-(N)-S-H made it more stable resisting decomposition in such elevated temperature level (Park, Jang et al. 2016, Yang, Wu et al. 2017). However, at higher levels of exposure temperatures (i.e., > 200 °C), AAS mixtures achieved significantly low residual compressive strengths as the activation level increased. As explained before, higher activation levels result in greater hydration products, which will be vulnerable to decomposition, harming AAS strength.

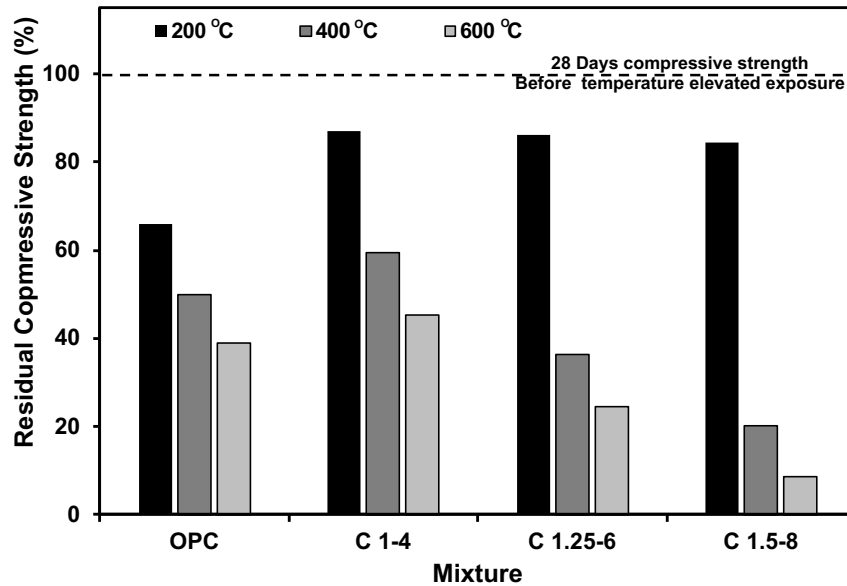


**Fig. 5.12 Residual compressive strength percentage after exposure to elevated temperatures.**

### 5.2.3.2 Tensile strength

**Fig. 5.13** shows the tensile strength after exposure to different temperatures. Tensile strength results followed the same trend for compressive strength. However, tensile strength degradation was lower than that of compressive strength after exposure to 200 °C. This can be explained by the minimal pre-existing microcracking developed by drying shrinkage. Since the OPC mixture did not show a high level of drying shrinkage, the pre-existing microcracks magnification during exposure had a minor aggressive effect on the tensile strength.

On the other hand, at temperatures above 400 °C, the portlandite starts to decompose, as indicated by the thermogravimetric analysis. However, there will be a reversible rehydration reaction and reformation of portlandite during cooling down, leading to a volumetric instability. These volumetric changes will induce internal stresses, and consequently, the development of micro-cracks.

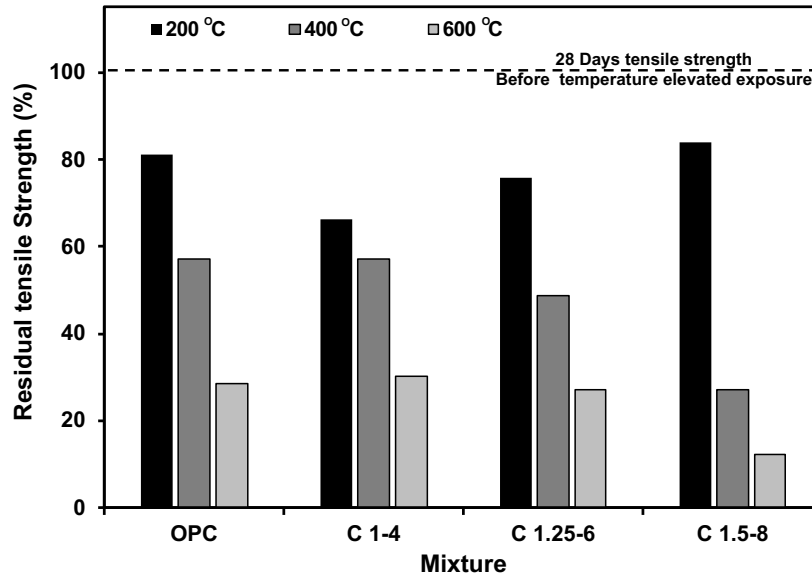


**Fig. 5.13 Concrete residual tensile strength (%) after elevated temperature exposure.**

At the exposure temperature of 200 °C, AAS specimens showed an increase in the residual tensile strength as the activation level increased. This behaviour was expected due to the synergetic effect of low drying shrinkage and high stability of formed hydration products at such temperature. At higher temperatures (i.e., >200 °C), mixtures with high activation level exhibited low residual tensile strength due to aggressive microstructure degradation. This can be ascribed to the effect of different thermal expansion coefficient between the coarse aggregate and the binder matrix, magnified at higher exposure temperatures (Jumppanen, Diederichs et al. 1986, Phan and Carino 2001, Guerrieri, Sanjayan et al. 2010). Moreover, a higher amount of formed hydration products resulted in a lower pore volume at these mixtures (i.e., high activation level). As a result, the effect of exposure to elevated temperature will be aggressive at high-temperature levels due to non-released pressure during exposure (Seleem, Rashad et al. 2011). This will consequently result in a weak microstructure while developing micro-cracks to release these pressures. **Fig. 5.14 (a, b and c)** shows the tested specimens for mixture C 1.5-8 after exposure to the three exposure

temperatures. The white outlined aggregate are particles split during tensile failure, and the black intact outlined aggregate, indicating the popping out aggregate during the failure. At 200°C, the coarse aggregate particles' crack paths indicated the matrix's high strength and strong bond with aggregates. However, at the high temperatures (i.e., 600°C), crack paths passed through the matrix, indicating its weakness and degradation of the microstructure.

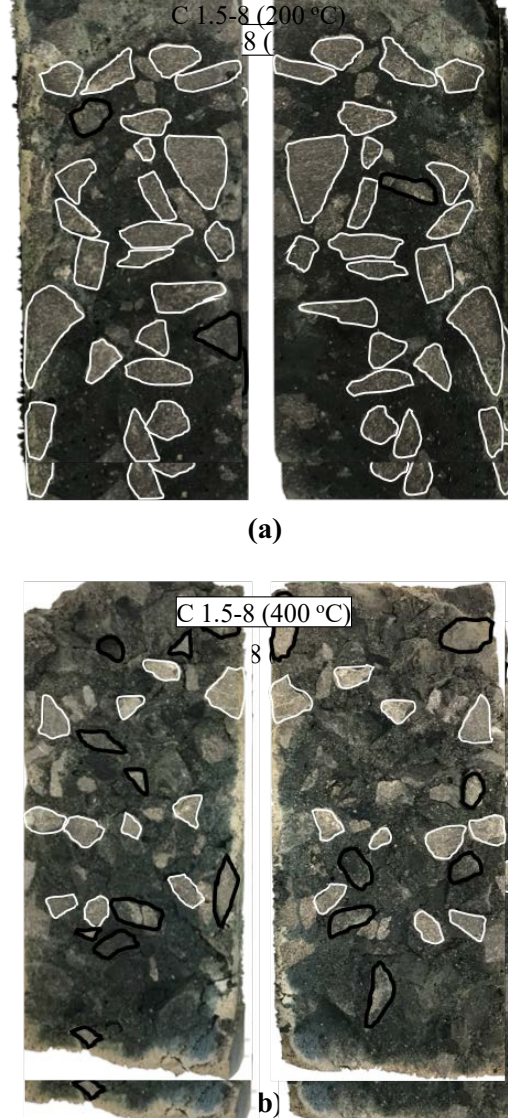


**Fig. 5.14 Concrete specimens exposed to various elevated temperatures after tensile strength test.**

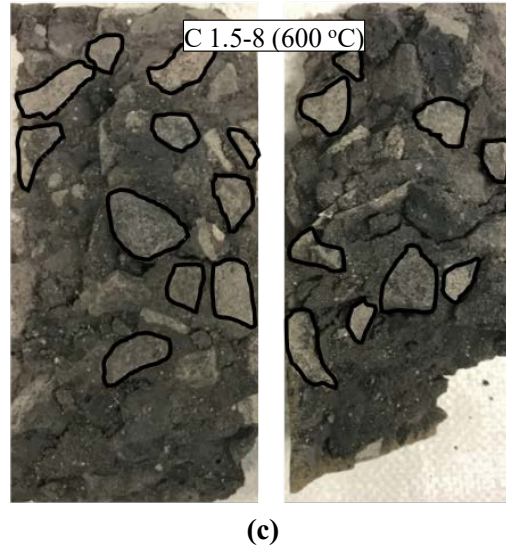


**Fig. 5.14 Cont'd Concrete specimens exposed to various elevated temperatures after tensile strength test.**

### **5.2.3.3 Impact energy absorption capacity**

For impact behaviour, regardless of the exposure temperature, all specimens' performance was aggressively affected after exposure to elevated temperature. The OPC concrete specimens lost around 90 %, 95% and 97.5% of their original impact energy absorption capacity at temperatures 200 °C, 400 °C, and 600 °C, respectively. This is ascribed to the hydration products decomposition and the volumetric unstable induced by the portlandite rehydration process, as explained earlier. However, for AAS mixtures, the dominant factor affecting the impact behaviour after exposure was the hydration products decomposition beating the pre-existed microcracking profile. This can be attributed to the amount of hydration products formed at each activation level, and consequently, decomposed during exposure to the different exposure temperatures. The lower the activation level, the lower the hydration products decomposed and vice versa (**Fig. 5.15**). The high decomposition for hydration products will weaken the specimen's microstructure leading to lower residual impact energy absorption. Moreover, water absorption profile of specimens

activated by different activation levels was reflecting the pore structure and its capability to release the build up pore water pressure induced during exposure to elevated temperatures. High activation level (i.e  $M_s=1.5$  and  $Na_2O$  dosage =8%) showed the lowest level of water absorption during the second stage ( $S_2$ ). This reflects the existed capillary pores as a result of well densified microstructure (Aitcin 2003). These capillary pores plays a great rule to relief the pore pressure during exposure to elevated temperatures. Lower level of capillary pores exhibited at the high activation level, resulted in increasing build up pore pressure, leading to sever micro cracking development, which affected the impact behavior after exposure to different temperature

For example, increasing the activation dosage and the silica modulus from 4% to 8% and 1 to 1.5 decreased the residual impact energy absorption by more than 80% at 200 °C, respectively.

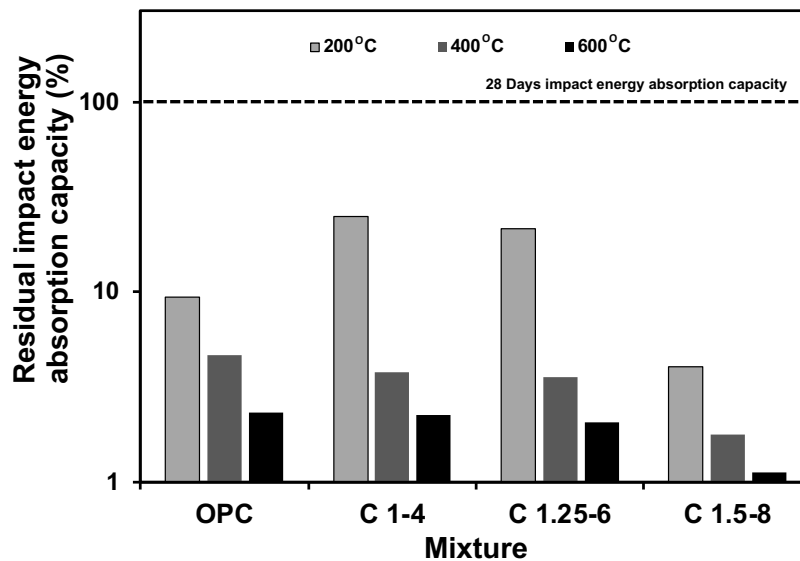


**Fig. 5.15 Residual impact energy absorption capacity after exposure to temperatures.**

The failure modes for low activation mixtures (C 1-4) under impact load after exposure to elevated temperatures exhibited the highest resistance. Specimens of C 1-4 had reserved relative integrity during failure. Crack propagation during failure showed that more cracks are required to

achieve the failure criteria for higher residual impact resistance specimens. High activated AAS specimens just failed with the first crack formation after exposure to elevated temperature. At the first crack initiating impact load, cracks start to shape through three stages; stress-free crack, tension softening zone, and the uncracked zone, described as the cohesive zone (**Fig. 5.16. a**) (Papanastasiou and Sarris 2017). Cracks will propagate at the crack tip once stresses exceed the maximum traction stress, which is considered a function of the binder microstructure ability to hold cohesive (Rashad, Bai et al. 2012). **Fig. 5.16 (b, c, and d)** shows the failure under impact loads for C 1-4, C 1.25-6 and C 1.5-8 mixtures after exposure to 400 °C. For mixture C 1-4, the surface cracks were more distributed through the specimen, which indicates the specimen's integrity during failure. It required higher transferred impact energy to overcome the tension softening zone critical stress for the first crack. As a result, new cracks started to be initiated from any pre-existing flaw, while the first developed crack still needs a higher impact load to achieve the critical value to propagate through the cohesive zone. Conversely, at a high activation level (i.e., C 1.5-8), the specimen failed into two parts, indicating an easy initiation for the first-crack path with fewer successive blows. This also indicates a low cohesive zone capacity, which is evident in the loose binder microstructure after exposure to the same level of elevated temperature.

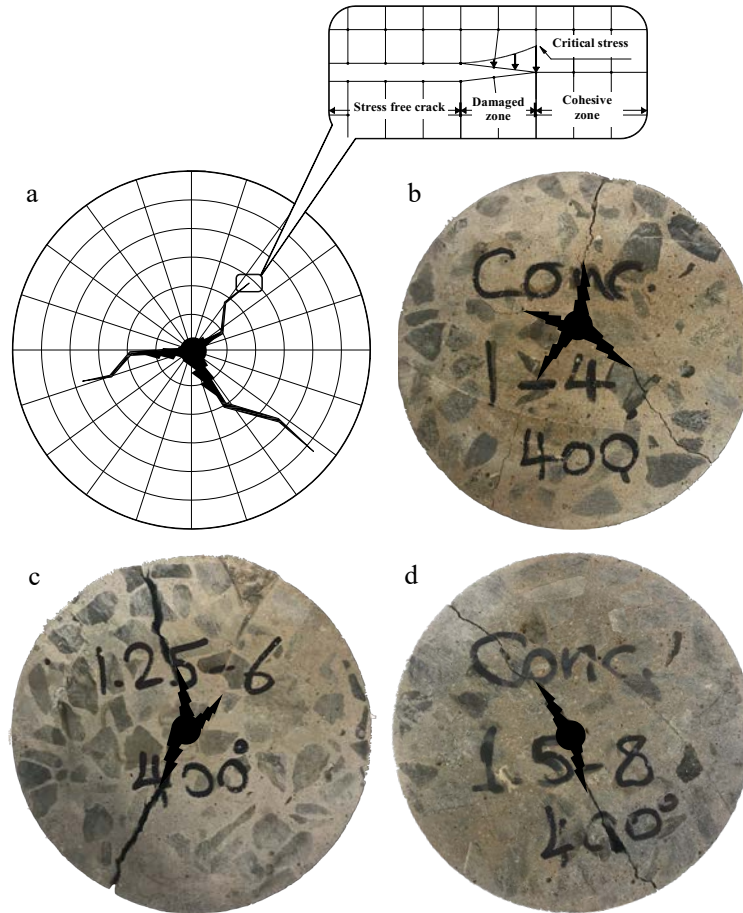


**Fig. 5.16 Failure modes of impact test specimens exposed to 400 °C.**

### 5.3 Conclusions

1- AAS concrete performs better in terms of impact energy absorption capacity under ambient temperature than OPC concrete.

2- The impact behaviour of AAS concrete was greatly affected by the activation level in terms of  $\text{Na}_2\text{O}$  % dosage and silica modulus.

3- Depending on the activation level, both amount and nature of formed hydration products significantly influence AAS concrete mechanical properties at ambient and elevated temperatures.

## *Chapter 5*

4- High activation level is favourable to obtain AAS with good mechanical properties and impact behaviour at ambient temperature. However, low activation levels provide better residual strength and impact energy absorption capacity after exposure to elevated temperatures. Reducing the silica modulus and Na<sub>2</sub>O % dosage from 1.5 and 8% to 1 and 4%, respectively, resulting in higher residual impact energy absorption up to 6 times after exposure to 200 °C, and up to the double capacity after exposure to 400 °C and 600 °C.

5- The impact force needed to achieve certain penetration in AAS concrete varied with the activation level. High activation level provides better resistance of AAS concrete to penetration.

6- The threshold value of stresses induced by the impact loads to overcome a crack tension softening zone and continuing to damage the cohesive zone significantly affected by the activation level of AAS concrete.

---

## Chapter 6    Impact Behavior of Rubberized AAS Concrete at Ambient and Elevated Temperatures

### 6.1 Introduction

One AAS concrete mixture was chosen according to the mentioned criteria in **section 3.2.2** to be tested with the enhancement techniques. For this chapter, rubber incorporation will be employed as an impact energy absorption booster as a partial replacement of fine aggregate. It acts as impact dissipation spots through the concrete matrix, enhancing the impact energy absorption compared to conventional concrete. However, at elevated temperature, the degradation in the concrete performance is expected to be associated with the changes in the concrete binder properties and rubber particles characteristics. Therefore, this chapter will investigate the impact performance of rubberized AAM exposed to elevated temperatures. **Table 6.1** illustrate the mixing proportions for all prepared concrete mixtures. The first two litters (PC or CR) refer to plain concrete or concrete with rubber, respectively, followed by the ratio of rubber as a replacement of fine aggregate.

**Table 6.1 Concrete mixture proportions.**

Mixture	Binder (kg/m <sup>3</sup> )	Fine agg. (kg/m <sup>3</sup> )	Rubber (kg/m <sup>3</sup> )	Coarse agg. (kg/m <sup>3</sup> )	NaOH (kg/m <sup>3</sup> )	Na <sub>2</sub> SiO <sub>3</sub> (kg/m <sup>3</sup> )	Added Water (L/m <sup>3</sup> )
<b>PC</b>	400	650	0	1138	22	167	72
<b>CR 5%</b>	400	618	14	1137	22	167	72
<b>CR 10%</b>	400	585	28	1137	22	167	72
<b>CR 15%</b>	400	552	42	1137	22	167	72

## 6.2 Results and discussion

### 6.2.1 Degradation mechanism

During exposure to elevated temperatures, there are two responsible mechanisms for concrete deterioration. According to the visual inspection and TGA results of heated rubber samples, the first mechanism is associated with the rubber particles deterioration as exposed to elevated temperatures. **Fig. 6.1** illustrates the different states of rubber particles at different temperatures. Rubber starts to melt at around 200 °C. However, it needs a higher temperature to decompose (i.e., up to 400°C). Above 400 °C, rubber particles continue decomposing, turning to ash eventually at 600 °C.

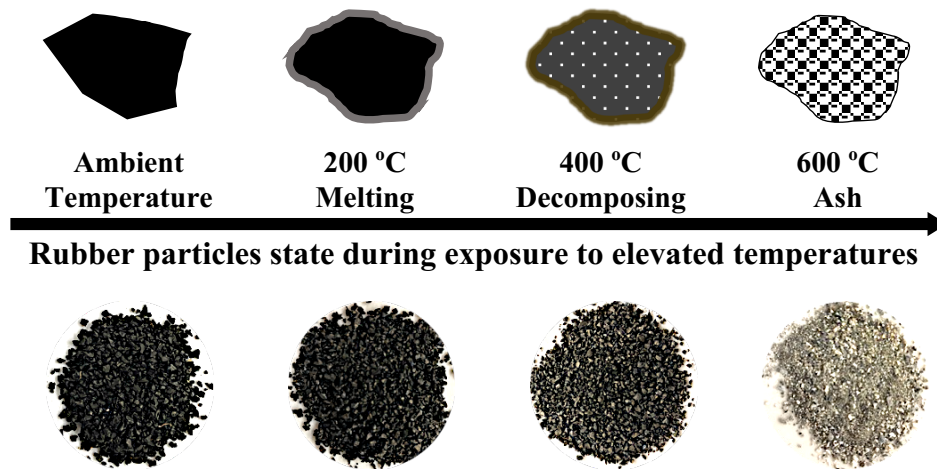


**Fig. 6.1 Effect of various elevated temperatures on rubber particles.**

Thermogravimetric analyses of a rubber sample were performed to quantify the effect of elevated temperatures on the rubber particles. Results could explain the rubber deterioration level at each exposure temperature. It was clear that up to 200 °C, the rubber was still semi-stable approaching the initial melting stage. At this level, the rubber didn't show a significant weight loss (i.e., 2%). However, increasing the temperature up to 400 °C, resulted in a 12% weight loss

reflecting the rubber decomposition into combustible chemical ingredients. At the range of (400 °C to 600 °C), rubber suffered a considerable weight loss associated with the total decomposition and combustion of the particles and turning into ash leading to 65 % weight loss (**Fig. 6.2**).

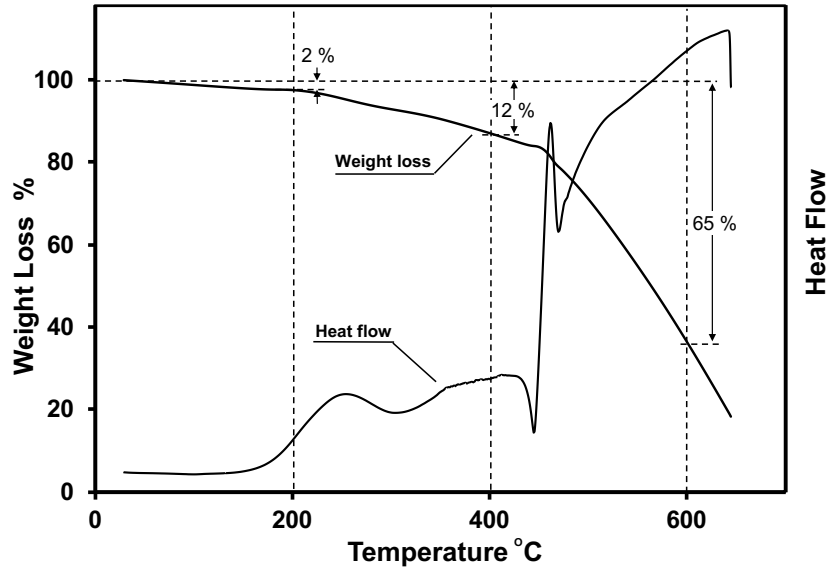


**Fig. 6.2 Thermogravimetric analysis (TGA) of rubber.**

The second mechanism controlling concrete degradation is binder deterioration. Each hydration product of AAS, such as C-S-H, Hydrotalcite, and C-N-(A)-S-H can be considered stable during elevated temperatures up to a certain level. Since the AAS concrete mixture is fixed for all specimens in terms of activation level (i.e.,  $M_s=1.5$  and  $\text{Na}_2\text{O}$  Dosage of 8%), then the effect of elevated temperatures on the binder microstructure can be considered as a constant factor for all rubber mixtures. The availability of Si species will increase bridges to accommodate the Al species dissolve from the precursor (i.e. slag), and the Na species provided by the activator solution. These will lead to the formation of amorphous C-N-(A)-S-H in a larger quantity compared to crystalline C-S-H. The effect of elevated temperatures on the binder was measured in terms of residual hydration products and the consequent weight losses after exposure to each

temperature level. According to the TGA analysis (**Section 4.2.3**), The weight losses for samples exposed to elevated temperatures compared to samples tested at ambient temperature showed an increase in the amount of decomposed hydration products as exposure temperature increased. Up to 200 °C, the calcium silicate hydrate products showed some stability while other products such as hydrotalcite were not affected. However, at higher levels, all hydration products started to decompose. For instance, after exposure to 600 °C, the weight loss was almost 4%, representing a minimal amount of reserved hydration products compared to 26% weight loss for a sample at ambient temperature.

## 6.2.2 Concrete compressive strength

**Fig. 6.3** summarizes compressive strength results for plan concrete and rubber concrete mixtures at ambient temperature. Results showed that crumb rubber addition had reduced the compressive strength of AAM, which agreed with previous findings (Long, Li et al. 2018, Aly, El-Feky et al. 2019). The higher the rubber content, the lower the achieved compressive strength. This is ascribed to rubber's hydrophobic nature, and consequently, weak bond with the surrounding binder. Increasing the rubber content resulted in increased weaker bond zones (Guo, Dai et al. 2017). Also, the higher deformability of rubber compared to rigid sand will affect the binder resistance to compression loads (Shu and Huang 2014, Karimipour, Ghalehnovi et al. 2020). The high concentrated stresses in the surrounding binder will lead to early initiated cracks and, consequently, earlier failure, which is expected to increase as rubber content increased. For instance, at a low level of rubber replacement (i.e., 5%), the compressive strength was reduced by 3% compared to 9% when rubber content increased to 15% with respect to control mixtures without the rubber.

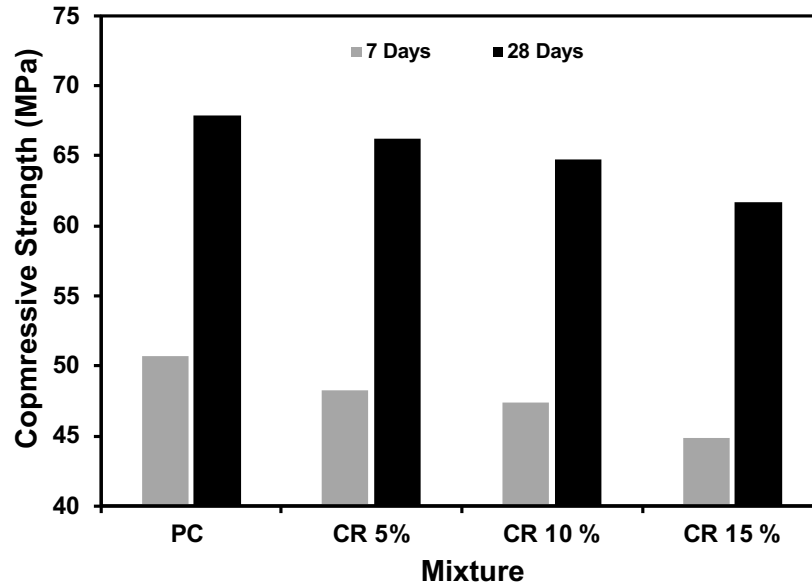


**Fig. 6.3 Compressive strength for all mixtures at ambient temperature.**

Ultrasonic pulse velocity test results came in agreement with the strength results. The non-homogeneous structure of the specimens due to rubber incorporation reduced the pulse velocity. The higher the rubber content, the lower the pulse velocity. This means that these specimens will suffer strength degradation due to non-uniform stress resistance (Mohammadi, Khabbaz et al. 2016). For instance, a specimen containing 15% rubber as a replacement of fine aggregate recorded 4.62 km/s pulse velocity comparing to 5.0 km/s achieved by the plain concrete specimen at 28 days (**Fig. 6.4**). The same specimen with 15% rubber replacement of sand exhibited 54.7 MPa compressive strength compared to 67.8 MPa for the plain concrete. This can confirm that the rubber incorporation in AAS concrete harms the compressive strength.

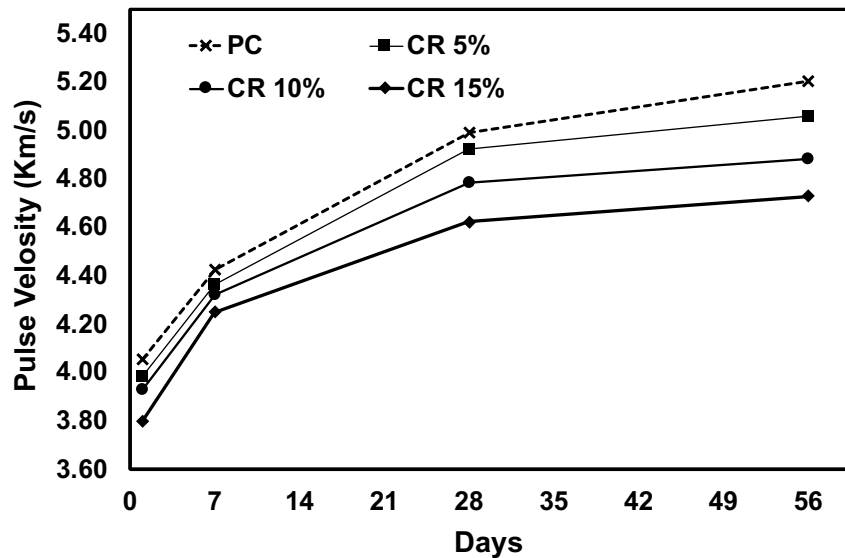


**Fig. 6.4 Ultrasonic pulse velocity results for various tested concrete mixtures.**

After exposure to different elevated temperatures, rubber incorporation had shown different behaviours. This indicated that different criteria are dominating the strength reduction at each level of temperature. At a low level of elevated temperature exposure (200°C), the rubber particles' surface started to melt, leading to a stronger cohesiveness to the surrounding binder during the cooling stage. This can be observed in the strength results after exposure to low elevated temperature (i.e. 200 °C), as the residual strength changes were not significant. The rubber enhanced bond with the surrounding binder could compensate for the weak bond effect at ambient temperature on the compressive strength. Hence, at this level of exposure, the binder decomposition will be dominating the reduction in strength. As mentioned earlier, all mixtures had the same binder compositions, which explains having almost the same residual strength ratio to that at ambient temperature. At high elevated temperature levels (i.e., 400 °C and 600 °C), it was found that the deterioration became aggressive as a result of the synergetic effect of the binder deterioration along with the decomposition of the rubber particles, leaving voids instead, which

led to a fragile structure, especially, at higher values of rubber replacement of fine aggregate (**Fig. 6.5**). For instance, after exposure to 400 °C, the residual compressive strength of specimens containing 5%, 10%, and 15% rubber as a replacement of sand was 18%, 14%, and 13%, respectively comparing to 20% achieved by the plain concrete specimen.

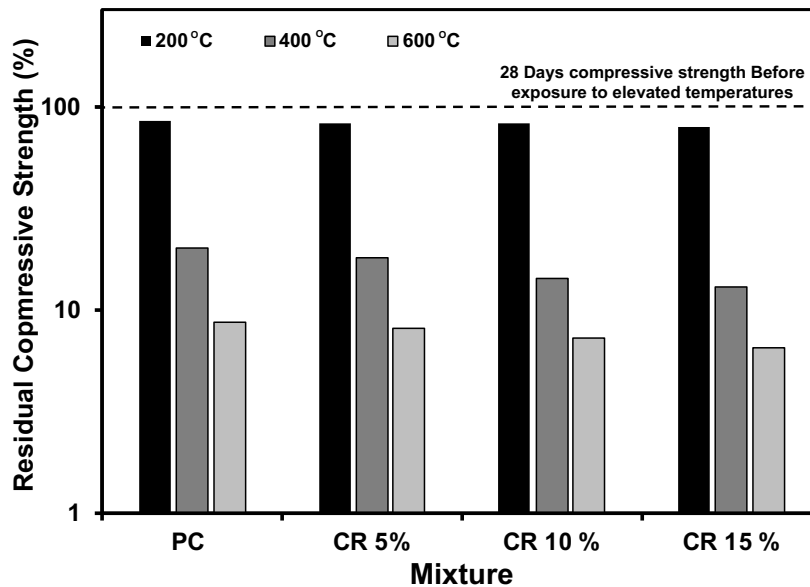


**Fig. 6.5 Concrete residual compressive strength (%) after elevated temperature exposure.**

### 6.2.3 Concrete tensile strength

Tensile strength results for tested specimens are illustrated in **Fig. 6.6**. The degradation in tensile strength due to rubber inclusion was higher compared to that of compressive strength. This can be ascribed to the difference in the stress resistance mechanism. During tensile loading, the surface bond between rubber particles and the surrounding binder has a considerable role in resisting the generated stresses. This bond is anticipated to be lower than that of mineral sand due to the different physical properties between sand and rubber particles. Hence, the detachment of rubber particles will be easier, resulting in a lower tensile strength. For instance, mixtures incorporating

15% rubber exhibited around 13.5% reduction in the tensile strength compared to plain concrete strength, while the same mixture showed only a 9% reduction in the compressive strength.

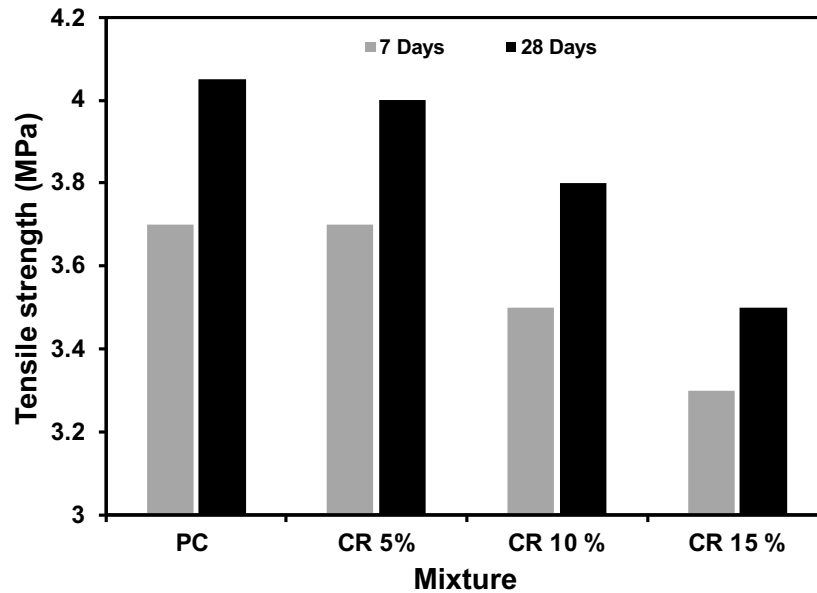


**Fig. 6.6 Tensile strength for all mixtures at ambient temperature.**

Moreover, the micro-cracks development accompanied by the drying shrinkage is another factor affecting the tensile strength. Increasing the rubber incorporation had led to increased micro-strain and shrinkage (**Fig. 6.7**). Consequently, a higher density of developed micro-cracks due to the reduction in the internal restraining action due to replacing stiff sand particles with rubber leading to higher shrinkage (Sukontasukkul and Tiamlom 2012). Hence, the developed micro-cracks will reduce achieved tensile strength as the rubber content increased.

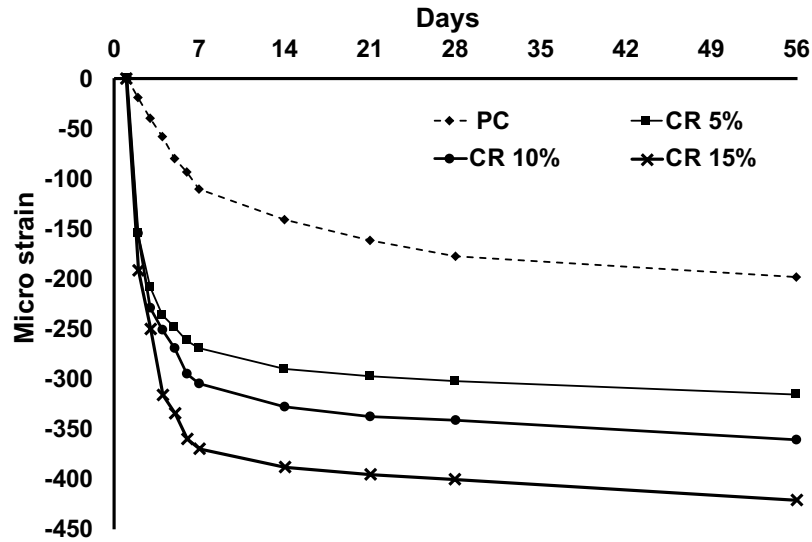


**Fig. 6.7 Drying shrinkage micro-strain for all mixtures at ambient temperature.**

After exposure to various elevated temperatures for tested specimens, it was found that increasing the rubber content resulted in a lower residual tensile strength at all temperature levels (Fig. 6.8). However, with a closer focus on the residual tensile strength after exposure to a high-temperature level (i.e., 600 °C), the residual strength percentage did not significantly decrease. This can be explained by the temperature threshold at which all the rubber particles can be considered as totally decomposed, leaving the whole responsibility of stress resistance to the binder along with the coarse aggregate. For example, the reduction in tensile strength for samples CR 5%, CR10%, and CR 15% after exposure to 200 °C, was 33 %, 42%, and 49% of their original strengths at ambient temperature compared to 16% reduction for PC, respectively. However, after exposure to 600 °C, the reduction in tensile strength of PC was 88%, and around 90% for all rubber incorporated specimens.

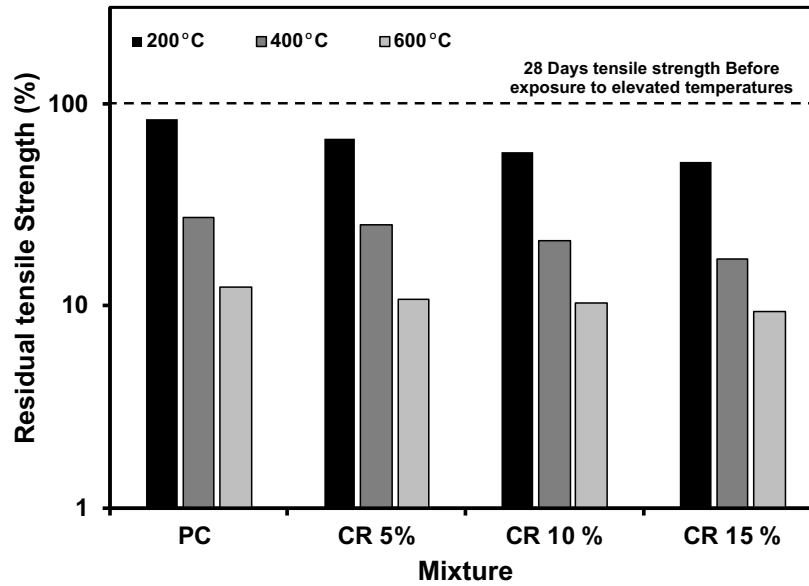


**Fig. 6.8 Concrete residual tensile strength (%) after elevated temperature exposure.**

#### 6.2.4 Concrete static modulus of elasticity

**Fig. 6.9 (a, b, c, and d)** illustrates the modulus of elasticity changes for concrete mixtures at ambient temperature and after exposure to elevated temperatures. At ambient temperature, it was found that rubberized AAS concrete has a lower static modulus of elasticity than that of the control AAS concrete, which agreed with previous researches (Zheng, Huo et al. 2008, Ganjian, Khorami et al. 2009, Aslani 2016). The relatively low stiffness and modulus of elasticity of rubber particles will eliminate its contribution in resisting applied loads during the elastic zone (Benazzouk, Mezreb et al. 2003, Gupta, Chaudhary et al. 2016, Li, Tu et al. 2016). Hence, concrete will deform easily at low-stress levels. After exposure to elevated temperatures, the same behaviour was observed due to the extensive degradation during the exposure. Binder and rubber decomposition will result in a crispy structure containing many voids. This eventually will affect the strain behaviour for different specimens. This explains the reduction in the static modulus of elasticity as the rubber content and exposure temperature increased. For instance, at ambient temperature,

the reduction in modulus of elasticity for rubberized mixtures were 4%, 11%, and 17% compared to that of the plain mixtures without the rubber. However, after exposure to 400 °C, the same mixtures' reductions increased to 12%, 22%, and 30% compared to the plain mixtures exposed to the same temperature level, respectively. This confirms the synergetic negative effect of increasing the incorporation level and increasing the temperature on concrete elasticity modulus.

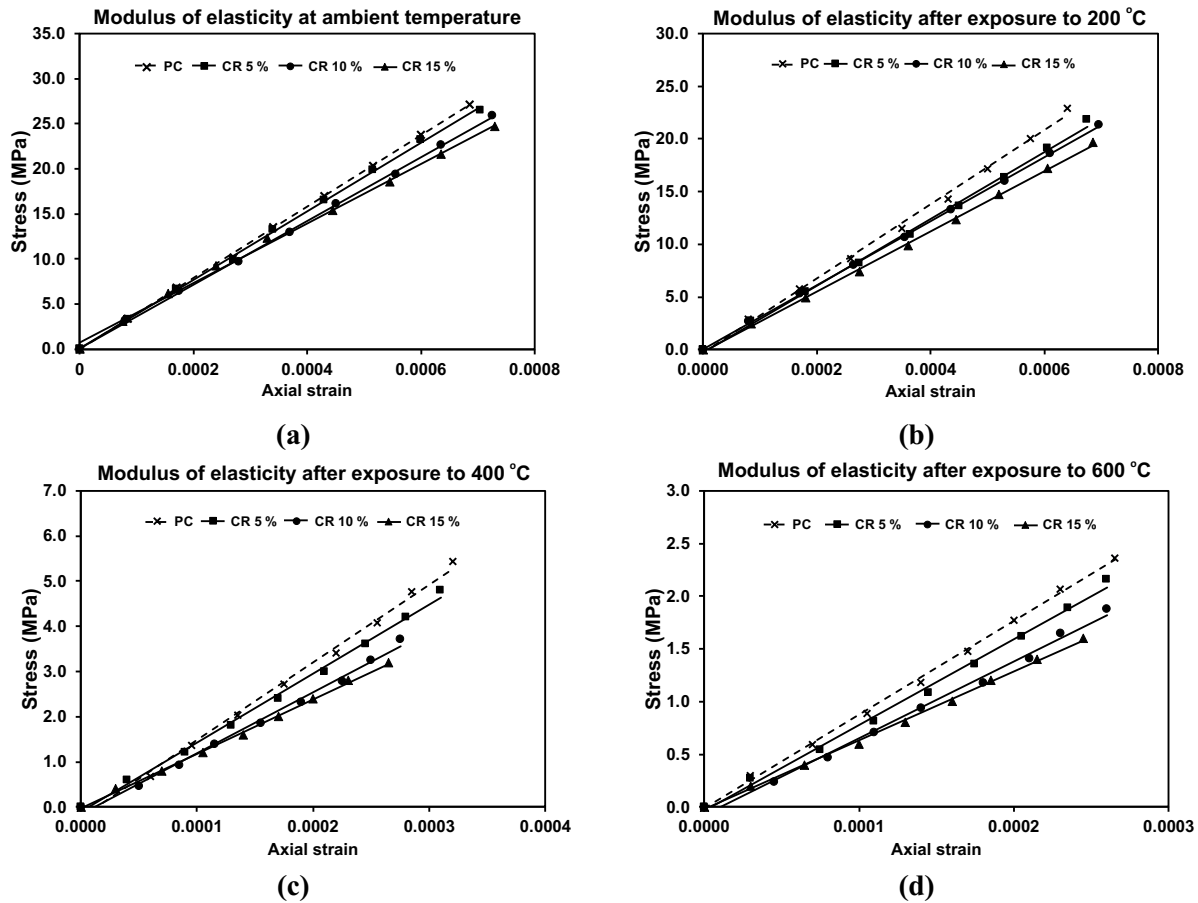


Fig. 6.9 Concrete modulus of elasticity before and after exposure to elevated temperature.

### 6.2.5 Impact energy absorption

Incorporating rubber as a replacement of sand improved the impact load resistance for AAS concrete in agreement with previous research (Aly, El-Feky et al. 2019, Jie, Yao et al. 2020). This improvement is attributed to the matrix flexibility, and consequently, lower brittleness comparing

to that of plain concrete and higher ability to absorb the impact energy (Zheng, Huo et al. 2008, Liu, Chen et al. 2012). Results revealed that replacing 10% of sand with rubber was the optimum level. Increasing the rubber content above this level did not show enhancement in the impact energy absorption capacity. For instance, 5 % and 10% rubber replacement resulted in around 34% and 83% enhancement in impact energy absorption compared to mixtures without rubber, respectively. However, using 15% rubber replacement of sand showed a reduction in the impact energy absorption capacity with respect to 10% replacement with about 16% (Fig. 6.10).

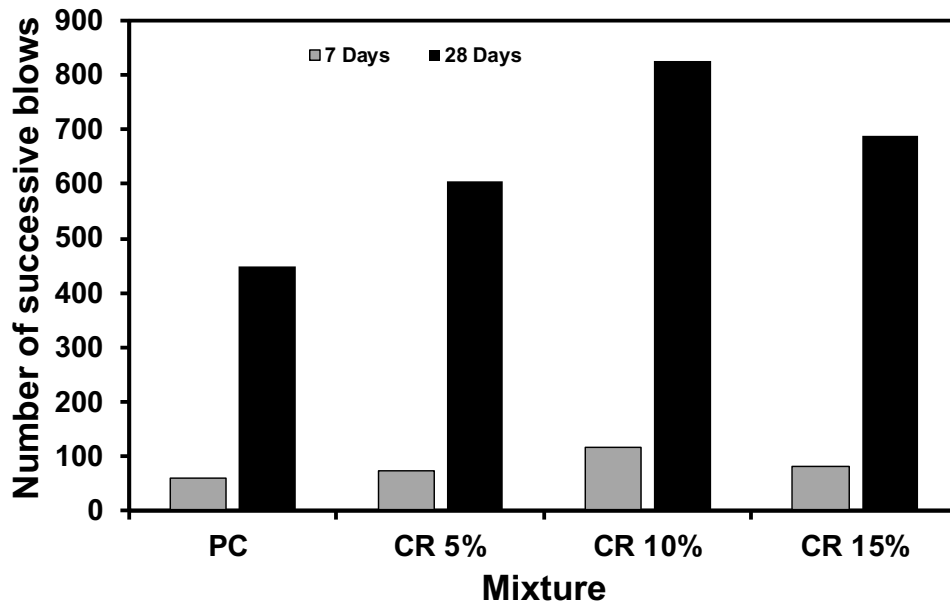


Fig. 6.10 Concrete impact absorption for plain and rubber AAS concrete.

Variation in the behaviour under static and dynamic loadings can be explained by the changes in the Dynamic Increase Factor (DIF), representing the ratio between the dynamic and static strength achieved at various rubber contents. Under static loading, increasing the rubber content reduced the mechanical properties, as mentioned earlier. However, the impact energy absorption was enhanced by the addition of rubber as a replacement for sand. The dynamic modulus of elasticity was calculated for all mixtures as a function of the bulk density and the ultra-

sonic pulse velocity for different mixtures using the equation proposed by other researches (Eq. 1). Although both the static and dynamic modulus of elasticity decrease as the rubber content increases, DIF has increased to 10% rubber content (Fig. 6.11). This can explain the rubber incorporation's enhancement in case of dynamic loading (Liu, Chen et al. 2012).

$$E_d = (V^2 \rho / g) \quad \text{(Eq. 6.1)}$$

Where  $E_d$  is the dynamic modulus of elasticity in GPa, and  $V$  is the ultrasonic pulse velocity in km/s,  $\rho$  is the concrete density in  $\text{kg/m}^3$ , and  $g$  is the gravity acceleration in  $\text{cm/s}^2$ .

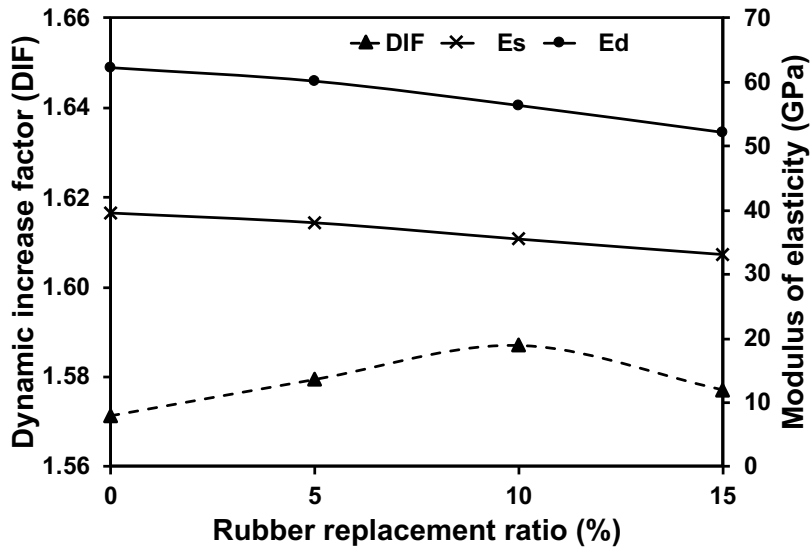


**Fig. 6.11 Concrete dynamic increase factor (DIF) at different levels of rubber incorporation.**

During the impact test, the penetration level achieved by the steel ball was continuously monitored. This was used to quantify the concrete specimen's work to resist the impact force causing the ball penetration. Hence, the energy absorbed by the specimen can be represented by the relationship between the impact force and the penetration level as the area under the curve (Korol and Sivakumaran 2012). The impact accumulated force applied to achieve failure increased

as the rubber content increased up to 10%. Moreover, the work done to achieve the same penetration level was found to vary between specimens having CR 10% with the highest work (Fig. 6.12).

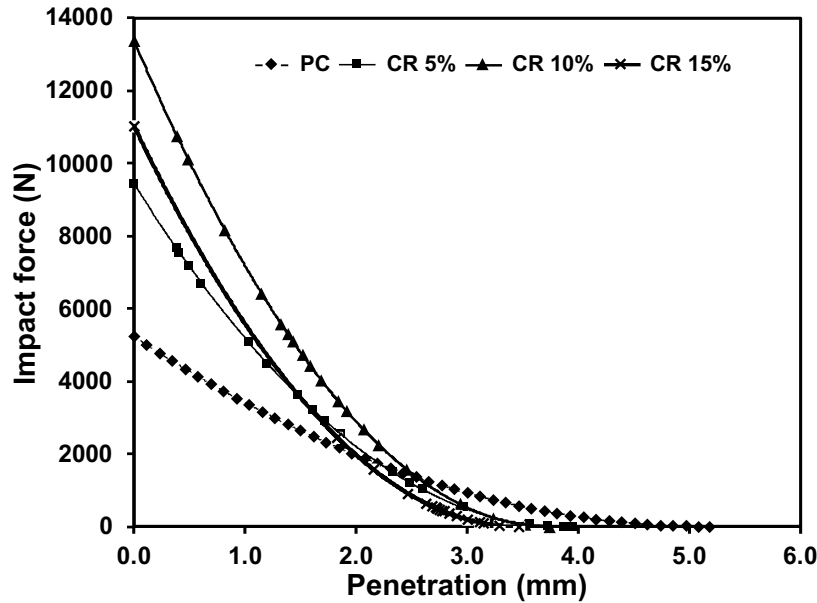
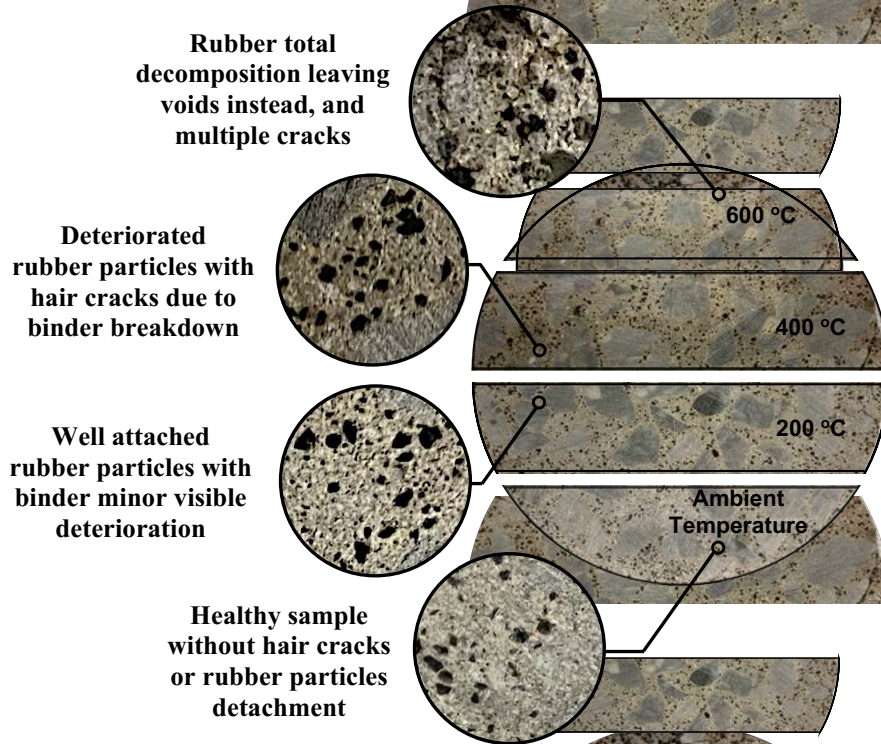


Fig. 6.12 Steel ball penetration level vs cumulative impact force.

After exposure to elevated temperatures, all concrete mixtures showed noticeable degradations and reductions in their impact energy absorption values. The visual inspection for tested specimens showed a contrast between the effects of each exposure temperature (Fig. 6.13). The specimen cross-section looked intact at ambient temperature with no visible cracks or voids due to rubber detachment. However, increasing the temperature up to 600 °C resulted in specimens gradually deterioration. Initially, the 200 °C temperature level didn't significantly affect the rubber particles, as mentioned earlier. However, the binder deterioration is initiated. Similar observations were obvious for specimen exposed to 400 °C, while limited hair cracks were visible on the specimen surface along with deteriorated rubber particles. Ultimately, after exposure to 600 °C,

the sample was aggressively deteriorated, showing clear voids at the rubber particles locations with multiple micro-cracks.



**Fig. 6.13** The effect of various elevated temperatures on impact test samples.

Although all elevated temperatures had negatively affected the impact absorption capacity of concrete, rubber incorporation was still beneficial to reserve better residual impact energy after exposure to elevated temperatures (i.e., especially at 200 °C, and up to 400 °C). Up to 400 °C, some portion of the rubber content might not be hardly affected by the elevated temperature. Hence, this remaining rubber contributes to the concrete matrix resistance for impact loads. However, after exposure to 600 °C, rubber became a harmful guest on the concrete matrix due to its decomposition, leaving semi-voids. For instance, at a temperature level of 200 °C, the residual impact absorption capacity for mixtures with 10% rubber was enhanced by 500% compared to plain concrete (**Fig. 6.14**). At 400 °C, all concrete specimens exhibited a relatively low impact

absorption capacity. However, in a closer focus, rubber incorporation still had a slight positive effect on the impact behaviour. At 600 °C, all concrete specimens showed substantial degradations in residual impact absorption, especially specimens incorporated with rubber.

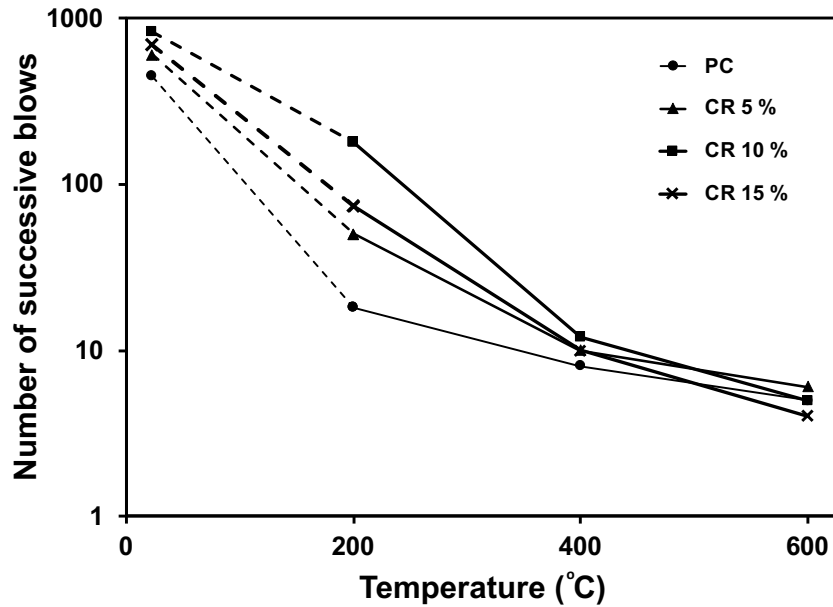


**Fig. 6.14 Concrete residual impact energy absorption after exposure to various elevated temperatures levels.**

Moreover, the modulus of resilience ( $U$ ), which represents the strain energy that concrete can absorb within the elastic deformation limit, was another evident explaining the impact behaviour for each level of rubber incorporation at both ambient and elevated temperatures. **Fig. 6.15. (a, b, d, and c)** indicates the changes in resilience modulus, which will affect the impact energy absorption behaviour at all temperature levels (Li and Aoude 2020). At ambient temperature and up to 200 °C, increasing the rubber content enhanced the modulus of resilience, although it was a reason for the static mechanical property's reduction, such as modulus of elasticity. However, at higher levels of elevated temperatures (i.e., 400 °C and 600 °C), the modulus of resilience started to decrease regardless of the rubber content. This can be attributed to the high

brittleness induced by the exposure to such elevated temperatures and the highly formed voids due to the rubber decomposition, leading to faster cracks development.

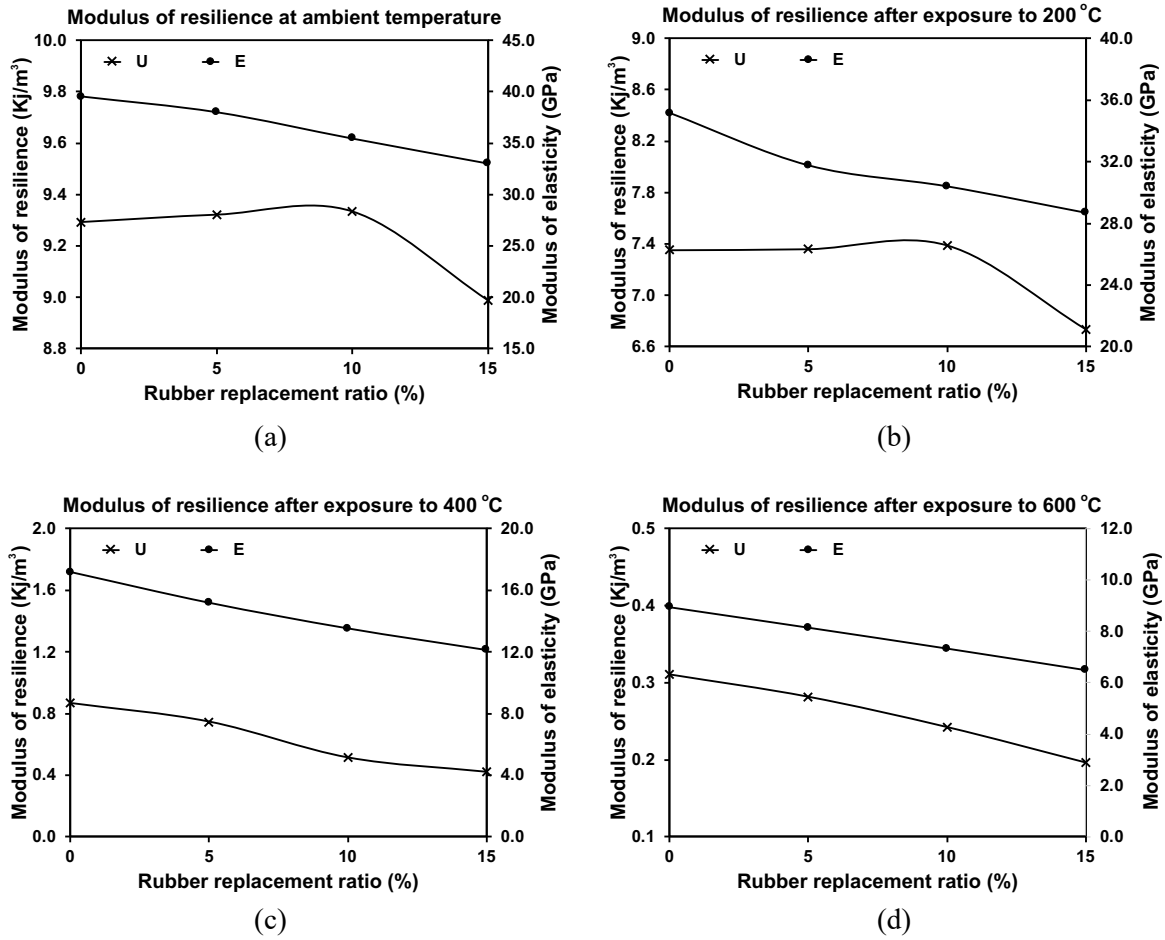


Fig. 6.15 Concrete modulus of resilience Vs modulus of elasticity at ambient and various elevated temperatures.

### **6.3 Conclusions**

1- Rubber incorporation into AAS concrete as a replacement of sand slightly reduced the static mechanical properties.

2- Impact energy absorption of AAS concrete was enhanced by rubber incorporation up to 10% as a replacement of sand. Moreover, the rubberized concrete's work to resist penetration during the impact event varied according to the rubber content. 10% rubber content was found to achieve the optimum work done by concrete to resist penetration.

3- At ambient temperature, the dynamic increase factor (DIF) increased by incorporating rubber up to 10% replacement of fine aggregate.

4- At elevated temperatures, static behaviour for rubberized AAS concrete changed with respect to that at ambient temperature. Both compressive and tensile strength decreased as rubber content increased.

5- The residual impact energy absorption capacity had enhanced after exposure to 200 °C as a result of reserving increased modulus of resilience achieved by rubber incorporation.

6- At high-temperature levels, regardless of rubber content, all mixtures showed an aggressive degradation in impact energy absorption capacity due to both binder and rubber decomposition.

## Chapter 7 Impact Behaviour of Fibre Reinforced Alkali-Activated Slag Concrete Exposed to Elevated Temperatures

In this chapter, different fibre types' ability to enhance the AAS impact absorption capacity while maintaining adequate mechanical properties after exposure to elevated temperatures was assessed. Three types of fibre, namely polypropylene fibre, basalt fibre, and steel fibre, were tested. Various fibre reinforced AAS concrete mixtures were prepared with 0%, 0.25%, 0.5%, and 1% fibre added by volume. **Table 7.1** illustrate the mixing proportions of plain AAS concrete (named PC), polypropylene fibre reinforced AAS concrete (named PFC), Basalt fibre reinforced AAS concrete (named BFC), and steel fibre reinforced AAS concrete (named SFC). All mixtures were prepared with the same activation level (i.e.  $M_s=1.5$  and  $Na_2O$  dosage =8%) following the previous phase's findings (i.e., **Phase II**). Samples of the cast specimens for fibre-reinforced AAS concrete before and after exposure to various levels of elevated temperatures are shown in **Fig. 7.1**.



**Fig. 7.1** Cylinder fibre reinforced AAS concrete specimens before and after exposure to elevated temperatures.

**Table 7.1 plain concrete and Fibre reinforced Concrete mixing proportions.**

<b>Mixture</b>	<b>Binder (kg/m<sup>3</sup>)</b>	<b>Fine Agg. (kg/m<sup>3</sup>)</b>	<b>Coarse agg. (kg/m<sup>3</sup>)</b>	<b>Fibre (kg/m<sup>3</sup>)</b>	<b>NaOH (kg/m<sup>3</sup>)</b>	<b>Na<sub>2</sub>SiO<sub>3</sub> (kg/m<sup>3</sup>)</b>	<b>Additional Water (L/m<sup>3</sup>)</b>
<b>PC</b>	400	650	1137	0	22	167	72
<b>PFC 0.25%</b>	400	650	1137	2.275	22	167	72
<b>PFC 0.5%</b>	400	650	1137	4.55	22	167	72
<b>PFC 1%</b>	400	650	1137	9.1	22	167	72
<b>BFC 0.25 %</b>	400	650	1137	5.25	22	167	72
<b>BFC 0.5 %</b>	400	650	1137	10.5	22	167	72
<b>BFC 1 %</b>	400	650	1137	21	22	167	72
<b>SFC 0.25 %</b>	400	650	1137	19.625	22	167	72
<b>SFC 0.5 %</b>	400	650	1137	39.25	22	167	72
<b>SFC 1 %</b>	400	650	1137	78.5	22	167	72

Besides the AAS concrete binder behaviour at ambient temperature and the deterioration mechanism during exposure to elevated temperatures, the interaction mechanism of each fibre type with the concrete matrix at ambient temperature and elevated temperatures is different. The following sections will detail the behaviour of each fibre type. Then, a comparison will be performed to specify the research findings.

## 7.1 Polypropylene fibre

Concrete pores are usually filled or partially filled with water; hence, during exposure to different elevated temperatures, this pore water's pressure starts to increase (Akca and Zihnioğlu 2013, Felicetti and Monte 2013). The porosity of concrete will dominate the situation by allowing or preventing the migration of gaseous or vapour pressure to the surface (Kalifa, Chene et al. 2001). The selected mixture for Plain AAS concrete was marked with relatively low porosity (**Section 5.2.2.3**) due to high quality densified formed hydration products (Aitcin 2003). This results in extensive non-released pressure spreading micro-cracks development (Bangi and Horiguchi 2011). Moreover, the pore water pressure will logically increase as the temperature level increased. This is anticipated to scale the severity of the induced damages during exposure to elevated temperatures. Conversely, increasing the concrete porosity and capillary pores will allow concrete to release the higher pore water pressure developed during exposure to high temperatures.

Water absorption test results were utilized to understand the effect of pore water pressure development in plain and fibre-reinforced concrete. **Fig. 7.2** represents the water absorption of PC and PFC mixtures. At the initial stage ( $S_1$ ), water is being absorbed through the pre-existed micro cracks such as drying shrinkage microcracks as mentioned earlier (**5.2.2.3**). Fibre-reinforced mixtures exhibited lower water absorption rates due to limited micro-cracking due to fibre incorporation (Sanjuán and Moragues 1997). However, at the second stage ( $S_2$ ), although the total absorbed water by the PFC specimens regarding the elapsed time was lower than that absorbed by the PC, they showed a higher absorption rate (i.e. almost double). This will eventually facilitate the release of pressured water vapour during the early exposure to elevated temperatures (i.e. below the fibre's melting temperature).

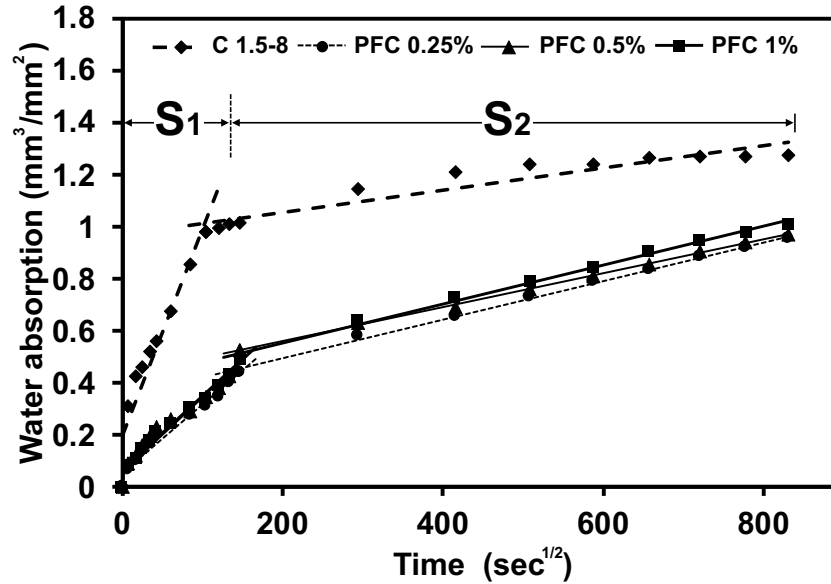


**Fig. 7.2 AAS plain and polypropylene fibre concrete water absorption.**

Moreover, when the temperature inside the concrete reaches the melting point of the polypropylene fibre (160 ~ 180 °C), the physical state of the fibre will start to change occupying less volume. This will eventually result in a formation of connected network of pores and canals easing the pressure transfer, leading to lower stresses induced inside the concrete. This comes in agreement with other researches which reported that the build-up pore pressure during exposure to elevated temperatures was lower for PFC compared to that of PC (Tanyildizi 2009). **Fig. 7.3** explains the passive beneficial effect of polypropylene fibre in AAS concrete during exposure to elevated temperatures. As the polypropylene fibre melting point is relatively low, the mitigation which occur through fibre melting starts to be active at early levels of induced pore pressure during exposure to elevated temperatures, and consequently, reduces the damages severity. However, at higher levels of temperatures, the binder deterioration due to the hydration products decomposition at different temperatures' levels will take the responsibility of the concrete degradation. Moreover, after exposure to these high temperature levels, the void traces that replaced the melted fiber will

result in a relatively weak structure, which will negatively affect the concrete mechanical properties.

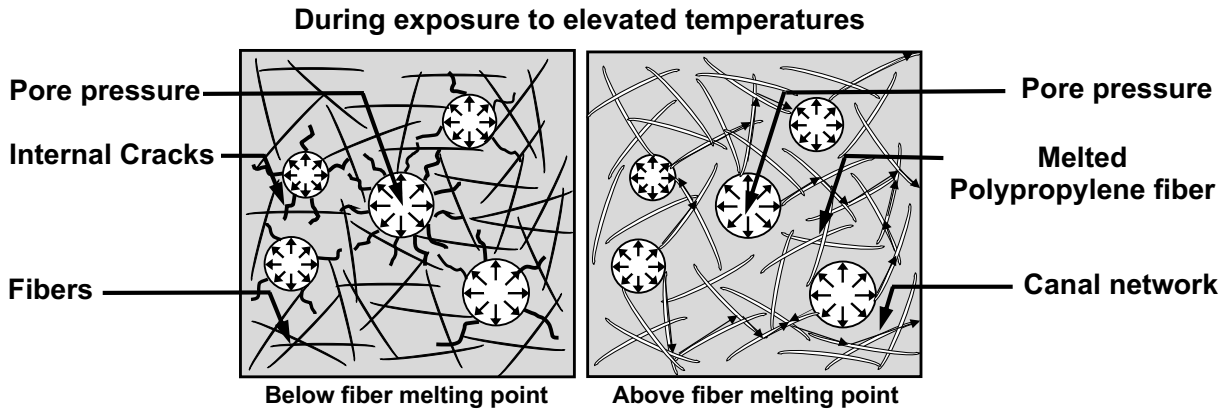


**Fig. 7.3 Polypropylene fibre mechanism during exposure to elevated temperatures.**

### 7.1.1 Compressive strength

**Fig. 7.4** summarizes the compressive strength at 7 and 28 days of all concrete mixtures at ambient temperature. At low fibre contents (i.e., 0.25% and 0.5%), it can be observed that polypropylene fibre has an insignificant positive effect on the AAS concrete compressive strength. Moreover, in a closer focus, it might negatively affect the strength by increasing the fibre content ( $> 0.5\%$ ). This agreed with previous studies about the polypropylene fibre inclusion in OPC or AAM concrete (jun Li, gang Niu et al. 2016, Yuan and Jia 2021). The concrete strength is greatly affected by the matrix homogeneity (Simões, Costa et al. 2017, Abaeian, Behbahani et al. 2018). In general, the fibre incorporation concept is a useful technique that tends to limit the crack propagation during the compression loading and, consequently, increase the failure stress level and the toughness during loading. However, at a certain level of fibre content, at which the binder cannot wrap all the existing fibre, the matrix homogeneity will be affected, resulting in weak spots containing non-held fibre.

On the other hand, the polypropylene fibre belongs to the micron diameter family, which allow the fibre density (i.e., the number of fibres per unit volume) to be extensively high at high fibre contents. As a result, the concrete matrix harmfully becomes a heterogeneous composite at high levels of fibre content. Moreover, the relatively low modulus of elasticity of polypropylene fibre resulted in a limited ability to hold the initiated cracks during loading, leading to a rapid failure. For instance, at fibre contents of 0.25% and 0.5%, the concrete compressive strength was increased by 9% and 7%, respectively. Increasing the fibre content up to 1% had decreased the compressive strength with 5% compared to plain AAS concrete.

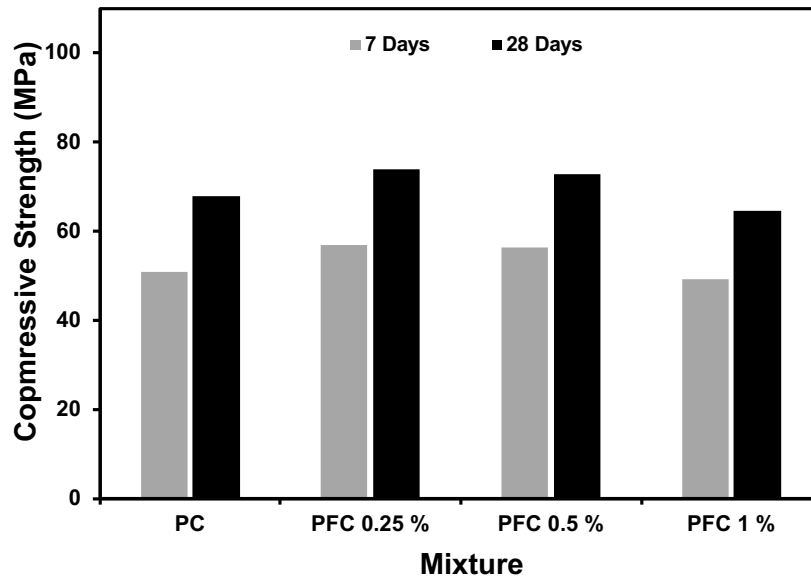


**Fig. 7.4 Compressive strength of plain and polypropylene fibre concrete at 7 and 28 days.**

**Fig. 7.5** illustrates the residual compressive strength results of AAS PC and PFC after exposure to three levels of temperatures (i.e., 200 °C, 400 °C, and 600 °C). PC was found to lose a moderate percentage of its original 28 days compressive strength after exposure to 200 °C. However, above this temperature level, the compressive strength was significantly decreasing by increasing the temperature level. For instance, PC lost 15%, 80%, and 92 % of its 28 days strength

after exposure to 200 °C, 400 °C, and 600 °C. These high strength losses at high elevated temperatures (i.e., 400 °C and 600 °C) are attributed to the severe microcracking induced by the pore water pressure during the exposure mentioned earlier. For PFC, at a low level of temperature exposure (i.e., 200 °C), the dominant factor controlling the strength losses was the binder as the case at ambient temperature. Increasing the fibre content at this level of exposure had slightly decreased the residual compressive strength. However, after exposure to higher levels of temperatures (i.e., 400 °C and 600 °C), polypropylene fibre inclusion was found to reduce the strength losses as it melts, leaving a connected network helping to release the build-up pore pressure as mentioned earlier. It was clear that lower fibre content was more efficient as it provides the pressure relief mechanism without extensively affecting the concrete matrix homogeneity. For example, AAS fibre concrete containing 0.25%, 0.5%, and 1% of polypropylene fibre by volume exhibited 53%, 40, and 33% residual compressive strength compared to 20% achieved by PC.

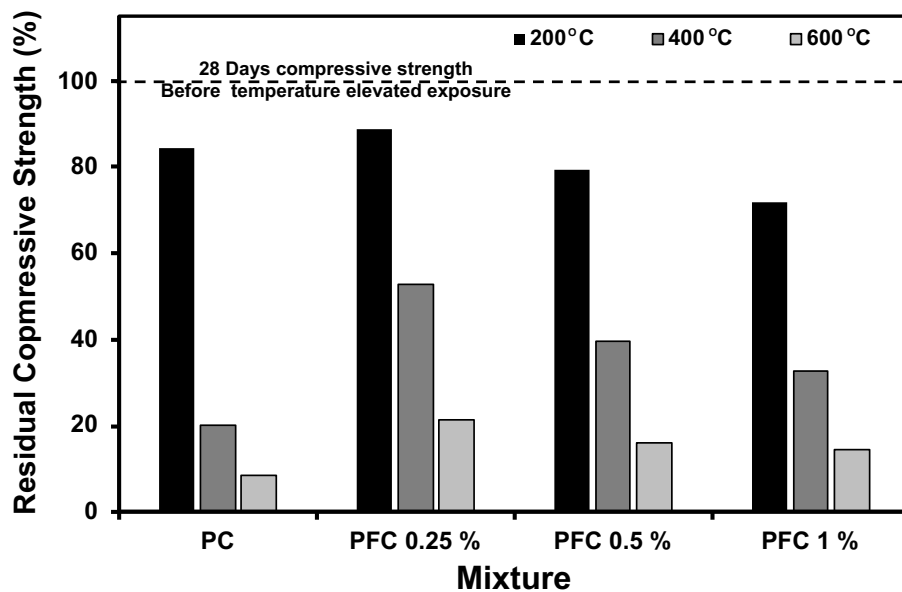
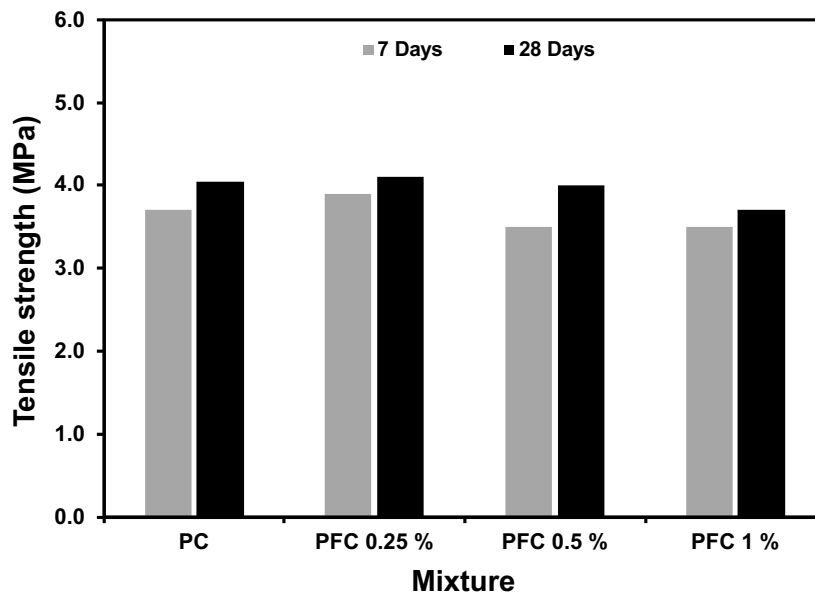


Fig. 7.5 Residual compressive strength after exposure to elevated temperatures.

### 7.1.2 Tensile strength

Concrete splitting tensile strength results at 7 and 28 days are represented in **Fig. 7.6**. Like the compressive strength, the splitting tensile strength of AAS concrete was found to slightly decreasing by increasing the fibre content. Although the fibre role as a crack bridging agent was obvious by visual inspection, the relatively low modulus of elasticity executed the fibre efficiency to enhance the tensile strength. Moreover, the concrete matrix heterogeneity became the dominant factor that downgraded the tensile strength.



**Fig. 7.6** Tensile strength of plain and fibre reinforced concrete at 7 and 28 days.

After exposure to various elevated temperatures, the deterioration in PFC tensile strength after exposure to high levels of elevated temperatures (i.e., 400 °C, and 600 °C) was less than that of PC as a result of melted fibre inside the concrete leading to easier pore pressure relief, resulting in lower pre-existed microcracking. For instance, PC lost 73% of its 28 days tensile strength after exposure to 400 °C, while PFC lost (~50%) for all fibre contents after exposure to the same temperature level (**Fig. 7.7**). This can be explained by the cross elimination between the two effects

of fibre during exposure to this level of elevated temperatures. Firstly, the higher contents would be reducing micro-cracking due to pore pressure due to higher density of left canals, and consequently, faster releasing of the build-up pore pressure as mentioned earlier. However, regarding the concrete matrix, high fibre content would negatively affect the residual strength as it will result in a concrete with high density of voids and a highly deteriorated binder, which will scale the strength degradation.

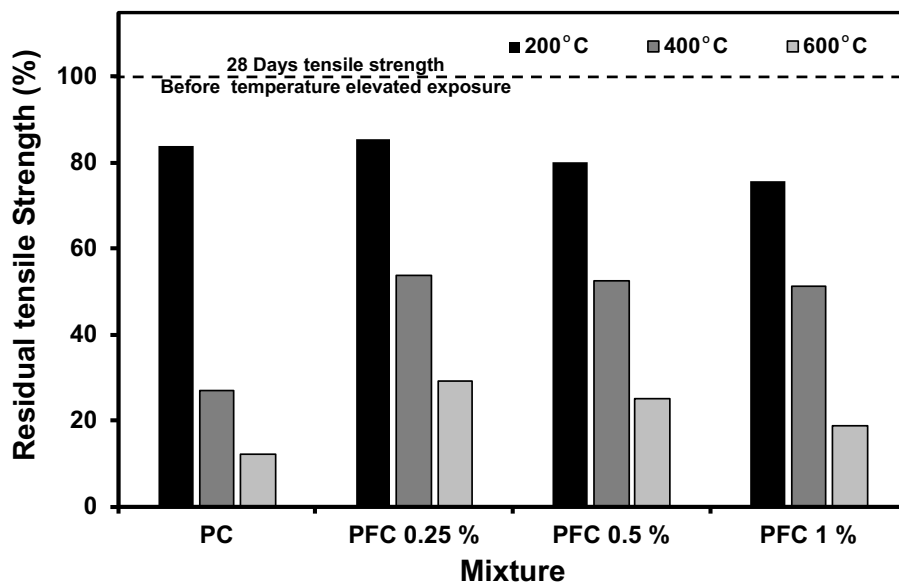


**Fig. 7.7 Residual splitting tensile strength after exposure to elevated temperatures.**

By visual inspection, polypropylene fibre was found to show up in the tested specimen's opened cracks without exposure to elevated temperatures. For specimens exposed to 200 °C, few fibre traces were observed, confirming that the fibre started the melting phase during exposure. While for tested specimens after exposure to 400 °C or more, no traces were detected for the polypropylene fibre as they were fully melted during the exposure. After exposure to 600 °C, specimen dramatically separated into many pieces (**Fig. 7.8 a, b, and c**).

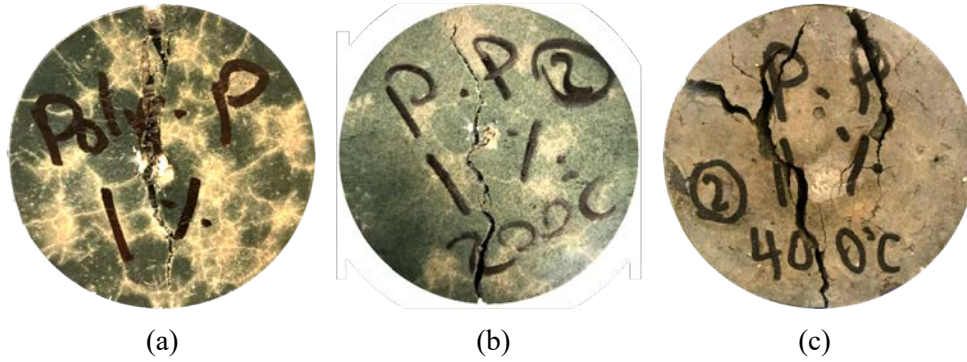


**Fig. 7.8 AAS polypropylene fibre of content 1% at failure before and after exposure to elevated temperatures.**

### 7.1.3 Modulus of elasticity

**Fig. 7.10** Represents the modulus of elasticity of plain AAS concrete along with polypropylene fibre concrete with different fibre contents at ambient temperature and after exposure to various elevated temperatures. At ambient temperature, the modulus of elasticity was matching the same trend as for compressive strength. For instance, the modulus of elasticity achieved at 0.25% fibre content was 41.3 GPa compared to 40.7 GPa, and 37.1 GPa achieved by 0.5% and 1% fibre content, respectively. This can be attributed to the higher strain levels achieved at higher fibre content due to the fibre clumping (Mehdipour, Vahdani et al. 2013, Emdadi, Mehdipour et al. 2015), leading to stress zoning, and consequently, faster crack development (**Fig. 7.9**).

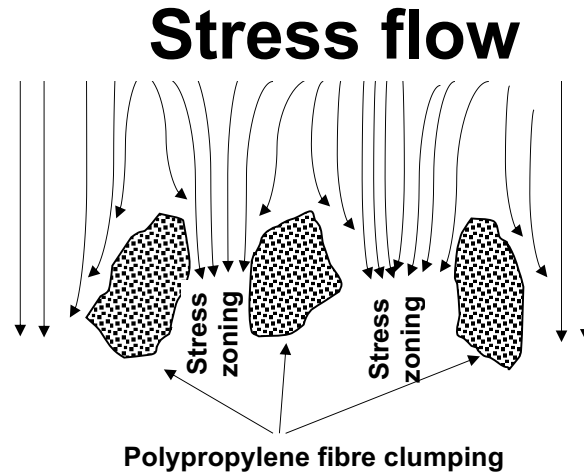


**Fig. 7.9 stress zoning due to polypropylene fiber clumping at high contents.**

After exposure to various elevated temperatures, the modulus of elasticity showed similar behaviour to ambient temperature. This could be attributed to the same benefits of this ratio in terms of homogeneity and less clumping. However, the binder deterioration would be interrupting the behaviour as the brittleness of the AAS concrete matrix increased by increasing the temperature level. This resulted in a lower strain capacity of the matrix, while the fibre's ability to compensate for this effect was terminated due to fibre partial or full melting at different temperatures' levels.

Moreover, the AAS concrete modulus of elasticity was similarly affected by the polypropylene fibre content. However, after exposure to 400 °C, fibre content of 0.25% was efficiently reserving a high modulus of elasticity. This can be attributed to the moderate effect of temperature on the binder hydration products. Also, the formation of a network after the fibre melting will keep the matrix consistent in terms of homogeneity. For instance, after exposure to 400 °C, fibre content of 0.25% could enhance the modulus of elasticity of PC exposed to the same temperature level by 68% compared to 44% and 19% enhancement achieved by fibre contents of 0.5% and 1%, respectively.

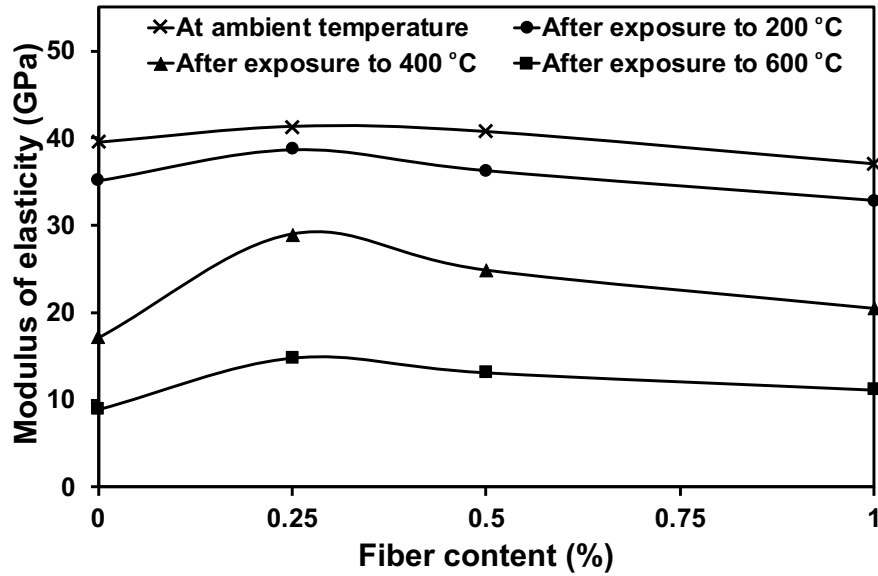


**Fig. 7.10** Modulus of elasticity of polypropylene fibre concrete before and after exposure to elevated temperatures.

#### 7.1.4 Impact energy absorption

**Fig. 7.11** illustrates the impact absorption capacity of AAS plain and fibre concrete at ambient temperature. Unlike the static mechanical properties, the impact absorption capacity at an early age (i.e. 7 days) was too low regarding the achieved absorption capacity at 28 days. Moreover, the impact energy absorption capacity did not show any difference by increasing the fibre content. This indicates that binder behaviour is the dominant agent at an early age. At this age, the high shrinkage micro-cracking rate (**Fig. 7.12**) and the not wholly densified hydration products can significantly affect the concrete matrix's response to impact load, while the high elongation factor of the polypropylene fibre will limit its capability to compensate for this response.

At 28 days, increasing the polypropylene fibre content increased the impact absorption capacity of AAS concrete. This can be attributed to the formed elastic buffer network, held with

well-densified hydration products, which secure the elastic strain of AAS concrete not to be exceeded during the impact event. Moreover, the brittleness of PFC was relatively decreased compared to that of PC due to the low elastic modulus of polypropylene fibre. This would help to avoid rapid crack development. AAS containing 0.25%, 0.5, and 1% of polypropylene fibre by volume exhibited 640%, 870%, and 1170% enhancement in the impact energy absorption comparing to that of PC.

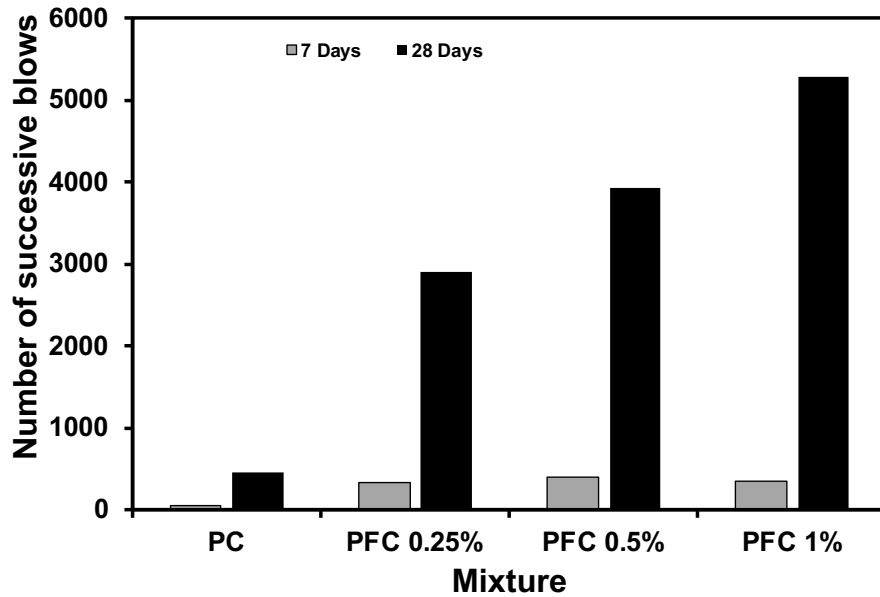


**Fig. 7.11 Impact energy absorption of plain and fibre AAS at ambient temperature.**

Besides the fibre role to limit the crack initiation and lower the concrete brittleness, polypropylene fibre was found to be efficient to control the drying shrinkage microcracking, leading to reduced pre-existed cracking during the impact loading (**Fig. 7.12**). For instance, 0.25%, 0.5%, and 1% fibre content could reduce the drying shrinkage micro-strain to 63%, 77%, and 88% of its value in plain concrete.

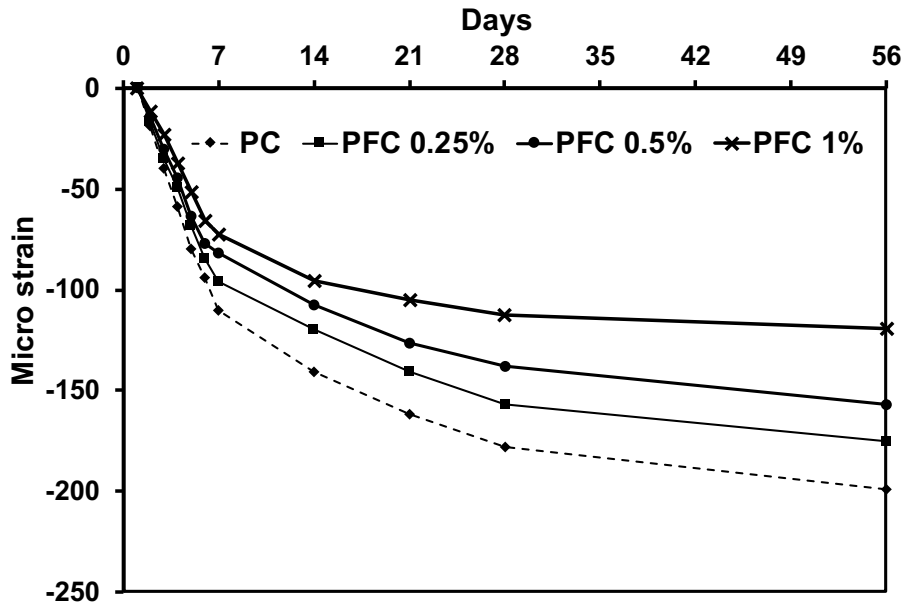


**Fig. 7.12 Drying shrinkage micro-strain of AAS concrete with different contents of fibre.**

To monitor the effect of polypropylene fibre incorporation on the impact toughness during failure, after the first visual crack development, the number of blows up to failure was counted (Table 7.2) The role of the binder to limit the crack propagation (as explained earlier in section 5.2.3.3) will be minor comparing to the fibre responsibility to limit this action. This number will then directly reflect the fibre's ability to hold the first crack, and the secondary formed cracks until achieving the failure criteria.

Polypropylene fibre was found to be beneficial to the AAS concrete impact toughness during failure. This can be expressed as the impact ductility index, which is the ratio between the total absorbed impact energy at the failure to the energy absorbed up to the first crack initiation due to the ductility phenomenon added by the fibre incorporation. Polypropylene fibre incorporation resulted in a higher ductility index during AAS concrete failure under impact loads (Fig. 7.13). However, it was observed that the effect of increasing the fibre content was marginal. This can

suggest that 0.25% is an optimum ratio in terms of impact toughness and the impact behaviour after exposure to elevated temperatures, as will be indicated later.

**Table 7.2 Number of successive blows at 1<sup>st</sup> crack and failure of PFC.**

Mixture	Number of blows at 1 <sup>st</sup> crack ( $N_C$ )				Number of blows at failure ( $N_F$ )			
	28 Days	200 °C	400 °C	600 °C	28 Days	200 °C	400 °C	600 °C
PC	442	16	7	4	450	18	8	5
PFC 0.25 %	2712	298	38	24	2898	316	46	25
PFC 0.5 %	3630	544	122	15	2244	1012	430	164
PFC 1 %	4858	924	22	6	5284	958	24	7

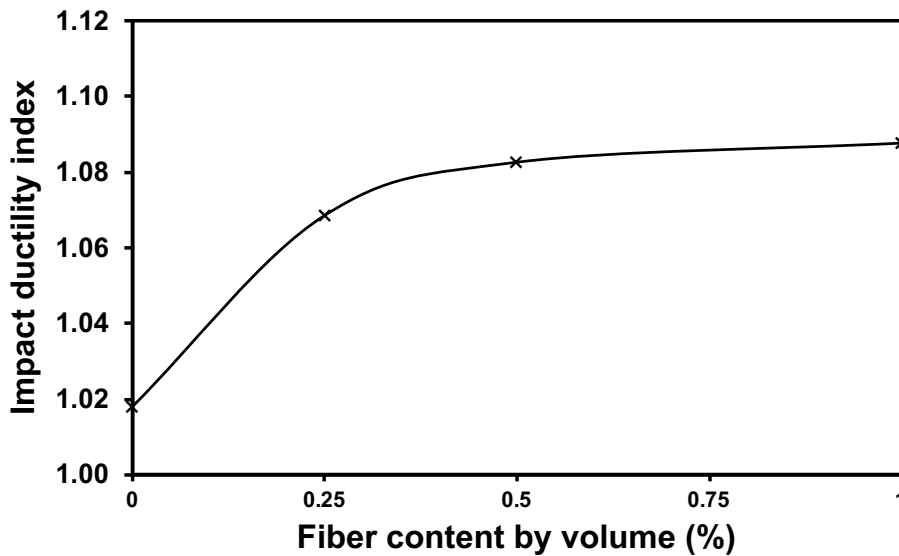


**Fig. 7.13 Impact ductility index of AAS with different fibre content.**

Exposure to elevated temperatures was found to significantly affect AAS plain and polypropylene fibre concrete's impact behaviour. However, PFC specimens showed fewer degradation levels. **Fig. 7.14** illustrates the impact absorption capacity exhibited by PC and PFC

after exposure to various elevated temperatures. At a low level of temperature exposure (i.e., 200 °C) the fibre starts to melt. However, full melting needs higher levels of temperature. Then, a portion of the fibre can survive this level of temperature. At the same temperature level, the binder did not suffer a significant degradation. As a result, the fibre could achieve a relative enhancement in the impact energy absorption. In a different behaviour compared to that of mechanical properties, especially at a low level of temperature exposure (i.e. 200 °C), increasing the fibre content was found to keep increasing the residual impact energy absorption capacity.

This can be attributed to the partially melted polypropylene fibre leading to lower build up pore pressure along with the ability of the nonmelted portion to limit the crack initiation and propagation during the impact event, which gives a higher opportunity to the high fibre content to keep acting as a strain limiting agent during impact.

At higher levels of exposure temperatures (i.e., 400 °C, and 600 °C), a low level of fibre content (i.e., 0.25%) was found to be more efficient to reduce the impact absorption capacity losses as a result of the synergetic effect of pore pressure relief during exposure to temperature leading to less-developed micro-cracks, and the lower developed internal voids left by the melted fibre compared to higher content levels. However, for higher fibre contents, the binder deterioration, which is still lower than that of PC as mentioned earlier, and the concrete matrix's high brittleness resulted in decreasing the residual impact absorption. This can explain the higher residual impact absorption capacity of PFC at all fibre content levels compared to PC at all temperature exposure levels.

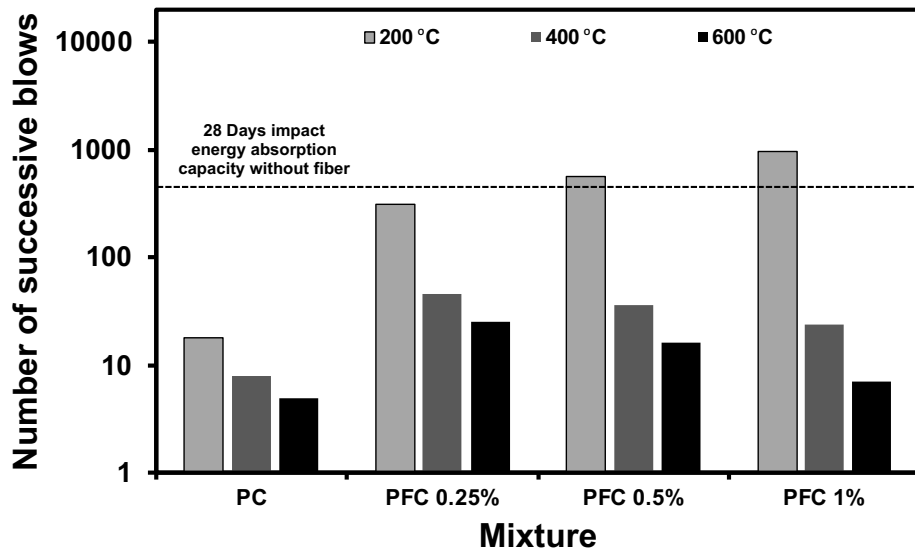


**Fig. 7.14 Residual impact absorption capacity of PFC after exposure to various elevated temperatures.**

On a different scale, although the impact toughness was significantly decreased by exposure to elevated temperatures, there is still an enhancement trend that can be observed at 0.25% fibre content after exposure to up to 200 °C. However, the total deterioration in the concrete matrix and the high levels of left voids after exposure to higher levels were enough to decrease the toughness at high fibre content levels. **Fig. 7.15** shows the number of blows after the first crack and up to failure. For instance, PFC of 0.25%, 0.5 %, and 1% fibre content achieved 18, 24, and 34 blows after the first crack compared to 2 blows achieved by the PC specimen exposed to 200 °C. At 400 °C, the impact toughness was decreasing for fibre contents above 0.25%. Ultimately, after exposure to 600 °C, the impact loads could easily cause the specimen's failure at a very low number of blows after the first crack development.

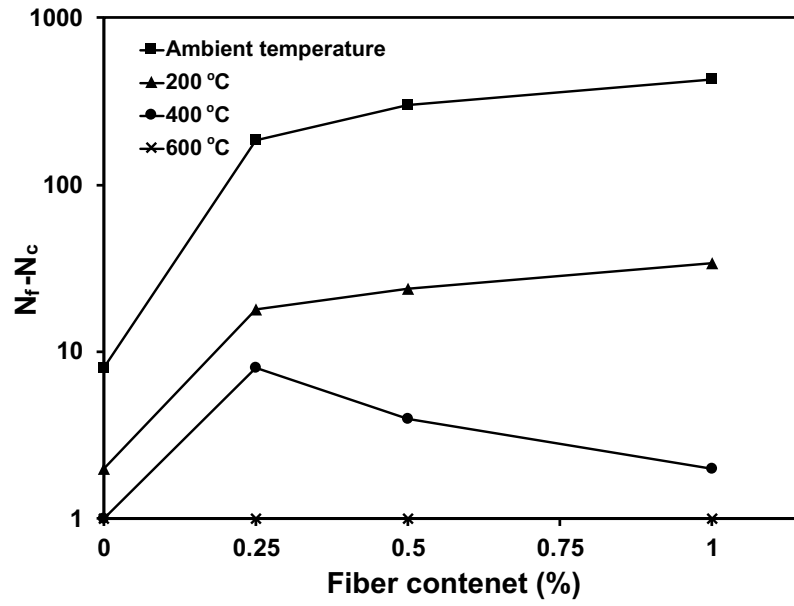
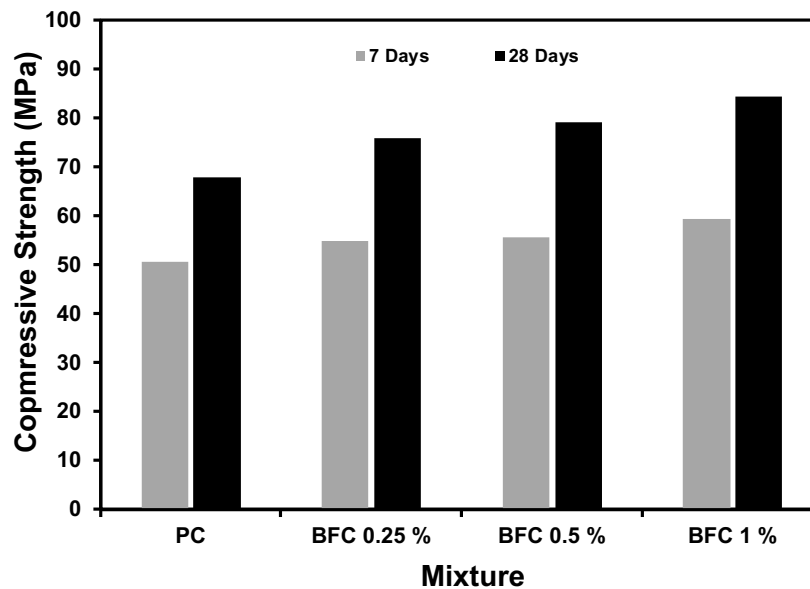


Fig. 7.15 Number of successive blows after the first visual crack for PFC.

## 7.2 Basalt fibre

### 7.2.1 Compressive strength

**Fig. 7.16** summarizes the compressive strength of PC along with BFC with different contents. It can be observed that at low basalt fibre content, the compressive strength slightly increased compared to that of PC. However, at high content (i.e. 1%), fibre-reinforced concrete's compressive strength was significantly increased. This agreed with other researches reporting that basalt fiber inclusion in concrete increased the compressive strength up to 1% content (Algin and Ozen 2018, Bheel 2021).



**Fig. 7.16 Concrete compressive strength at ambient temperature.**

This can be ascribed to the fibre density inside the concrete regarding the fibre relatively large dimensions. Fibre density is the number of fibres per unit volume. This number would affect the fibre distribution through the matrix (Mínguez, González et al. 2018), and consequently, its ability to limit the crack propagation during the compression loading while a good bond between

the fibre and the binder is secured due to its helix shape (**Fig. 7.17**). For instance, AAS concrete containing 0.25%, 0.5%, and 1% of basalt fibre by volume achieved 11%, 16%, and 24% higher compressive strength than that of PC.

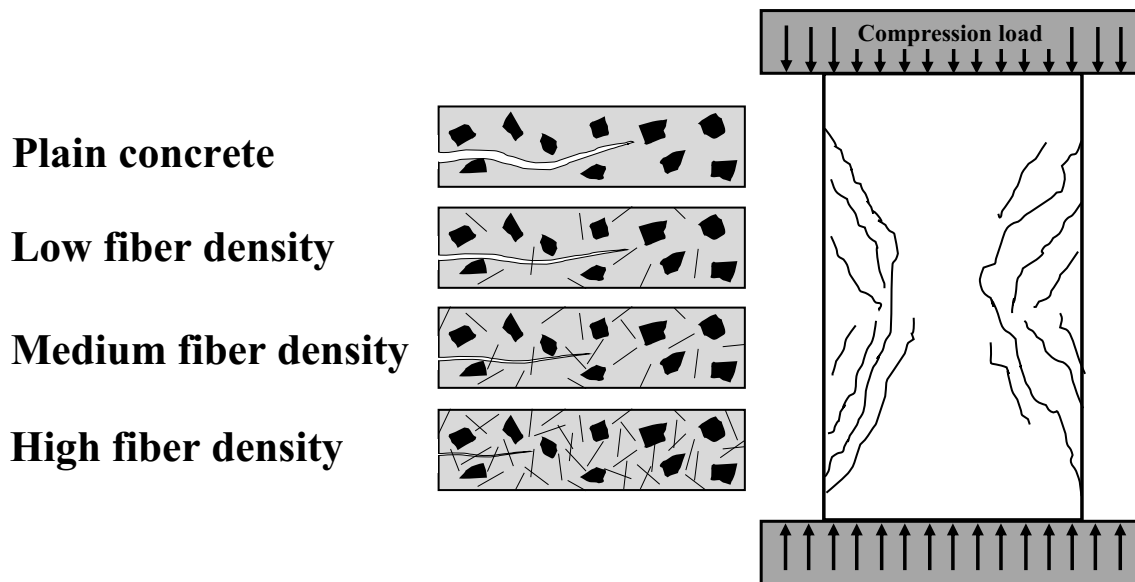


**Fig. 7.17** Effect of fiber density on the crack limiting ability.

After exposure to different levels of elevated temperatures, it was found that PC suffered a considerable degradation in terms of residual compressive strength, especially after exposure to high levels of elevated temperatures (i.e., > 400 °C). This can be attributed to the severe effect of high elevated temperatures on the binder microstructure due to hydration products decomposition, as mentioned earlier. For instance, PC lost 14%, 86%, and 91% of its 28 days compressive strength at ambient temperature after exposure to 200 °C, 400 °C, and 600 °C, respectively. However, for BFC, higher residual compressive strength was achieved at all levels of elevated temperature exposure. For example, BFC of 1% fiber content exhibited 41%, 300%, and 430% enhancement in concrete compressive strength of PC after exposure to 200 °C, 400 °C, and 600 °C (**Fig. 7.18**).

This can be attributed to the high stability of basalt fibre at elevated temperature, which reserved its ability to limit the crack propagation during the compression loading (Chidighikaobi 2019).

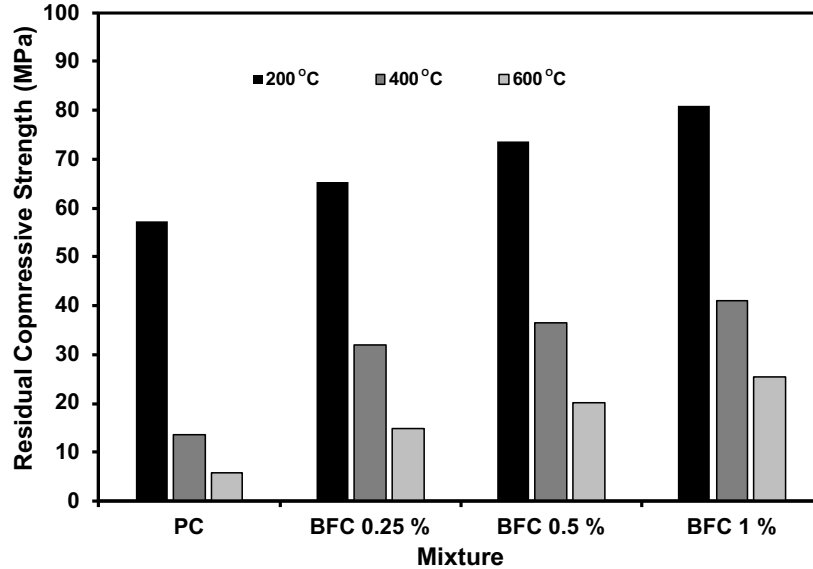


**Fig. 7.18 Residual compressive strength of AAS plain and basalt fibrous concrete after exposure to various elevated temperatures.**

### 7.2.2 Tensile strength

**Fig. 7.19** summarizes the effect of basalt fibre content on the splitting tensile strength. Basalt fibre incorporation contributed to enhancing the concrete tensile strength at ambient temperature. For instance, BFC containing 1% of basalt fibre achieved around 25% improvement in tensile strength than that of PC. The fibre mechanism to prevent crack development and propagation through concrete during the splitting tensile test depends on two factors. Firstly, the fibre tensile strength, and secondly, the bond strength with the concrete binder. Since basalt fibre tensile strength is extremely higher than that of the concrete, then the dominant factor affecting the splitting tensile strength will be the bond strength between the fibre and the binder. The helix shape

of basalt fibre develops inter shear, which leads to higher resistance to pull out forces(Hadi, Hasan et al. 2017). As a result, the tensile strength was increasing by increasing the fibre content.

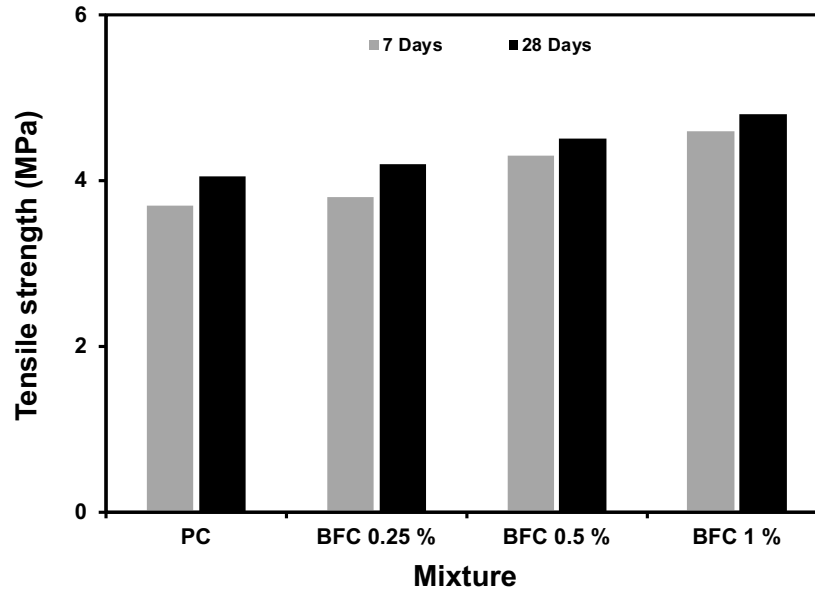


**Fig. 7.19 Concrete tensile strength at ambient temperature.**

The visual inspection of BFC specimens could also confirm this after failure under indirect tensile loading. The basalt fibre bridged the main formed crack during the test. While the load was increasing, a secondary crack was developed. This indicates that the pullout strength was relatively high, leading to a secondary crack formation before failure (**Fig. 7.20**).

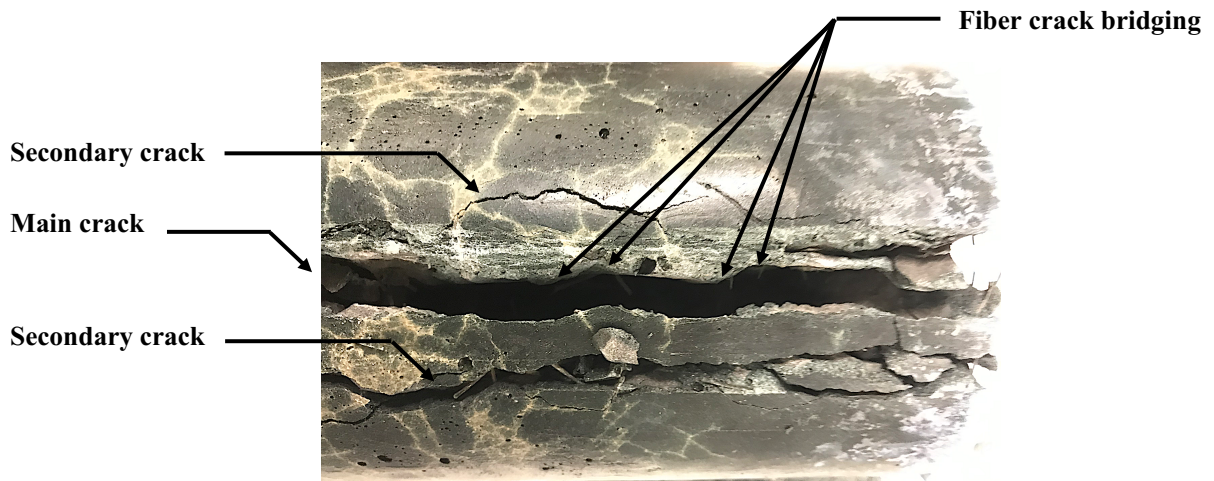


**Fig. 7.20 Main and secondary developed cracks during splitting tensile test.**

As a secondary factor, the pre-existing micro-cracks in concrete would be another agent affecting the tensile strength. Basalt fibre inclusion was also found to have a positive effect on the concrete drying shrinkage behaviour. The higher the fibre content, the lower the drying shrinkage micro-strain (**Fig. 7.21**), and consequently, the lower level of formed micro-cracks.

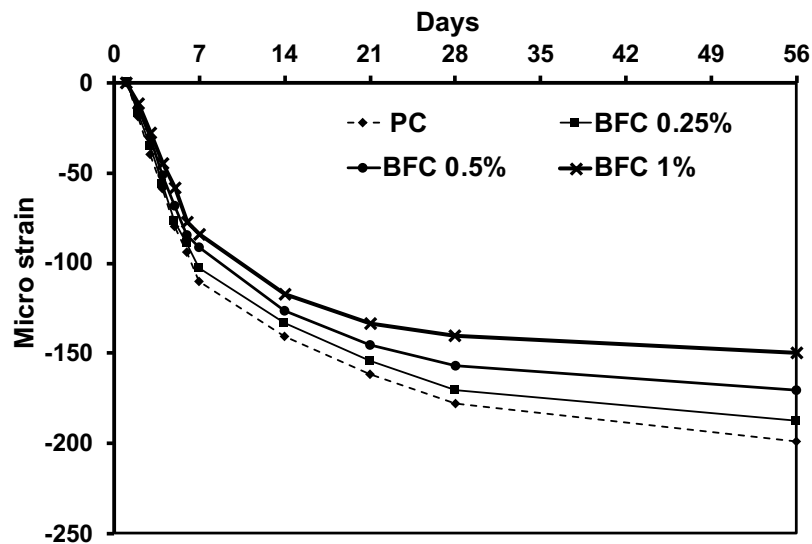


**Fig. 7.21 AAS plain and basalt fiber concrete drying shrinkage micro-strain.**

For AAS concrete specimens exposed to various elevated temperatures, basalt fibre significantly affected the tensile strength after exposure to elevated temperatures. For instance, the tensile strength of BFC containing 1% of basalt fibre after exposure to 200 °C was even higher than the original tensile strength (at ambient temperature) of PC. at higher temperature levels (i.e., 400 °C, and 600 °C), BFC was still achieving considerable enhancement in the residual tensile strength compared to that of PC after exposure to the same temperature levels (**Fig. 7.22**)

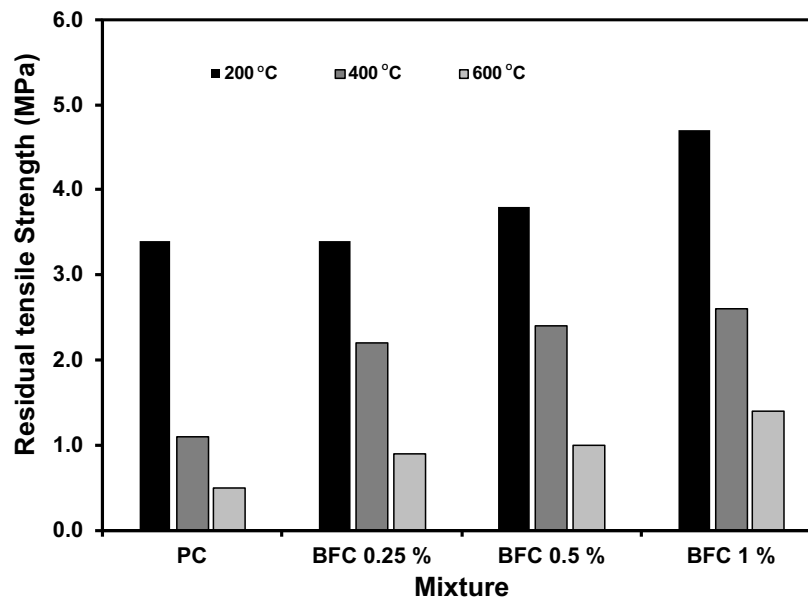
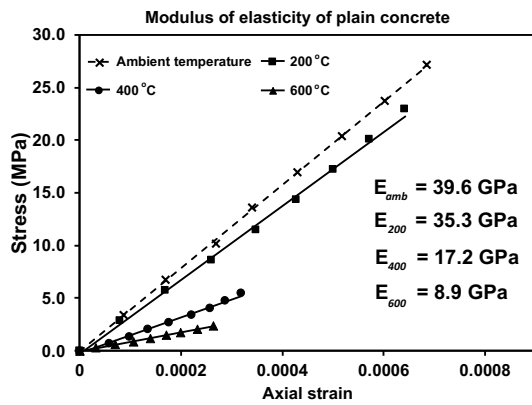


**Fig. 7.22 Residual tensile strength of AAS plain and basalt fibrous concrete after exposure to various elevated temperatures.**

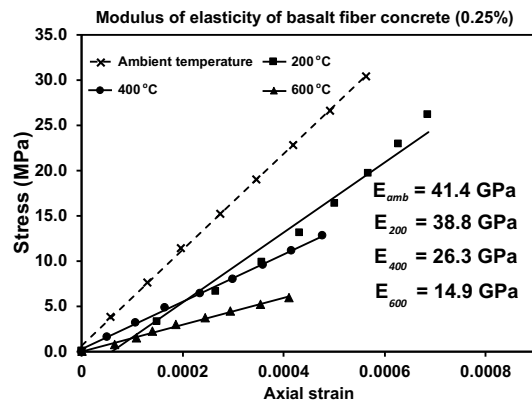
### 7.2.3 Modulus of elasticity

**Fig. 7.23 (a, b, c, and d)** plots the stress-strain behaviour of PC and BFC at ambient temperature and after exposure to the assigned elevated temperatures. It was found that all AAS concrete is suffering a reduction in its elastic modulus after exposure to various elevated

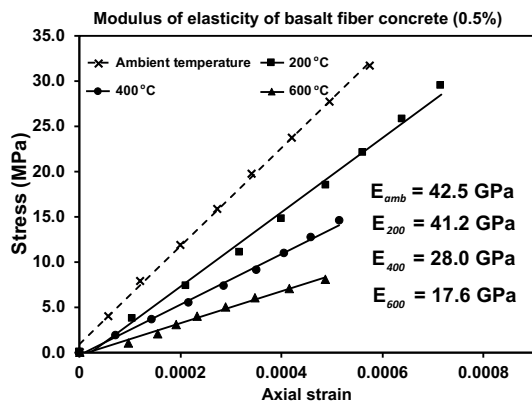
temperatures. However, this reduction was mitigated through basalt fibre incorporation. Increasing the fibre content was incredibly beneficial to increase the concrete modulus of elasticity after exposure to elevated temperatures. This could be attributed to the basalt fibre's capability to limit the strains induced by the applied load, delaying the crack propagation, which eventually led to higher fracture energy showed by specimens containing fibre at all levels of temperature exposure. For instance, 0.5% basalt fibre content could enhance the concrete elastic modulus at ambient temperature and after exposure to 200 °C, 400 °C, and 600 by 7%, 17%, 63%, and 97%. This indicates the significant effect of basalt fibre incorporation on the modulus of elasticity after exposure to elevated temperatures, especially at, high level of temperature, as the plain concrete would become very brittle and weak at this temperature, which leads to a significantly reduced modulus of elasticity.



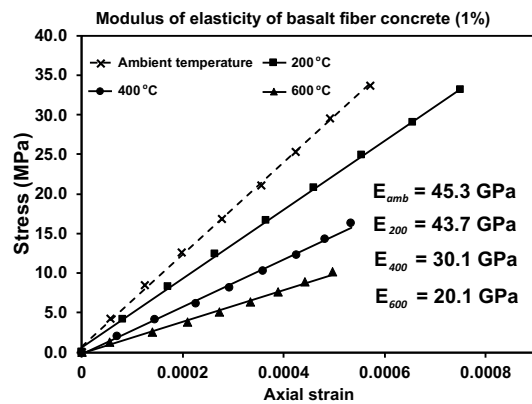
(a)



(b)



(c)



(d)

**Fig. 7.23 Modulus of elasticity of AAS plain and basalt fiber concrete before and after exposure to various elevated temperatures.**

#### 7.2.4 Impact energy absorption

At ambient temperature, basalt fibre was found to have a remarkable effect on the impact energy absorption capacity of AAS concrete regarding the fibre relatively low density. **Fig. 7.24** summarizes the number of successive blows, which led to AAS PC and BFC's failure during the impact test. Compared to the static mechanical properties enhancement through increasing the fiber content, the increase in the impact energy absorption was on a larger scale. This could be ascribed to the high dynamic increase factor (DIF) achieved through the basalt fibre incorporation in concrete. This factor can explain the difference in response of AAS concrete to dynamic load compared to the static load, especially in basalt fibre high content. For instance, AAS concrete with 1% achieved around 10 times the plain concrete's impact energy absorption.

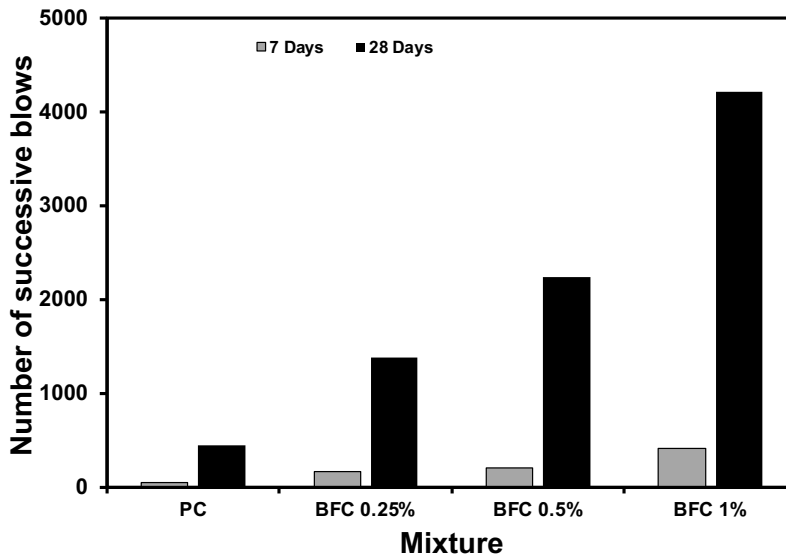


**Fig. 7.24 Impact energy absorption of plain and fibrous concrete at ambient temperature.**

During the static load application, the strain rate would be considered relatively low. This will control the developed cracks to avoid obstacles, such as fibre and coarse aggregate, as much as possible depending on the fibre density through the matrix. However, in the impact event, the strain rate would be relatively very high comparing to that of the static loads. This leads to an uncontrolled crack path, which increases the chance to be stopped by the fibre, especially in high fibre density(Fu, Niu et al. 2018) (**Fig. 7.25**).

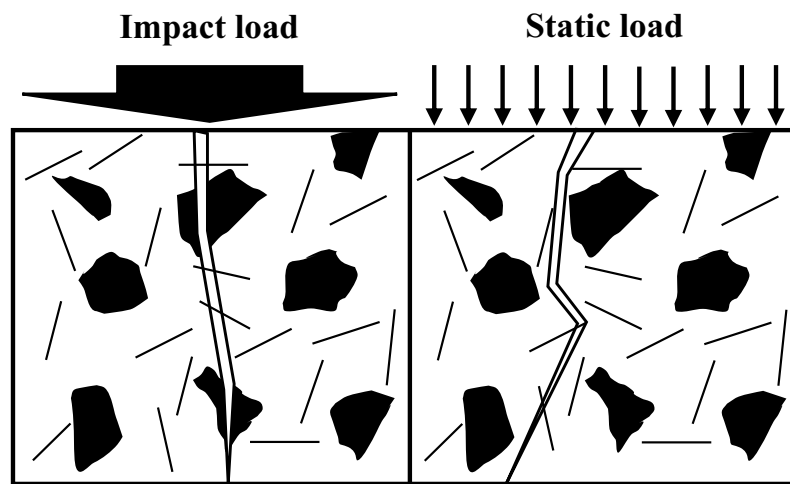


**Fig. 7.25 Different crack propagation behavior according to the load strain rate.**

Moreover, the visual inspection of the sample during failure confirmed the crack path doing through the coarse aggregate and the crossing the fibre, which confirm the significant role of fibre to act as a crack bridging agent after the developed 1<sup>st</sup> crack (**Fig. 7.26**). During this stage, the fibre's potential to limit the crack propagation leading to delay the specimen failure represents the fibrous concrete toughness. The more energy absorbed by the specimen after the first crack, the more toughness showed by the specimen before failure.

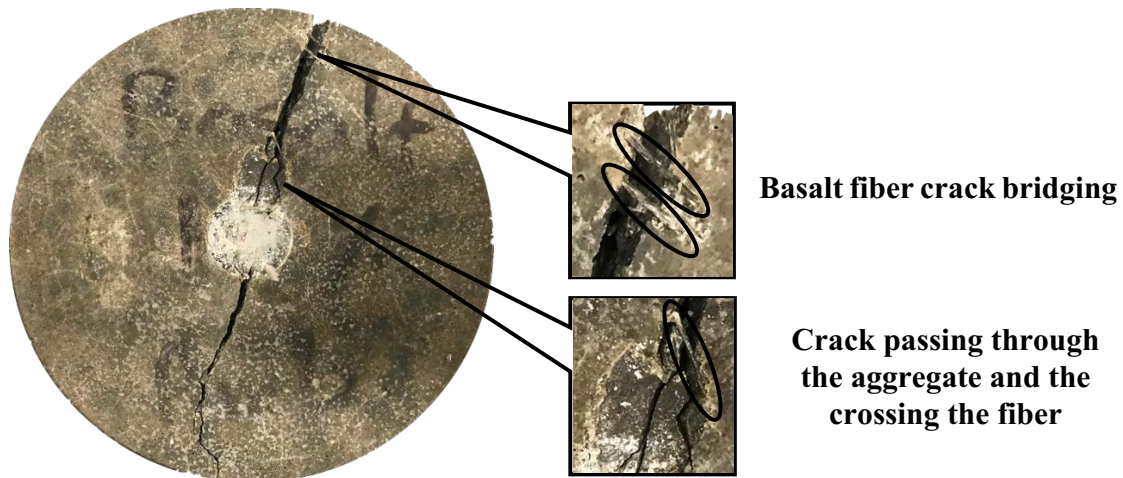


**Fig. 7.26** Fiber crack bridging after development of the 1st crack.

On the other hand, the steel ball's penetration during the impact test was monitored to assess the effect of basalt fibre incorporation on the AAS concrete penetration resistance. **Fig. 7.27** Illustrates the achieved penetration levels for different basalt fibre AAS concrete along with the plain concrete. It was obvious that increasing the basalt fibre content can reduce penetration during the impact event. While stresses are transferring from the high-stress zone to the outer zone (large strain zone), depending on the fibre density (number of fibres per unit volume), concrete can withstand the considerable strains at this zone (i.e., the high strain zone), leading to a lower penetration level. For instance, at 1000 blow, AAS concrete containing 0.25%, 0.5%, and 1% of basalt fibre achieved 2.8, 2.1, and 1.6 penetration below the specimen surface.

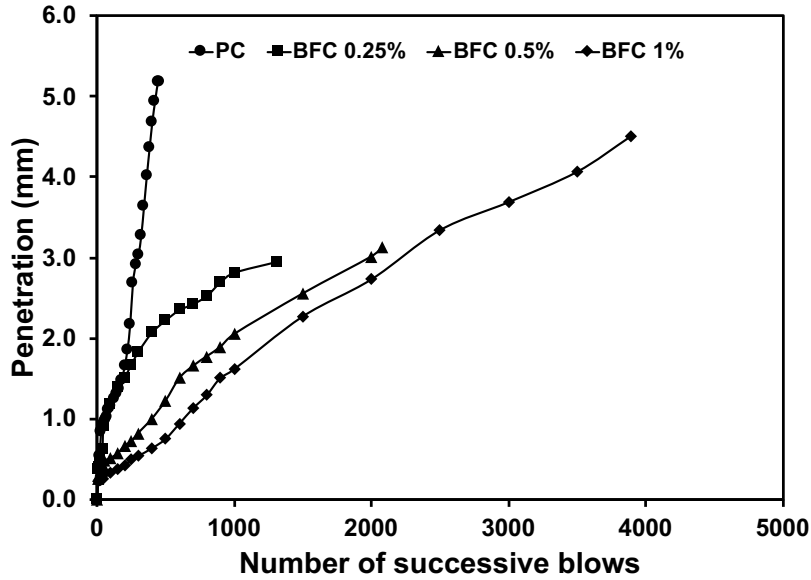


**Fig. 7.27** Penetration level achieved by the steel ball below the concrete specimen surface.

After exposure to various elevated temperatures, Specimens containing basalt fibre exhibited higher impact energy absorption at all exposure levels. Also, it was obvious by visual inspection that all basalt fibre specimens could show integrity during the failure. Comparing to the plain AAs concrete, which was producing many fragments during failure and separated into many parts as a result of high brittleness achieved as a side effect of the elevated temperature exposure, fibrous concrete specimens were failing into attached parts as a result of fibre existence holding the initiated cracks (**Fig. 7.28**).





**Fig. 7.28 Failure of AAS basalt fiber concrete with different fiber contents.**

**Fig. 7.29** summarizes the impact energy absorption capacity of PC and BFC. It can be observed that plain AAS concrete suffered a considerable loss in its capacity to absorb impact energy, as previously mentioned. However, for AAS BFC, increasing the fibre content resulted in a relatively high impact behaviour enhancement. For instance, after exposure to a high level of elevated temperature (i.e., 600°C), concrete containing 0.5% of basalt fibre could achieve the same level of impact energy absorption capacity as the plain concrete at ambient temperature. While at 1% content, basalt fibre concrete exhibited higher impact energy absorption after exposure to all levels of elevated temperature than that achieved by the plain concrete at ambient temperature.

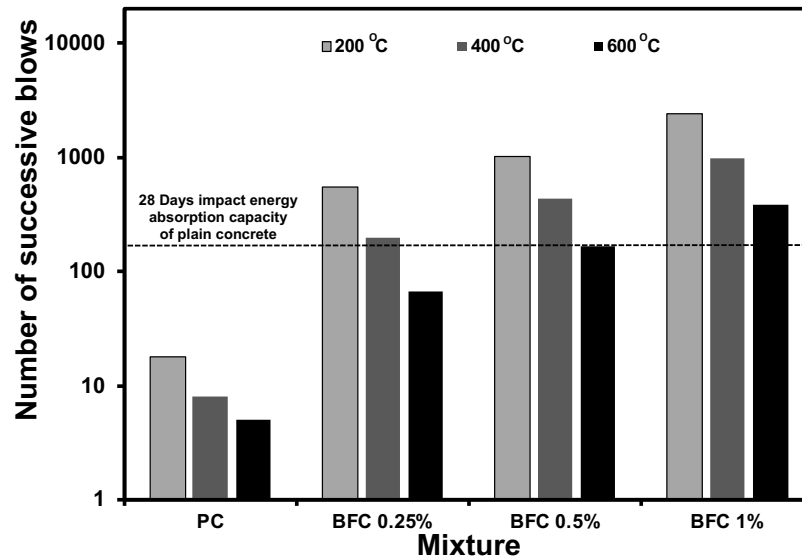


**Fig. 7.29 Residual impact absorption capacity of BFC after exposure to various elevated temperatures.**

Moreover, the toughness of plain and basalt fibre concrete was showing a notable contrast during their failure. Up to the first visible crack, the binder is responsible for stress resistance along with the fibre while the specimen is still behaving within its elastic range. However, after exceeding the elastic strain limit leading to cracks development, the fibre takes over this responsibility while a minor contribution from the binder through its bond with the fibre is still in charge. **Table 7.3** shows the number of blows at the first visible crack ( $N_C$ ) and failure ( $N_F$ ). Both numbers increased by increasing the fibre content at all levels of elevated temperature exposure. By observing the number of blows after the first crack ( $N_F - N_C$ ), fibre content dramatically affects the AAS concrete toughness before failure at ambient temperature and after exposure to elevated temperatures (Fig. 7.30). For instance, after exposure to 200 °C, 400 °C, and 600 °C, AAS specimens containing 1% needed 242, 116, and 38 blows after the first visible crack comparing to 2, 1, and 1 blow needed by the plain AAS concrete to achieve the failure criteria (**Fig. 7.30**).

**Table 7.3** Number of successive blows at 1<sup>st</sup> crack and failure of BFC.

Mixture	Number of blows at 1 <sup>st</sup> crack ( $N_C$ )				Number of blows at failure ( $N_F$ )			
	28 Days	200 °C	400 °C	600 °C	28 Days	200 °C	400 °C	600 °C
PC	442	16	7	4	450	18	8	5
BFC 0.25 %	1314	486	176	58	1386	542	198	66
BFC 0.5 %	2078	900	354	137	2244	1012	430	164
BFC 1 %	3894	2170	872	350	4212	2412	988	388

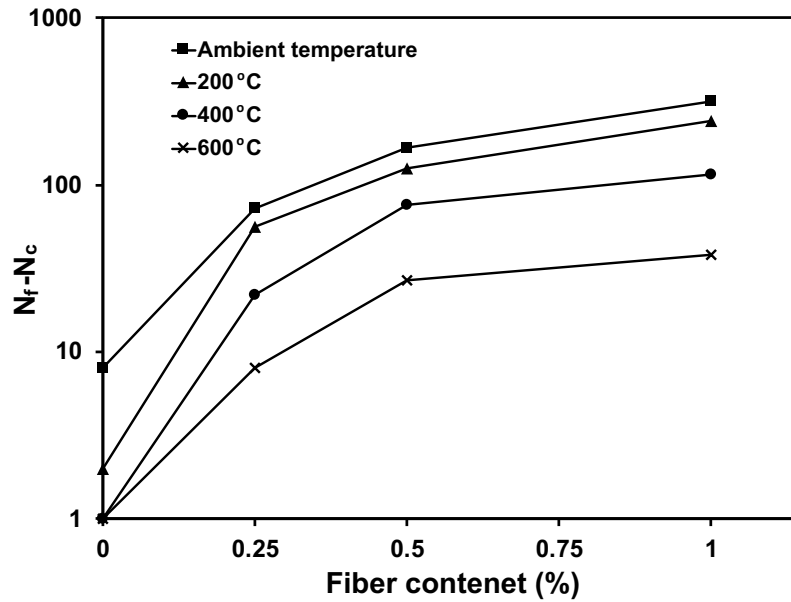


**Fig. 7.30** Number of successive blows after the first visual crack for BFC.

### 7.3 Steel fibre

#### 7.3.1 Compressive strength

The compressive strength test results for all mixtures at 7 and 28 days are represented in **Fig. 7.31**. Steel fibre was very beneficial to the AAS concrete in terms of strength regardless of its addition rate, which agreed with previous findings (Gao, Sun et al. 1997, Song and Hwang 2004, Shende, Pande et al. 2012, Gao, Yu et al. 2017). Steel fibre enhances the concrete behaviour during the compression loading at both the pre-cracking and post-cracking zone (Islam, Alengaram et al. 2017). Before cracking, steel fibre enhances the concrete ductility, increasing its load carrying capacity during the elastic zone (Gul, Bashir et al. 2014). This can be attributed to the excellent bond between the fibre and the surrounding AAS binder due to the densified high-quality hydration products formation. Hence, the load sufficiently transferred from the binder to the steel fibre leading to a successful unity between the binder and fibre to behave harmonically (Simões, Octávio et al. 2017). Moreover, after the elastic zone, steel fibre will increase the concrete capacity to absorb more straining energy through bridging cracks, leading to a higher peak compression load before failure and higher toughness (Holschemacher, Mueller et al. 2010).

Moreover, the higher the fibre content, the greater the achieved compressive strength. This reflected the optimized benefits of enhancing the pre- and post-cracking of concrete behaviour within the acceptable workability limits of fresh concrete. For instance, specimens incorporated by 0.25%, 0.5%, and 1% of steel fibre by volume, achieved 28%, 33%, and 44% increase in compressive strength than plain mixtures at 28 days.

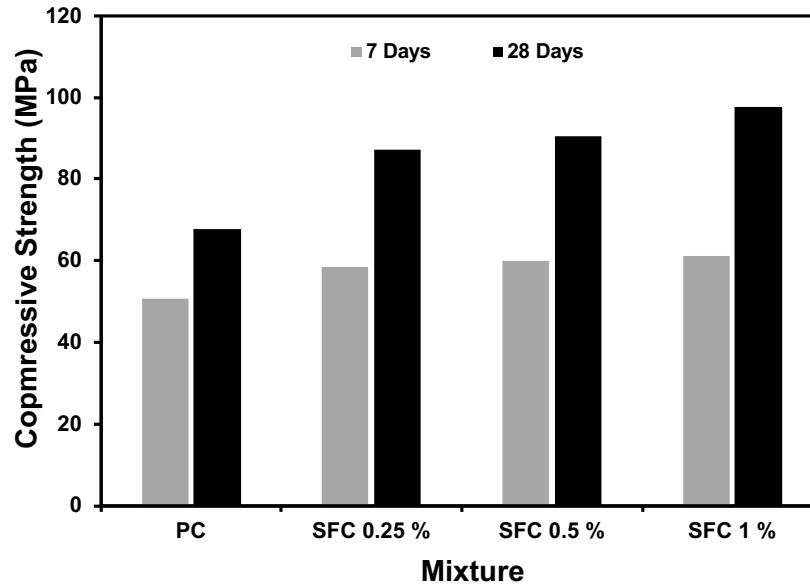


**Fig. 7.31 Compressive strength of plain and steel fibre concrete at ambient temperature.**

Ultrasonic pulse velocity measured for AAS concrete specimens at different ages confirmed the compressive strength results. Concrete density increased by increasing the steel fibre content in the concrete matrix (**Fig. 7.32**). As a result, the ultra-sonic pulse's measured velocities through the concrete matrix had increased as the steel fibre content increased. This can be attributed to the higher density of the steel resulting in a higher pulse velocity (i.e., ~1.2 the velocity through concrete). Consequently, a shorter time was measured, which supported the compressive strength test findings.

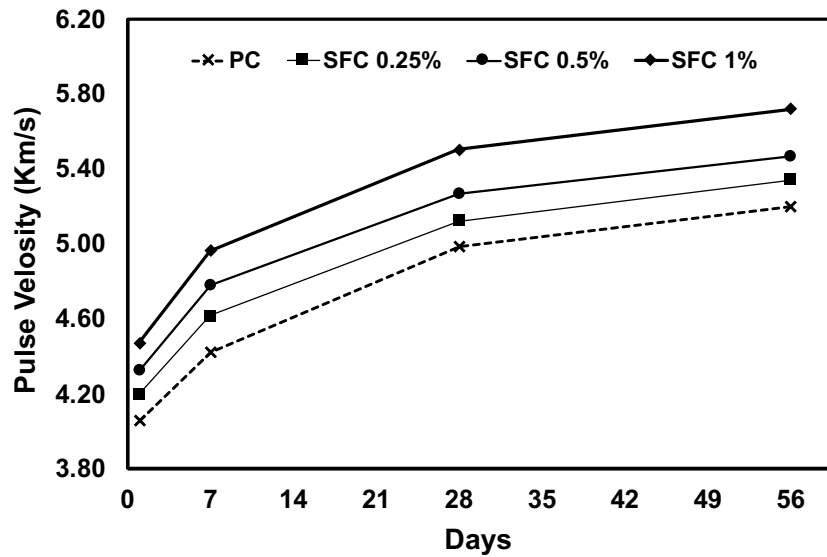
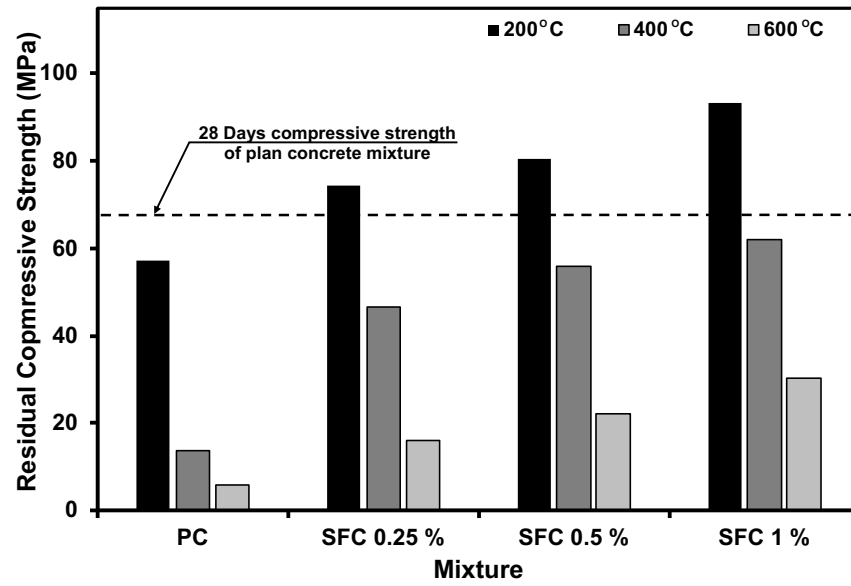


Fig. 7.32 Ultra-sonic pulse velocity of all concrete mixtures.

The residual strengths of SFC and PC after exposure to various temperature levels were compared to quantify the enhancement induced by steel fibre addition. Fig. 7.33 illustrates the residual strength of all mixtures after exposure to elevated temperatures. As expected, steel fibre incorporation significantly mitigates the binder deterioration due to exposure to elevated temperatures. The higher the steel fibre content, the greater the enhancement in the residual compressive strength. At 200 °C, all SFC specimens achieved higher strength than PC strength at ambient temperature. At higher exposure temperature, PC exhibited lower residual strength. SFC showed similar behaviour but with a lower reduction. For instance, the mixture with 1% steel fibre exhibited 30.4 MPa compressive strength compared to 6 MPa for PC specimen after exposure to 600 °C. This showed the steel fibre high potential to enhance the concrete compressive strength before and after exposure to elevated temperatures.



**Fig. 7.33 Residual compressive strength of all concrete mixtures after exposure to different levels of elevated temperatures.**

### 7.3.2 Tensile strength

**Fig. 7.34** summarizes all SFC mixtures' tensile strength results at 7 and 28 days at ambient temperatures. As expected, steel fibre addition had enhanced tensile strength significantly. Moreover, its effect on tensile strength was higher than that on the compressive strength. For instance, a specimen containing 1% steel fibre exhibited almost double the plain concrete mixture's strength, while the achieved increase in compressive strength was only 44%. This agreed with other researches reporting that steel fibre can significantly boost the concrete tensile strength by greater values than the compressive strength (Atiş and Karahan 2009). Fibre bridging action minimizes crack development and consequently delays the crack development and propagation during tensile loading. Hence, higher tensile strength is achieved. Visual inspection for tested specimens confirmed the crack bridging action as the specimen could hardly separate into two parts, as shown in **Fig. 7.35 (a, b, and c)**.

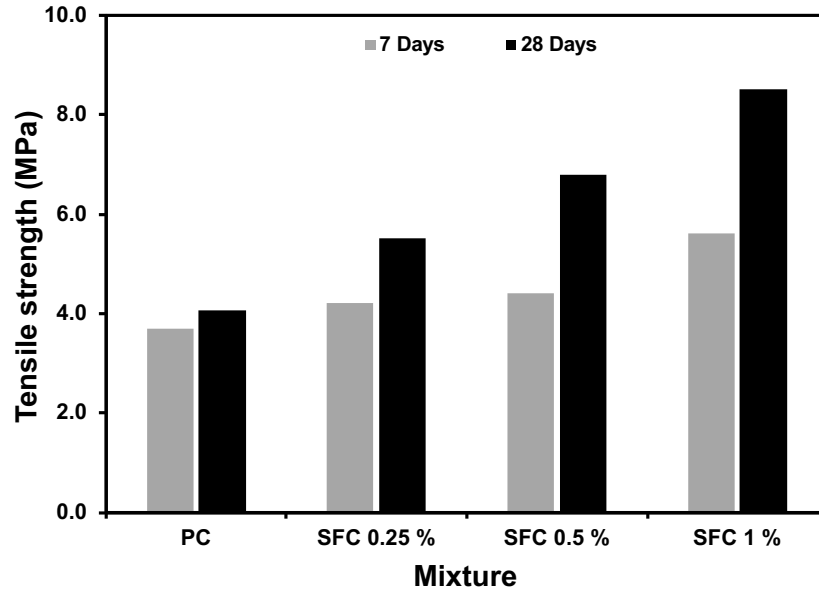


Fig. 7.34 Tensile strength of plain and steel fibre concrete at ambient temperature.

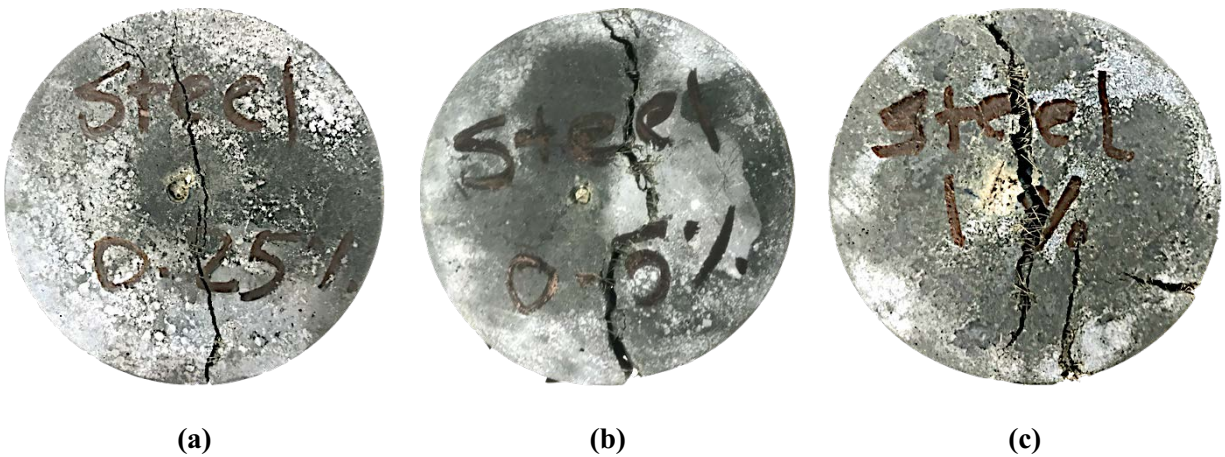


Fig. 7.35 Specimen's failure after tensile strength test at ambient temperature.

Moreover, the measured micro-strain drying shrinkage for SFC was lower compared to that of the PC. The higher the fibre content, the lower the micro-strain drying shrinkage (Fig. 7.36). During the drying shrinkage, the coarse aggregate's partial restraining action results in crack development in the surrounding binder. However, the steel fibre compensated for this action,

resulting in a lower cracking density, which reduced the pre-existed micro-cracks and increased the concrete tensile strength (Wu, Shi et al. 2019).

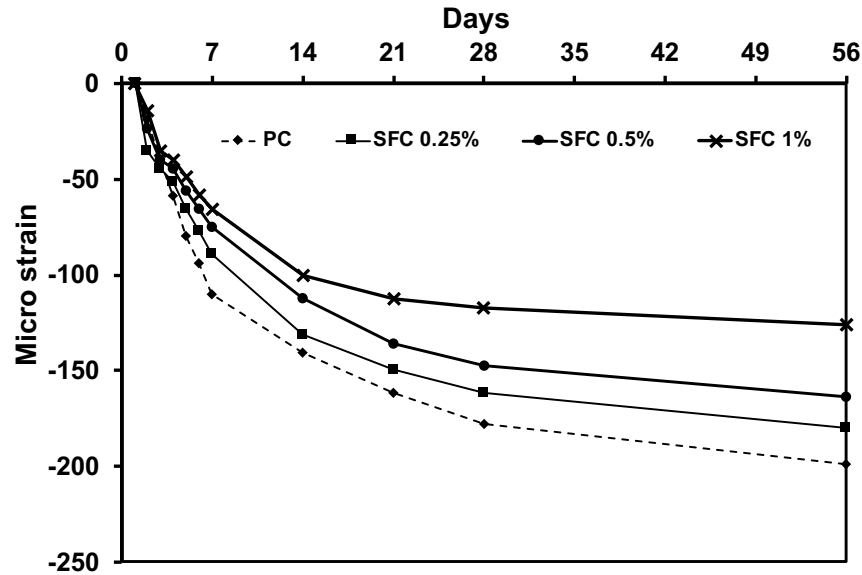
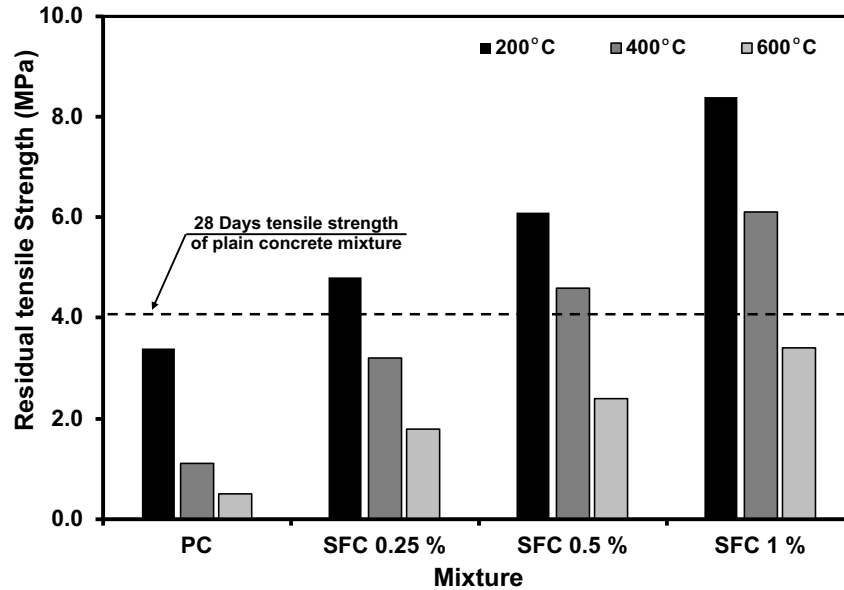


Fig. 7.36 Concrete drying shrinkage micro-strain.

After exposure to various elevated temperatures, PC tensile strength was found to suffer a considerable loss in tensile strength, as shown in Fig. 7.37. This can be attributed to the binder degradation during exposure to elevated temperature. Hence, concrete brittleness increased, leading to a noticeable reduction in the tensile strength. For instance, the tensile strength of PC after exposure to 200 °C, 400 °C and 600 °C was reduced by 16%, 73%, and 88% compared to that at ambient temperature. However, steel fibre kept the specimen integrity during the tensile test, greatly enhancing tensile strength compared to PC. Generally, high steel fibre content increased the residual tensile strength regardless of the elevated temperatures level. For instance, after exposure to 600 °C, specimens with 1% of steel fibre showed around 6% only reduction in the tensile strength than the PC at ambient temperature. Moreover, specimens with 1% of steel fibre

tensile strength after exposure to the highest temperature (i.e., 600 °C) was better than that of PC exposed to the lowest elevated temperature (i.e., 200 °C).



**Fig. 7.37 Concrete residual tensile strength after exposure to different levels of elevated temperatures.**

### 7.3.3 Modulus of elasticity and modulus of resilience

The elastic modulus of fibre-reinforced concrete relies on the modulus of elasticity and tensile strength for both the matrix and used fibre along with the bond between them. At ambient temperature, increasing the steel fibre content increased the concrete modulus of elasticity. The steel fibre relatively high modulus of elasticity and a good bond with the surrounding matrix limit the strain development during loadings. For instance, as steel fibre content increased from 0.25% to 1%, the modulus of elasticity increased in the range of 13% up to 23% compared to plain concrete. On the other hand, at elevated temperatures, the binder deterioration dominated the concrete's elastic modulus changes. This can be attributed to the limited steel fibre ability to reduce the strain due to the binder deterioration, which significantly affected the matrix-fibre bond.

Moreover, the increase in the binder brittleness due to elevated temperature exposure will lower the load capacity within the concrete elastic behaviour zone. Consequently, earlier cracks will develop and propagate due to the insufficient restraining induced by the used fibre through bridging these cracks.

Plain concrete mixtures suffered from notable degradations in modulus of elasticity at 400 °C and 600 °C by losing about 57% and 78% of their original value at ambient temperature, respectively. However, steel fibre addition resulted in a higher elastic modulus than PC and showed a uniform reduction at various temperature levels (**Fig. 7.38**). For instance, 1% steel fibre concrete achieved an elastic modulus of 47.17 GPa, 37.8 GPa, and 22.1 GPa, comparing to 35.2 MPa, 17.2 MPa, and 8.9 MPa achieved by PC after exposure to 200 °C, 400 °C, and 600 °C, respectively.

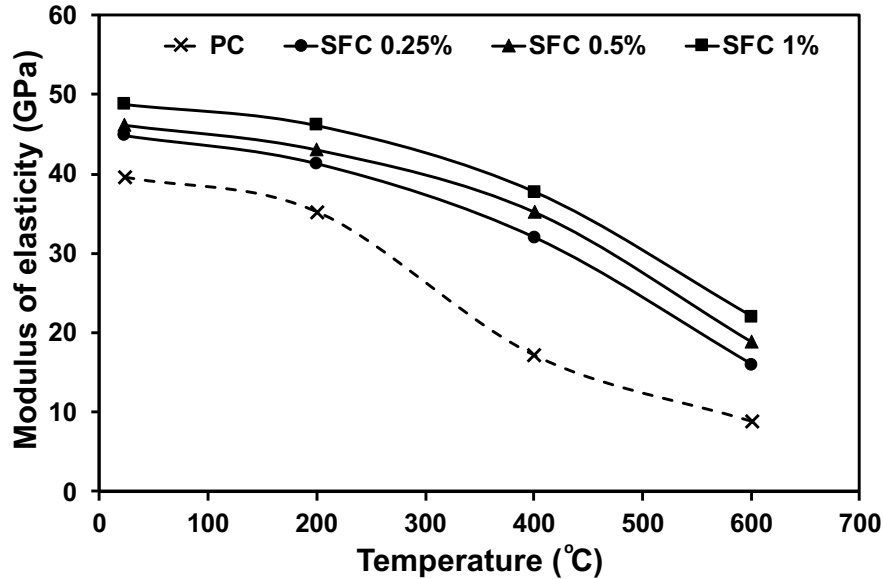


**Fig. 7.38 Concrete modulus of elasticity at ambient temperature and after exposure to various elevated temperatures.**

On the other hand, the dynamic modulus of elasticity was calculated as a function of the ultrasonic pulse velocity measured for various mixtures. The dynamic elastic modulus ( $E_d$ ) increased by increasing the steel fibre content in the mixture. For instance,  $E_d$  for SFC mixtures containing 0.25% and 1% of steel fibre was 65.8 GPa, and 77.3 GPa comparing to 62.1 GPa for PC, respectively. The modulus of resilience, which represents the concrete capability to retrieve the induced strain during loading within the elastic zone, was enhanced as the fibre content increased. This mainly depends on the strain energy absorption capacity of concrete before cracking, limiting the retrieved strain after unloading. **Fig. 7.39** represents the resilience modulus achieved by PC, and SFC with different steel contents at ambient temperature and after exposure to various elevated temperatures. Steel fibre addition had significantly enhanced concrete modulus of resilience at ambient temperature. However, after exposure to elevated temperatures, all mixtures' resilience modulus exhibited a reduction trend as the exposure temperature increased. Fibre-reinforced concrete mixtures had reserved a relatively high concrete resilience, especially at high fibre content (i.e., 1%). For instance, the resilience modulus of concrete mixtures containing 1% steel fibre was 14.9 kJ/m<sup>3</sup>, 8.2 kJ/m<sup>3</sup> and 3.3 kJ/m<sup>3</sup> compared to 7.3 kJ/m<sup>3</sup>, 0.8 kJ/m<sup>3</sup>, and 0.3 kJ/m<sup>3</sup> for PC specimens after exposure to 200 °C, 400 °C, and 600 °C, respectively. This indicates the great steel fibre ability to enhance the concrete resilience modulus after exposure to elevated temperatures.

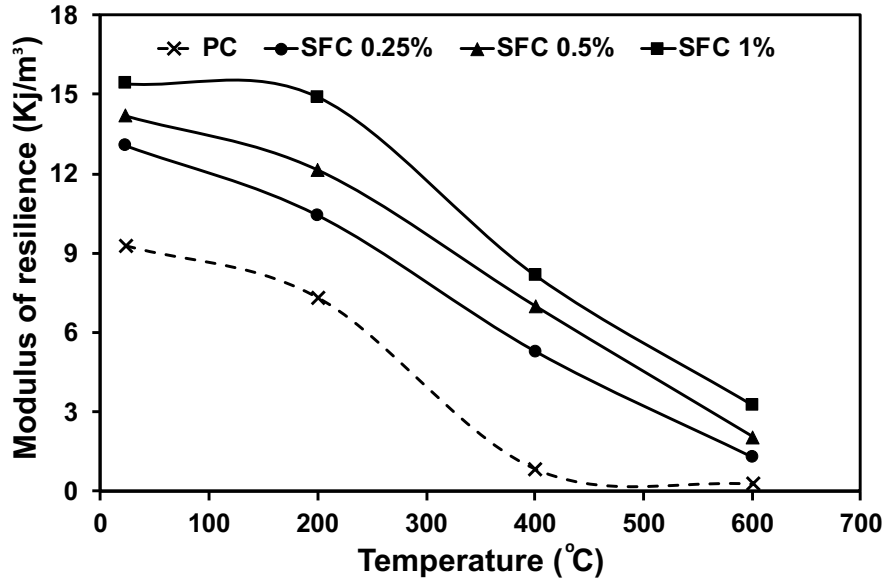


**Fig. 7.39** Concrete modulus of resilience at ambient temperature and after exposure to various elevated temperatures.

#### 7.3.4 Impact energy absorption

**Fig. 7.40** illustrates the number of successive blows received by concrete mixtures before failure. The number of successive blows will reflect the impact energy absorption capacity for each mixture. The impact energy absorption capacity will be equivalent to the total accumulative impact energy delivered by these blows. Generally, SFC mixtures exhibited higher impact energy absorption than the PC mixtures at ambient temperature. PC mixtures absorb impact energy until the first crack development. However, after the first crack, it will not take a high amount of impact energy to cause failure. This happens due to the high brittleness of plain concrete and the non-controlled strain while accumulative energy is absorbed. Conversely, in SFC, the fibre existence controlled the specimen strain during the impact event and consequently limited the crack initiation up to a high level of absorbed impact energy (Islam, Alengaram et al. 2017). Moreover, the higher

resilience achieved through fibre incorporation, as previously mentioned, resulted in increasing the specimen internal stresses capacity, above which cracks would be initiated.

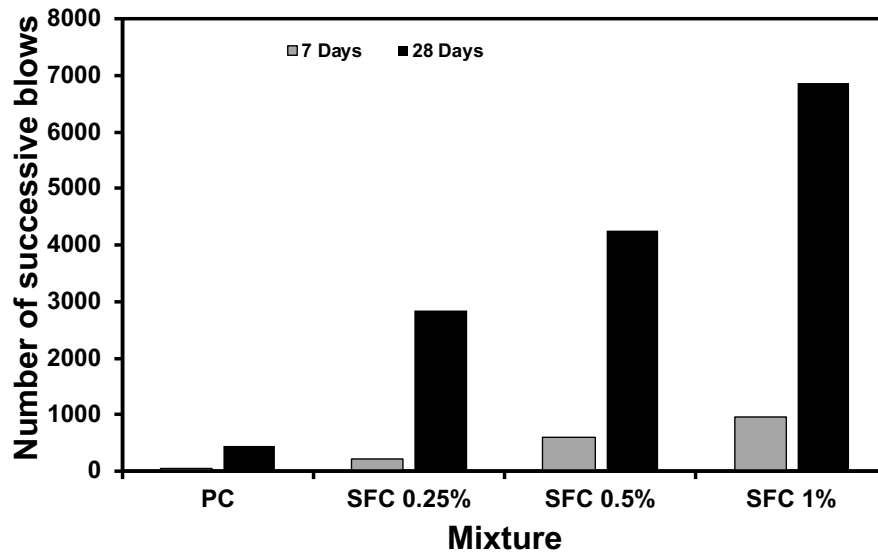


**Fig. 7.40 Concrete Impact energy absorption capacity at ambient temperature.**

Impact loads induce a higher strain rate compared to static loading. Hence, concrete will possess higher resistance impact loads. This can be quantified by measuring the dynamic increase factor (DIF) achieved by various concrete mixtures. The DIF is the magnification in the specimen's stress capacity in dynamic loading relative to the static loading. It was observed that the higher the steel fibre content, the higher the achieved DIF (**Fig. 7.41**). This could explain the considerable enhancement in the impact resistance, which is a dynamic load relative to static mechanical properties. For instance, plain concrete specimen initially cracked after 442 blows, comparing to 2366, 3678, and 6024 successive blows during the impact test for concrete mixtures incorporating 0.25%, 0.5% and 1% of steel fibre at age 28 days.

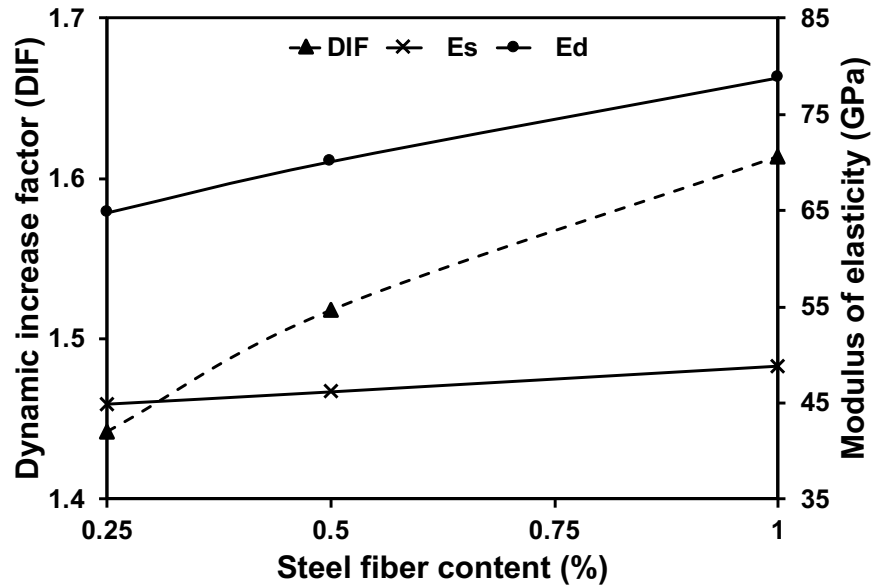
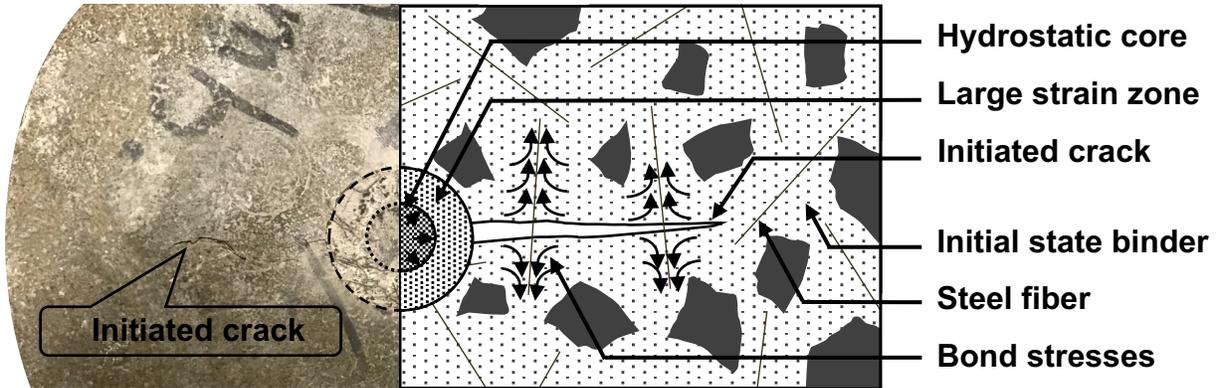


Fig. 7.41 Steel fibre concrete dynamic increase factor (DIF).

During the impact test and directly beneath the steel ball, a damage mechanism starts to occur (mentioned earlier in **section 4.2.6**). Due to considerable compression applied by the steel ball on the contact surface with the specimen, a hydrostatic core starts to form. This core starts to collapse, transferring the pressure to the surrounding zone inducing large strains. Once the strains in this zone exceed the elastic limit of concrete, cracks develop and propagate to the outer zone (initial state zone). After cracking, the fibre itself and generated matrix-fibre bond will dominate the resistance behaviour for impact loads (**Fig. 7.42**). As mentioned earlier, increasing the steel fibre content was beneficial through the bridging action and limiting cracks propagation. This could greatly increase the concrete toughness after the first crack development, which increases the number of successive blows until failure (i.e., the ultimate impact absorption capacity). For instance, mixtures incorporating 0.25%, 0.5%, and 1% steel fibre needed 474, 566, and 836 blows after the first visible crack to achieve the failure criteria crack compared to only 8 blows for plain concrete mixture.



**Fig. 7.42 Steel fibre mechanism to limit the initiated crack propagation.**

The number of secondary initiated cracks developed after the first visual crack and up to the specimen failure confirms the different mixtures toughness during the impact test. Secondary cracks are initiated due to the steel fibre contribution to contain and limit the first initiated crack (Islam, Alengaram et al. 2017). For instance, the plain concrete specimen had only one crack upon failure. However, by increasing the steel fibre content, the number of secondary cracks had increased (**Fig. 7.43**). This confirms that steel fibre could greatly enhance the AAS concrete capacity to absorb impact energy before failure.

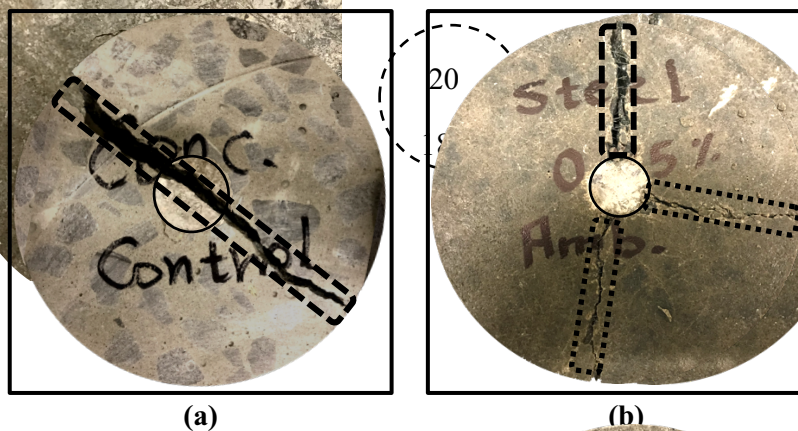


**Fig. 7.43 First crack and secondary developed cracks at the failure of AAS concrete.**

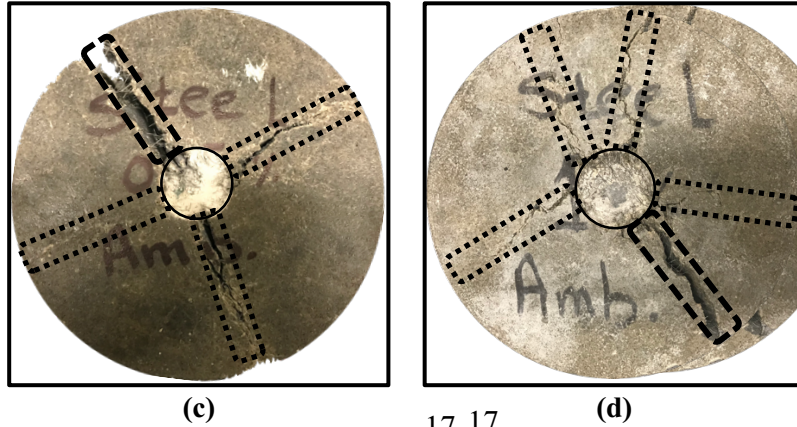


**Fig. 7.43 Cont'd First crack and secondary developed cracks at the failure of AAS concrete.**

The steel ball's penetration level under the specimen's surface was monitored during the impact test. The achieved penetration level had reduced as the steel fibre content increased. This can be attributed to the steel fibre existence, especially in the large strain zone. In this zone, steel fibres limit the strains to maintain the AAS concrete's elastic limit up to higher stress levels than plain concrete. As a result, the crushing zone (i.e., the hydrostatic core previously) will be limited, leading to a lower steel ball penetration level. For instance, a penetration level of 3 mm was achieved after 2140, 2460, and 2940 successive blows for mixtures incorporating 0.25%, 0.50% and 1% steel fibre compared to 300 blows for the plain concrete specimen (**Fig. 7.44**). This shows the significant effect of the steel fibre addition in resisting ball penetration during the impact event.

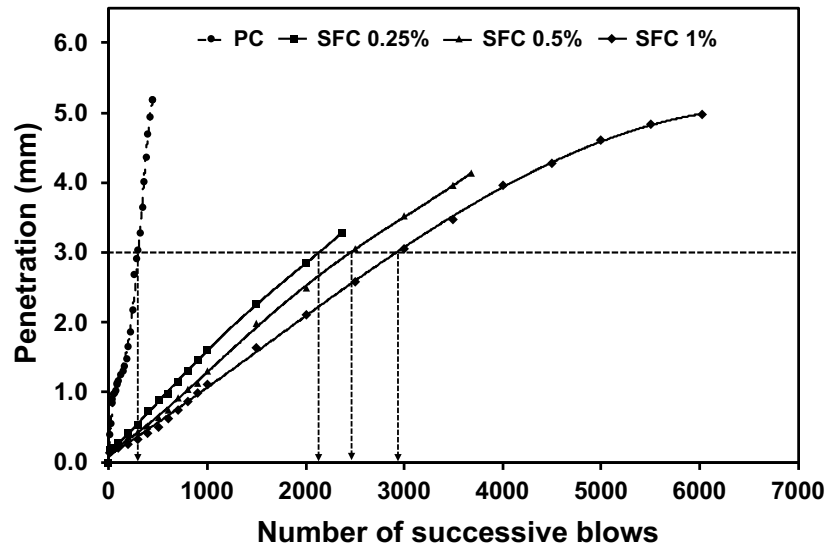


**Fig. 7.44 Penetration level by steel ball below AAS fibrous and the plain concrete surface.**

Besides the steel fibre content, the binder deterioration will affect the impact behaviour after exposure to elevated temperatures. As the binder is exposed to elevated temperatures, different hydration products start to decompose according to each product's stability. This decomposition will lead to binder weight losses accompanied by a reduction in its density. This will eventually result in a lower matrix-fibre bond. **Fig. 7.45** shows the relative residual impact absorption capacity for each mixture, which is the impact absorption capacity after exposure to elevated temperatures with respect to its original capacity at ambient temperature, and the relative weight loss, which is the binder weight loss after exposure to elevated temperature with respect to the weight loss without exposure to elevated temperature during the TGA test.

During the thermogravimetric analysis test (TGA), the tested sample's measured weight loss reflects the weight loss due to hydration products decomposition. The measured weight loss will be proportion to the amount of decomposed hydration products. Two groups of samples were tested from each mixture to quantify the change in the hydration products before and after exposure

to elevated temperatures. The first group includes samples from specimens that cured at ambient temperature. The second group includes samples from specimens that were exposed to various elevated temperatures. The difference in weight loss between samples from the two groups for each mixture was compared. Before the TGA test, increasing the exposure temperature level resulted in higher relative weight loss, and consequently lower binder density compared to that of sample tested without exposure to elevated temperature. For instance, tested samples after exposure to 200 °C, 400 °C, 600 °C exhibited 27.1 %, 41.4%, and 78.7% relative weight loss with respect to that of the tested sample without exposure to elevated temperature before the test. This can explain the effect of elevated temperature individually on the binder.

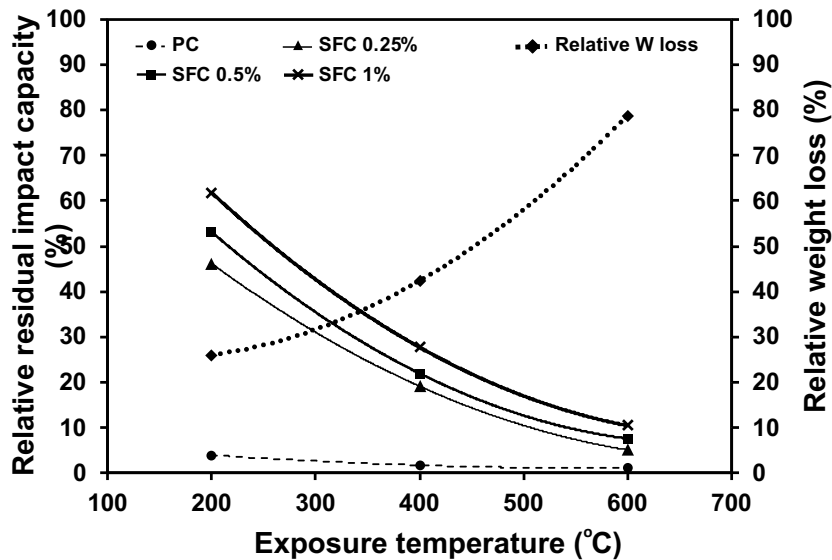


**Fig. 7.45 Relative residual impact absorption capacity vs the binder relative weight loss during exposure to elevated temperatures.**

Moreover, fibre-reinforced concrete's toughness was considerably higher than that of plain concrete after exposure to elevated temperatures. **Table 7.4** represents the numbers of blows up

to the first crack ( $N_c$ ) along with the failure numbers of blows ( $N_f$ ) for mixtures with different steel fibre contents after exposure to different temperatures.

The number of blows required to achieve the failure criteria after the first visual crack development increased as the fibre content increased regardless of the exposure temperature. For example, after exposure to 200 °C, specimens containing 0.25%, 0.5%, and 1% fibre required more 256, 334, and 492 blows to fail compared to only 2 blows needed by plain concrete (**Fig. 7.46**). This can be ascribed to steel fibre's reserved capability with different incorporation levels along with the binder to limit the crack propagation, maintaining high toughness before failure under impact loads.

**Table 7.4 Number of successive blows at 1<sup>st</sup> crack and failure of SFC.**

Mixture	Number of blows at 1 <sup>st</sup> crack ( $N_c$ )				Number of blows at failure ( $N_f$ )			
	28 Days	200 °C	400 °C	600 °C	28 Days	200 °C	400 °C	600 °C
PC	442	16	7	4	450	18	8	5
SFC 0.25 %	2366	1056	386	104	2840	1312	544	146
SFC 0.5 %	3678	1922	732	258	4244	2256	934	328
SFC 1 %	6024	3748	1594	628	6860	4240	1904	720

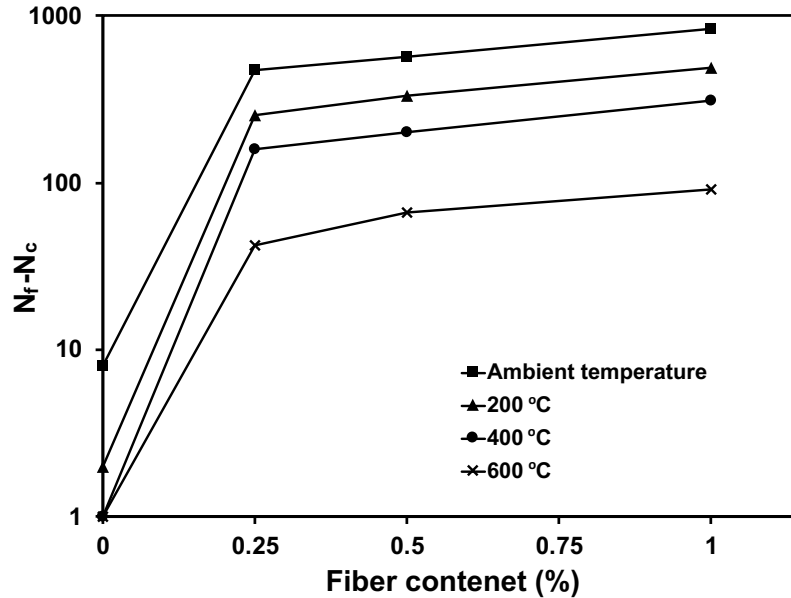


**Fig. 7.46** Number of successive blows after the first visual crack for SFC.

Regarding the residual impact absorption, steel fibre incorporation was efficiently compensating for the negative effect of elevated temperatures on the binder. Higher steel fibre content resulted in a higher residual impact absorption capacity at each elevated temperature level. For example, mixtures incorporating 1% of steel fibre exhibited 68%, 28%, and 11% relative residual impact strength as a ratio of its original absorption capacity compared to 4%, 2%, and 1% for AAS plain concrete.

In terms of absolute impact energy absorption capacity, which is the number of successive blows up to failure, all steel fibre contents could achieve significantly higher impact absorption capacity than that achieved by plain ASS concrete after exposure to all elevated temperatures levels. For instance, after exposure to 600°C, SFC containing 0.25%, 0.5%, and 1% of fibre could absorb the accumulative impact energy induced by 146, 324, and 720 successive blows, comparing to 5 blows at the failure of PC exposed to the temperature level (**Fig. 7.47**). This can show the quantum leap achieved in the impact behaviour of AAS concrete after exposure to various elevated

temperatures by adding steel fiber. Steel fibre can significantly limit the crack development in concrete starting from the early age, while steel fiber showed a powerful performance to reduce the drying shrinkage micro cracking. And to minimize the effect of pore water pressure due to exposure to elevated temperatures achieving the minimum level of induced microcracking, and finally, it showed an excellent behaviour during the impact event while it could achieve a significantly enhanced resilience, which upgraded the concrete strain capacity level to a considerable higher impact energy level. Moreover, the high penetration resistance achieved by the steel fiber inclusion, delayed the crack initiation from the hydrostatic core to the initial state concrete.

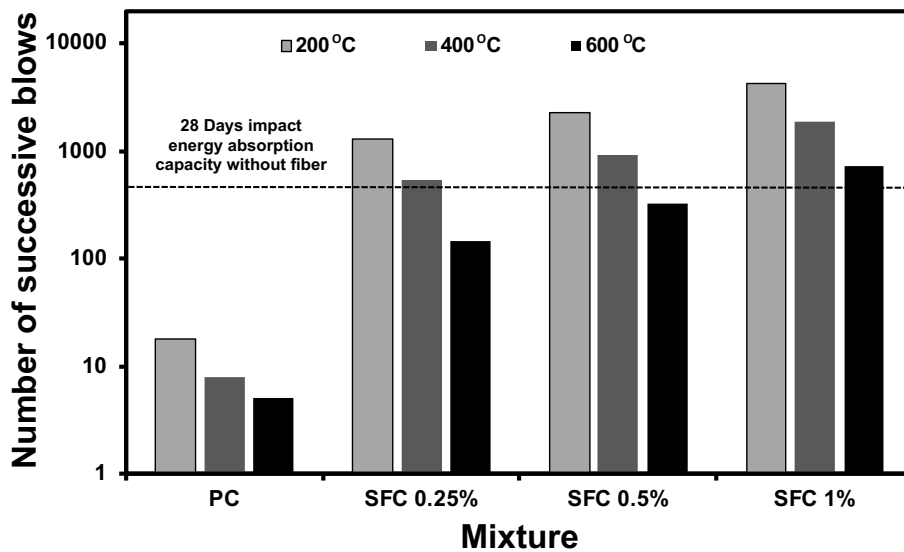


**Fig. 7.47 Residual impact absorption capacity of SFC after exposure to various elevated temperatures.**

## 7.4 Conclusions

1- Polypropylene fibre doesn't significantly contribute to enhance the static mechanical properties such as compressive strength and modulus of elasticity as a result of the high fiber density which in turn negatively affect the concrete matrix homogeneity. Moreover, the relatively low modulus of elasticity of polypropylene fibre limits its capability of containing the developed cracks during loading.

2- The performance of AAS concrete under impact loads at ambient temperature can be significantly enhanced by polypropylene fiber incorporation as a result of the high ability of the integrated fibre to act as a buffer elastic network, limiting the induced strains during the impact event.

3- The low melting point of polypropylene fiber was beneficial to the AAS concrete during exposure to elevated temperatures as it provides the matrix with a network of pore water pressure relief canals, leading to less developed micro-cracks.

4- The impact behaviour of AAS concrete after exposure to elevated temperatures can be enhanced by polypropylene fibre inclusion. However, the optimum fiber content might differ according to the exposure temperature level.

5- AAS concrete mechanical properties could be enhanced through incorporation of basalt fiber. The reason for that is the behavior of the fiber inside the concrete to limit the crack initiation to higher levels of stresses achieving lower strains comparing to that of plain concrete at the same stress level. Also, the pre-existed micro-cracks developed during the AAS concrete drying shrinkage was found to be reduced as the fiber content increased.

6- The static mechanical properties of AAS concrete after exposure to various levels of elevated temperatures were found to suffer a significant degradation as a result of the binder hydration products deterioration at different elevated temperatures. However, the existence of basalt fiber could reduce this degradation as a result of its high stability at elevated temperatures and the good, reserved bond with the binder after exposure to elevated temperatures.

7- the impact behavior of AAS concrete could be significantly enhanced through basalt fiber incorporation. Increasing the basalt fiber content was found to have a magnified positive effect on the impact absorption capacity comparing to the enhancement in the static mechanical properties as a result of the high DIF achieved by basalt fiber AAS concrete. the higher fiber content, the higher impact energy absorption capacity of AAS concrete.

8- Basalt fiber has a great role to increase the AAS concrete penetration resistance. This would contribute to reduce the physical damages in concrete that occur during the impact event.

9- Elevated temperatures was found to have a sever effect on AAS plain concrete in terms of impact energy absorption. However, basalt fiber could notably mitigate this degradation, showing high toughness during the failure due to impact loads compared to the plain AAS concrete.

10- The steel fibre incorporation greatly enhanced the mechanical properties of alkali-activated slag concrete due to the increased modulus of elasticity and the decreased deteriorating agents such as drying shrinkage.

11- At ambient temperature, alkali-activated slag concrete impact behaviour was efficiently enhanced by steel fibre incorporation due to the increased concrete resilience. The higher steel fibre content, the higher impact energy absorption capacity.

12- During the impact loading, steel fibrous alkali-activated slag concrete was fond of higher resistance to penetration than plain concrete.

## *Chapter 7*

13- After exposure to elevated temperatures, alkali-activated slag binder suffered a notable degradation in terms of weight losses. However, fibrous concrete could sufficiently mitigate the negative effect induced by the binder deterioration on the impact behaviour.

**Chapter 8 Summary, Conclusions and Recommendations**

Alkali-activated slag systems follow different reaction mechanisms comparing to that of ordinary Portland cement. This results in different formed hydration products with variant properties. Controlling the reaction mechanism of alkali-activated slag and the formed hydration nature comes through the activation process. The alkaline activator nature in terms of silica modulus and sodium oxide dosage dominates the reaction kinetics as it is responsible for the dissolution rate of the precursor and the supply of the desired species. This will eventually shape the final hydration product properties and corresponding mechanical properties and respond to dynamic loads.

However, it is hard to collect all the positive sides of these novel binders unless a balance between various factors is achieved. For that, chapter 4 had investigated various factors related to activator nature individually. Static mechanical properties, resistance to impact loads, and performance after exposure to elevated temperatures were the three main monitored performance evaluation criteria. The findings of this phase revealed the methodology for selecting the activator properties based on the desired criteria. However, it was hard to target the best behaviour regarding these different criteria altogether.

Hence, the next level of the investigation focused on finding an adequate balance between activation properties and performance criteria. This was illustrated in Chapter 5 to assess each success level for the selected activator to achieve the desired performance criteria while monitoring the other. This phase's outcome highlighted each concrete mixture's ability to reserve adequate performance depending on the assigned evaluation (i.e. static mechanical properties, impact

behaviour, and performance under elevated temperatures conditions). Low activation level could achieve excellent behaviour after exposure to elevated temperatures in terms of residual mechanical properties, which is considered a critical requirement in this study. However, both impact resistance and static mechanical properties were very low at ambient temperature. For the medium activation level, alkali-activated slag concrete could achieve medium to low performance regarding all the targeted criteria. However, the high activation level showed outstanding impact behaviour and excellent static mechanical properties, while the performance after exposure to elevated temperature was shocking. This resulted from the high amount of formed hydration products which was the main reason for the competitive mechanical properties at ambient temperatures. However, during exposure to temperature, the higher the formed hydration products, the higher the decomposed materials during this harsh exposure.

Hence, Chapters 6 and 7 focused on dealing with this challenge. The outstanding mechanical properties and impact behaviour encouraged the research to investigate the possible techniques that can boost the behaviour after exposure to elevated temperatures. Rubber incorporation as a passive mitigation technique was investigated in Chapter 6 to assess its ability to enhance the impact behaviour after exposure to elevated temperatures. This technique was successful regarding the rubber content level up to the rubber decomposition degree of temperature (200 ~300 °C). Above this level, rubber decomposes, leaving a high volume of voids resulting in severely deteriorated concrete.

In chapter 7, the implementation of fibre as an active agent to enhance the concrete impact behaviour after exposure to elevated temperatures was investigated. Three types of fibre were incorporated in alkali-activated slag concrete at three content levels. Polypropylene fibre does not significantly enhance the static mechanical properties such as compressive strength

and modulus of elasticity due to the high fibre density, which negatively affects the concrete matrix homogeneity. Moreover, the relatively low modulus of polypropylene fibre elasticity limits its capability to contain the developed cracks during loading. Polypropylene fibre had enhanced impact performance of AAS concrete at ambient temperature as it acted as an elastic buffer network, limiting the induced strains during the impact event. Moreover, the low melting point of polypropylene fibre was beneficial to the AAS concrete during exposure to elevated temperatures as it helps to evacuate the pore water pressure due to its low melting point (~200 °C). However, for the same reason (i.e. low melting point), Polypropylene fibre's ability to enhance the concrete performance during exposure to temperature was limited. The optimum fibre content might differ according to the exposure temperature level.

Basalt fibre showed moderate to high ability to enhance the impact behaviour at ambient temperature and after exposure to elevated temperatures. Like Polypropylene fibre, basalt fibre inclusion reduced the drying shrinkage micro-strain, leading to a lower micro-crack's formation. Also, increasing the basalt fibre content reduced penetration during the impact event due to its high ability to transfer stresses from the high-stress zone to the outer zone. Moreover, the stability for basalt fibre was higher than that of Polypropylene fibre at elevated temperatures leading to a better performance.

The steel fibre incorporation greatly enhanced the mechanical properties of alkali-activated slag concrete due to the increased modulus of elasticity and the decreased deteriorating agents such as drying shrinkage. At ambient temperature, alkali-activated slag concrete impact behaviour was efficiently enhanced by steel fibre incorporation due to the increased concrete resilience. The

higher the steel fibre content, the higher impact energy absorption capacity. Also, steel fibred alkali-activated slag concrete showed higher resistance to penetration compared to plain concrete. After exposure to elevated temperatures, steel fibre addition sufficiently mitigated the adverse effect induced by the AAS binder deterioration on the impact behaviour.

### **RECOMMENDATIONS FOR FUTURE WORK**

- 1- There is a current trend to utilize various powder activator to generate one-part alkali-activated materials. Hence, the effects of changing the nature of the activator and its stability at elevated temperature on the impact behaviour need more investigation.
- 2- Rubberized alkali-activated concrete has a promising performance. However, combining this technique with others (such as fibre) could lead to better performance.
- 3- Each fibre individual showed promising mechanical and dynamic performance. However, based on the current thesis's findings, there are drawbacks for each type of fibre. Hence, combining more than one fibre and optimize the mixture to achieve optimum performance need a future study.
- 4- Further research and development are required to investigate the long-term properties of concrete, incorporating single and hybrid fibres.
- 5- The available experimental data are a beneficial utility that can be used as a predictive model data base. This will help to save time to get experimental results for further work.

## References

- AASHTO (2006). 194M/M 194-06. Standard Specification for Chemical Admixtures for Concrete,” American Association of State and Highway Transportation Officials, Washington, DC.
- AASHTO (2009). 132-87. Standard Method of Test for Tensile Strength of Hydraulic Cement Mortars. American Association of State and Highway Transportation Officials.
- Abaeian, R., Behbahani, H. P., & Moslem, S. J. (2018). Effects of high temperatures on mechanical behavior of high strength concrete reinforced with high performance synthetic macro polypropylene (HPP) fibres. *Construction and Building Materials*, 165, 631-638.
- Aıtcin, P. (2003). The durability characteristics of high performance concrete: a review. *Cement and Concrete Composites*, 25(4-5), 409-420.
- Akca, A. H., & Zihnioglu, N. Ö. (2013). High performance concrete under elevated temperatures. *Construction and Building Materials*, 44, 317-328.
- Alarcon-Ruiz, L., Platret, G., Massieu, E., & Ehlacher, A. (2005). The use of thermal analysis in assessing the effect of temperature on a cement paste. *Cement and Concrete research*, 35(3), 609-613.
- Algin, Z., & Ozen, M. (2018). The properties of chopped basalt fibre reinforced self-compacting concrete. *Construction and Building Materials*, 186, 678-685.
- Aly, A. M., El-Feky, M., Kohail, M., & Nasr, E.-S. A. (2019). Performance of geopolymer concrete containing recycled rubber. *Construction and Building Materials*, 207, 136-144.
- Aslani, F. (2016). Mechanical properties of waste tire rubber concrete. *Journal of Materials in Civil Engineering*, 28(3), 04015152.
- ASTM C109 / C109M-20b, Standard Test Method for Compressive Strength of Hydraulic Cement Mortars (Using 2-in. or [50 mm] Cube Specimens), ASTM International, West Conshohocken, PA, 2020, [www.astm.org](http://www.astm.org)
- ASTM C128-15, Standard Test Method for Relative Density (Specific Gravity) and Absorption of Fine Aggregate, ASTM International, West Conshohocken, PA, 2015, [www.astm.org](http://www.astm.org)
- ASTM C136 / C136M-19, Standard Test Method for Sieve Analysis of Fine and Coarse Aggregates, ASTM International, West Conshohocken, PA, 2019, [www.astm.org](http://www.astm.org)
- ASTM C143 / C143M-20, Standard Test Method for Slump of Hydraulic-Cement Concrete, ASTM International, West Conshohocken, PA, 2020, [www.astm.org](http://www.astm.org)

ASTM C1437-20, Standard Test Method for Flow of Hydraulic Cement Mortar, ASTM International, West Conshohocken, PA, 2020, [www.astm.org](http://www.astm.org)

ASTM C157 / C157M-17, Standard Test Method for Length Change of Hardened Hydraulic-Cement Mortar and Concrete, ASTM International, West Conshohocken, PA, 2017, [www.astm.org](http://www.astm.org)

ASTM C1585-20, Standard Test Method for Measurement of Rate of Absorption of Water by Hydraulic-Cement Concretes, ASTM International, West Conshohocken, PA, 2020, [www.astm.org](http://www.astm.org)

ASTM C192 / C192M-19, Standard Practice for Making and Curing Concrete Test Specimens in the Laboratory, ASTM International, West Conshohocken, PA, 2019, [www.astm.org](http://www.astm.org)

ASTM C230 / C230M-21, Standard Specification for Flow Table for Use in Tests of Hydraulic Cement, ASTM International, West Conshohocken, PA, 2021, [www.astm.org](http://www.astm.org)

ASTM C39 / C39M-20, Standard Test Method for Compressive Strength of Cylindrical Concrete Specimens, ASTM International, West Conshohocken, PA, 2020, [www.astm.org](http://www.astm.org)

ASTM C469 / C469M-14e1, Standard Test Method for Static Modulus of Elasticity and Poisson's Ratio of Concrete in Compression, ASTM International, West Conshohocken, PA, 2014, [www.astm.org](http://www.astm.org)

ASTM C494 / C494M-19, Standard Specification for Chemical Admixtures for Concrete, ASTM International, West Conshohocken, PA, 2019, [www.astm.org](http://www.astm.org)

ASTM C496 / C496M-17, Standard Test Method for Splitting Tensile Strength of Cylindrical Concrete Specimens, ASTM International, West Conshohocken, PA, 2017, [www.astm.org](http://www.astm.org)

ASTM C596-18, Standard Test Method for Drying Shrinkage of Mortar Containing Hydraulic Cement, ASTM International, West Conshohocken, PA, 2018, [www.astm.org](http://www.astm.org)

ASTM C597-16, Standard Test Method for Pulse Velocity Through Concrete, ASTM International, West Conshohocken, PA, 2016, [www.astm.org](http://www.astm.org)

Atiş, C. D., Bilim, C., Çelik, Ö., & Karahan, O. (2009). Influence of activator on the strength and drying shrinkage of alkali-activated slag mortar. *Construction and building materials*, 23(1), 548-555.

Atiş, C. D., & Karahan, O. (2009). Properties of steel fiber reinforced fly ash concrete. *Construction and Building Materials*, 23(1), 392-399.

Bakharev, T. (2005). Durability of geopolymer materials in sodium and magnesium sulfate solutions. *Cement and concrete research*, 35(6), 1233-1246.

- Bakharev, T., Sanjayan, J. G., & Cheng, Y.-B. (2003). Resistance of alkali-activated slag concrete to acid attack. *Cement and Concrete Research*, 33(10), 1607-1611.
- Bangi, M. R., & Horiguchi, T. (2011). Pore pressure development in hybrid fibre-reinforced high strength concrete at elevated temperatures. *Cement and Concrete Research*, 41(11), 1150-1156.
- Banthia, N., Mindess, S., Bentur, A., & Pigeon, M. (1989). Impact testing of concrete using a drop-weight impact machine. *Experimental Mechanics*, 29(1), 63-69.
- Barbosa, V. F., MacKenzie, K. J., & Thaumaturgo, C. (2000). Synthesis and characterisation of materials based on inorganic polymers of alumina and silica: sodium polysialate polymers. *International Journal of Inorganic Materials*, 2(4), 309-317.
- Bazant, Z. P., Kaplan, M. F., & Bazant, Z. P. (1996). Concrete at high temperatures: material properties and mathematical models.
- Beddoe, R. E., & Dorner, H. W. (2005). Modelling acid attack on concrete: Part I. The essential mechanisms. *Cement and Concrete Research*, 35(12), 2333-2339.
- Benazzouk, A., Mezreb, K., Doyen, G., Goullieux, A., & Quéneudec, M. (2003). Effect of rubber aggregates on the physico-mechanical behaviour of cement-rubber composites-influence of the alveolar texture of rubber aggregates. *Cement and Concrete Composites*, 25(7), 711-720.
- Bernal, S. A., de Gutiérrez, R. M., & Provis, J. L. (2012). Engineering and durability properties of concretes based on alkali-activated granulated blast furnace slag/metakaolin blends. *Construction and Building Materials*, 33, 99-108.
- Bheel, N. (2021). Basalt fibre-reinforced concrete: review of fresh and mechanical properties. *Journal of Building Pathology and Rehabilitation*, 6(1), 1-9.
- Bilim, C., Karahan, O., Atiş, C. D., & Ilkentapar, S. (2013). Influence of admixtures on the properties of alkali-activated slag mortars subjected to different curing conditions. *Materials & Design*, 44, 540-547.
- Bindiganavile, V., Banthia, N., & Aarup, B. (2002). Impact response of ultra-high-strength fiber-reinforced cement composite. *Materials Journal*, 99(6), 543-548.
- Bisschop, J., & Van Mier, J. (2002). Effect of aggregates on drying shrinkage microcracking in cement-based composites. *Materials and Structures*, 35(8), 453-461.
- Burciaga-Díaz, O., & Escalante-García, J. I. (2013). Structure, mechanisms of reaction, and strength of an alkali-activated blast-furnace slag. *Journal of the American Ceramic Society*, 96(12), 3939-3948.
- Caijun, S., & Yinyu, L. (1989). Investigation on some factors affecting the characteristics of alkali-phosphorus slag cement. *Cement and Concrete Research*, 19(4), 527-533.

Callister Jr, W. D., & Rethwisch, D. G. (2020). Callister's materials science and engineering: John Wiley & Sons.

Callister, W., & Rethwisch, D. (2007). The structure of crystalline solids. Materials science and engineering: an introduction. New York: John Wiley & Sons, Inc, 38-79.

Chang, C.-F., & Chen, J.-W. (2006). The experimental investigation of concrete carbonation depth. Cement and Concrete Research, 36(9), 1760-1767.

Chang, J. (2003). A study on the setting characteristics of sodium silicate-activated slag pastes. Cement and Concrete Research, 33(7), 1005-1011.

Cheema, D., Lloyd, N., & Rangan, B. V. (2009). Durability of geopolymer concrete box culverts- A green alternative. Paper presented at the Proceedings of 34th Conference on Our World in Concrete and Structures.

Chiaia, B. (2001). Fracture mechanisms induced in a brittle material by a hard cutting indenter. International Journal of Solids and Structures, 38(44-45), 7747-7768.

Chidighikaobi, P. C. (2019). Thermal effect on the flexural strength of expanded clay lightweight basalt fiber reinforced concrete. Materials Today: Proceedings, 19, 2467-2470.

Cohen, M. (1983). Theories of expansion in sulfoaluminate-type expansive cements: schools of thought. Cement and Concrete Research, 13(6), 809-818.

Costello, A., Abbas, M., Allen, A., Ball, S., Bell, S., Bellamy, R., . . . Kett, M. (2009). Managing the health effects of climate change: lancet and University College London Institute for Global Health Commission. The Lancet, 373(9676), 1693-1733.

Criado, M., Palomo, A., & Fernández-Jiménez, A. (2005). Alkali activation of fly ashes. Part 1: Effect of curing conditions on the carbonation of the reaction products. Fuel, 84(16), 2048-2054.

Cusatis, G. (2011). Strain-rate effects on concrete behavior. International Journal of Impact Engineering, 38(4), 162-170.

Davidovits, J. (1984). Synthetic mineral polymer compound of the silicoaluminates family and preparation process: Google Patents.

Davidovits, J. (1988). Geopolymer chemistry and properties. Paper presented at the Geopolymer.

Davidovits, J. (1991). Geopolymers: inorganic polymeric new materials. Journal of Thermal Analysis and calorimetry, 37(8), 1633-1656.

Davidovits, J. (1993). Geopolymer cements to minimize carbon dioxide greenhouse warming. Ceram. Trans., 37, 165-182.

Davidovits, J. (1994). Method for obtaining a geopolymeric binder allowing to stabilize, solidify and consolidate toxic or waste materials: Google Patents.

Davidovits, J. (2005). The polysialate terminology: a very useful and simple model for the promotion and understanding of green-chemistry. Paper presented at the Geopolymer, Green Chemistry and Sustainable Development Solutions: Proc. of the World Congress Geopolymer.

Davidovits, J. (2008). Chemistry and applications. Institut Geopolymer, 3rd printing, Saint-Quentin, France.

Davidovits, J., & Cordi, S. (1979). Synthesis of new high temperature geo-polymers for reinforced plastics/composites. *Spe Pactec*, 79, 151-154.

de Sa, C., Benboudjema, F., Thiery, M., & Sicard, J. (2008). Analysis of microcracking induced by differential drying shrinkage. *Cement and Concrete Composites*, 30(10), 947-956.

Dragon, A., & Mroz, Z. (1979). A continuum model for plastic-brittle behaviour of rock and concrete. *International Journal of Engineering Science*, 17(2), 121-137.

Duxson, P., Fernández-Jiménez, A., Provis, J. L., Lukey, G. C., Palomo, A., & van Deventer, J. S. (2007). Geopolymer technology: the current state of the art. *Journal of Materials Science*, 42(9), 2917-2933.

Eguchi, K., & Teranishi, K. (2005). Prediction equation of drying shrinkage of concrete based on composite model. *Cement and Concrete Research*, 35(3), 483-493.

Emdadi, A., Mehdipour, I., Libre, N. A., & Shekarchi, M. (2015). Optimized workability and mechanical properties of FRCC by using fiber factor approach: theoretical and experimental study. *Materials and Structures*, 48(4), 1149-1161.

Falcone, J. S. (1982). *Soluble silicates* (Vol. 194): American Chemical Society.

Felicetti, R., & Monte, F. L. (2013). Concrete spalling: Interaction between tensile behaviour and pore pressure during heating. Paper presented at the MATEC Web of Conferences.

Fernández-Jiménez, A., & Palomo, A. (2005). Composition and microstructure of alkali activated fly ash binder: Effect of the activator. *Cement and Concrete Research*, 35(10), 1984-1992.

Fernández-Jiménez, A., Palomo, A., & Criado, M. (2005). Microstructure development of alkali-activated fly ash cement: a descriptive model. *Cement and Concrete Research*, 35(6), 1204-1209.

Fernández-Jiménez, A., Palomo, A., Sobrados, I., & Sanz, J. (2006). The role played by the reactive alumina content in the alkaline activation of fly ashes. *Microporous and Mesoporous Materials*, 91(1-3), 111-119.

- Fernández-Jiménez, A., & Puertas, F. (1997). Alkali-activated slag cements: kinetic studies. *Cement and Concrete Research*, 27(3), 359-368.
- Fernández-Jiménez, A., & Puertas, F. (2003). Effect of activator mix on the hydration and strength behaviour of alkali-activated slag cements. *Advances in Cement Research*, 15(3), 129-136.
- Fernandez-Jimenez, A., Puertas, F., Sobrados, I., & Sanz, J. (2002). Structure of calcium silicate hydrate formed in alkali activated slag cement pates. *Non-traditional Cement and Concrete*, 29-41.
- Fernández-Jiménez, A., Puertas, F., Sobrados, I., & Sanz, J. (2003). Structure of calcium silicate hydrates formed in alkaline-activated slag: influence of the type of alkaline activator. *Journal of the American Ceramic Society*, 86(8), 1389-1394.
- Fu, H., Erki, M., & Seckin, M. (1991). Review of effects of loading rate on concrete in compression. *Journal of Structural Engineering*, 117(12), 3645-3659.
- Fu, Q., Niu, D., Zhang, J., Huang, D., & Hong, M. (2018). Impact response of concrete reinforced with hybrid basalt-polypropylene fibers. *Powder Technology*, 326, 411-424.
- Fu, Y., & Li, L. (2011). Study on mechanism of thermal spalling in concrete exposed to elevated temperatures. *Materials and Structures*, 44(1), 361-376.
- Ganjian, E., Khorami, M., & Maghsoudi, A. A. (2009). Scrap-tyre-rubber replacement for aggregate and filler in concrete. *Construction and Building Materials*, 23(5), 1828-1836.
- Gao, J., Sun, W., & Morino, K. (1997). Mechanical properties of steel fiber-reinforced, high-strength, lightweight concrete. *Cement and Concrete Composites*, 19(4), 307-313.
- Gao, X., Yu, Q., Yu, R., & Brouwers, H. (2017). Evaluation of hybrid steel fiber reinforcement in high performance geopolymer composites. *Materials and Structures*, 50(2), 1-14.
- García-Lodeiro, I., Palomo, A. y., & Fernández-Jiménez, A. (2007). Alkali–aggregate reaction in activated fly ash systems. *Cement and Concrete Research*, 37(2), 175-183.
- Georgali, B., & Tsakiridis, P. (2005). Microstructure of fire-damaged concrete. A case study. *Cement and Concrete Composites*, 27(2), 255-259.
- Glukhovsky, V. (1959). *Soil silicates*. Kiev. USSR: Gostroiizdat Publish.
- Glukhovsky, V. (1965). *Soil silicates: their properties, technology and manufacturing and fields of application*. DTech. Sc. Thesis, Civil Engineering Institute, Kiev, Ukraine.
- Glukhovsky, V. (1981). *Slag-alkali concretes produced from fine-grained aggregate*. Kiev: Vishcha Shkolay.

Glukhovskiy, V., Rostovskaja, G., & Rumyna, G. (1980a). High strength slag-alkaline cements. Paper presented at the Proceedings of the seventh international congress on the chemistry of cement.

Glukhovskiy, V., Rostovskaja, G., & Rumyna, G. (1980b). High strength slag-alkaline cements. Paper presented at the 7th International Congress on the Chemistry of Cement.

Grassl, P., Wong, H. S., & Buenfeld, N. R. (2010). Influence of aggregate size and volume fraction on shrinkage induced micro-cracking of concrete and mortar. *Cement and Concrete Research*, 40(1), 85-93.

Gruber, K., Ramlochan, T., Boddy, A., Hooton, R., & Thomas, M. (2001). Increasing concrete durability with high-reactivity metakaolin. *Cement and Concrete Composites*, 23(6), 479-484.

Gruskovnjak, A., Lothenbach, B., Holzer, L., Figi, R., & Winnefeld, F. (2006). Hydration of alkali-activated slag: comparison with ordinary Portland cement. *Advances in Cement Research*, 18(3), 119-128.

Guerrieri, M., Sanjayan, J., & Collins, F. (2010). Residual strength properties of sodium silicate alkali activated slag paste exposed to elevated temperatures. *Materials and Structures*, 43(6), 765-773.

Gul, M., Bashir, A., & Naqash, J. A. (2014). Study of modulus of elasticity of steel fiber reinforced concrete. *International Journal of Engineering and Advanced Technology*, 3(4), 304-309.

Guo, S., Dai, Q., Si, R., Sun, X., & Lu, C. (2017). Evaluation of properties and performance of rubber-modified concrete for recycling of waste scrap tire. *Journal of Cleaner Production*, 148, 681-689.

Gupta, T., Chaudhary, S., & Sharma, R. K. (2016). Mechanical and durability properties of waste rubber fiber concrete with and without silica fume. *Journal of Cleaner Production*, 112, 702-711.

Gupta, T., Sharma, R. K., & Chaudhary, S. (2015). Impact resistance of concrete containing waste rubber fiber and silica fume. *International Journal of Impact Engineering*, 83, 76-87.

Hadi, M. N., Hasan, H. A., & Sheikh, M. N. (2017). Experimental investigation of circular high-strength concrete columns reinforced with glass fiber-reinforced polymer bars and helices under different loading conditions. *Journal of Composites for Construction*, 21(4), 04017005.

Haha, M. B., Le Saout, G., Winnefeld, F., & Lothenbach, B. (2011). Influence of activator type on hydration kinetics, hydrate assemblage and microstructural development of alkali activated blast-furnace slags. *Cement and Concrete Research*, 41(3), 301-310.

Hajilar, S., & Shafei, B. (2016). Assessment of structural, thermal, and mechanical properties of portlandite through molecular dynamics simulations. *Journal of Solid State Chemistry*, 244, 164-174.

- Hajimohammadi, A., Provis, J. L., & Van Deventer, J. S. (2010). Effect of alumina release rate on the mechanism of geopolymer gel formation. *Chemistry of Materials*, 22(18), 5199-5208.
- Hajimohammadi, A., & van Deventer, J. S. (2017). Characterisation of one-part geopolymer binders made from fly ash. *Waste and Biomass Valorization*, 8(1), 225-233.
- Hardjito, D., Wallah, S. E., Sumajouw, D. M., & Rangan, B. V. (2004). On the development of fly ash-based geopolymer concrete. *Materials Journal*, 101(6), 467-472.
- Heinstein, M. W., Mello, F. J., Attaway, S. W., & Laursen, T. A. (2000). Contact—impact modeling in explicit transient dynamics. *Computer Methods in Applied Mechanics and Engineering*, 187(3-4), 621-640.
- Hendriks, C. A., Worrell, E., De Jager, D., Blok, K., & Riemer, P. (1998). Emission reduction of greenhouse gases from the cement industry. Paper presented at the Proceedings of the fourth international conference on greenhouse gas control technologies.
- Hertz, K. D. (2003). Limits of spalling of fire-exposed concrete. *Fire safety journal*, 38(2), 103-116.
- Hester, D., McNally, C., & Richardson, M. (2005). A study of the influence of slag alkali level on the alkali–silica reactivity of slag concrete. *Construction and Building Materials*, 19(9), 661-665.
- Holschemacher, K., Mueller, T., & Ribakov, Y. (2010). Effect of steel fibres on mechanical properties of high-strength concrete. *Materials & Design (1980-2015)*, 31(5), 2604-2615.
- Hughes, G. (1984). Hard missile impact on reinforced concrete. *Nuclear Engineering and Design*, 77(1), 23-35.
- Huntzinger, D. N., & Eatmon, T. D. (2009). A life-cycle assessment of Portland cement manufacturing: comparing the traditional process with alternative technologies. *Journal of Cleaner Production*, 17(7), 668-675.
- Idiart, A., Bisschop, J., Caballero, A., & Lura, P. (2012). A numerical and experimental study of aggregate-induced shrinkage cracking in cementitious composites. *Cement and Concrete Research*, 42(2), 272-281.
- Islam, A., Alengaram, U. J., Jumaat, M. Z., Ghazali, N. B., Yusoff, S., & Bashar, I. I. (2017). Influence of steel fibers on the mechanical properties and impact resistance of lightweight geopolymer concrete. *Construction and Building Materials*, 152, 964-977.
- Jang, J. G., Lee, N., & Lee, H.-K. (2014). Fresh and hardened properties of alkali-activated fly ash/slag pastes with superplasticizers. *Construction and Building Materials*, 50, 169-176.

- Jiang, W., Silsbee, M., & Roy, D. (1997). Alkali activation reaction mechanism and its influence on microstructure of slag cement. Paper presented at the 10th International Congress on the Chemistry of Cement.
- Jie, X., Yao, Z., Yang, G., & Han, Q. (2020). Research on crumb rubber concrete: From a multi-scale review. *Construction and Building Materials*, 232, 117282.
- Jumppanen, U.-M., Diederichs, U., & Hinrichsmeyer, K. (1986). Material properties of F-concrete at high temperatures: VTT Technical Research Centre of Finland.
- jun Li, J., gang Niu, J., jun Wan, C., Jin, B., & liu Yin, Y. (2016). Investigation on mechanical properties and microstructure of high performance polypropylene fiber reinforced lightweight aggregate concrete. *Construction and Building Materials*, 118, 27-35.
- Kalifa, P., Chene, G., & Galle, C. (2001). High-temperature behaviour of HPC with polypropylene fibres: From spalling to microstructure. *Cement and Concrete Research*, 31(10), 1487-1499.
- Karimipour, A., Ghalehnovi, M., & De Brito, J. (2020). Mechanical and durability properties of steel fibre-reinforced rubberised concrete. *Construction and Building Materials*, 257, 119463.
- Keller, D. P., Feng, E. Y., & Oshlies, A. (2014). Potential climate engineering effectiveness and side effects during a high carbon dioxide-emission scenario. *Nature communications*, 5, 3304.
- Khoury, G. (1992). Compressive strength of concrete at high temperatures: a reassessment. *Magazine of Concrete Research*, 44(161), 291-309.
- Komnitsas, K., & Zaharaki, D. (2007). Geopolymerisation: A review and prospects for the minerals industry. *Minerals Engineering*, 20(14), 1261-1277.
- Kong, D. L., & Sanjayan, J. G. (2008). Damage behavior of geopolymer composites exposed to elevated temperatures. *Cement and Concrete Composites*, 30(10), 986-991.
- Kong, D. L., & Sanjayan, J. G. (2010). Effect of elevated temperatures on geopolymer paste, mortar and concrete. *Cement and Concrete Research*, 40(2), 334-339.
- Korol, R. M., & Sivakumaran, K. (2012). Energy absorption potential of light weight concrete floors. *Canadian Journal of Civil Engineering*, 39(11), 1193-1201.
- Krizan, D., & Zivanovic, B. (2002). Effects of dosage and modulus of water glass on early hydration of alkali-slag cements. *Cement and Concrete Research*, 32(8), 1181-1188.
- Kupwade-Patil, K., & Allouche, E. N. (2013). Impact of alkali silica reaction on fly ash-based geopolymer concrete. *Journal of materials in Civil Engineering*, 25(1), 131-139.

- Leelalerkiet, V., Kyung, J.-W., Ohtsu, M., & Yokota, M. (2004). Analysis of half-cell potential measurement for corrosion of reinforced concrete. *Construction and Building Materials*, 18(3), 155-162.
- Li, L.-J., Tu, G.-R., Lan, C., & Liu, F. (2016). Mechanical characterization of waste-rubber-modified recycled-aggregate concrete. *Journal of Cleaner Production*, 124, 325-338.
- Li, W., & Xu, J. (2009). Impact characterization of basalt fiber reinforced geopolymeric concrete using a 100-mm-diameter split Hopkinson pressure bar. *Materials Science and Engineering: A*, 513, 145-153.
- Li, Y., & Aoude, H. (2020). Effects of detailing on the blast and post-blast resilience of high-strength steel reinforced concrete (HSS-RC) beams. *Engineering Structures*, 219, 110869.
- Li, Y., Zhang, X., Wang, R., & Lei, Y. (2019). Performance enhancement of rubberised concrete via surface modification of rubber: A review. *Construction and Building Materials*, 227, 116691.
- Liu, F., Chen, G., Li, L., & Guo, Y. (2012). Study of impact performance of rubber reinforced concrete. *Construction and Building Materials*, 36, 604-616.
- Long, W.-J., Li, H.-D., Wei, J.-J., Xing, F., & Han, N. (2018). Sustainable use of recycled crumb rubbers in eco-friendly alkali activated slag mortar: Dynamic mechanical properties. *Journal of Cleaner Production*, 204, 1004-1015.
- Lothenbach, B., & Winnefeld, F. (2006). Thermodynamic modelling of the hydration of Portland cement. *Cement and Concrete Research*, 36(2), 209-226.
- Maalej, M., Quek, S. T., & Zhang, J. (2005). Behavior of hybrid-fiber engineered cementitious composites subjected to dynamic tensile loading and projectile impact. *Journal of Materials in Civil Engineering*, 17(2), 143-152.
- Mainstone, R. J. (1975). Properties of materials at high rates of straining or loading. *Matériaux et Construction*, 8(2), 102-116.
- Malhotra, V. M., & Mehta, P. K. (2002). High-performance, high-volume fly ash concrete: materials, mixture proportioning, properties, construction practice, and case histories: Supplementary Cementing Materials for Sustainable Development, Incorporated.
- Malvar, L. J., & Ross, C. A. (1998). Review of strain rate effects for concrete in tension. *ACI Materials Journal*, 95, 735-739.

- Mehdipour, I., Vahdani, M., Libre, N. A., & Shekarchi, M. (2013). Relationship between workability and mechanical properties of fibre-reinforced self-consolidating mortar. *Magazine of Concrete Research*, 65(17), 1011-1022.
- Mehta, P. K. (1983). Mechanism of sulfate attack on portland cement concrete—Another look. *Cement and Concrete Research*, 13(3), 401-406.
- Mehta, P. K. (1989). Pozzolanic and cementitious by-products in concrete--another look. *Special Publication*, 114, 1-44.
- Metso, J., & Kajaus, E. (1983). Activation of blast furnace slag by some inorganic materials. *Special Publication*, 79, 1059-1074.
- Meyer, C. (2009). The greening of the concrete industry. *Cement and concrete composites*, 31(8), 601-605.
- Mínguez, J., González, D. C., & Vicente, M. A. (2018). Fiber geometrical parameters of fiber-reinforced high strength concrete and their influence on the residual post-peak flexural tensile strength. *Construction and Building Materials*, 168, 906-922.
- Mohammadi, I., Khabbaz, H., & Vessalas, K. (2016). Enhancing mechanical performance of rubberised concrete pavements with sodium hydroxide treatment. *Materials and Structures*, 49(3), 813-827.
- Mohammadi, S., Forouzan-Sepéhr, S., & Asadollahi, A. (2002). Contact based delamination and fracture analysis of composites. *Thin-walled Structures*, 40(7-8), 595-609.
- Morsy, M. S., Galal, A., & Abo-El-Enein, S. (1998). Effect of temperature on phase composition and microstructure of artificial pozzolana-cement pastes containing burnt kaolinite clay. *Cement and Concrete Research*, 28(8), 1157-1163.
- Myers, R. J., Bernal, S. A., San Nicolas, R., & Provis, J. L. (2013). Generalized structural description of calcium–sodium aluminosilicate hydrate gels: the cross-linked substituted tobermorite model. *Langmuir*, 29(17), 5294-5306.
- Neupane, K., Chalmers, D., & Kidd, P. (2018). High-Strength Geopolymer Concrete—Properties, Advantages and Challenges. *Adv. Mater*, 7, 15-25.
- Nonat, A. (2004). The structure and stoichiometry of CSH. *Cement and Concrete Research*, 34(9), 1521-1528.
- Odler, I., & Gasser, M. (1988). Mechanism of sulfate expansion in hydrated Portland cement. *Journal of the American Ceramic Society*, 71(11), 1015-1020.
- Olivia, M., & Nikraz, H. (2012). Properties of fly ash geopolymer concrete designed by Taguchi method. *Materials & Design (1980-2015)*, 36, 191-198.

- Pacheco-Torgal, F., Castro-Gomes, J., & Jalali, S. (2008). Alkali-activated binders: A review: Part 1. Historical background, terminology, reaction mechanisms and hydration products. *Construction and Building Materials*, 22(7), 1305-1314.
- Pal, S., Mukherjee, A., & Pathak, S. (2003). Investigation of hydraulic activity of ground granulated blast furnace slag in concrete. *Cement and Concrete Research*, 33(9), 1481-1486.
- Palomo, A., Grutzeck, M., & Blanco, M. (1999). Alkali-activated fly ashes: a cement for the future. *Cement and Concrete Research*, 29(8), 1323-1329.
- Panias, D., Giannopoulou, I. P., & Perraki, T. (2007). Effect of synthesis parameters on the mechanical properties of fly ash-based geopolymers. *Colloids and Surfaces A: Physicochemical and Engineering Aspects*, 301(1-3), 246-254.
- Papanastasiou, P., & Sarris, E. (2017). Cohesive zone models Porous Rock Fracture Mechanics (pp. 119-144): Elsevier
- Parameswaran, P. (1986). Alkali Activation of India Blast Furnace Slag. Paper presented at the Proceedings, 8th International Congress on Chemistry of Cement, Rio de Janeiro.
- Park, S. M., Jang, J. G., Lee, N., & Lee, H.-K. (2016). Physicochemical properties of binder gel in alkali-activated fly ash/slag exposed to high temperatures. *Cement and Concrete Research*, 89, 72-79.
- Peng, G.-F., & Huang, Z.-S. (2008). Change in microstructure of hardened cement paste subjected to elevated temperatures. *Construction and Building Materials*, 22(4), 593-599.
- Petzold, A., & Röhrs, M. (1970). *Concrete for high temperatures*: Maclaren.
- Pham, T. M., Chen, W., & Hao, H. (2018). Failure and impact resistance analysis of plain and fiber-reinforced-polymer confined concrete cylinders under axial impact loads. *International Journal of Protective Structures*, 9(1), 4-23.
- Phan, L. T., & Carino, N. J. (2001). Mechanical properties of high-strength concrete at elevated temperatures.
- Provis, J., Duxson, P., Van Deventer, J., & Lukey, G. (2005). The role of mathematical modelling and gel chemistry in advancing geopolymer technology. *Chemical Engineering Research and Design*, 83(7), 853-860.
- Provis, J. L. (2006). Modelling the formation of geopolymers.
- Provis, J. L., Lukey, G. C., & van Deventer, J. S. (2005). Do geopolymers actually contain nanocrystalline zeolites? A reexamination of existing results. *Chemistry of Materials*, 17(12), 3075-3085.

- Puertas, F., Palacios, M., Manzano, H., Dolado, J., Rico, A., & Rodríguez, J. (2011). A model for the CASH gel formed in alkali-activated slag cements. *Journal of the European Ceramic Society*, 31(12), 2043-2056.
- Puertas, F., Varga, C., & Alonso, M. (2014). Rheology of alkali-activated slag pastes. Effect of the nature and concentration of the activating solution. *Cement and Concrete Composites*, 53, 279-288.
- Rajamane, N., Nataraja, M., Dattatreya, J., Lakshmanan, N., & Sabitha, D. (2012). Sulphate resistance and eco-friendliness of geopolymer concretes. *Indian Concrete Journal*, 86(1), 13.
- Rashad, A., Bai, Y., Basheer, P., Collier, N., & Milestone, N. (2012). Chemical and mechanical stability of sodium sulfate activated slag after exposure to elevated temperature. *Cement and Concrete Research*, 42(2), 333-343.
- Rashad, A. M., Sadek, D. M., & Hassan, H. A. (2016). An investigation on blast-furnace slag as fine aggregate in alkali-activated slag mortars subjected to elevated temperatures. *Journal of Cleaner Production*, 112, 1086-1096.
- Reddy, A. A., Tulyaganov, D. U., Goel, A., Kapoor, S., Pascual, M. J., & Ferreira, J. M. (2013). Sintering and devitrification of glass-powder compacts in the akermanite–gehlenite system. *Journal of Materials Science*, 48(11), 4128-4136.
- Richardson, I. (2000). The nature of the hydration products in hardened cement pastes. *Cement and Concrete Composites*, 22(2), 97-113.
- Richardson, I., Brough, A., Groves, G., & Dobson, C. (1994). The characterization of hardened alkali-activated blast-furnace slag pastes and the nature of the calcium silicate hydrate (CSH) phase. *Cement and Concrete Research*, 24(5), 813-829.
- Ross, C. (1996). Review of strain rate effects in materials. *ASME-PUBLICATIONS-PVP*, 351, 255-262.
- Rozière, E., Loukili, A., El Hachem, R., & Grondin, F. (2009). Durability of concrete exposed to leaching and external sulphate attacks. *Cement and Concrete Research*, 39(12), 1188-1198.
- Sanjuán, M. A., & Moragues, A. (1997). Polypropylene-fibre-reinforced mortar mixes: optimization to control plastic shrinkage. *Composites Science and Technology*, 57(6), 655-660.
- Seleem, H. E. D. H., Rashad, A. M., & Elsokary, T. (2011). Effect of elevated temperature on physico-mechanical properties of blended cement concrete. *Construction and Building Materials*, 25(2), 1009-1017.
- Shende, A., Pande, A., & Pathan, M. G. (2012). Experimental study on steel fiber reinforced concrete for M-40 grade. *International Refereed Journal of Engineering and Science*, 1(1), 043-048.

Shi, C., Roy, D., & Krivenko, P. (2003). Alkali-activated cements and concretes: CRC press.

Shu, X., & Huang, B. (2014). Recycling of waste tire rubber in asphalt and portland cement concrete: An overview. *Construction and Building Materials*, 67, 217-224.

Siddique, R., & Kaur, D. (2012). Properties of concrete containing ground granulated blast furnace slag (GGBFS) at elevated temperatures. *Journal of Advanced Research*, 3(1), 45-51.

Sierakowski, R. L., & Chaturvedi, S. K. (1997). Dynamic loading and characterization of fiber-reinforced composites.

Simões, T., Costa, H., Dias-da-Costa, D., & Júlio, E. (2017). Influence of fibres on the mechanical behaviour of fibre reinforced concrete matrixes. *Construction and Building Materials*, 137, 548-556.

Simões, T., Octávio, C., Valença, J., Costa, H., Dias-da-Costa, D., & Júlio, E. (2017). Influence of concrete strength and steel fibre geometry on the fibre/matrix interface. *Composites Part B: Engineering*, 122, 156-164.

Singh, B., Ishwarya, G., Gupta, M., & Bhattacharyya, S. (2015). Geopolymer concrete: A review of some recent developments. *Construction and building materials*, 85, 78-90.

Singh, B., Rahman, M., Paswan, R., & Bhattacharyya, S. (2016). Effect of activator concentration on the strength, ITZ and drying shrinkage of fly ash/slag geopolymer concrete. *Construction and Building Materials*, 118, 171-179.

Song, P., & Hwang, S. (2004). Mechanical properties of high-strength steel fiber-reinforced concrete. *Construction and Building Materials*, 18(9), 669-673.

Soufeiani, L., Raman, S. N., Jumaat, M. Z. B., Alengaram, U. J., Ghadyani, G., & Mendis, P. (2016). Influences of the volume fraction and shape of steel fibers on fiber-reinforced concrete subjected to dynamic loading—A review. *Engineering Structures*, 124, 405-417.

Sukontasukkul, P., & Tiamlom, K. (2012). Expansion under water and drying shrinkage of rubberized concrete mixed with crumb rubber with different size. *Construction and Building Materials*, 29, 520-526.

Tanyildizi, H. (2009). Statistical analysis for mechanical properties of polypropylene fiber reinforced lightweight concrete containing silica fume exposed to high temperature. *Materials & Design*, 30(8), 3252-3258.

Taylor, H. (1997). *Cement chemistry*. 2nd. Ed., T Telford, London, 459pp.

Taylor, H. F. (1986). Proposed structure for calcium silicate hydrate gel. *Journal of the American Ceramic Society*, 69(6), 464-467.

- Thokchom, S., Ghosh, P., & Ghosh, S. (2010). Performance of fly ash based geopolymer mortars in sulphate solution. *Journal of Engineering Science and Technology review*, 3(1), 36-40.
- Turner, L. K., & Collins, F. G. (2013). Carbon dioxide equivalent (CO<sub>2</sub>-e) emissions: A comparison between geopolymer and OPC cement concrete. *Construction and Building Materials*, 43, 125-130.
- Van Jaarsveld, J., Lukey, G., Van Deventer, J., & Graham, A. (2000). The stabilisation of mine tailings by reactive geopolymerisation. *Publications of the Australasian Institute of Mining and Metallurgy*, 5(2000), 363-371.
- van Jaarsveld, J., & Van Deventer, J. (1999). Effect of the alkali metal activator on the properties of fly ash-based geopolymers. *Industrial & Engineering Chemistry Research*, 38(10), 3932-3941.
- Van Jaarsveld, J., Van Deventer, J., & Lorenzen, L. (1998). Factors affecting the immobilization of metals in geopolymerized flyash. *Metallurgical and Materials Transactions B*, 29(1), 283-291.
- Van Jaarsveld, J., Van Deventer, J., & Lukey, G. (2002). The effect of composition and temperature on the properties of fly ash-and kaolinite-based geopolymers. *Chemical Engineering Journal*, 89(1-3), 63-73.
- Vossoughi, F., Ostertag, C. P., Monteiro, P. J., & Johnson, G. C. (2007). Resistance of concrete protected by fabric to projectile impact. *Cement and Concrete Research*, 37(1), 96-106.
- Wang, S.-D., & Scrivener, K. L. (1995). Hydration products of alkali activated slag cement. *Cement and Concrete Research*, 25(3), 561-571.
- Wang, S.-D., & Scrivener, K. L. (2003). <sup>29</sup>Si and <sup>27</sup>Al NMR study of alkali-activated slag. *Cement and Concrete Research*, 33(5), 769-774.
- Wang, S.-D., Scrivener, K. L., & Pratt, P. (1994). Factors affecting the strength of alkali-activated slag. *Cement and Concrete Research*, 24(6), 1033-1043.
- White, C. E., Provis, J. L., Kearley, G. J., Riley, D. P., & Van Deventer, J. S. (2011). Density functional modelling of silicate and aluminosilicate dimerisation solution chemistry. *Dalton transactions*, 40(6), 1348-1355.
- Wu, Z., Shi, C., & Khayat, K. H. (2019). Investigation of mechanical properties and shrinkage of ultra-high performance concrete: Influence of steel fiber content and shape. *Composites Part B: Engineering*, 174, 107021.
- Wu, Z., Wong, H., & Buenfeld, N. (2015). Influence of drying-induced microcracking and related size effects on mass transport properties of concrete. *Cement and Concrete Research*, 68, 35-48.

- Wu, Z., Wong, H., Chen, C., & Buenfeld, N. (2019). Anomalous water absorption in cement-based materials caused by drying shrinkage induced microcracks. *Cement and Concrete Research*, 115, 90-104.
- Xu, H., & Van Deventer, J. (2000). The geopolymerisation of alumino-silicate minerals. *International Journal of Mineral processing*, 59(3), 247-266.
- Xu, H., Van Deventer, J., & Lukey, G. (2001). Effect of alkali metals on the preferential geopolymerization of stilbite/kaolinite mixtures. *Industrial & Engineering Chemistry Research*, 40(17), 3749-3756.
- Yang, H., Lin, Y., Hsiao, C., & Liu, J.-Y. (2009). Evaluating residual compressive strength of concrete at elevated temperatures using ultrasonic pulse velocity. *Fire Safety Journal*, 44(1), 121-130.
- Yang, K.-H., Song, J.-K., Ashour, A. F., & Lee, E.-T. (2008). Properties of cementless mortars activated by sodium silicate. *Construction and Building Materials*, 22(9), 1981-1989.
- Yang, T., Wu, Q., Zhu, H., & Zhang, Z. (2017). Geopolymer with improved thermal stability by incorporating high-magnesium nickel slag. *Construction and Building Materials*, 155, 475-484.
- Yardımcı, M. Y., Aydın, S., & Tuyan, M. (2017). Flexural performance of alkali-activated slag cements under quasi-static and impact loading. *Journal of Materials in Civil Engineering*, 29(1), 04016192.
- Youssf, O., Mills, J. E., & Hassanli, R. (2016). Assessment of the mechanical performance of crumb rubber concrete. *Construction and Building Materials*, 125, 175-183.
- Yuan, Z., & Jia, Y. (2021). Mechanical properties and microstructure of glass fiber and polypropylene fiber reinforced concrete: An experimental study. *Construction and Building Materials*, 266, 121048.
- Yunsheng, Z., Wei, S., & Zongjin, L. (2006). Impact behavior and microstructural characteristics of PVA fiber reinforced fly ash-geopolymer boards prepared by extrusion technique. *Journal of Materials Science*, 41(10), 2787-2794.
- Zhang, J., Maalej, M., & Quek, S. T. (2007). Performance of hybrid-fiber ECC blast/shelter panels subjected to drop weight impact. *Journal of Materials in Civil Engineering*, 19(10), 855-863.
- Zhang, Q., Ji, T., Yang, Z., Wang, C., & Wu, H.-c. (2020). Influence of different activators on microstructure and strength of alkali-activated nickel slag cementitious materials. *Construction and Building Materials*, 235, 117449.
- Zhang, Y. J., Zhao, Y. L., & Li, H. H. (2008). Structure characterization of hydration products generated by alkaline activation of granulated blast furnace slag. *Journal of Materials Science*, 43(22), 7141-7147.

Zheng, L., Huo, X. S., & Yuan, Y. (2008). Strength, modulus of elasticity, and brittleness index of rubberized concrete. *Journal of Materials in Civil Engineering*, 20(11), 692-699.